LBL-31122

Lawrence Berkeley Laboratory

UNIVERSITY OF CALIFORNIA

Materials & Chemical Sciences Division

Two-Dimensional Nuclear Magnetic Resonance Studies of Molecular Structure in Liquids and Liquid Crystals

S.P. Rucker
(Ph.D. Thesis)

July 1991

LOAN COPY
Circulates
for 4 weeks
Bldg. 50 Library.
LBL-31122
Copy 2

Prepared for the U.S. Department of Energy under Contract Number DE-AC03-76SF00098

DISCLAIMER

This document was prepared as an account of work sponsored by the United States Government. While this document is believed to contain correct information, neither the United States Government nor any agency thereof, nor the Regents of the University of California, nor any of their employees, makes any warranty, express or implied, or assumes any legal responsibility for the accuracy, completeness, or usefulness of any information, apparatus, product, or process disclosed, or represents that its use would not infringe privately owned rights. Reference herein to any specific commercial product, process, or service by its trade name, trademark, manufacturer, or otherwise, does not necessarily constitute or imply its endorsement, recommendation, or favoring by the United States Government or any agency thereof, or the Regents of the University of California. The views and opinions of authors expressed herein do not necessarily state or reflect those of the United States Government or any agency thereof or the Regents of the University of California.

LBL-31122

Two-Dimensional Nuclear Magnetic Resonance Studies of Molecular Structure in Liquids and Liquid Crystals

Steven P. Rucker

Department of Chemistry
University of California

and

Materials Sciences Division
Lawrence Berkeley Laboratory
University of California
Berkeley, California 94720

July 1991

This work was supported by the Director, Office of Energy Research, Office of Basic Energy Sciences, Materials Sciences Division, of the U.S. Department of Energy under Contract No. DE-AC03-76SF00098.

Two-Dimensional Nuclear Magnetic Resonance Studies of Molecular Structure in Liquids and Liquid Crystals

Copyright © 1991

by

Steven Paul Rucker

The U.S. Department of Energy has the right to use this thesis
for any purpose whatsoever including the right to reproduce
all or any part thereof

Two-Dimensional Nuclear Magnetic Resonance Studies of Molecular Structure in Liquids and Liquid Crystals

by

Steven Paul Rucker

Abstract

Magnetic couplings between protons, such as through-space dipole couplings, and scalar J-couplings depend sensitively on the structure of the molecule. Two-dimensional nuclear magnetic resonance experiments provide a powerful tool for measuring these couplings, correlating them to specific pairs of protons within the molecule, and calculating the structure. This work discusses the development of NMR methods for examining two such classes of problems - determination of the secondary structure of flexible molecules in anisotropic solutions, and primary structure of large biomolecules in aqueous solutions.

The anisotropic environment of liquid crystals prevents complete averaging of the proton-proton dipolar interaction, leading to intractably complex spectra. By a series of synthetic and spectroscopic steps, the residual dipole couplings for a series of alkanes (n-hexane through n-decane) are measured and assigned. These are used as experimental constraints for mean field models of the solute-solvent interaction. Such calculations yield values for the trans-gauche energy difference for the carbon-carbon bonds, and give a time-averaged picture of the alkane's conformation and

orientation within the liquid cystalline environment.

Proton J-couplings in liquid-phase molecules provide a direct measure of the bond connectivities within the molecule, from which a structure can be derived. A new heteronuclear decoupling sequence, DIPSI-2, has been employed to transfer polarization between coupled spins. This windowless radiofrequency pulse sequence generates much more efficient magnetization transfer than earlier sequences, yielding two-dimensional spectra with better cross-peak intensity and cleaner lineshapes.

Two additional developments are also discussed: the implementation of iterative schemes to the generation of multiple-pulse echo techniques, and the measurement of the geometric component of the transition probability in a two-level system. By phase-shifting the pulses of a Carr-Purcell echo train, its ability to preserve both the amplitude and phase of the magnetization is improved dramatically. These echo sequences find application in imaging experiments, where they are employed for volume selection, or improvement in signal-to-noise. The second topic involves measuring the effect of a Hamiltonian's geometry on the transition probability of a two-level system during a near-adiabatic radiofrequency sweep. This experiment verifies the existence of a component of the probability that depends only on the *shape* of the sweep profile, and not the rate of passage.

Contents

1 Introduction **1**

1.1 The Spin Hamiltonians 1

1.1.1 Zeeman Interaction 1

1.1.2 Scalar Coupling 2

1.1.3 Dipole Coupling 3

1.2 Two-Dimensional NMR 4

1.2.1 COSY 4

1.2.2 Double-Quantum Filtered COSY 7

1.3 Topological phases 9

1.3.1 Gauge Theory 9

1.3.2 Berry's Phase 12

1.3.3 Landau-Zener Theory 15

2 Conformations of Flexible Molecules **18**

2.1 Introduction 18

2.2 Experimental dipole couplings 20

2.2.1 Random Deuteration 22

2.2.2 Multiple-Quantum Filtration 24

2.2.3 Correlation Spectroscopy 25

2.2.4 Multiple-Quantum Spectroscopy 27

2.3 Experimental Results 29

2.3.1 Two-Proton Filtering 30

2.3.2 COSY Spectra 31

2.3.3 Multiple-Quantum NMR of the Methylene Chain 34

2.3.4 Reduced Temperature Corrections 38

2.3.5 Assignment of the Dipole Couplings 39

2.4 Model Calculations 64

2.4.1 Parametrization of the Models 65

2.4.2 Results and Discussion of the Model Calculations 70

2.5 Conclusions 75

3 Homonuclear Cross-Polarization **79**

3.1 Introduction 79

3.2 The TOCSY Experiment 80

3.2.1 The Isotropic Mixing Hamiltonian 80

3.3 Generating a Pure Scalar Evolution Operator 83

3.4 Cross-Polarization Schemes 86

3.4.1 One-Dimensional Experiment 86

3.4.2 Two-Dimensional Experiment 90

3.5 Comparison of Experimental Results 92

3.5.1 CW Mixing 93

3.5.2 MLEV Mixing 94

3.5.3 DIPSI Mixing 102

3.6 ROESY Interference 108

3.7 Conclusions 110

4 Iterative Carr-Purcell Trains **111**

4.1 Introduction 111

4.2 Background 112

4.3 Iterative Schemes 114

4.3.1 The MLEV Sequences 115

4.4 Simulations and Experimental Results 118

4.5 Conclusions 127

5 The Geometric Amplitude **128**

5.1 Introduction 128

5.2 Theory 130

5.3 Experimental Implementation 136

5.3.1 Generating the Hamiltonian 136

5.3.2 Measurement of P 144

5.4 Results 145

5.5 Discussion 149

5.5.1 Determination of Γ_g 149

5.5.2 Behavior with Respect to Time-Reversal 154

5.5.3 Determination of ω_1 157

5.6 Conclusions 162

6 Two-Channel Spectrometer **164**

6.1 Introduction 164

6.2 Superconducting Magnet 165

6.3 Intermediate Frequency 165

6.4 Local Oscillator 168

6.5 Radiofrequency Generation 170

6.6 Sample Probe 173

6.7 Temperature Controller 175

6.8 Receiver 176

6.9 Digital Section 178

6.9.1 Computer 178

6.9.2 Pulse Programmer 178

6.9.3 Software 179

6.9.4 Signal Distribution Box 183

6.9.5 Signal Averager 185

A Pulse Programs **189**

A.1 Pulse-acquire 189

A.2 Hahn Echo 191

A.3 2-Quantum Filter 192

A.4 Multiple-Quantum NMR 193

A.5 Quadrature Phase Test 194

List of Figures

1.1 Pulse sequence for COSY experiment 4

1.2 Spectrum for two-spin COSY experiment 6

1.3 Pulse sequence for double-quantum-filtered COSY 7

1.4 Spectrum for double-quantum-filtered COSY 10

1.5 Electronic state potential energy diagram 15

2.1 One-quantum spectrum of n-hexane 21

2.2 Overview of the experiment 23

2.3 Protonation distribution for deuterated n-hexane 24

2.4 COSY cross-peak patterns for dipole coupled spins 28

2.5 One-dimensional spectra for deuterated n-hexane 32

2.6 Numbering scheme for n-alkanes 33

2.7 Pulse sequence for two-quantum filtered COSY 34

2.8 Pulse sequence for multiple-quantum excitation 36

2.9 Six and seven-quantum spectra of n-hexane-d_6 37

2.10 COSY of n-hexane, complete view 47

2.11 COSY of n-hexane, enlarged view 48

2.12 COSY of n-hexane, central section 49

2.13 COSY of *n*-heptane, complete view 50

2.14 COSY of *n*-heptane, enlarged view 51

2.15 COSY of *n*-heptane, central section 52

2.16 COSY of *n*-octane, complete view 53

2.17 COSY of *n*-octane, enlarged view 54

2.18 COSY of *n*-octane, central section 55

2.19 COSY of *n*-nonane, complete view 56

2.20 COSY of *n*-nonane, enlarged view 57

2.21 COSY of *n*-nonane, central section 58

2.22 COSY of *n*-decane, complete view 59

2.23 COSY of *n*-decane, enlarged view 60

2.24 COSY of *n*-decane, central section 61

2.25 Comparison of geminal dipole couplings 62

2.26 Comparison of methyl-ethyl dipole couplings 63

2.27 Minimum circumference projection of an alkane 68

2.28 Orientational potential energy surfaces 74

2.29 Isomer statistics for long alkanes 78

3.1 Comparison of DIPSI and WALTZ at high power 87

3.2 Comparison of DIPSI and WALTZ at low power 88

3.3 Magnetization transfer experiments 91

3.4 Cross-polarization with a 4 kHz RF field 95

3.5 Cross-polarization with a 1.7 kHz RF field 96

3.6 Cross-polarization with a 1.2 kHz RF field 97

3.7 The MLEV-17 cross-polarization sequence 98

3.8 MLEV-17 cross-polarization; no trim pulses 101

3.9 Comparison of transfer efficiency for DIPSI, WALTZ, and MLEV . 103

3.10 Cross-polarization with 4 cycles of DIPSI-2 105

3.11 Cross-polarization with 6 cycles of DIPSI-2 106

3.12 Cross-polarization with 10 cycles of DIPSI-2 107

4.1 The Hahn echo 112

4.2 Echo train pulse sequence 119

4.3 On-resonance simulations 120

4.4 Off-resonance simulations 121

4.5 On-resonance experiments 123

4.6 Off-resonance experiments 124

4.7 Misset pulse experiments, on resonance 125

4.8 Misset pulse experiments, off-resonance 126

5.1 Avoided crossing for a two-level system 132

5.2 Crossing points in the complex time plane 133

5.3 Landau-Zener sweep 138

5.4 Non-uniform sweep 140

5.5 Sweep frequency relationships 141

5.6 Pulse sequence 146

5.7 Magnetization sweep paths 147

5.8 Transverse excursion of the magnetization 148

5.9 P vs. $1/\delta$ 150

5.10 Log(P) vs. $1/\delta$ 152

5.11 Log(P) vs. $1/\delta$; expanded view 153

5.12 $\frac{1}{2}\log(P_{B>0}/P_{B<0})$ vs. $1/\delta$ 155

5.13 Determination of the ω_1 distribuition 160

5.14 ω_1 distribution profile; experiment 161

6.1 Delta spectrometer, schematic overview 166

6.2 Static magnetic field profile 167

6.3 Quadrature phase box - Schematic 169

6.4 Frequency switch card - pcb mask 171

6.5 Radiofrequency generator box – schematic 172

6.6 Inverse detection probe – schematic 174

6.7 Temperature controller - schematic 177

6.8 The microcontrol word 180

6.9 TECMAG program commands 184

6.10 LED driver schematic 185

6.11 LED driver printed circuit board mask 186

6.12 Microcontrol word gate assignments 187

A.1 Timing diagram for data acquisition 191

List of Tables

2.1 Isomer deuteration statistics 26

2.2 Alkane reduced temperature data 38

2.3 Dipole couplings - temperature dependence 40

2.4 Dipole couplings for *n*-hexane 41

2.5 Dipole couplings for *n*-heptane 42

2.6 Dipole couplings for *n*-octane 43

2.7 Dipole couplings for *n*-nonane 44

2.8 Dipole couplings for *n*-decane 45

2.9 Mean field model alkane parameters 69

2.10 Results from mean field modelling 71

2.11 Conformer distributions - hexane, heptane, octane 72

2.12 Conformer distributions - nonane, decane 73

2.13 Ordering matrix components 75

2.14 Dipole couplings *vs.* chain length 77

3.1 Polarization rates for DIPSI *vs.* WALTZ 89

3.2 DIPSI pulse components 102

4.1 Cancellation of error terms by MLEV-4 117

4.2 Phase cycling for the MLEV sequences 117

6.1 Preamp specifications for Delta spectrometer 178

Acknowledgments

A host of people have contributed both to the work in this thesis and to my general education. First, I would like to thank Professor Alex Pines for his constant support over the past five years, and for allowing me the latitude to work on the rather eclectic variety of topics presented herein. His youthful vigor, and enthusiasm for learning, have made my stay in Berkeley most enjoyable.

My deepest thanks go to Professor A.J. Shaka, who took a first year graduate student under his wing and taught him NMR. His skill as a teacher is unparalleled, and I owe him a debt of gratitude for allowing me to work with him on the Carr-Purcell experiments and on the homonuclear cross-polarization experiments. More importantly, though, A.J. has been a tried and true friend through many a difficult time, whether running all-night experiments, or skirting death on the PCT.

I would also like to thank Professor Josef Zwanziger, who provided me the opportunity to try my hand at Berry's Phase. Joe has been not only a mentor, but also a good friend, with whom discussions of P.J. O'Rourke and Hunter Thompson mingle freely with gauge theory and magnetic resonance. Working with Joe has always been as fun as it has been educational.

Mark Rosen, Dr. Claudia Schmidt and Dr. Peter Neidig deserve thanks for all their work on the liquid crystal project. Without them, the project would be nowhere near where it is today. Dr. David Shykind and Dr. Gerard Chingas spent a lot of time with an electronics-illiterate first-year, teaching me not only the nuances

of radio-frequency electronics, but also the spectroscopy that motivates it. Mark's programming and Dave's and Gerry's help with electronics facilitated the work of Chapter 6. I also thank Dave for affording me the distinction of sharing an office with him briefly, and thus allowing me to immerse myself in an environment of irreverent humor. I thank Gerry for always having a simple and elegant solution to a thorny problem. His seat-of-the-pants intuition about electronics and NMR never ceases to amaze me.

Life in the Pines Group was anything but dull, and I would like to thank at least a subset of the people I remember for making it so much fun. Dr. Karl Mueller, Dr. Wrenn Wooten, and Mark Rosen were ever-present Roma companions – always ready for a cup of coffee and an escape from the dungeon. In fact, Karl was probably singlehandedly responsible for my wasting more money at Roma than I spent on car insurance. I thank him for this. My Berkeley years benefitted from many hours (days?) spent socializing with Dr. Jeff Chang, Dr. Tom Jarvie, Malaine Trecoske, Dr. Zbigniew Olejniczak, Dr. John Harwood, Dr. Chuck Connor, Dr. John Pearson, Bruce Black, and Dan Raftery. If I were to list all the Pinenuts who have helped shape my character, these acknowledgments would qualify for inclusion as a chapter. I therefore thank them in collective anonymity.

No discussion of the Pines Group would be complete without my deepest thanks to the matriarch of the group, Dione Carmichael. Dione provides continuity and character to an ever-changing group of 25 disparate personæ. I thank her for always being willing to lend an ear, offer a helping hand, and provide a cup of coffee (no matter how strong).

I would like to thank my family – Craig, Donald, Janet, Tom, Libby, and Mimi

– for a lifetime of love and camaraderie. The past year and a half of my life have been made extraordinarily special by the love of my fiancée, Becca.

I would never have reached this point in my career were it not for the undying love and devotion of my parents, Klaus and Daisy. They have always provided an atmosphere where learning was given the highest priority, and more importantly, they have made tremendous sacrifices to provide a better life for their four children. For their herculean efforts, we will never be able to thank them enough.

To the taxpayers of the United States,

who selflessly supported this research

Chapter 1

Introduction

1.1 The Spin Hamiltonians

Nuclear magnetic resonance (NMR) provides a singularly powerful technique for determining the structure of solvated molecules. Rapid molecular motion narrows spectral lines enough to allow measurement of chemical shift dispersion of, and magnetic couplings between, the nuclei of interest. This information, quantified in one- and two-dimensional experiments, allows the spectroscopist to determine internuclear distances and hence, the molecular structure. In this chapter, we introduce the evolution Hamiltonians governing the behavior of spin-$\frac{1}{2}$ systems under a variety of experiments, both in anisotropic solutions (*e.g.* liquid crystals) and isotropic solutions (liquids).

1.1.1 Zeeman Interaction

A spin-$\frac{1}{2}$ nucleus at equlibrium in a static magnetic field will have two quantized energy states, denoted $|\alpha\rangle$ and $|\beta\rangle$. The splitting in this two-level system is defined

by the Zeeman interaction:

$$\mathcal{H}_Z = -\gamma \mathbf{B}_o \cdot \mathbf{I}, \tag{1.1}$$

where γ is the gyromagnetic ratio of the nucleus, and $\mathbf{B}_o$ the strength of the magnetic field at the nucleus, and $\mathbf{I}$ is the spin angular momentum operator. For this Hamiltonian and subsequent ones, we work with reduced units, such that $\hbar = 1$. A more general case of the Zeeman interaction allows for differences in the electron distribution (bonding environment) about the nucleus. This tensorial interaction, known as the chemical shift, can be expressed as follows:

$$\mathcal{H}_{CS} = -\gamma \mathbf{B}_o \cdot \sigma \cdot \mathbf{I}, \tag{1.2}$$

where the tensor σ incorporates the shielding of the nucleus by its neighboring electrons. In liquid-state NMR, rapid tumbling averages the tensor elements such that only a single value remains - the isotropic chemical shift for that nuclear environment.

1.1.2 Scalar Coupling

Electron-nucleus coupling causes not only the chemical shift interaction, but also a bilinear coupling between dissimilar nuclei separated by only a few bonds. The tensorial J-coupling

$$\mathcal{H}_J = \mathbf{I}_1 \cdot \mathcal{J} \cdot \mathbf{I}_2 \tag{1.3}$$

can be divided into a traceless part

$$\mathcal{J}_{\alpha\beta}^{\overline{T}} = \mathcal{J}_{\alpha\beta} - \delta_{\alpha\beta} J \tag{1.4}$$

and a diagonal contribution

$$\mathcal{J}_{\alpha\beta}^{T} = \delta_{\alpha\beta} J, \tag{1.5}$$

where $J = \frac{1}{3}\mathrm{Tr}(\mathcal{J})$. Fast isotropic tumbling in liquids leaves only the scalar J-coupling. In ^{1}H NMR studies of liquid crystalline solvents, such as those discussed in Chapter 2, the motional averaging is sufficient to scale the anisotropic component enough that it remains unresolved.

This coupling (on the order of a few hertz) gives connectivity information (since it falls sharply with an increasing number of interstitial carbons) which can be used to solve the primary structure of large molecules. Chapter 3 describes experiments designed to help elucidate these coupling networks.

1.1.3 Dipole Coupling

In addition to the electron-mediated J-coupling, nuclei experience a direct dipole-dipole coupling of the form:

$$\mathcal{H}_D = \frac{\gamma_1\gamma_2}{r_{12}^3}\left(\mathbf{I}_1 \cdot \mathbf{I}_2 - \frac{3(\mathbf{I}_1 \cdot \vec{\mathbf{r}}_{12})(\mathbf{I}_2 \cdot \vec{\mathbf{r}}_{12})}{r_{12}^2}\right). \tag{1.6}$$

With the static magnetic field aligned along the $\hat{z}$-axis, we can expand the Hamiltonian into the familiar "dipolar alphabet" [1]:

$$\mathcal{H}_D = \frac{\gamma_1\gamma_2}{r_{12}^3}(A + B + C + D + E + F), \tag{1.7}$$

where

$$\begin{aligned}
A &= I_{1z}I_{2z}(1 - 3\cos^2\theta) \\
B &= \frac{1}{2}(I_{1z}I_{2z} - \mathbf{I}_1 \cdot \mathbf{I}_2)(1 - 3\cos^2\theta) \\
C &= -\frac{3}{2}(I_{1z}I_{2+} + I_{1+}I_{2z})\sin\theta\cos\theta e^{-i\phi} \\
D &= -\frac{3}{2}(I_{1z}I_{2-} + I_{1-}I_{2z})\sin\theta\cos\theta e^{i\phi} \\
E &= -\frac{3}{4}(I_{1+}I_{2+})\sin^2\theta e^{-2i\phi} \\
F &= -\frac{3}{4}(I_{1-}I_{2-})\sin^2\theta e^{2i\phi}.
\end{aligned} \tag{1.8}$$

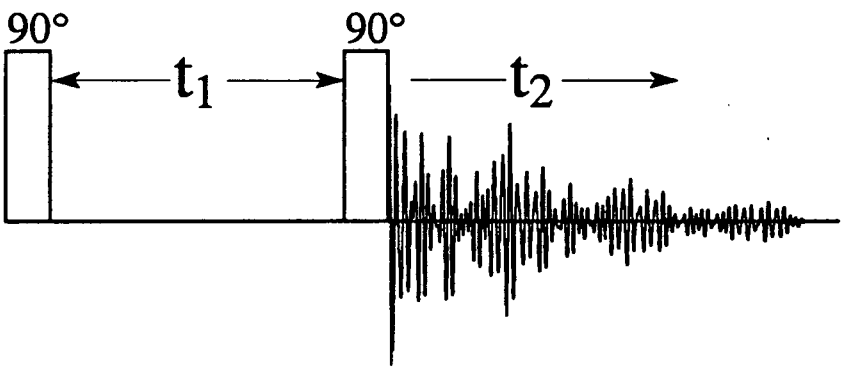

Figure 1.1: The pulse sequence for the COSY experiment.

In high field, the static field will truncate the Hamiltonian to:

$$\begin{aligned} \mathcal{H}_D &= \frac{\gamma_1\gamma_2}{r_{12}^3}(A+B) \\ &= \frac{\gamma_1\gamma_2}{2r_{12}^3}(1-3\cos^2\theta)(3I_{1z}I_{2z}-\mathbf{I}_1\cdot\mathbf{I}_2). \end{aligned} \tag{1.9}$$

Spectral intensities and splittings for coupled spin systems are derived in several references [2, 3].

1.2 Two-Dimensional NMR

1.2.1 COSY

The cross-polarization experiment follows from several earlier two-dimensional correlation experiments. The first, COSY (COrrelated SpectroscopY) [4], creates coherences between spins through *J*- or dipole coupling. Figure 1.1 shows a schematic diagram for the simplest COSY experiment. A product operator analysis [5] traces

the evolution of two coupled spins under this pulse sequence. The 90° pulse tips the spins into the transverse plane,

$$I_{1z} + I_{2z} \xrightarrow{(\frac{\pi}{2})_{\bar{x}}} -I_{1y} - I_{2y}, \tag{1.10}$$

where the spins evolve under their characteristic chemical shift and the scalar J-coupling:

$$\begin{aligned}
-I_{1y} - I_{2y} \xrightarrow{\omega_1 t_1 + \omega_2 t_1 + 2\pi J_{12} t_1 I_{1z} I_{2z}} & \\
& [-I_{1y}\cos(\omega_1 t_1) + I_{1x}\sin(\omega_1 t_1) \\
& -I_{2y}\cos(\omega_2 t_1) + I_{2x}\sin(\omega_2 t_1)]\cos(\pi J_{12} t_1) \\
& +[2I_{1x}I_{2z}\cos(\omega_1 t_1) + 2I_{1y}I_{2z}\sin(\omega_1 t_1) \\
& +2I_{1z}I_{2x}\cos(\omega_2 t_1) + 2I_{1z}I_{2y}\sin(\omega_2 t_1)]\sin(\pi J_{12} t_1).
\end{aligned} \tag{1.11}$$

After a time t_1, a 90° mixing pulse is applied. This pulse yields the observable signal:

$$\begin{aligned}
\xrightarrow{(\frac{\pi}{2})_{\bar{x}}} & \\
& [-I_{1z}\cos(\omega_1 t_1) + I_{1x}\sin(\omega_1 t_1) \\
& -I_{2z}\cos(\omega_2 t_1) + I_{2x}\sin(\omega_2 t_1)]\cos(\pi J_{12} t_1) \\
& -[2I_{1x}I_{2y}\cos(\omega_1 t_1) + 2I_{1y}I_{2x}\cos(\omega_2 t_1) \\
& +2I_{1y}I_{2z}\sin(\omega_2 t_1) + 2I_{1z}I_{2y}\sin(\omega_1 t_1)]\sin(\pi J_{12} t_1).
\end{aligned} \tag{1.12}$$

Evolution under the chemical shift and J-coupling interactions during t_2 gives the observable magnetization:

$$\begin{aligned}
\xrightarrow{\omega_1 t_1 + \omega_2 t_1 + 2\pi J_{12} t_1 I_{1z} I_{2z}} & \\
& I_{1x}\sin(\pi J_{12} t_1)\sin(\pi J_{12} t_2)\sin(\omega_1 t_1)\cos(\omega_2 t_1)
\end{aligned}$$

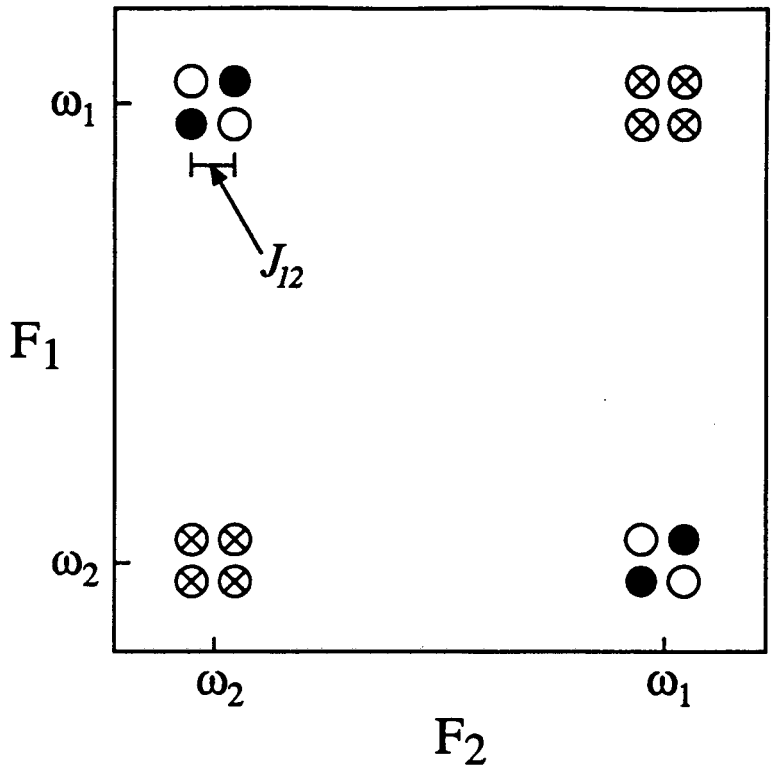

Figure 1.2: Spectrum for two spins-$\frac{1}{2}$ for a COSY experiment. The filled circles, (•), denote peaks with positive intensity, and the open circles, (○), denote negative intensity. The cross-peaks have an antiphase absorption structure, while the diagonal peaks (⊗) have a dispersive character.

$$
\begin{aligned}
&+I_{1x}\cos(\pi J_{12}t_1)\cos(\pi J_{12}t_2)\sin(\omega_1 t_1)\cos(\omega_2 t_1)\\
&+I_{1y}\sin(\pi J_{12}t_1)\sin(\pi J_{12}t_2)\sin(\omega_1 t_1)\sin(\omega_2 t_1)\\
&+I_{1y}\cos(\pi J_{12}t_1)\cos(\pi J_{12}t_2)\sin(\omega_1 t_1)\sin(\omega_2 t_1)\\
&+I_{2x}\sin(\pi J_{12}t_1)\sin(\pi J_{12}t_2)\sin(\omega_1 t_1)\cos(\omega_2 t_1)\\
&+I_{2x}\cos(\pi J_{12}t_1)\cos(\pi J_{12}t_2)\sin(\omega_1 t_1)\cos(\omega_2 t_1)\\
&+I_{2y}\sin(\pi J_{12}t_1)\sin(\pi J_{12}t_2)\sin(\omega_1 t_1)\sin(\omega_2 t_1)\\
&+I_{2y}\cos(\pi J_{12}t_1)\cos(\pi J_{12}t_2)\sin(\omega_1 t_1)\sin(\omega_2 t_1). \qquad (1.13)
\end{aligned}
$$

After double Fourier transformation, the resultant spectrum has antiphase ab-

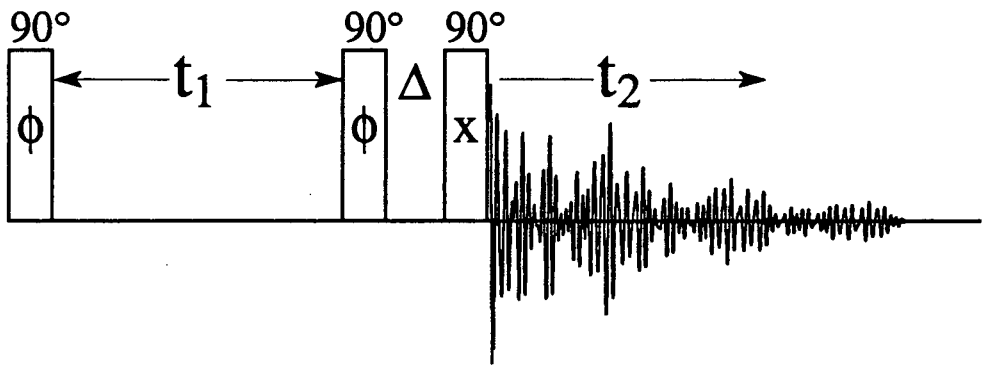

Figure 1.3: The traditional 90° – t_1 – 90° sequence for COSY is followed immediately by another 90° pulse to convert double-quantum coherence into observable magnetization.

sorption quartets (with an interpeak splitting the size of J) at the cross-peak positions (ω_1, ω_2) and (ω_2, ω_1). There are dispersive diagonal quartets at (ω_1, ω_1) and (ω_2, ω_2). Figure 1.2 shows the spectral pattern for the two-spin system.

1.2.2 Double-Quantum Filtered COSY

For complicated spin networks, it is often of value to select signal only from coupling networks of a certain size. Chapter 2 presents such an example – the contribution from mono-protonated deutero-alkanes must be removed from the COSY spectrum of diprotic deuterated alkanes. Double-quantum filtered correlation spectroscopy [6, 7] allows this by filtering the signal through a double-quantum coherence, as shown in Figure 1.3. Considering both the observable and non-observable terms in the final

density matrix (Equation 1.12) for the COSY experiment treated above, gives:

$$\begin{aligned}\rho &= [-I_{1z}\cos(\omega_1 t_1) + I_{1x}\sin(\omega_1 t_1) \\ &\quad -I_{2z}\cos(\omega_2 t_1) + I_{2x}\sin(\omega_2 t_1)]\cos(\pi J_{12} t_1) \\ &\quad -[2I_{1x}I_{2y}\cos(\omega_1 t_1) + 2I_{1y}I_{2x}\cos(\omega_2 t_1) \\ &\quad +2I_{1y}I_{2z}\sin(\omega_2 t_1) + 2I_{1z}I_{2y}\sin(\omega_1 t_1)]\sin(\pi J_{12} t_1). \qquad (1.14)\end{aligned}$$

The two-spin coherence terms can be expanded into double-quantum and zero-quantum operators $I_{1x}I_{2y} + I_{1y}I_{2x}$ and $I_{1x}I_{2y} - I_{1y}I_{2x}$:

$$\begin{aligned}&[-I_{1z}\cos(\omega_1 t_1) + I_{1x}\sin(\omega_1 t_1) \\ &-I_{2z}\cos(\omega_2 t_1) + I_{2x}\sin(\omega_2 t_1)]\cos(\pi J_{12} t_1) \\ &+[\frac{1}{2}[(2I_{1x}I_{2y} + 2I_{1y}I_{2x}) - (2I_{1y}I_{2x} - 2I_{1x}I_{2y})]\cos(\omega_1 t_1) \\ &+\frac{1}{2}[(2I_{1x}I_{2y} + 2I_{1y}I_{2x}) + (2I_{1y}I_{2x} - 2I_{1x}I_{2y})]\cos(\omega_2 t_1) \\ &+2I_{1y}I_{2z}\sin(\omega_2 t_1) + 2I_{1z}I_{2y}\sin(\omega_1 t_1)]]\sin(\pi J_{12} t_1). \qquad (1.15)\end{aligned}$$

Rather than allowing these coherences to evolve under the weak coupling Hamiltonian, we immediately apply another 90°_x pulse. This pulse, in conjunction with proper phase-cycling for ϕ ($\phi = 0, \frac{\pi}{2}, \pi, \frac{3\pi}{2}$) will convert the double-quantum coherence to antiphase magnetization at the beginning of the detection period,

$$[\tfrac{1}{2}(2I_{1x}I_{2y} + 2I_{1y}I_{2x})\cos(\omega_1 t_1) + \tfrac{1}{2}(2I_{1x}I_{2y} + 2I_{1y}I_{2x})\cos(\omega_2 t_1)]\sin(\pi J_{12} t_1)$$

$$\downarrow$$

$$[\tfrac{1}{2}(2I_{1x}I_{2z} + 2I_{1z}I_{2x})\cos(\omega_1 t_1) + \tfrac{1}{2}(2I_{1x}I_{2z} + 2I_{1z}I_{2x})\cos(\omega_2 t_1)]\sin(\pi J_{12} t_1). \qquad (1.16)$$

Under the weak coupling Hamiltonian, the system then evolves with the following observable magnetization during t_2:

$$\xrightarrow{\omega_1 t_1+\omega_2 t_1+2\pi J_{12} t_1 I_{1z} I_{2z}}$$

$$\begin{aligned}
&+\frac{1}{2} I_{1y} \sin(\pi J_{12} t_1) \sin(\pi J_{12} t_2) \sin(\omega_1 t_1) \cos(\omega_1 t_2) \\
&-\frac{1}{2} I_{1x} \sin(\pi J_{12} t_1) \sin(\pi J_{12} t_2) \cos(\omega_1 t_1) \sin(\omega_1 t_2) \\
&+\frac{1}{2} I_{2y} \sin(\pi J_{12} t_1) \sin(\pi J_{12} t_2) \sin(\omega_1 t_1) \cos(\omega_2 t_2) \\
&-\frac{1}{2} I_{2x} \sin(\pi J_{12} t_1) \sin(\pi J_{12} t_2) \cos(\omega_1 t_1) \sin(\omega_2 t_2) \\
&+\frac{1}{2} I_{1y} \sin(\pi J_{12} t_1) \sin(\pi J_{12} t_2) \cos(\omega_2 t_1) \cos(\omega_1 t_2) \\
&-\frac{1}{2} I_{1x} \sin(\pi J_{12} t_1) \sin(\pi J_{12} t_2) \sin(\omega_2 t_1) \sin(\omega_1 t_2) \\
&+\frac{1}{2} I_{2y} \sin(\pi J_{12} t_1) \sin(\pi J_{12} t_2) \sin(\omega_2 t_1) \cos(\omega_2 t_2) \\
&-\frac{1}{2} I_{2x} \sin(\pi J_{12} t_1) \sin(\pi J_{12} t_2) \sin(\omega_2 t_1) \sin(\omega_2 t_2). \qquad (1.17)
\end{aligned}$$

Double Fourier transformation (with a hypercomplex transform) gives a spectrum of the form shown in Figure 1.4. Such a spectrum does not suffer from the broad dispersive tails of the diagonal peaks which afflict the regular COSY (thus obscuring cross-peaks close to the diagonal). Also, in the case of the alkane studies presented in Chapter 2, the double-quantum filter will cancel the signal contribution from one-proton isomers.

1.3 Topological phases

1.3.1 Gauge Theory

In order to define reference frames for testing physical laws, we often make reference to *gauge transformations* [8]. In quantum mechanics, these comprise unitary oper-

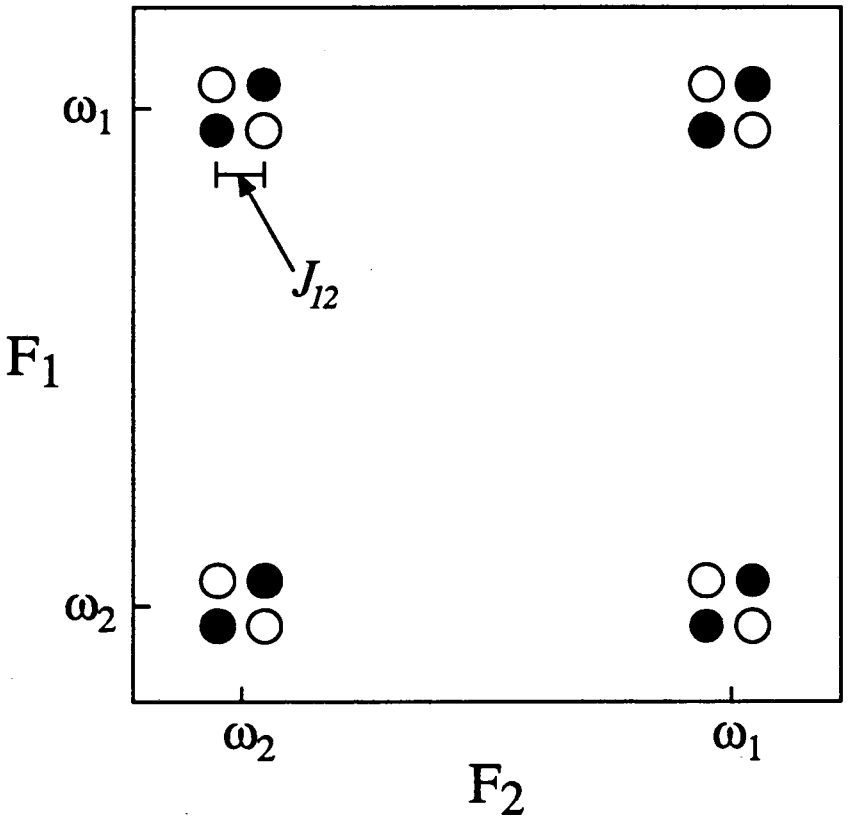

Figure 1.4: In the double-quantum filtered COSY, both the diagonal and cross-peaks have absorptive antiphase quartet structure.

ations which allow one to transform coordinates for a system under examination. The gauge of a system is characterized by the symmetry inherent in the system, and the classification for the gauge is based on the underlying symmetry group describing the system. If, for example, we consider a one-parameter system, with propagators of the form $\exp(i\theta)$, then successive unitary operations commute, and the gauge group is Abelian, since the underlying symmetry group is $U(1)$. The simplest such case would be spin-$\frac{1}{2}$, where we can write the 2×2 Hermitian density matrix, ρ_S

$$\rho_S = \frac{1}{2}(1 + \vec{p} \cdot \vec{\sigma}) \tag{1.18}$$

where $\vec{p}$ is the polarization vector, and $\vec{\sigma}$ is a vector of Pauli spin matrices. Evolution under the gauge transformation then gives:

$$\begin{pmatrix} U(1) & 0 \\ 0 & U(1) \end{pmatrix} \begin{pmatrix} \rho_a & 0 \\ 0 & \rho_b \end{pmatrix} \begin{pmatrix} U(1) & 0 \\ 0 & U(1) \end{pmatrix}^{\dagger} = \begin{pmatrix} \rho_a & 0 \\ 0 & \rho_b \end{pmatrix}. \tag{1.19}$$

In the case of rotation operators quantified by the three Euler angles, the unitary operations do not commute, so the non-Abelian symmetry groups, $SO(3)$ for classical rotations, and $SU(2)$ for spin-angular momentum, lead to a non-Abelian gauge. Another feature of the gauge symmetry is that Abelian gauges, having the form

$$U = \exp\left[i(\text{Diagonal matrix})\right] \tag{1.20}$$

can cause a phase shift of the wave function, but can not induce coherences. A non-Abelian gauge, on the other hand, has the form

$$U = \exp\left[i(\text{Non}-\text{diagonal matrix})\right] \tag{1.21}$$

and can both cause phase changes and generate coherences.

1.3.2 Berry's Phase

A quantum system evolving adiabatically under some Hamiltonian, $\mathcal{H}$, will remain in an instantaneous eigenstate of that Hamiltonian. The adiabatic theorem [9] states that if the Hamiltonian is brought back to its original form, then a given eigenstate of that system will also be returned to itself, apart from some phase, γ. Berry has shown that this phase factor has contributions not only from the dynamical phase, but also from a term that depends only on the geometry of the Hamiltonian's path in parameter space [10]. This Berry phase exemplifies an anholonomy – the extent to which certain system variables fail to return to their original values after the system undergoes some evolution.

Following the derivation of Berry, we assume a Hamiltonian of the form $\mathcal{H}(R(t))$ where $R(t)$ describe the time-dependent parametrization of the Hamiltonian (*e.g.* R could assume the form $R = (x, y, z, ..)$ in cartesian space, or $R = (I_x, I_y, I_z)$ in spin space). We allow the system to evolve over a closed path, denoted C, in parameter space, *i.e.* $R(T) = R(0)$. To assure adiabaticity, T is chosen to be large. Evolution of the system is governed by the Schrödinger equation:

$$\mathcal{H}(R(t))|\psi(t)\rangle = i\hbar|\dot{\psi}(t)\rangle \tag{1.22}$$

such that we can choose a basis set, $|n(R)\rangle$, with eigenvalues, $E_n(R)$, satisfying the equation

$$\mathcal{H}(R)|n(R)\rangle = E_n(R)|n(R)\rangle. \tag{1.23}$$

A system initially in state $|n(R(0))\rangle$ will evolve under the influence of $\mathcal{H}$ into state $|n(R(t))\rangle$ at time t. The state of the system at that time is

$$|\psi(t)\rangle = \exp\left[\frac{-i}{\hbar}\int_0^t dt' E_n(R(t'))\right]\exp(i\gamma_n(t))|n(R(t))\rangle. \tag{1.24}$$

The first exponential represents the dynamical phase, and the second represents the geometrical, or Berry, phase. This phase, γ_n is non-integrable, meaning it can not be written as a function of R, nor is $\gamma_n(t) = \gamma_n(0)$. To derive an expression for γ_n, we substitute $|\psi(t)\rangle$ from Equation 1.24 back into Equation 1.22, and get

$$\dot{\gamma}_n(t) = i\langle n(R(t))|\nabla_R n(R(t))\rangle \cdot \dot{R}(t). \tag{1.25}$$

This gives a total geometric phase contribution for the trajectory of

$$\gamma_n(C) = i \oint \langle n(R)|\nabla_R n(R)\rangle \cdot dR \tag{1.26}$$

which is dependent only on the geometry of the circuit, and contains no time information about the trajectory. This line integral can be solved more conveniently by applying Stokes' theorem to convert it to a surface integral,

$$\begin{aligned} \gamma_n(C) &= -\mathrm{Im} \iint_C dS \cdot \nabla \times \langle n|\nabla n\rangle \\ &= -\mathrm{Im} \iint_C dS \cdot \langle \nabla n| \times |\nabla n\rangle \\ &= -\mathrm{Im} \iint_C dS \cdot \sum_{m\neq n} \langle \nabla n|m\rangle \times \langle m|\nabla n\rangle. \end{aligned} \tag{1.27}$$

The line integral over the circuit has now been replaced by a surface integral over the area enclosed by the circuit in parameter space. The integrand is obtained by substitution from Equation 1.23 as follows:

$$\langle m|\nabla n\rangle = \frac{\langle m|\nabla \mathcal{H}|n\rangle}{(E_n - E_m)}. \tag{1.28}$$

Substituting this result into the surface integral above, gives:

$$\gamma_n(C) = -\iint_C dS \cdot V_n(R), \tag{1.29}$$

where the integrand, $V_n(R)$, is

$$V_n(R) = \mathrm{Im} \sum_{m\neq n} \frac{\langle n(R)|\nabla_R \mathcal{H}(R)|m(R)\rangle \times \langle m(R)|\nabla_R \mathcal{H}(R)|n(R)\rangle}{(E_m(R) - E_n(R))^2}. \tag{1.30}$$

Any solutions to the Schrödinger equation (Equation 1.23) can be used to define $V_n(R)$, and the value of the geometric phase depends only on the enclosed area of the path $R(t)$.

Both classical and quantum mechanics present many examples of this purely geometric phase [11, 12, 13]. Parallel transport (no local rotation) of a pencil, for example, along a path on the surface of the sphere can result in an accumulated phase equal to the solid angle subtended by the circuit. If a pencil at the north pole is brought to the equator along a line of longitude (for $\frac{\pi}{2}$ radians), traversed along the equator for $\frac{\pi}{2}$ radians, and then translated back up to the north pole, it will point in a direction 90° away from the original. This value equals $\Omega(C)$, the solid angle included by the circuit on the sphere surface. The value of the accumulated phase depends *only* on the *geometry* of the circuit, and contains no dynamical information about how fast the circuit was traversed.

Berry's phase has been observed in a host of physical systems. Polarized light passing through a coiled optical fiber will have the polarization direction rotated by an amount proportional to the helicity of the fiber [14, 15]. In nuclear magnetic and quadrupole resonance, spins evolving in a slowly varying magnetic field exhibit a geometric phase [16, 17, 18, 19]. The effect of the geometric phase of electronic wave functions upon nuclear wave functions in Jahn-Teller systems has been observed in molecular spectroscopy [20, 21, 22]. Classically, Berry's phase has been applied to analyze systems as diverse as classical oscillators [23, 24], and the propulsion of deformable bodies in non-viscous media [25]. For a thorough review of the research to date, the reader is encouraged to consult Zwanziger *et al.* [26].

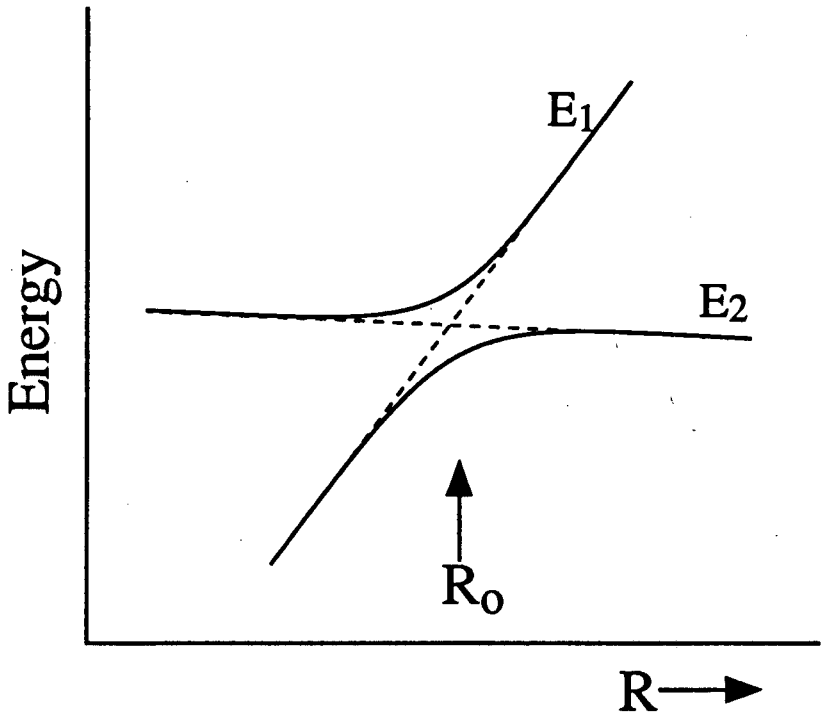

Figure 1.5: Zener *et al.* discuss adiabatic evolution in terms of the transition probability for a molecule to pass from one potential surface to the other. The states ψ_1 and ψ_2 describe the adiabatic basis where there is no exchange between the states.

1.3.3 Landau-Zener Theory

Studies of the Berry phase involve the evolution of a system under an adiabatically changing Hamiltonian. Zener *et al.* [27, 28] first calculated an expression for the transition probability for a two-level system as a function of the adiabaticity of evolution. The problem was first couched in terms of molecular electronic states such as those pictured in Figure 1.5. The system can be described, as a function of internuclear separation, R, by the wave function ψ:

$$\psi\left(\frac{x}{R}\right) = a_1(R)\psi_1\left(\frac{x}{R}\right) + a_2(R)\psi_2\left(\frac{x}{R}\right). \tag{1.31}$$

Assuming the Born-Oppenheimer separation of nuclear and electronic coordinates, this gives the state of the electron wave function as a function of explicit position, x, depending implicitly on the internuclear separation, R. We seek to develop an expression for the transition probability between the state

$$a_1 = 0 \qquad |a_2| = 1 \tag{1.32}$$

and

$$|a_1| = 1 \qquad a_2 = 0. \tag{1.33}$$

Zener undertook the solution of this problem by considering pure states, ϕ_1 and ϕ_2 which can be written as linear combinations of ψ_1 and ψ_2. We can then write:

$$\begin{aligned} \mathcal{H}\phi_1 &= \varepsilon_1\phi_1 + \varepsilon_{12}\phi_2 \\ \mathcal{H}\phi_2 &= \varepsilon_{12}\phi_1 + \varepsilon_2\phi_2. \end{aligned} \tag{1.34}$$

If we assume that the center-of-mass motion is negligible, we can rewrite the coordinate system as a function of the internuclear separation, and consider the difference between the eigenstates as a linear function of time

$$\frac{1}{\hbar}(\varepsilon_1 - \varepsilon_2) = 2\alpha t. \tag{1.35}$$

The eigenvalues of ψ_1 and ψ_2 (E_1 and E_2) fall on the nonintersecting hyperbolas. The states ϕ_1 and ϕ_2, on the other hand, cross at the transition point. E_1 and E_2 approach each other only as closely as $2\varepsilon_{12}(R_o)$.

Substitution into the Schrödinger equation then gives

$$\left(\mathcal{H} - \frac{\hbar}{i}\frac{\delta}{\delta t}\right)\left(c_1(t)e^{\frac{i}{\hbar}\int \varepsilon_1 dt}\phi_1(x) + c_2(t)e^{\frac{i}{\hbar}\int \varepsilon_2 dt}\phi_2(x)\right) = 0. \tag{1.36}$$

which gives:

$$
\begin{aligned}
-i\hbar\frac{\delta c_1(t)}{\delta t} &= \varepsilon_{12}e^{\frac{-2i}{\hbar}\int(\varepsilon_1-\varepsilon_2)dt}c_2(t) \\
-i\hbar\frac{\delta c_2(t)}{\delta t} &= \varepsilon_{12}e^{\frac{2i}{\hbar}\int(\varepsilon_1-\varepsilon_2)dt}c_2(t).
\end{aligned}
\tag{1.37}
$$

From the initial conditions,

$$
\begin{aligned}
c_1(-\infty) &= 0 \\
|c_2(-\infty)| &= 1
\end{aligned}
\tag{1.38}
$$

we can write a transition probability, P

$$
P = |c_2(\infty)|^2 = 1 - |c_1(\infty)|^2. \tag{1.39}
$$

After solution of the differential equations (1.37), we get transition probability,

$$
P = \exp\left(\frac{-\pi\varepsilon_{12}^2}{\alpha}\right). \tag{1.40}
$$

Thus, the transition probability is given in terms of the adiabaticity of the passage through the avoided crossing. As ε_{12} decreases (adiabatic passage), the transition probability for $\psi_1 \rightarrow \psi_2$ becomes vanishingly small. These calculation assume a time-independent Hamiltonian. The discussion of non-adiabatic transition probabilities in Chapter 5 extends this treatment to the case of time-varying Hamiltonians.

Chapter 2

Conformations of Flexible Molecules

2.1 Introduction

Liquid crystals provide an excellent solvent environment for structural studies of flexible molecules. A reasonable first step towards determining the structure of such a molecule would be to measure (pairwise) the distances between all its protons. Magnetic dipole couplings between the protons allow us to do exactly this. The anisotropy of the solvent environment prevents complete averaging of the intramolecular dipole couplings in the solute molecule, while allowing enough motion to yield motionally narrowed spectra. The residual dipole couplings (dependent both on the interproton distance and orientation) can serve as experimental constraints for mean field models, which allow us to develop a picture of the solute molecule's conformation and orientation in solution.

Since the first narrow-line NMR spectrum of a solute dissolved in a liquid crys-

tal [29], various studies have been undertaken towards using NMR in liquid crystals for molecular structure determination [30, 31, 32, 33, 34, 35, 36]. In some cases, the spectrum of the fully protonated molecule was analyzed, while in others selective or random deuteration was used to simplify the spectra. It was quickly realized that conventional one-dimensional proton NMR spectra rapidly become intractable with increasing molecular size and number of protons, and also uninterpretable for anything other than small rigid or highly symmetrical molecules.

One solution for somewhat larger molecules is to study the deuteron quadrupole couplings of the corresponding isotopically labeled molecules. However, the spectral simplicity thus achieved has a price — the quadrupole couplings are smaller in number than the dipole couplings and they provide little information about internuclear distances. An alternative is to use proton NMR of randomly deuterated molecules to determine the proton dipole-dipole couplings [37, 38, 39]. The determination of dipole couplings has proved particularly convenient when random deuteration is combined with two-dimensional and multiple-quantum NMR techniques [40, 41].

For flexible molecules, the observed dipole couplings between proton pairs i–j, $\langle D_{ij} \rangle$, are averages over complex molecular motions and cannot be interpreted directly in terms of molecular structure and orientation. The averaging (indicated by angular brackets $\langle\ \rangle$) involves both the interproton distance r_{ij} and the angle θ_{ij} between the vector $\mathbf{r}_{ij}$ and the external magnetic field:

$$\langle D_{ij} \rangle = -\frac{h\gamma^2}{4\pi^2} \left\langle \frac{1}{r_{ij}^3} (3\cos^2\theta_{ij} - 1) \right\rangle . \tag{2.1}$$

A priori, a separation of the coordinates r_{ij} and θ_{ij} is not possible, and models for the molecular motion are required to analyze the molecular structures and orientations. Earlier studies of the dipole couplings of n-hexane assumed that the orienta-

tional order is the same (the average) for all conformations of the molecule [42, 2]. We have used two newer models [43, 44] (where the ordering in solution is different for each conformer) to study the solution behavior of a series of n-alkanes. The models were originally developed for analysis of quadrupole splittings in perdeuterated alkyl chains [43, 45], but applying them with proton dipole couplings as experimental constraints gives a more rigorous test of the theories. We anticipate that the full set of experimental dipole couplings presented in this work provides a more rigorous test of such models.

This chapter details the spectroscopic studies of the alkanes from n-hexane through n-decane dissolved in a nematic liquid crystal, and the information obtained from these statistical mechanical models for the solvation. Section 2.2 outlines the synthetic and spectroscopic steps required to measure the dipole splittings in the alkane molecule. The assignment of the dipole splittings for the series are presented in Section 2.3 and its subsections. Applying the dipole couplings as experimental constraints for mean field calculations allows the separation of radial and angular contributions to the observed splitting. Furthermore, the models give information about the rotational energetics within the alkyl chain. Section 2.4 discusses these calculations. Section 2.5 concludes with a brief discussion of possible extensions of these experiments to more complicated molecules.

2.2 Experimental dipole couplings

One of the difficulties with high resolution NMR spectra in liquid crystals is the exponential rise in the number of transitions with the number (n) of coupled proton spins. Yet such complexity represents a vast redundancy since the unknowns in the

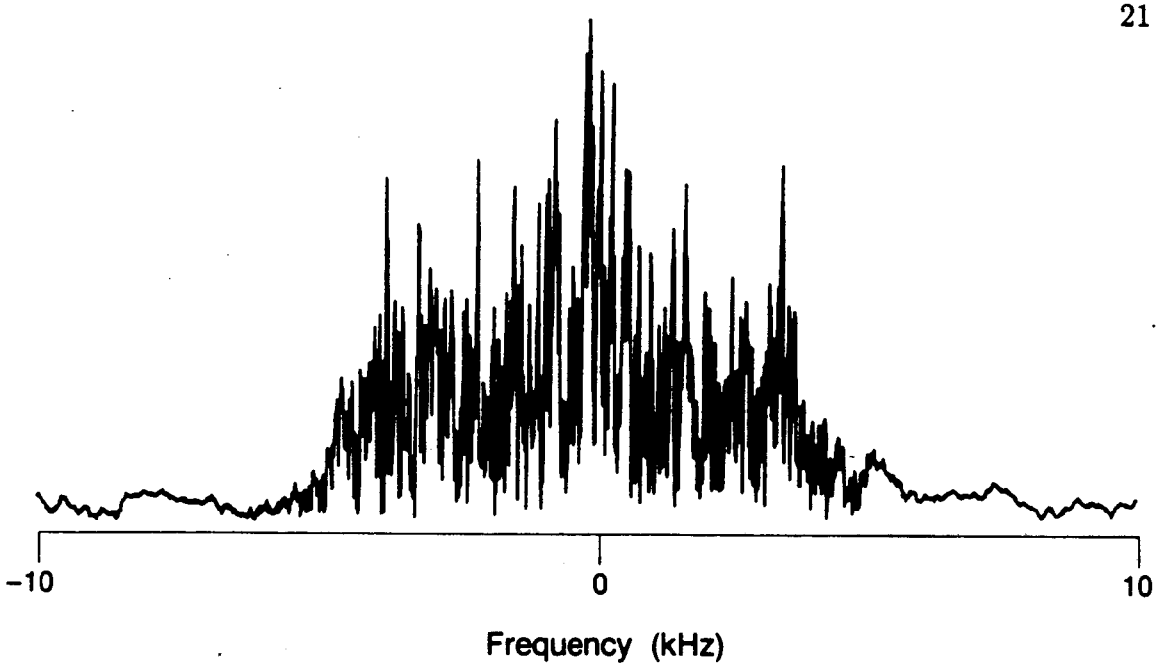

Figure 2.1: A simple Hahn echo acquisition of the spectrum of a solvated alkane, such as the n-hexane pictured here, is too complicated to interpret.

spin Hamiltonian,

$$\mathcal{H} = \sum_i \langle \delta_i \rangle I_{zi} + \frac{1}{2} \sum_{i<j} \langle D_{ij} \rangle (3 I_{zi} I_{zj} - \mathbf{I}_i \cdot \mathbf{I}_j), \tag{2.2}$$

are at most n averaged chemical shifts $\langle \delta_i \rangle$ and $n(n-1)/2$ dipole couplings $\langle D_{ij} \rangle$. For example, for the fourteen protons in n-hexane there are only three distinct chemical shifts and sixteen dipole couplings, but there are about 60,000 one-quantum transitions. Figure 2.1 shows the intractably complex one-quantum spectrum of n-hexane in a nematic liquid crystal; the proton chemical shifts and dipole couplings cannot be determined from such a spectrum.

A solution to this problem is provided by a series of synthetic and spectroscopic steps, the first three of which are represented in the scheme of Figure 2.2. The idea is to replace the intractable spectrum of a many-spin system by a superposition of simpler spectra of two-proton systems. Non-selective (random) deuteration reduces the number of protons on the solute molecules from $2n+2$ to primarily one, two, or

three; multiple-quantum spectroscopic filtering then essentially eliminates the signal from all but the two-proton molecules. Two-dimensional correlation spectroscopy facilitates the determination and assignment of dipole splittings between the proton pairs by unfolding the superposed two-spin spectra along a second axis. Multiple quantum spectroscopy, in conjunction with the correlation spectroscopy, helps in assigning the splittings to specific protons on the molecule.

2.2.1 Random Deuteration

Since the dipole splitting we seek to measure is a two-body interaction, we can envision the ideal situation where our sample comprises a series of alkane molecules, each with only two protons remaining (with one sample representing each possible proton pair). As a first step towards this goal, non-selective deuteration of the hexane molecule yields a statistical mixture of partially protonated molecules. Non-selective deuteration is far less synthetically demanding than specific deuteration, yet is satisfactory, since the success of the NMR experiments described here depend only on having all pairs of protons represented.

Through spectroscopic steps, we can overcome the non-ideality of having all the deuterated species mixed together. The probability of finding m protons on a statistically deuterated molecule is:

$$P(m) = d^{n-m}(1-d)^m \binom{n}{m}, \tag{2.3}$$

where d is the degree of deuteration ($0 \leq d \leq 1$), n the total number of hydrogen sites, and m the number of unsubstituted protons. The factor $\binom{n}{m}$ accounts for the number of ways that m distinct protons can be chosen from a pool of n protons. The degree of deuteration (d) is chosen so that the maximum of $P(m)$ occurs near

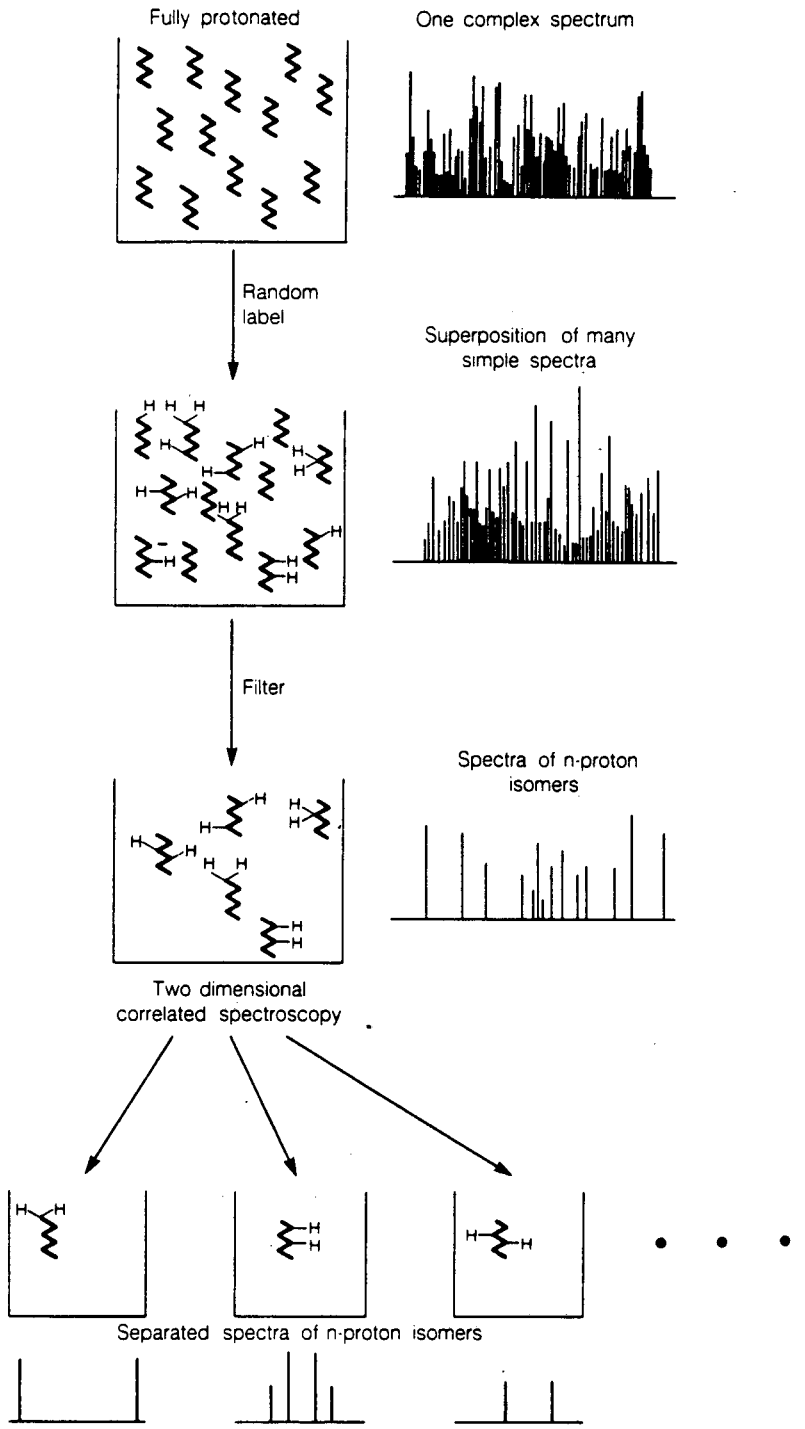

Figure 2.2: Random deuteration reduces the complexity of the $2n + 2$-proton spin systems to predominantly two-proton species. Multiple-quantum filtration and correlation spectroscopy select signal only from those molecules having two protons, and spread the signal over two frequency dimensions, allowing the dipole splittings to be measured and assigned.

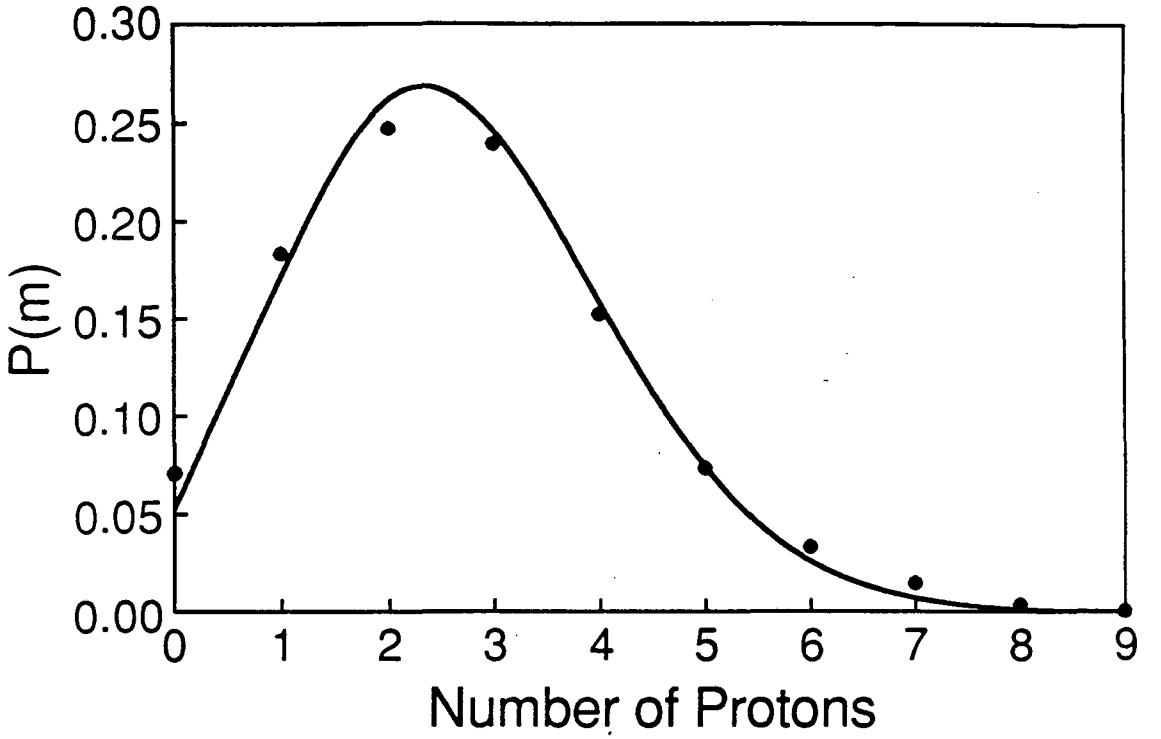

Figure 2.3: n-Hexane non-selectively deuterated to a level of $d = 0.81$ has predominantly two protons remaining on the molecule. There is still significant contribution to the signal from isomers with one proton, or more than two protons, remaining. The filled circles, (•), correspond to the experimentally determined mass spectrum.

$m = 2$. Figure 2.3 illustrates the protonation profile for a typical sample (n-hexane, with $d = 0.81$) used in our studies. Two- and three-proton species are the most abundant.

2.2.2 Multiple-Quantum Filtration

A one-quantum proton NMR spectrum of the non-selectively deuterated n-hexane yields a superposition of subspectra from the different isotopically labeled species in the mixture, with relative intensities determined by the symmetry-dictated isomer

distribution [46, 47]. Table 2.1 gives some statistical information for the series of n-alkanes at the optimum deuteration level (the one with the highest two-proton probability). Since the dipole coupling is a two-spin interaction, we are interested primarily in the two-proton isomers and seek to measure exclusively the NMR signal from these species. Two-quantum filtered spectroscopy [7, 6, 48], effected through coaddition of phase-shifted experiments, partially achieves this goal by selecting only coherences of order two or higher for detection. This removes signal from one-proton isomers. Still greater selectivity in multiple-quantum filtration can be achieved by averaging spectra with different multiple-quantum evolution times. In molecules with more than two protons, two-quantum coherence will be modulated by couplings to other protons, and signals from molecules with an odd number of protons will be averaged away. Signals from higher even-order coherences ($m = 4, 6, 8 \ldots$) still remain, but with minimal intensity, because of the low concentration of molecules giving rise to such signals (molecules with four or more protons, *cf.* Table 2.1) and because the intensity is distributed over many transitions.

2.2.3 Correlation Spectroscopy

The combination of random deuteration and multiple-quantum filtration reduces signals from all but two-proton molecules. Dipole splittings in the resulting one-dimensional spectrum can still not be assigned, though. Two-dimensional spectroscopy [49] is then used to separate the subspectra from different isomers by correlating peaks from the same subspectrum. Two-quantum-filtered correlation spectroscopy (COSY) [4] yields square patterns in the spectrum which elucidate correlated spins. The position of the square identifies the coupled spins, and the

Table 2.1: Distribution of isomers for optimally deuterated *n*-alkanes. Below each alkane, the deuteration level is listed in percent. P(m) gives the probability of finding m protons the a molecule at the stated deuteration level. For m protons, there are Z(m) NMR-distinguishable ways of arranging those protons. For the two-proton case, this corresponds to the number of dipole couplings. P(m)/Z(m) roughly indicates the attenuation in signal-to-noise as the chain length increases, since there is a lower probability of finding two-proton isomers, and an increasing number of ways to distribute the signal from them.

n-alkane		Number of protons remaining					
(%-deut.)		0	1	2	3	4	5
n-hexane	P(m)	.12105	.27589	.29193	.19009	.08510	.02771
(86%)	Z(m)	1	3	16	38	86	133
	P(m)/Z(m)	.12105	.09196	.01825	.00500	.00099	.00021
n-heptane	P(m)	.10772	.25754	.28863	.20126	.09774	.03505
(87%)	Z(m)	1	4	22	67	172	327
	P(m)/Z(m)	.10772	.06439	.01312	.00300	.00057	.00011
n-octane	P(m)	.12275	.27308	.28689	.18911	.08765	.03033
(89%)	Z(m)	1	4	29	102	316	700
	P(m)/Z(m)	.12275	.06827	.00989	.00185	.00028	.00004
n-nonane	P(m)	.12157	.27017	.28518	.19012	.08978	.03192
(90%)	Z(m)	1	5	37	156	541	1405
	P(m)/Z(m)	.12157	.05403	.00771	.00122	.00016	.00002
n-decane	P(m)	.12558	.27323	.28374	.18708	.08788	.03129
(91%)	Z(m)	1	5	46	218	874	2577
	P(m)/Z(m)	.12558	.05464	.00617	.00086	.00010	.00001

size of the square gives a measure of the strength of the coupling.

The two-dimensional patterns expected for two-spin systems are depicted in Figure 2.4, which shows the two-dimensional COSY patterns expected for A_2 and AB spin systems, assuming that J couplings can be neglected. With the COSY experiment, an A_2 system results in a square with sides of length

$$s = \frac{3}{2}\langle D_{ij}\rangle. \tag{2.4}$$

For a coupled AB system, the COSY patterns are more complex: the length of a side on the outermost square of the AB pattern is given by

$$s = \langle D_{ij}\rangle + \sqrt{\langle D_{ij}\rangle^2/4 + (\langle\delta_i\rangle - \langle\delta_j\rangle)^2}. \tag{2.5}$$

The average chemical shift of the two protons of a coupled pair can be read off from the position of the center of the peak pattern, and the dipole coupling can be determined from the magnitude of the splitting., by inverting Equation 2.5 to yield:

$$\langle D_{ij}\rangle = \tfrac{4}{3}s - \tfrac{2}{3}\sqrt{s^2 + 3(\Delta\nu)^2}. \tag{2.6}$$

2.2.4 Multiple-Quantum Spectroscopy

The synthetic and spectroscopic methods described thus far yield only the magnitude of the dipole couplings and average chemical shifts of the coupling partners. In the next step, multiple-quantum spectroscopy [49, 50] of the n-alkane with perdeuterated methyl, ethyl, or propyl endgroups (an eight-spin system) [51] can be used to help determine the relative signs of the couplings and in assigning the couplings to specific pairs of protons. A solution to the assignment problem is obtained from a faithful simulation of the experimental six- and seven-quantum

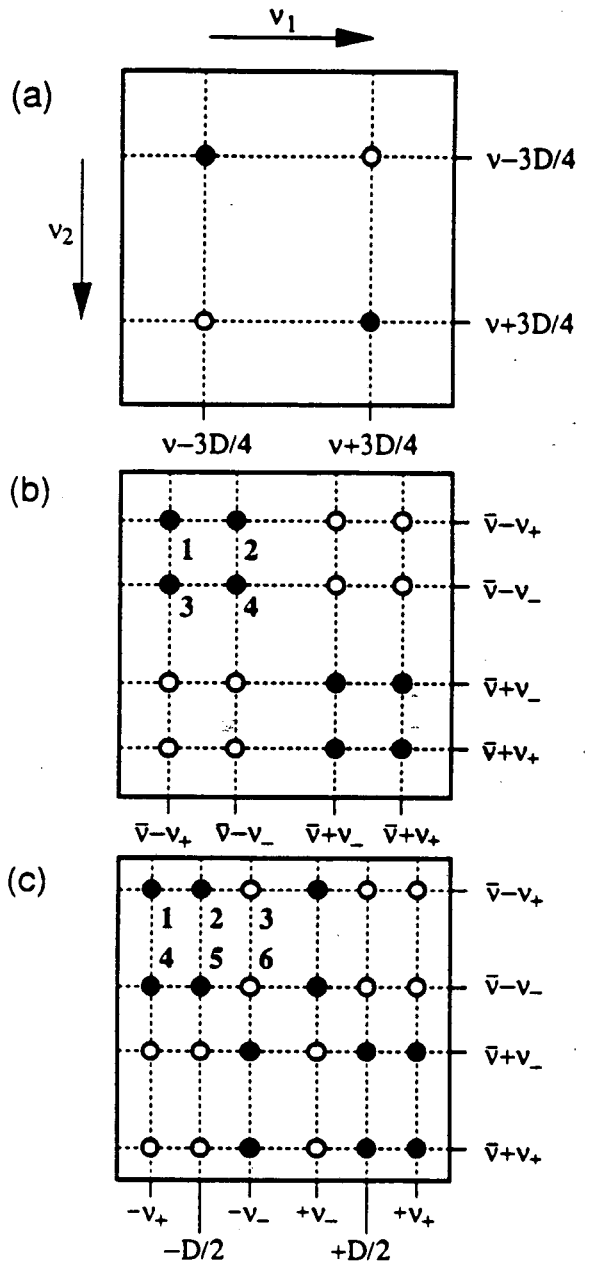

Figure 2.4: Cross-peak patterns for A_2 and AB dipole-coupled spins for the two-quantum filtered COSY experiment. Filled circles (•) denote peaks with positive intensity, and open (o) denote negative excursions. For the AB spectra, $\overline{\nu}$ is the average of the chemical shifts. $\nu_{\pm} = D/2 \pm C/2$ with $C = \sqrt{\Delta\nu^2 + (D/2)^2}$ and $\tan 2\theta = -D/(2\Delta\nu)$. The pattern in (a) and (b) show an A_2 and AB couplings after application of the pulse sequence in Figure 2.7 without the refocussing pulse in t_1. The pattern in (c) results from application of the sequence with the refocussing pulse to the AB system.

spectra. The assignment based on multiple-quantum spectroscopy is unique down to permutations which leave the spin-Hamiltonian invariant [52] — *i. e.* permutations between spins which have the same chemical shift and coupling partners. Experimental results for 1,1,1,6,6,6-d_6-*n*-hexane are presented later. For the larger alkane chains, such multiple-quantum experiments were not necessary, because the sign of the dipole coupling can be assigned based on assumptions about the ordering of the alkane derived from the hexane experiments.

2.3 Experimental Results

The randomly deuterated *n*-alkanes were synthesized by exchange of the protonated alkane in the gas phase with D_2 over Pd/charcoal catalyst at 190°C. The reaction was stopped after approximately 80 hours when an optimal deuteration level between 0.8 and 0.9 was attained. As shown in Figure 2.3, the mass spectrum of a sample (*e.g.* *n*-hexane) agrees well with the statistical distribution of molecules with different numbers of protons for an 0.81 deuteration level calculated from Equation 2.3. This agreement implies that the deuteration is essentially random, and therefore the sample can be expected to contain a selection of all possible two-proton-containing isomers. Eastman Kodak 11650 (EK 11650, *p*-pentylphenyl-2-chloro-(4-*p*-pentylbenzoyloxy)benzoate), a nematic liquid crystal, was used as the solvent in all the experiments. Solutions containing ~30 mole-percent of alkane were prepared for the NMR work.

The NMR experiments were carried out on the 362 MHz home-built spectrometer described in Chapter 6. Two-dimensional data sets, of 384 × 1024 points, were recorded in the time domain, and double Fourier transformed to 2048 × 2048.

The spectra were usually resolution-enhanced with a 45°-shifted sine-bell filter in each time domain. Proton spectra were observed with continuous two-quantum deuterium decoupling [53] over a 30 kHz bandwidth, and a Hahn spin-echo was employed to suppress the signal from the liquid crystal. The temperature control system described in Section 6.7 regulated the sample temperature (to within ±0.1°C) to avoid excessive sample heating from RF power deposited by the decoupler. Earlier experiments, performed with an on/off temperature controller yielded 20°C discrepancies between the setpoint and actual temperatures. Sample heating caused by deuterium decoupling was calibrated in a separate test spectrum, using a capillary of ethylene glycol centered in a tube of EK 11650/CCl_4. The line splitting in the ethylene glycol spectrum served as a measure of the temperature.

2.3.1 Two-Proton Filtering

The result of multiple-quantum filtration is demonstrated in Figure 2.5 for *n*-hexane. Figure 2.5a shows the unfiltered spectrum displaying three prominent lines from the one-proton molecules. These lines provide the chemical shifts for the protons at the carbon sites M, E_1 and E_2, etc. (*cf.* Figure 2.6). The two-quantum filtered spectrum of Figure 2.5b and the two-spin filtered spectrum of Figure 2.5c were both measured with the pulse sequence of Figure 2.7, using a fixed t_1 value. The phase ϕ was incremented in 90° steps, and the receiver phase alternated between 0° and 180° . For the spectrum with the high pass two-*quantum* filter (Figure 2.5b) τ_1 was kept constant and four scans completed the cycle, whereas the two-*proton* filtered spectrum (Figure 2.5c) was obtained by incrementing τ_1 after every 4th scan. Figure 2.5c is therefore a superposition of the eight A_2 and eight AB spectra

arising from the sixteen isomers of $C_6H_2D_{12}$. In order to separate these two-proton subspectra and to find the peak correlations, two-dimensional two-proton filtered COSY spectra were recorded.

2.3.2 COSY Spectra

The two-spin filtered COSY spectra were acquired with the pulse sequence of Figure 2.7, both without and (usually) with a refocusing π pulse in t_1, and with varying two-quantum evolution time (τ_1) for the two-proton filtration. The COSY spectra for our series of alkanes are shown in Figures 2.10 through 2.24.

The A_2 and AB patterns expected for the two types of COSY experiments were shown in Figures 2.4a–c. In the experimental refocused COSY spectra, typically no more than eight of the 24 peaks predicted for the AB patterns had sufficient intensity to be observed. The refocused COSY experiment was easier to analyze because of its slightly narrower lines. For many observed AB patterns, the ratio of coupling constant to chemical shift difference is greater than two, so that the inner peaks are very small. These subspectra resemble A_2 patterns, but from their chemical shift position they were recognized as AB patterns and interpreted according to Equation 2.5. J couplings are ignored because they are small (less than 10 Hz) relative to the $\langle D_{ij} \rangle$, and not resolved.

Without a π pulse in t_1, the Hamiltonians in t_1 and t_2 are identical, leading to AB patterns that are centered about the average chemical shift positions $\langle \delta_{AB} \rangle = \frac{1}{2}(\langle \delta_A \rangle + \langle \delta_B \rangle)$ along the main diagonal. In the refocused COSY experiment, the AB patterns are concentric about the points ($\nu_1 = 0$, $\nu_2 = \langle \delta_{AB} \rangle$). The shift of peaks from one experiment relative to the other allows for accidental overlap of

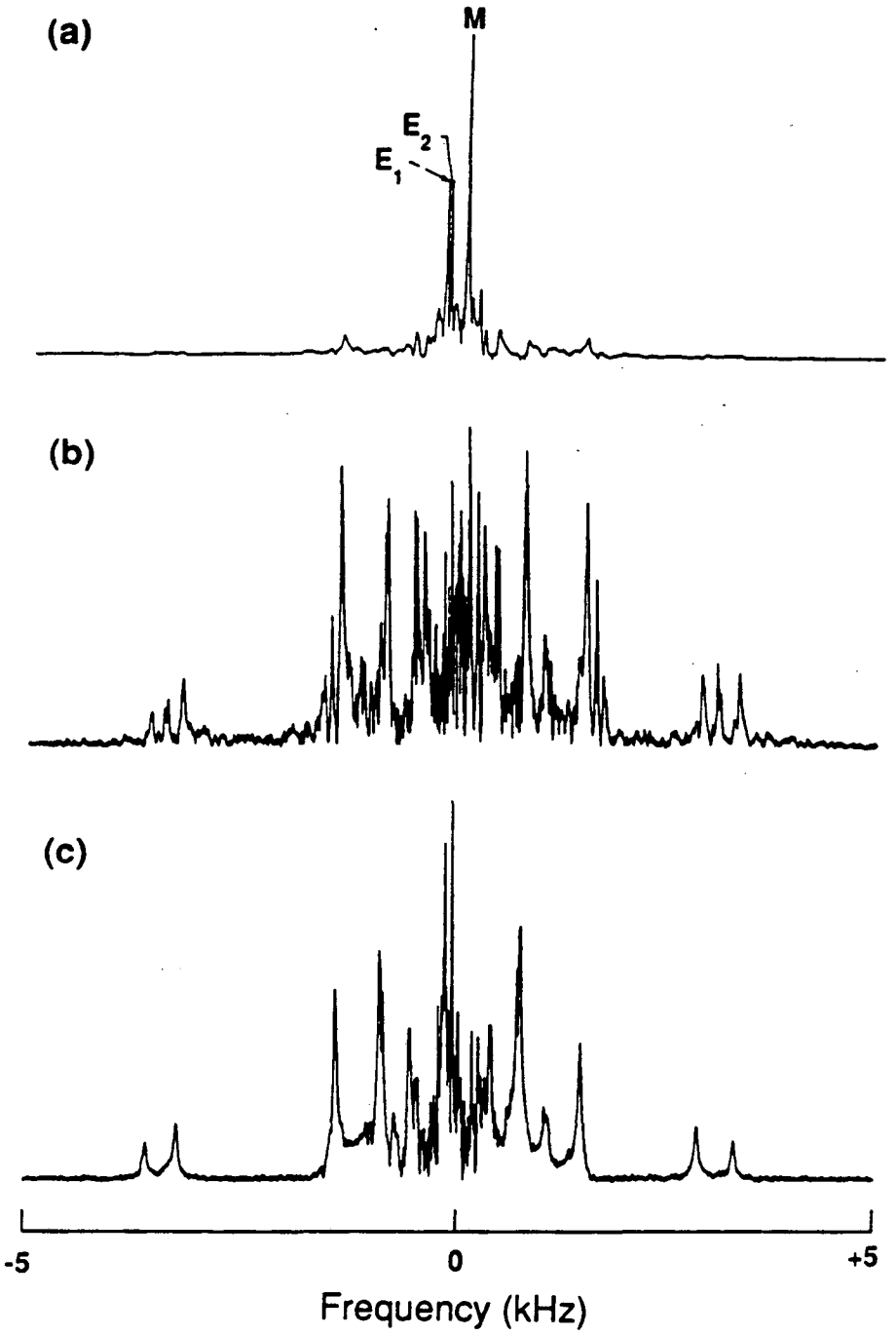

Figure 2.5: One-dimensional spectra of non-selectively deuterated *n*-hexane. The one-quantum spectrum (a) is dominated by the signal from molecules with only one proton remaining. Applying a two-quantum filter simplifies the spectrum greatly, but still leaves contributions from species with more than two protons remaining (b). The two-proton filter averages away all contributions except those from molecules with only two protons (c).

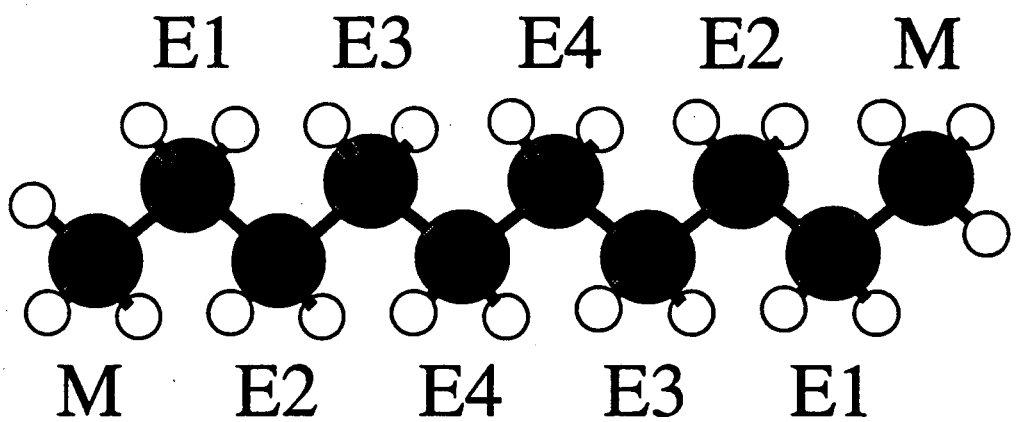

Figure 2.6: Numbering scheme for the series of alkanes. In the all-trans conformation, protons lying across the longitudinal symmetry plane of the molecule are referred to as "anti", and those on the same side as "syn". Methylene protons close to the methyl proton (in couplings such as ME_1, *etc.*) are referred to as "proximal", and those at the far end as "distal".

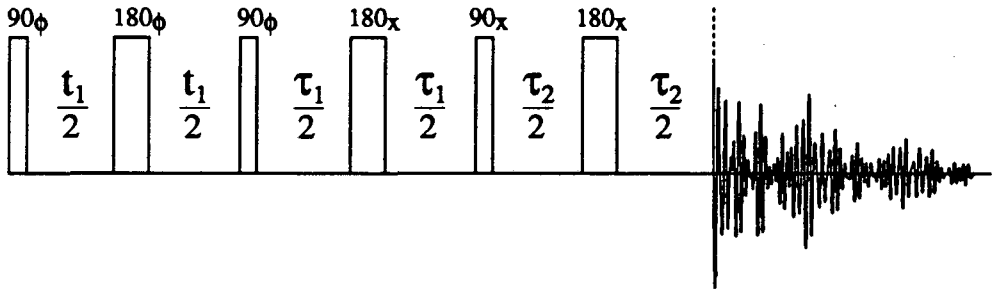

Figure 2.7: Two-quantum one-dimensional spectra were acquired with fixed values for t_1. For two-*proton* filtration, the value of τ_1 was incremented every four scans. For two-dimensional COSY experiments, the evolution time t_1 was incremented.

peaks to be resolved, although the non-refocussed spectrum is usually too poorly resolved to be of any use. Since each of the sites M, E_1, E_2, E_3, and E_4 has a different chemical shift, the $n!$ averaged chemical shift positions $\langle\delta_{MM}\rangle$, $\langle\delta_{ME_1}\rangle$, $\langle\delta_{ME_2}\rangle$, $\langle\delta_{E_1E_1}\rangle$, $\langle\delta_{E_2E_2}\rangle$, and $\langle\delta_{E_1E_2}\rangle$ etc. can be used to group the proton pairs into $n!$ categories. This narrows down the search for the exact assignment considerably.

2.3.3 Multiple-Quantum NMR of the Methylene Chain

The spatial component of the dipole coupling scales as the second Legendre polynomial of $\cos(\theta)$:

$$D \propto \frac{1}{2}(3\cos^2(\theta) - 1) \tag{2.7}$$

creating an amibiguity in the sign of the coupling. Without prior knowledge of the solute conformation and orientation, we can not determine the sign of the coupling.

On the other hand, assuming that the all-trans conformation predominates, and that its long axis aligns parallel to the static field and the liquid crystal director axis, certain couplings can be assigned. Geminal couplings will have a positive sign, while those couplings parallel to the carbon backbone will be negative. A multiple-quantum spectrum and simulation of the central methylene subchain can verify these assignments.

Multiple-quantum spectra were obtained and fit only for the 1,1,1,6,6,6-d_6-*n*-hexane and 1,1,1,2,2,7,7,8,8,8-d_{10}-*n*-octane samples. Presupposition of similar ordering/conformation behavior for the other alkanes in the series obviated the need to perform this synthetically demanding experiment for each alkane. The six- and seven-quantum spectra were recorded using time-proportional phase incrementation (TPPI) [54, 55]. The pulse sequence is given in Figure 2.8. The phase ϕ was incremented proportionately with t_1 in 22.5° increments, allowing 16 phase separated intervals for the 0 to ±8 quantum spectra (±8 quantum at the edge). The phase ψ was cycled through 0°, 90°, 180°, 270° for each t_1 point, with the receiver held constant to observe even-quantum transitions and alternated between 0° and 180° to observe odd-quantum transitions.

Figure 2.9 shows the experimental six- and seven-quantum spectra of hexane-d_6, obtained by adding the even- and odd-order spectra. The seven-quantum spectrum has two pairs of lines, which correspond to the number of distinct ways of selecting seven out of eight protons from a spin system with C_{2h} symmetry such as an *n*-alkane (with an even number of carbons) rapidly exchanging between different conformations. For the six-quantum spectrum nine of the possible pairs of lines are observed.

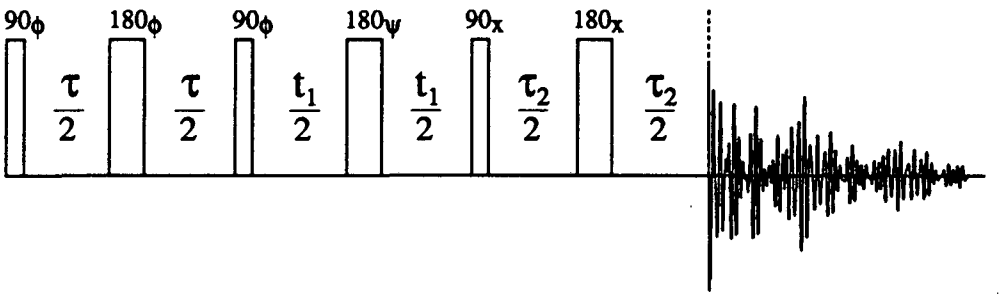

Figure 2.8: With the pictured sequence, six-, seven- and eight-quantum spectra of the central eight-proton methylene chain can be acquired.

To begin the simulations of the six- and seven-quantum spectra of hexane-d_6 the following assumptions were made:

1. The hexane molecules are predominantly oriented with their long axes parallel to the nematic director, which, for our sample, is parallel to the external magnetic field. Therefore (*cf.* equation 2.1), dipole couplings between geminal protons are positive, and couplings between protons which are separated by at least three carbon atoms are negative.

2. The strongest dipole couplings arise from geminal protons (those on the same carbon).

3. The inner methylene groups (E_n) have stronger couplings than the outer methylene groups (E_{n-k}) as k increases. As the chain lengthens, the geminal protons in the middle will be forced to a position increasingly perpendicular to the liquid crystal director.

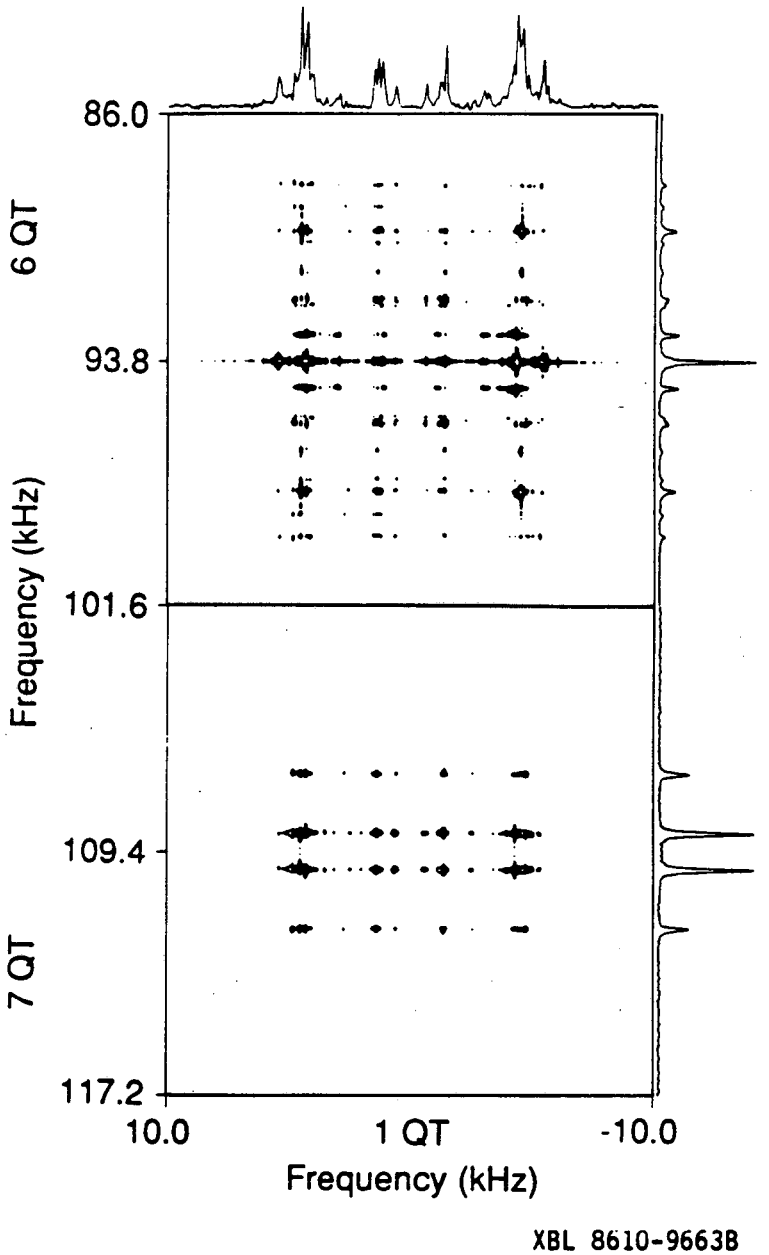

Figure 2.9: Six- and seven-quantum spectra of *n*-hexane-d_6 acquired with the sequence of Figure 2.8. The two-dimensional spectrum is plotted with the n-quantum orders along ω_1 and the one-quantum spectrum along ω_2. τ=11.706 msec for the even-quantum spectra and 12.000 msec for the odd-quantum spectra, with the absolute values of the spectra being added. Time domain data sets of 8192 t_1 points and 1024 t_2 points were collected with 6 scans per increment, and a recycle delay of 4.5 sec. From Ref [2].

Table 2.2: Nematic→isotropic transition temperatures for the 30 mole-percent mixtures of the alkanes in the liquid crystal EK11650. $T_{N\rightarrow I}$ is the transition temperature, and T_{reduced} is the reduced temperature characterizing an experiment performed at 32°C. The following row gives the temperature, in °C at which each alkane should be run, inorder to be at a reduced temperature of 0.875 (the value for decane). ΔT is the difference to be corrected.

	Number of carbons in alkane chain				
	6	7	8	9	10
$T_{N\rightarrow I}$	86.0	81.0	79.2	77.8	75.4
T_{reduced}(@32°C)	0.850	0.862	0.866	0.869	0.875
T(°C) (@ $T_{\text{reduced}} = 0.875$)	41.1	36.7	35.2	33.9	31.8
ΔT	9.3	4.9	3.4	2.1	0.0

More thorough discussions of the simulations of the multiple-quantum spectra are presented elsewhere [56, 2]. The salient feature of the higher-order multiple-quantum NMR and spectral simulations is that they provide a sensitive test of the assignments of the dipole couplings.

2.3.4 Reduced Temperature Corrections

The series of alkanes were all run at a constant temperature of 32°C to guarantee that the probe characteristics (tuning and matching) which affect power deposition in the sample (and the concomitant heating) remained constant for each sample. As the alkane chain length increases, though, the clearing point (the nematic → isotropic transition temperature) of the alkane/liquid crystal mixture increases. Thus, for a constant laboratory temperature, the reduced temperature for each sample, $T_{reduced} = T_{lab}/T_{N\rightarrow I}$, decreases as a function of chain length. This trend is evident in the data of Table 2.2. For calculating orientational distributions of

the solute molecules based on temperature-independent energy expressions, it is customary to parametrize the distribution function in terms of this reduced temperature [57, 58, 59, 60]. Measuring the temperature dependence of each different dipole coupling with variable temperature experiments for the *n*-hexane/11650 sample allows us to correct the couplings for the other alkanes in the series.

A 30 mole-percent mixture of *n*-hexane in 11650 displays nematic behavior over a temperature range of approximately 25 – 90°C. A series of COSY experiments were evaluated at temperatures within the nematic range: 28, 38, 45, 50, and 56°C. The dipole coupling for each different proton pair can then be plotted with respect to temperature. Table 2.3 shows the salient couplings at each temperature. The temperature dependence for each type of coupling can be fit by linear regression, yielding a correction of the form:

$$D_{\text{corrected}} = D_{\text{uncorrected}} - \left(\frac{\Delta D}{\Delta T(^{\circ}\text{C})}\right)(\Delta T(^{\circ}\text{C})) \tag{2.8}$$

The tables of dipole couplings presented in Section 2.3.5 show couplings that have already been corrected for the difference in reduced temperature. By assuming that a given type of dipole coupling (*e.g.* geminal methylene or methyl-methyl) will scale similarly with temperature for all the alkanes, we can apply the hexane-derived correction to all the alkanes in the series. In this fashion, both the solute concentration *and* the effective (reduced) temperature are kept constant throughout the series.

2.3.5 Assignment of the Dipole Couplings

The dipole couplings derived from the COSY experiments serve as constraints for the two-parameter fits described in Section 2.4. Spectral resolution and signal-to-

Table 2.3: Temperature dependence of the dipole couplings for a 30 mole-percent mixture of *n*-hexane in Kodak 11650. Linear least-squares fits for these data give correction functions needed to calibrate experiments for the series of solvated alkanes.

Dipole coupling	28°C	38°C	45°C	50°C	56°C
E_2E_2	4971.42	4729.17	4471.63	4418.05	4261.53
E_1E_1	4401.02	4185.67	4009.25	3907.99	3775.49
MM (proximal)	2104.77	1987.00	1892.78	1840.67	1768.33
E_1E_2 (syn)	1832.36	1713.76	1629.72	1576.70	1511.46
E_1E_2 (anti)	1158.63	1094.70	1071.80	1040.88	1017.94
ME_1 (proximal)	440.73	417.06	385.66	382.94	360.78
ME_2 (proximal)	1167.59	1071.86	1030.86	1000.93	962.89
ME_2 (distal)	649.40	618.93	599.95	590.14	562.02
ME_1 (distal)	348.19	338.34	326.39	319.24	307.08
MM (distal)	220.95	213.58	206.82	201.83	197.05

noise decrease quickly as the chain length increases, and it becomes impossible to identify and assign all the dipole couplings. Since the fitting process is overdetermined, we can operate with a reduced set of couplings. Empirically (in calculations for hexane and octane), it has been determined that fitting such a truncated data set yields a fit within 5–8% agreement with a fit performed for the full data set, allowing us to study complicated molecules for which a complete set of couplings is not resolvable.

The next task is to identify the primary couplings. The geminal couplings (E_nE_n), between protons on the same methylene unit, are resolvable and intense. These couplings have the same spatial dependence ($P_2(\cos\theta)$) as the deuterium quadrupole couplings employed in similar studies of flexible chains, providing a convenient basis for comparison with those experiments [43, 61, 62]. Other identi-

Table 2.4: Experimental and simulated dipole couplings for *n*-hexane. Only the truncated list of couplings discussed in the text is presented here. Models A and B are models of Samulski *et al.* and Burnell *et al.*, respectively.

Coupling	Experimental		Simulation A		Simulation B	
	Uncorr.	Corr.	Uncorr.	Corr.	Uncorr.	Corr.
E_2E_2	3876	3714	3904	3742	3865	3704
E_1E_1	3437	3294	3436	3290	3313	3172
MM (proximal)	1619	1545	1533	1463	1598	1524
E_1E_2 (syn)	-1398	-1329	-1460	-1329	-1581	-1507
E_1E_2 (anti)	-921	-888	-880	-845	-999	-960
ME_1 (proximal)	-335	-318	-312	-297	-294	-279
ME_2 (proximal)	-904	-859	-876	-837	-961	-920
ME_2 (distal)	-505	-483	-514	-496	-598	-576
ME_1 (distal)	-253	-244	-250	-240	-287	-276
MM (distal)	-171	-165	-159	-152	-184	-176

fiable couplings which also provide a good measure of the molecular conformation are the couplings between the methyl protons, and each methylene unit (ME_n), as well as with the distal methyl group (MM). The final class of couplings considered is that between protons on methylene unit separated by one carbon atom. The protons of these (E_nE_{n+2}) couplings lie either on the same side of the carbon backbone (syn) or on opposite sides (anti).

Tables 2.4, 2.5, 2.6, 2.7, and 2.8 list the experimental dipole couplings selected for the fitting process described in Section 2.4. The dipole couplings in the first column have been measured directly from the spectrum, without compensation for the difference between the actual and reduced temperatures. Temperature correction (which contracted the splitting for all molecules except decane) gives the couplings listed in column two of the tables. The remainder of the table compiles the results

Table 2.5: Experimental and simulated values for the truncated set of dipole couplings for *n*-heptane.

Coupling	Experimental		Simulation A		Simulation B	
	Uncorr.	Corr.	Uncorr.	Corr.	Uncorr.	Corr.
E_3E_3	4291	4196	4363	4268	4391	4296
E_2E_2	4078	3987	4079	3989	4103	4013
E_1E_1	3623	3544	3515	3454	3410	3331
MM (proximal)	1553	1516	1489	1453	1448	1413
E_1E_3 (syn)	-1536	-1496	-1607	-1566	-1624	-1583
E_1E_3 (anti)	-977	-959	-927	-908	-867	-849
E_2E_2 (syn)	-1656	-1613	-1739	-1696	-1781	-1737
E_2E_2 (anti)	-1004	-985	-977	-957	-923	-904
ME_1 (proximal)	-269	-262	-273	-266	-323	-315
ME_2 (proximal)	-953	-928	-919	-897	-1011	-987
ME_3	-532	-520	-528	-518	-621	-609
ME_2 (distal)	-296	-291	-272	-267	-313	-306
ME_1 (distal)	-191	-188	-183	-179	-214	-209
MM (distal)	-129	-126	-115	-113	-133	-131

Table 2.6: Experimental and simulated dipole couplings for *n*-octane.

Coupling	Experimental		Simulation A		Simulation B	
	Uncorr.	Corr.	Uncorr.	Corr.	Uncorr.	Corr.
E_3E_3	4503	4434	4614	4546	4611	4542
E_2E_2	4284	4219	4248	4183	4232	4168
E_1E_1	3685	3629	3566	3508	3511	3455
MM (proximal)	1708	1679	1559	1532	1580	1552
E_1E_3 (syn)	-1618	-1589	-1743	-1713	-1778	-1747
E_1E_3 (anti)	-1030	-1016	-951	-937	-947	-933
E_2E_3 (syn)	-1785	-1753	-1938	-1905	-1964	-1931
E_2E_3 (anti)	-1120	-1106	-1026	-1011	-1029	-1014
ME_1 (proximal)	-327	-321	-293	-288	-323	-317
ME_2 (proximal)	-969	-951	-952	-936	-1010	-994
ME_3 (proximal)	-558	-549	-524	-517	-572	-564
ME_3 (distal)	-305	-301	-280	-276	-305	-301
ME_2 (distal)	-204	-201	-191	-188	-211	-208
ME_1 (distal)	-154	-152	-127	-125	-142	-140
MM (distal)	-97	-96	-86	-85	-95	-94

Table 2.7: Experimental and simulated dipole couplings for *n*-nonane.

Coupling	Experimental		Simulation A		Simulation B	
	Uncorr.	Corr.	Uncorr.	Corr.	Uncorr.	Corr.
E_4E_4	4557	4514	4681	4638	4688	4645
E_3E_3	4557	4514	4590	4548	4559	4517
E_2E_2	4231	4191	4118	4080	4089	4050
E_1E_1	3685	3655	3460	3427	3404	3370
MM (proximal)	1602	1585	1478	1463	1439	1424
E_1E_3 (syn)	-1619	-1600	-1753	-1735	-1808	-1788
E_1E_3 (anti)	-1012	-1004	-906	-898	-909	-901
E_2E_4 (syn)	-1796	-1776	-1973	-1953	-2031	-2010
E_2E_4 (anti)	-1079	-1070	-1005	-997	-1015	-1007
E_3E_3 (syn)	-1837	-1816	-2037	-2017	-2085	-2064
E_3E_3 (anti)	-1133	-1124	-1033	-1024	-1046	-1037
ME_1 (proximal)	-248	-245	-268	-265	-267	-264
ME_2 (proximal)	-970	-959	-932	-923	-980	-970
ME_3 (proximal)	-553	-547	-488	-484	-523	-519
ME_4	-310	-308	-272	-269	-291	-288
ME_3 (distal)	-207	-206	-183	-182	-199	-197
ME_2 (distal)	-143	-141	-125	-124	-137	-136
ME_1 (distal)	?	?	-89	-88	-98	-98
MM (distal)	-72	-71	-62	-62	-69	-68

Table 2.8: Experimental and simulated dipole couplings for *n*-decane.

Coupling	Experimental Uncorr./Corr.	Simulation A Uncorr./Corr.	Simulation B Uncorr./Corr.
E_4E_4	4610	4733	4713
E_3E_3	4494	4517	4479
E_2E_2	4208	4056	3998
E_1E_1	3591	3414	3354
MM (proximal)	1634	1492	1568
E_1E_3 (anti)	-1626	-1789	-1841
E_1E_3 (syn)	-997	-862	-897
E_2E_4 (anti)	-1844	-2018	-2084
E_2E_4 (syn)	-1045	-960	-1005
E_3E_4 (anti)	-1916	-2119	-2177
E_3E_4 (syn)	-1100	-1017	-1065
ME_1 (proximal)	-286 (?)	-283	-300
ME_2 (proximal)	-963	-925	-952
ME_3 (proximal)	-549	-450	-478
ME_4 (proximal)	-308	-260	-276
ME_4 (distal)	-211	-173	-185
ME_3 (distal)	-177 (?)	-118	-129
ME_2 (distal)	-149 (?)	-86	-94
ME_1 (distal)	-94 (?)	-63	-70
MM (distal)	-54	-46	-50

of two mean field models described later in the chapter, for both the uncorrected and corrected couplings. From Table 2.2 we see that the decane sample has the lowest nematic→isotropic transition temperature, and thus its spectrum (being the "hotest") serves as a basis for the temperature correction.

In the following pages, we present the two-quantum-filtered COSY spectra for the alkane series. Figures 2.10, 2.11, and 2.12 show successively smaller sections of the spectrum for hexane, in order to resolve the detail in the center region. The time domain data sets for this spectrum and those that follow were acquired with the pulse sequence of Figure 2.7. Either 384 or 416 t_1 experiments with 1024 points each were acquired. The acquisition parameters were:

t_1 (initial)	83.4 μsec
t_1 (increment)	83.4 μsec; increment each t_1 experiment
τ_1 (initial)	2 μsec
τ_1 (increment)	600 μsec; 15 increments per t_1 experiment
τ_2	1.8 msec.

Similarly, Figures 2.13,2.14, and 2.15 show the spectrum for heptane, Figures 2.16, 2.17, and 2.18 for octane, Figures 2.19, 2.20, and 2.21 for nonane, and Figures 2.22, 2.23 and 2.24 for decane.

One interesting feature to note in the experimental dipole couplings plotted in Figures 2.25 and 2.26 is the appearance of an even-odd oscillation in several of the dipole couplings. Earlier studies have described the oscillation of the nematic→isotropic transition temperature and entropy as a function of alkyl chain length on liquid crystal molecules [63, 64]. The data of Figure 2.26 also shows that the methyl-

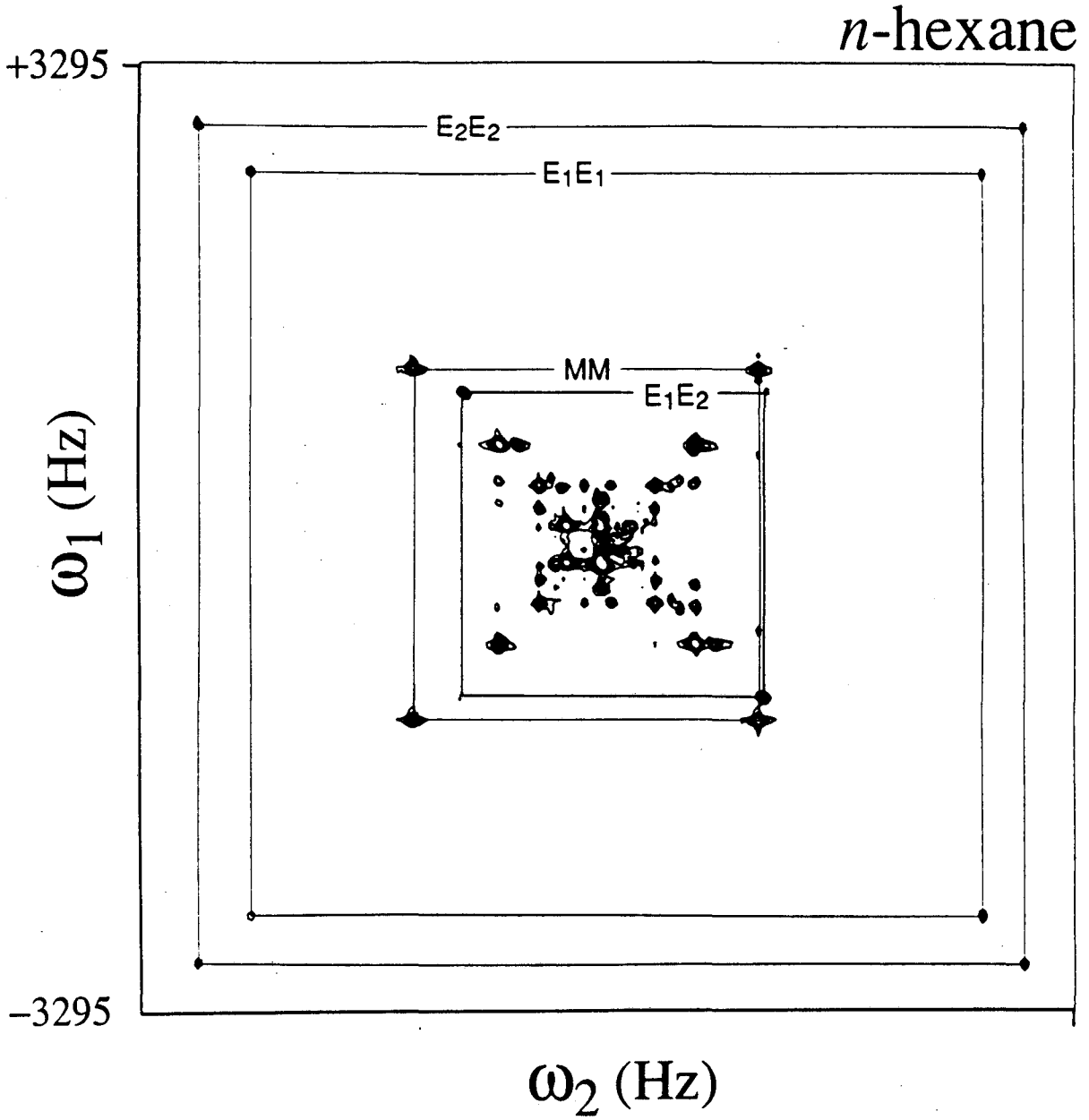

Figure 2.10: View of 2-quantum-filtered COSY of *n*-hexane - complete spectrum. 384 × 1024 points were collected in the time-domain, and double Fourier transformed to 2048 × 2048 points with a 45°-shifted sine bell filter in each direction. The square patterns arising from each coupling are labeled.

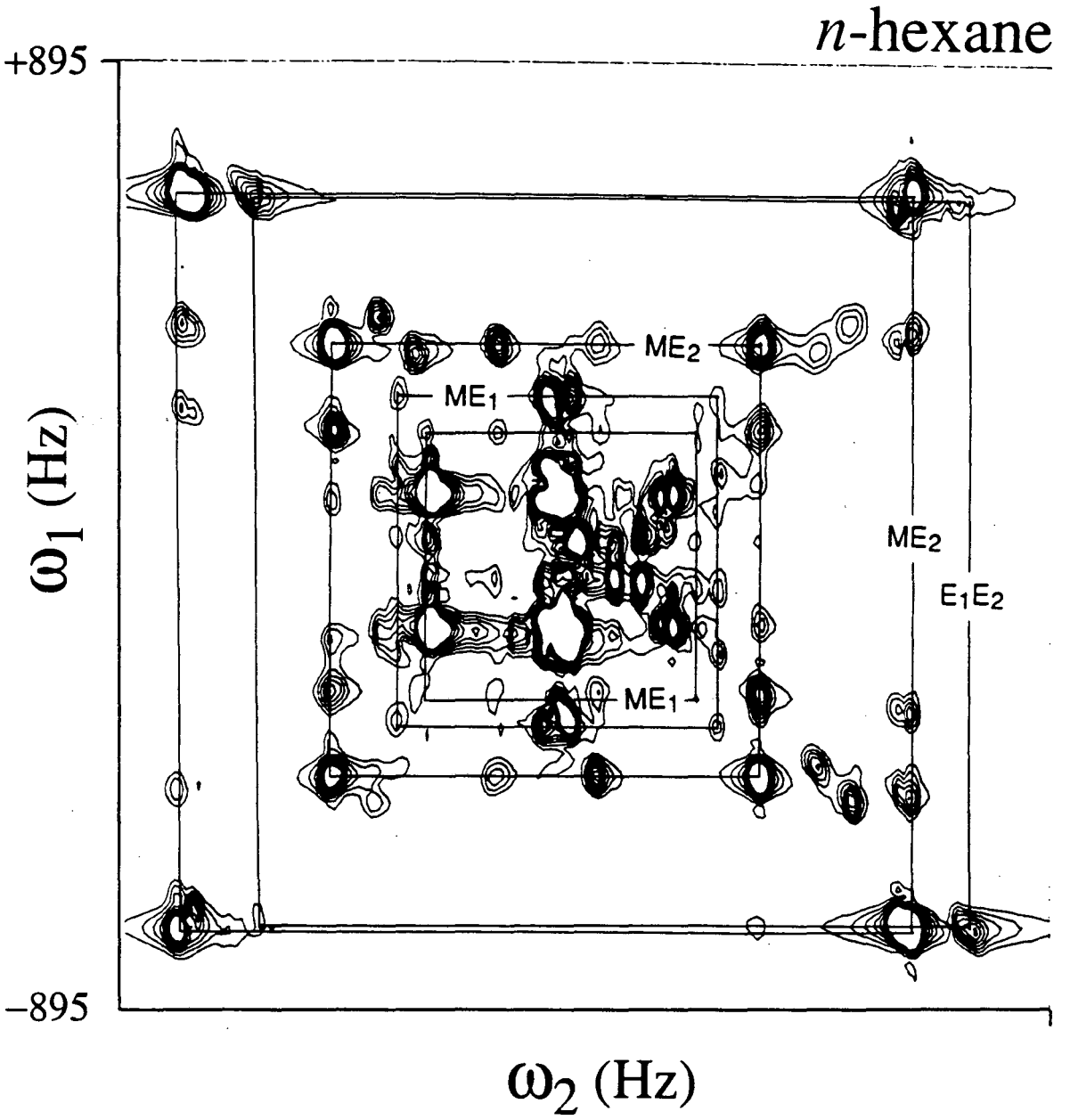

Figure 2.11: View of 2-quantum-filtered COSY of n-hexane - enlarged view. The square patterns of all the alkane spectra are shifted in the ω_2 direction by the average of the chemical shift offsets of the two coupled protons. In ω_1, they are symmetrically disposed about the zero frequency, because of the π-pulse in t_1.

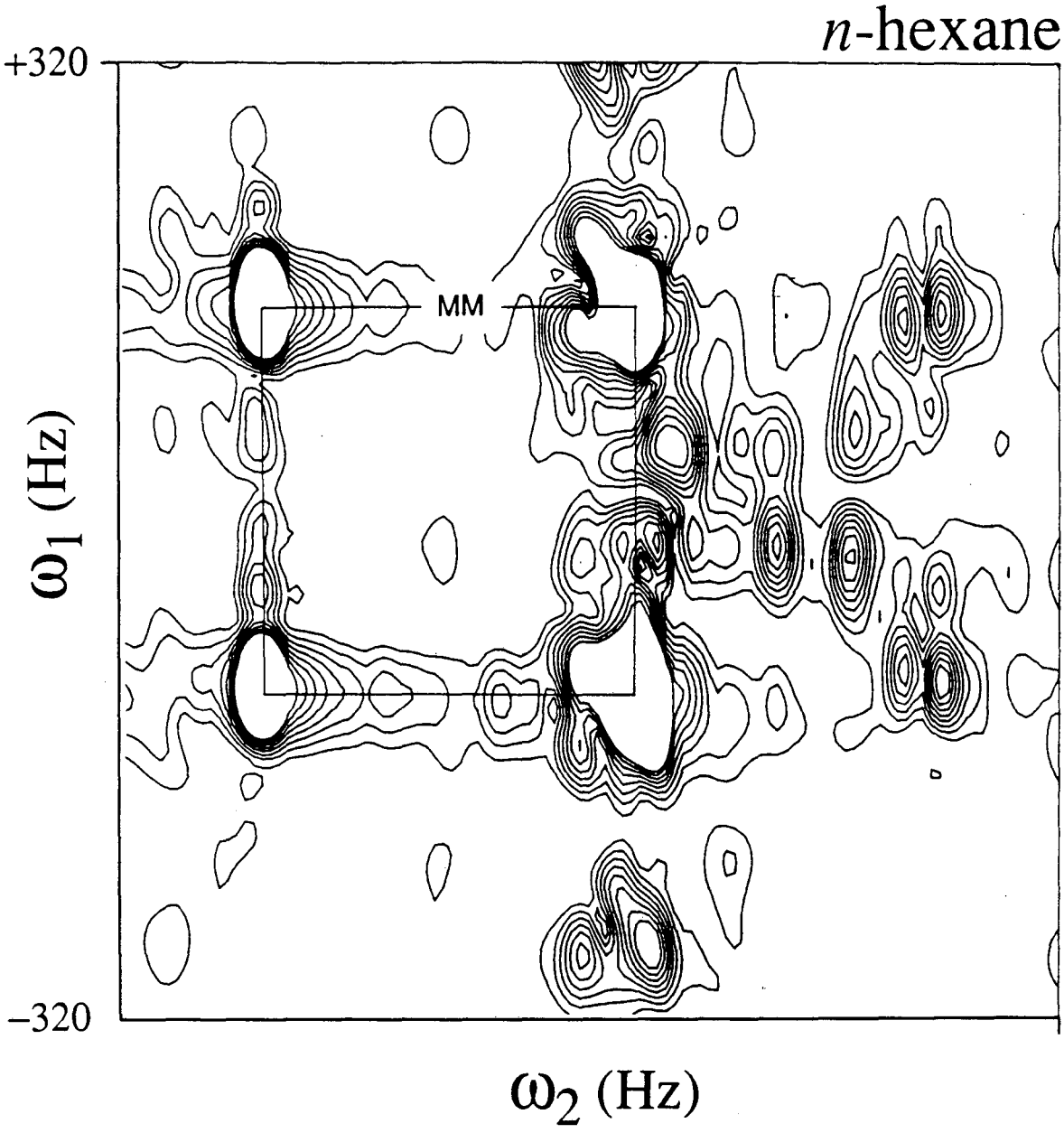

Figure 2.12: View of 2-quantum-filtered COSY of *n*-hexane - enlarged view of center section.

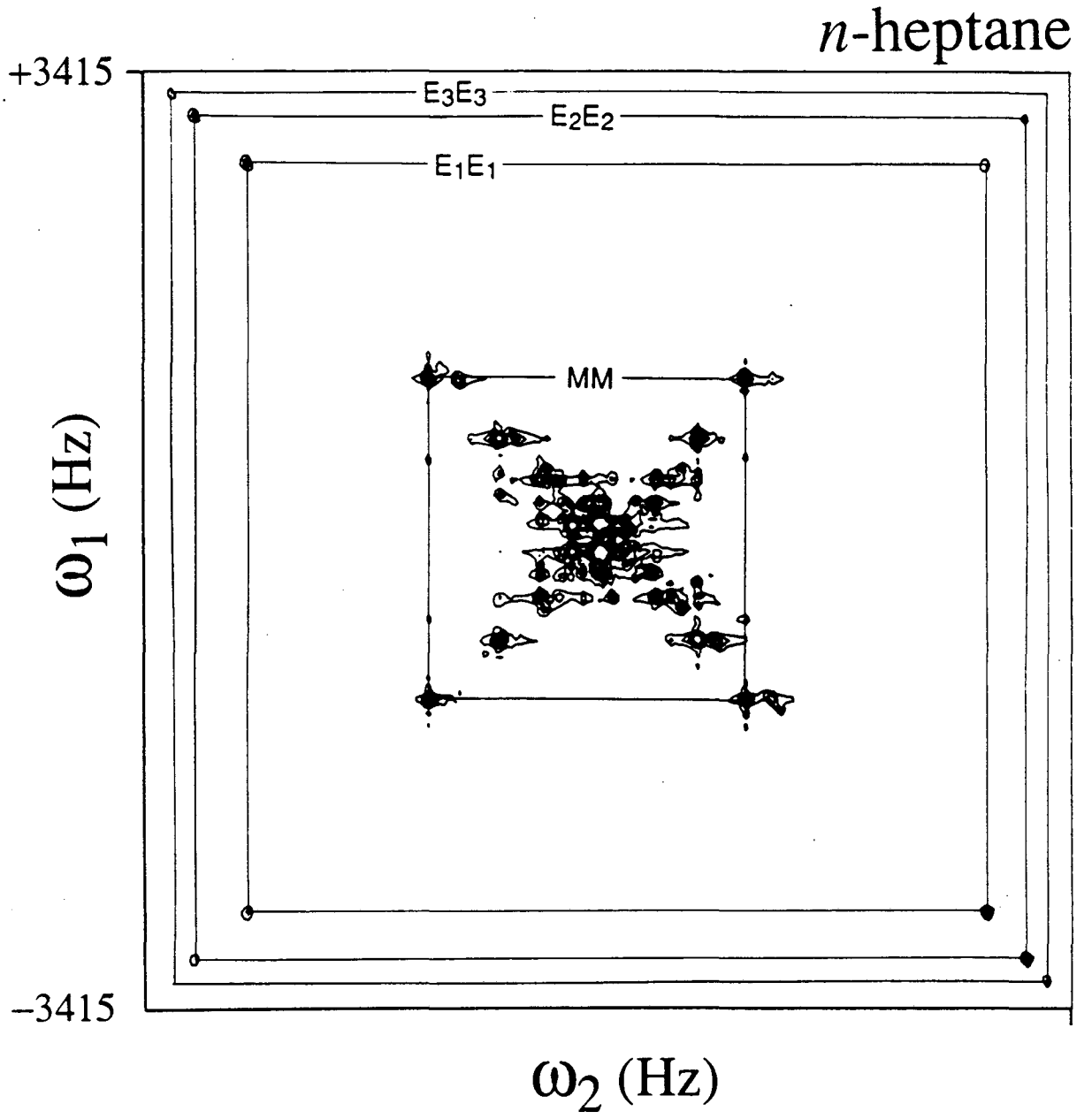

Figure 2.13: View of 2-quantum-filtered COSY of *n*-heptane - complete spectrum. Experimental conditions and data processing were identical to those used to acquire the hexane spectrum.

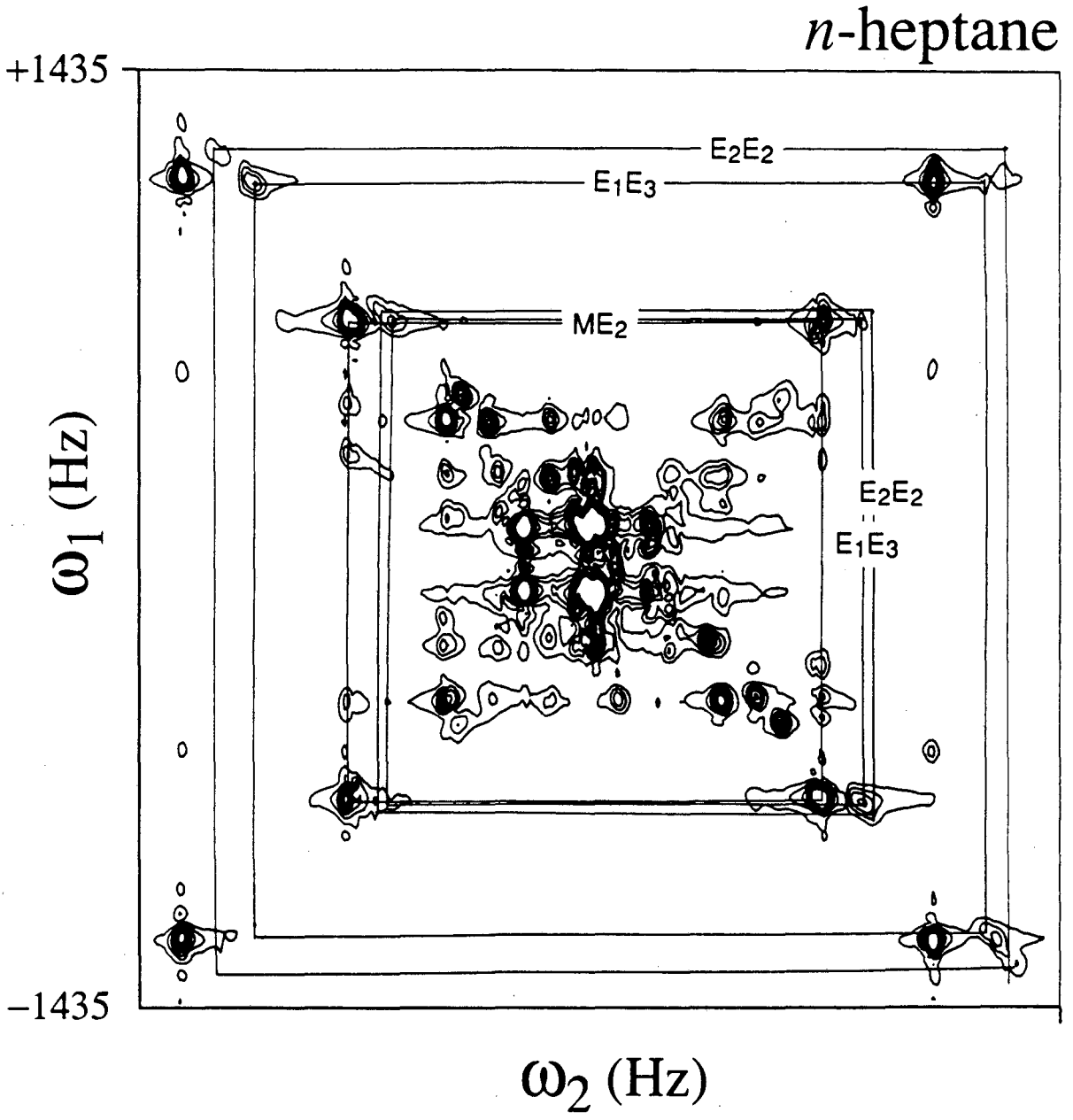

Figure 2.14: View of 2-quantum-filtered COSY of *n*-heptane - enlarged view.

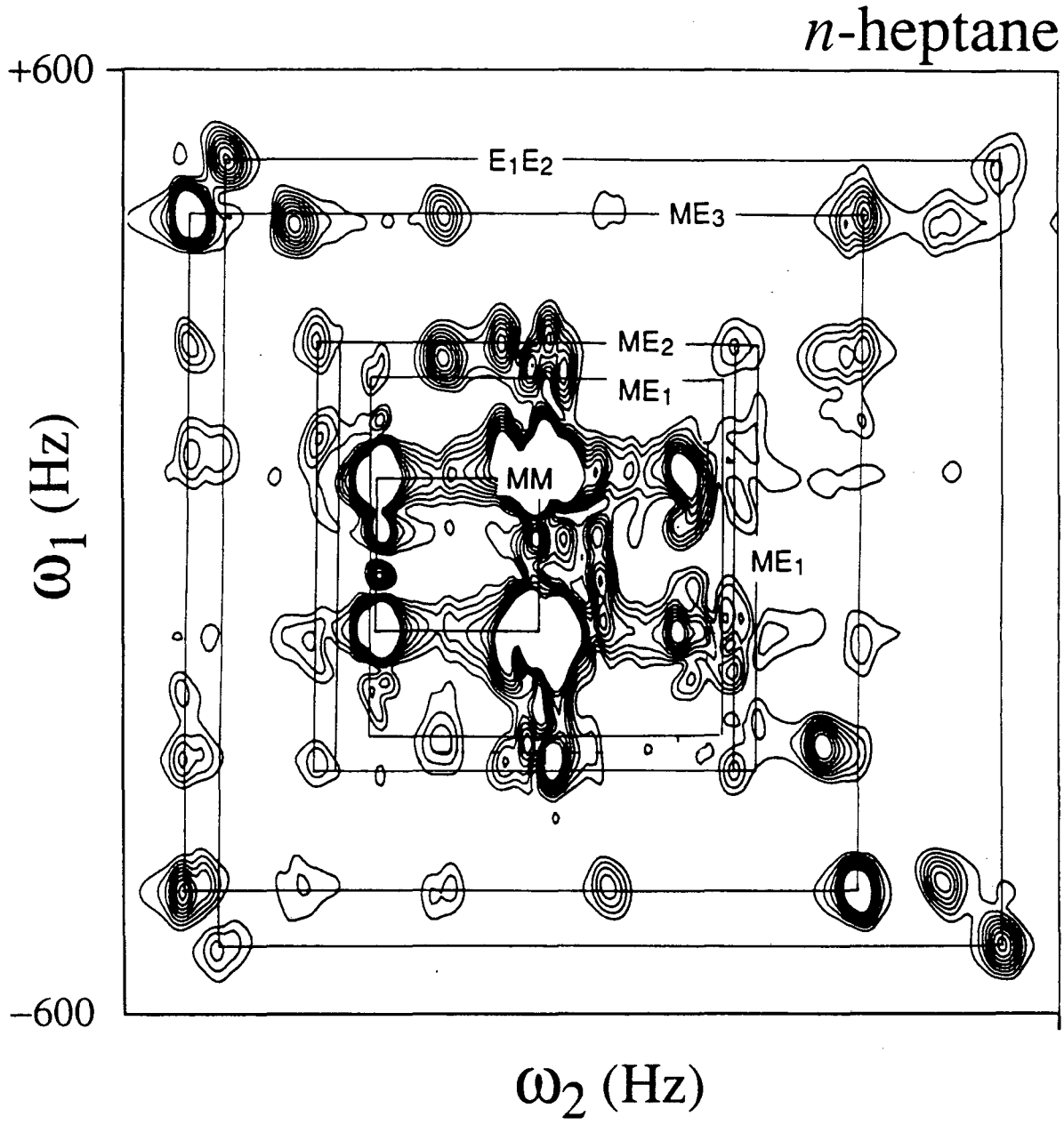

Figure 2.15: View of 2-quantum-filtered COSY of *n*-heptane - enlarged view of center section.

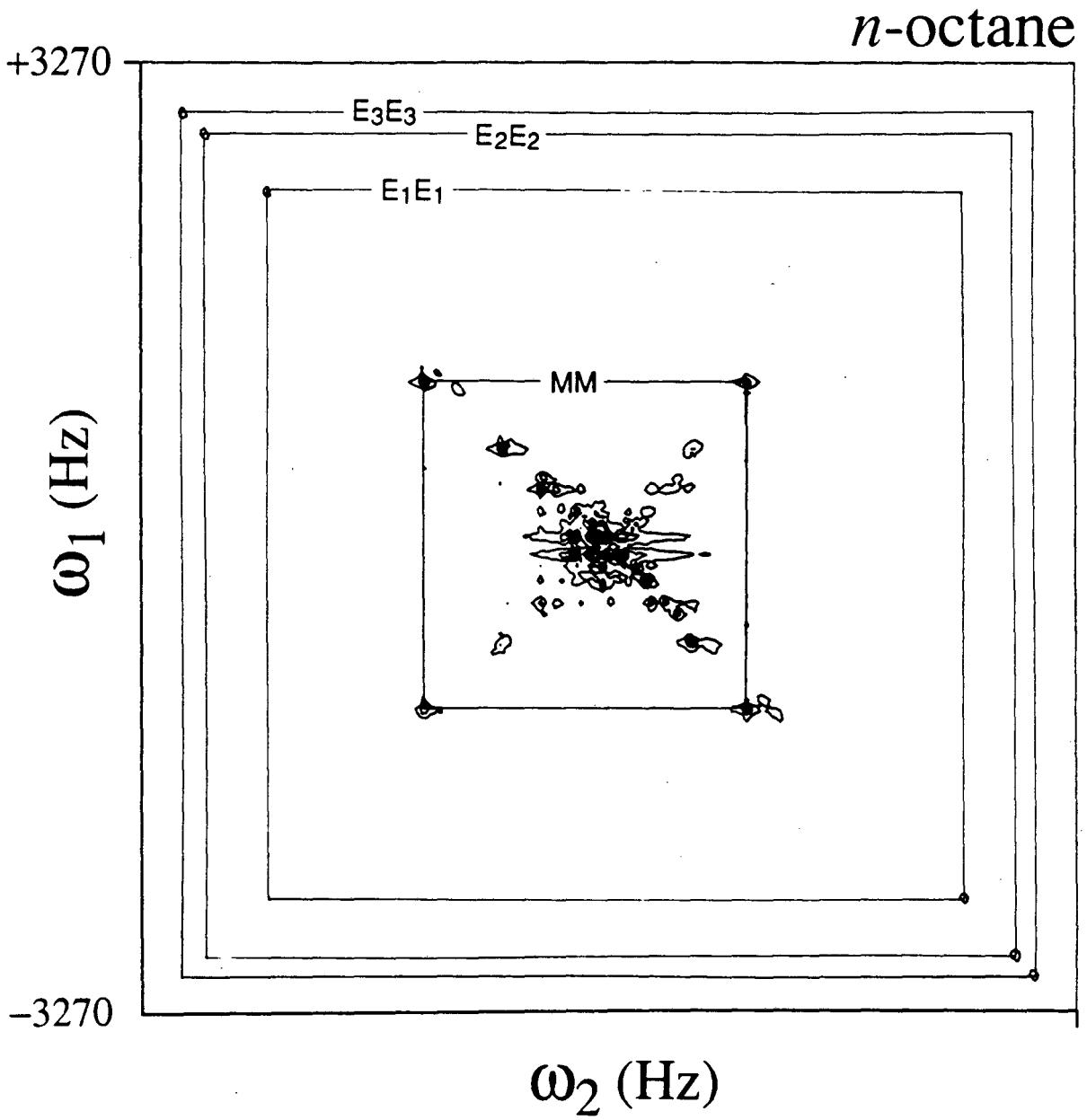

Figure 2.16: View of 2-quantum-filtered COSY of *n*-octane - complete spectrum.

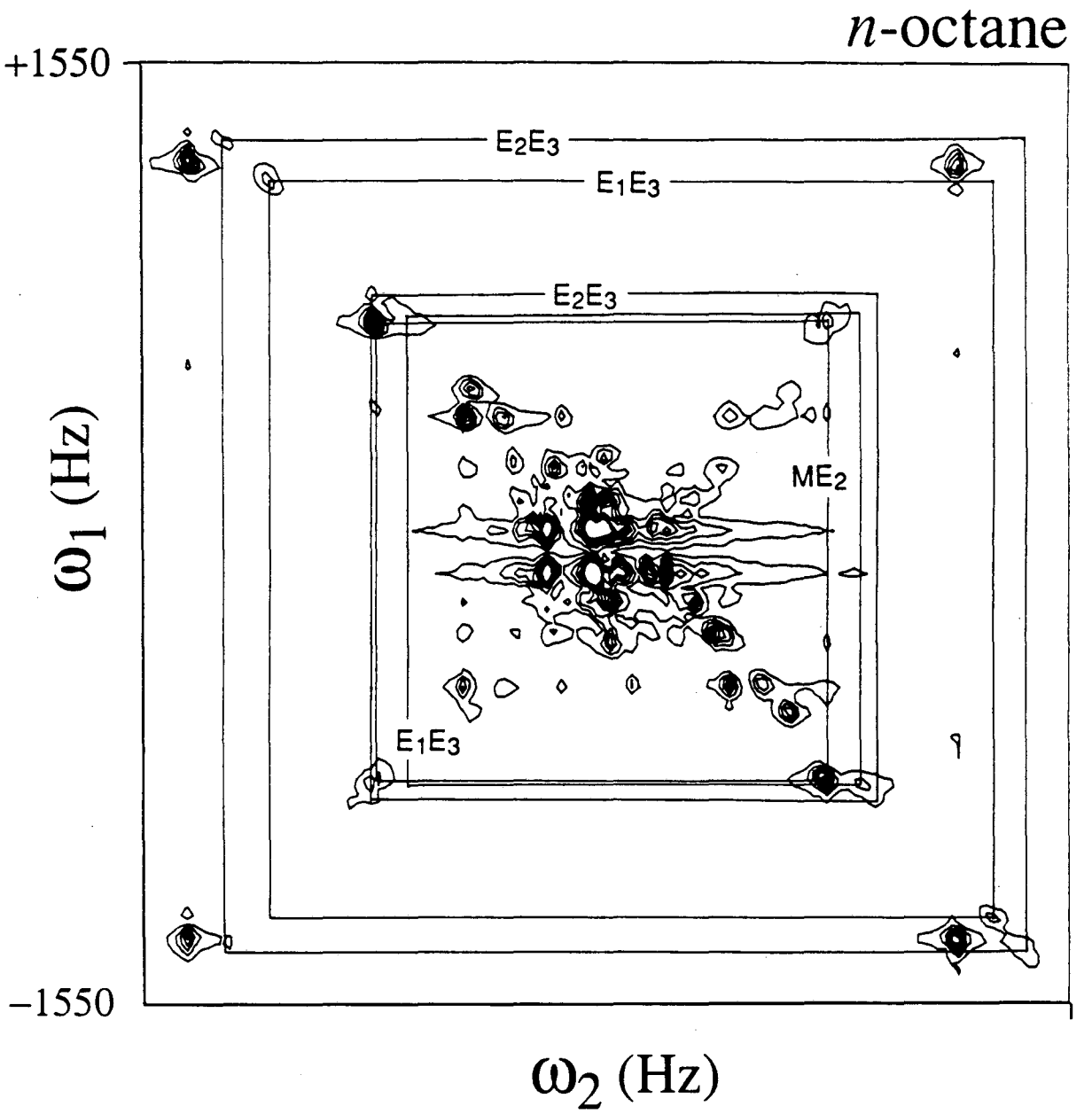

Figure 2.17: View of 2-quantum-filtered COSY of *n*-octane - enlarged view.

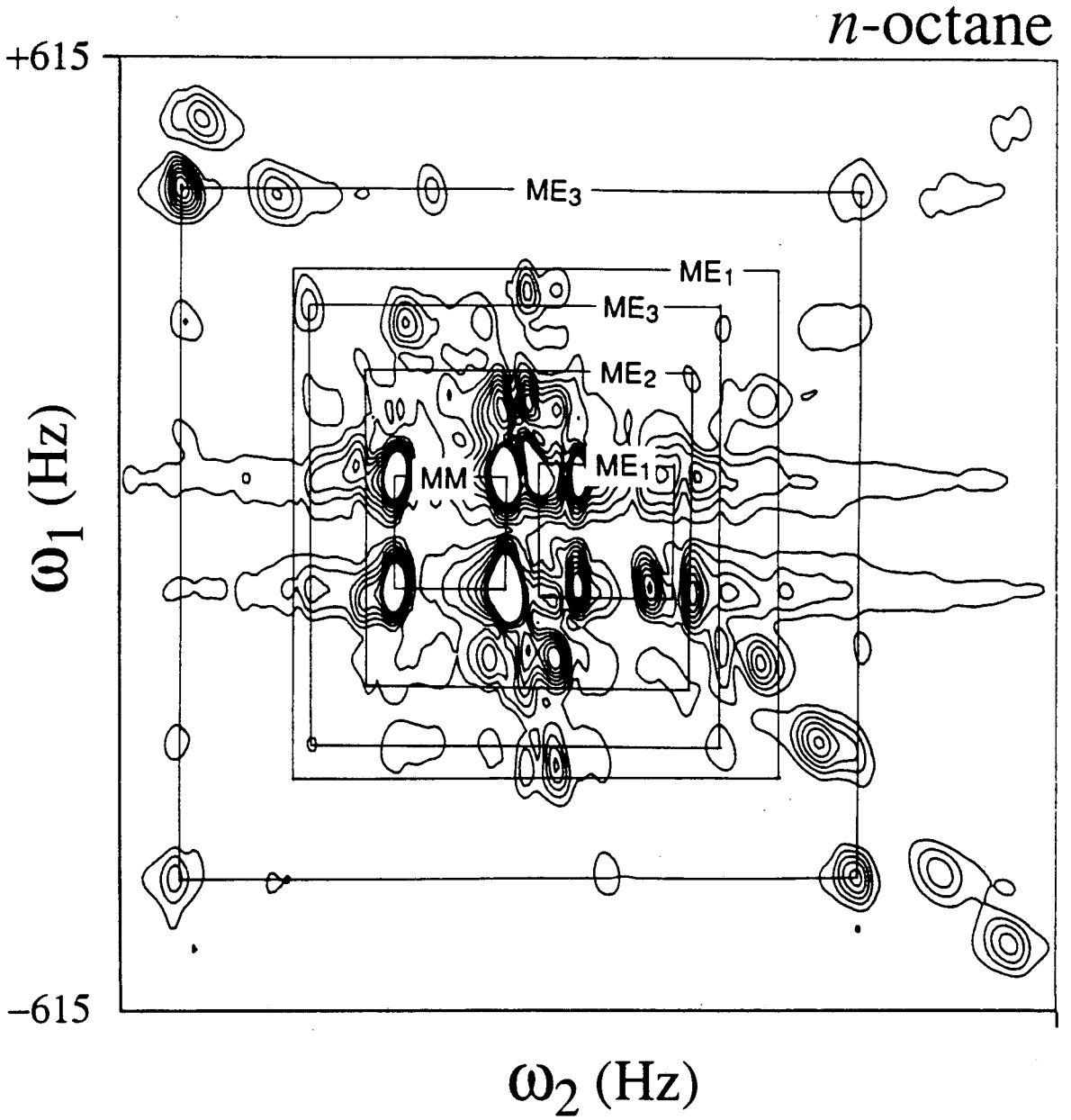

Figure 2.18: View of 2-quantum-filtered COSY of *n*-octane - enlarged view of center section.

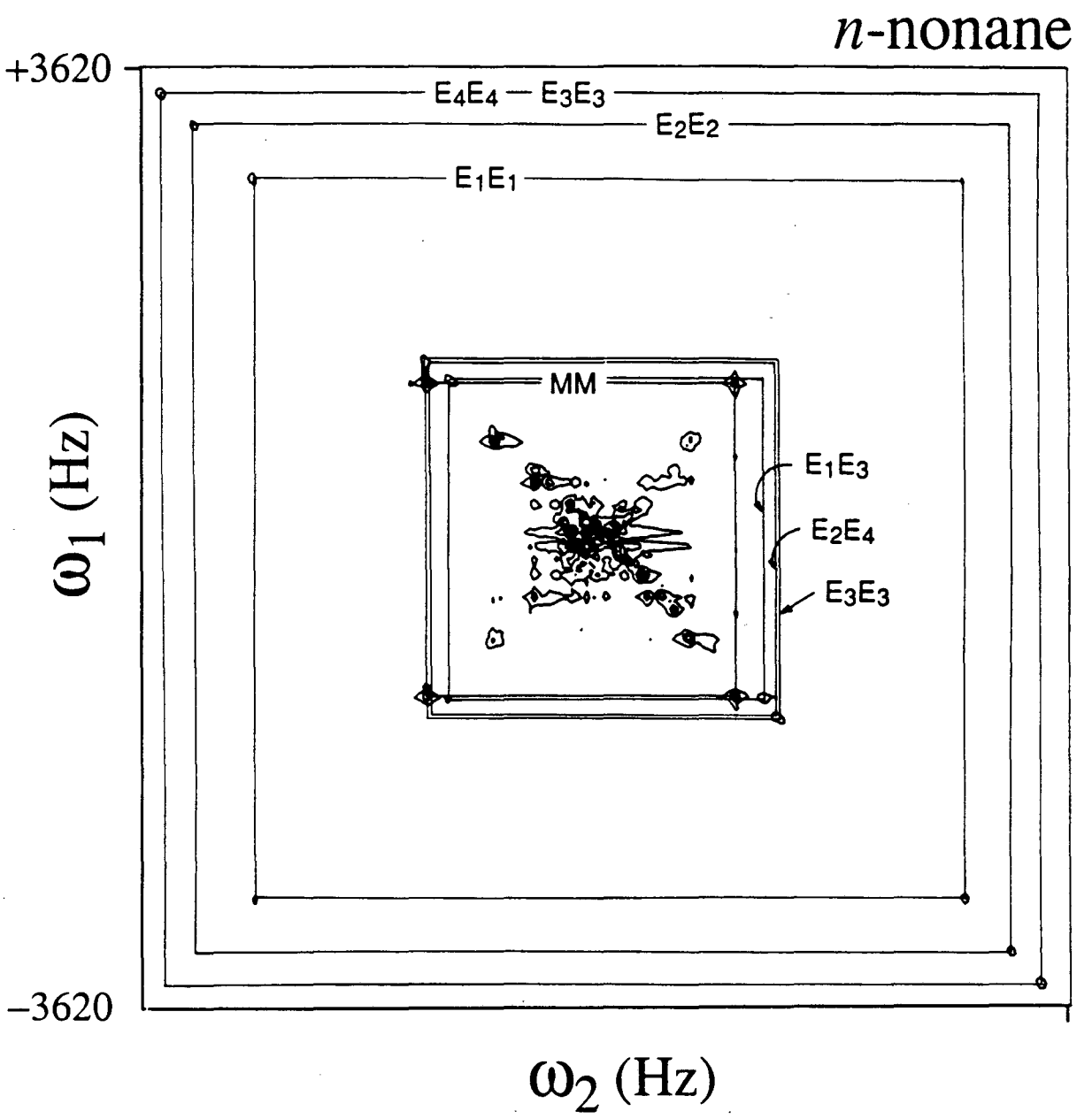

Figure 2.19: View of 2-quantum-filtered COSY of *n*-nonane - complete spectrum. The E_3E_3 and E_4E_4 geminal peaks are too close to resolve, although the intensity of the combined peak was approximately twice that of the E_1E_1 or E_2E_2.

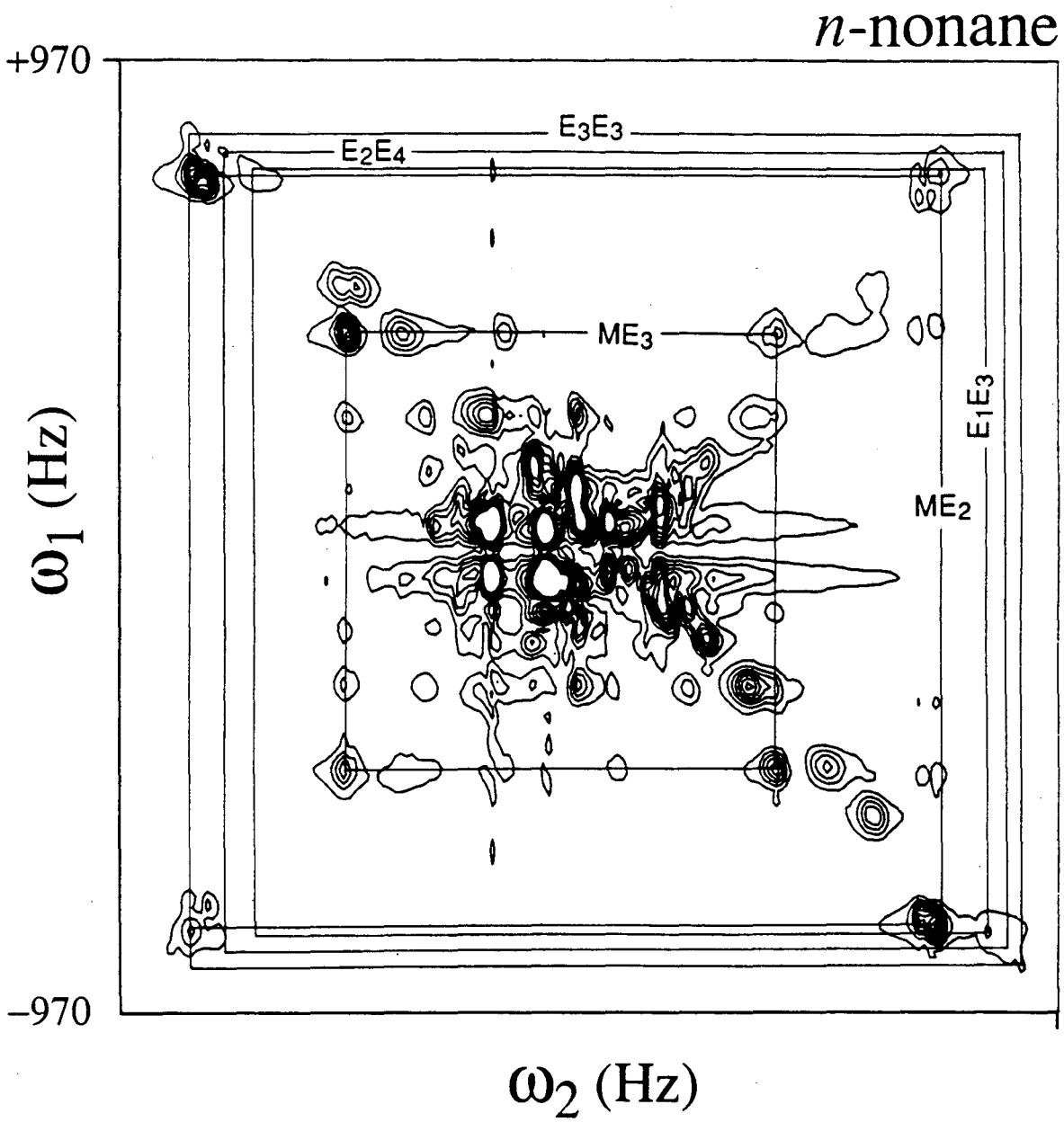

Figure 2.20: View of 2-quantum-filtered COSY of *n*-nonane - enlarged view.

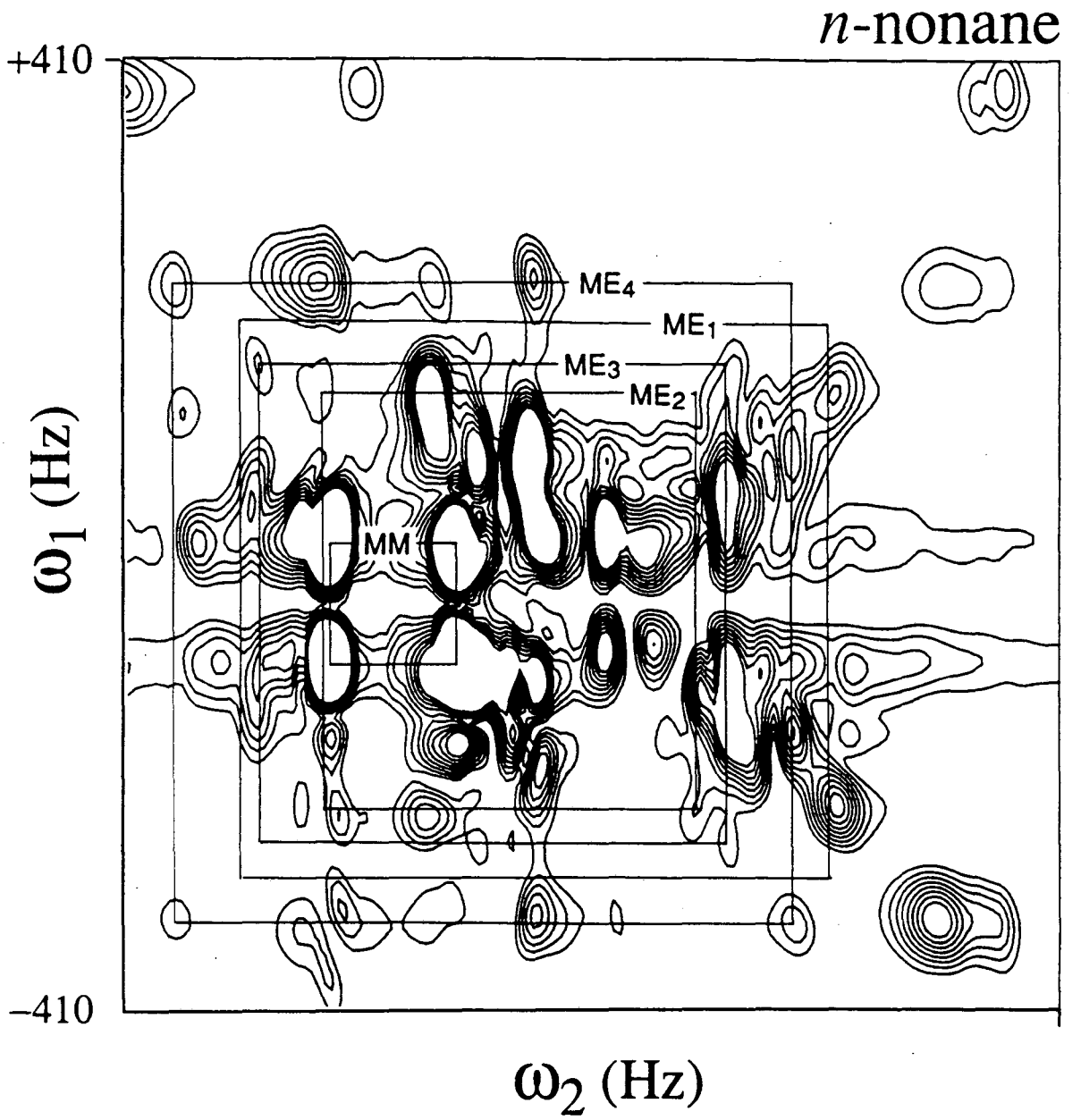

Figure 2.21: View of 2-quantum-filtered COSY of *n*-nonane - enlarged view of center section.

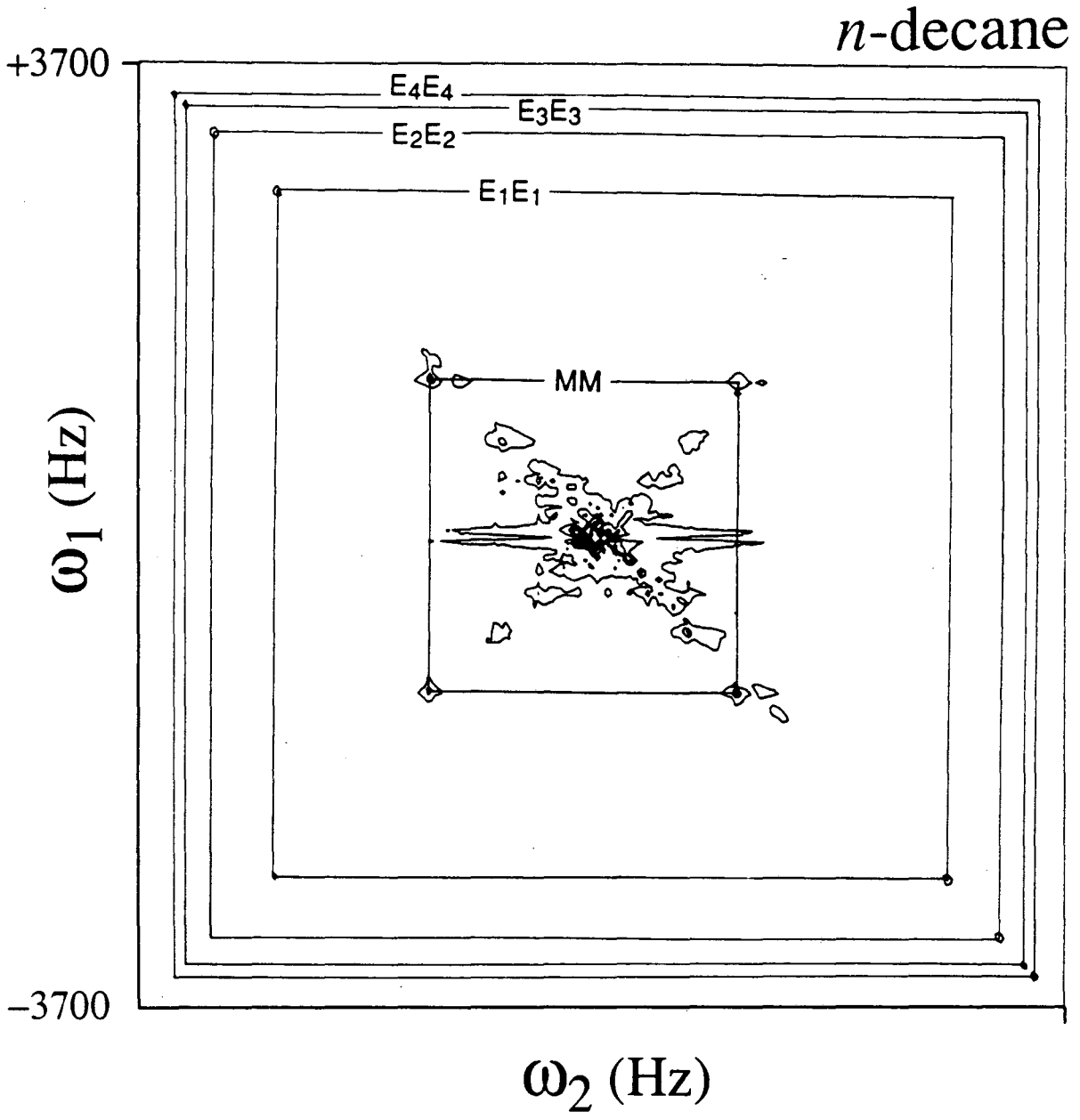

Figure 2.22: View of 2-quantum-filtered COSY of *n*-decane - complete spectrum.

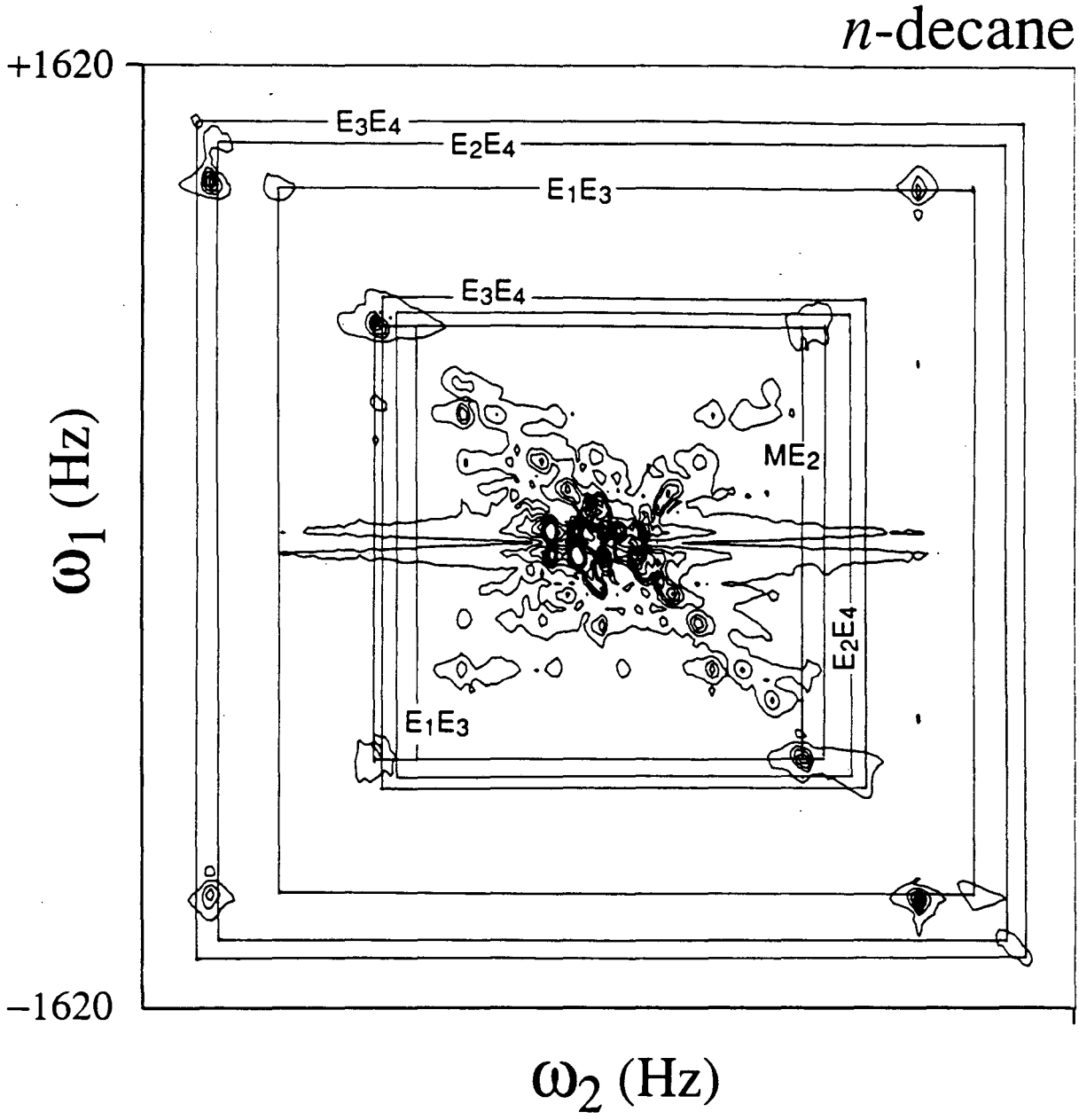

Figure 2.23: View of 2-quantum-filtered COSY of *n*-decane - enlarged view.

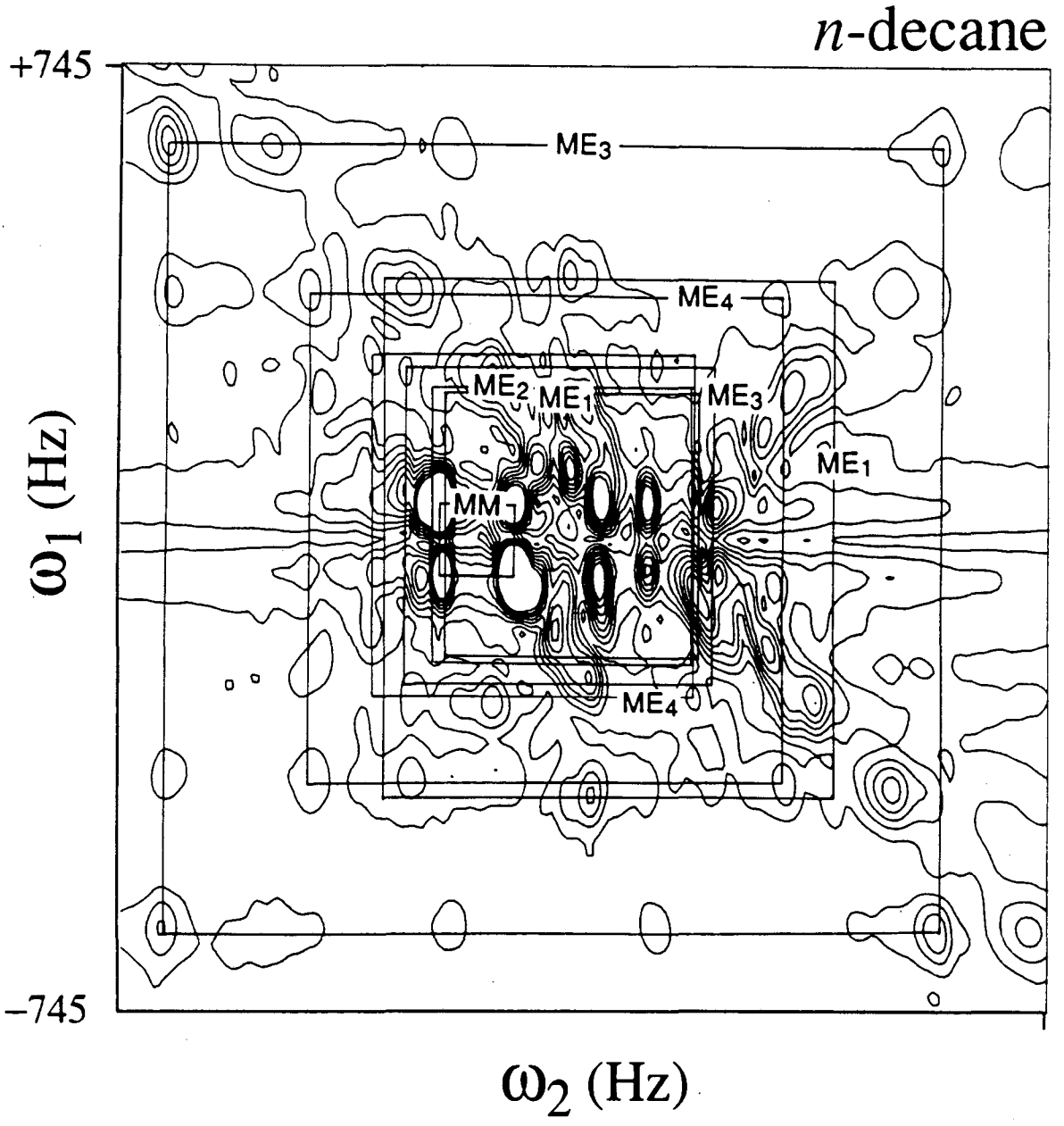

Figure 2.24: View of 2-quantum-filtered COSY of *n*-decane - enlarged view of center section.

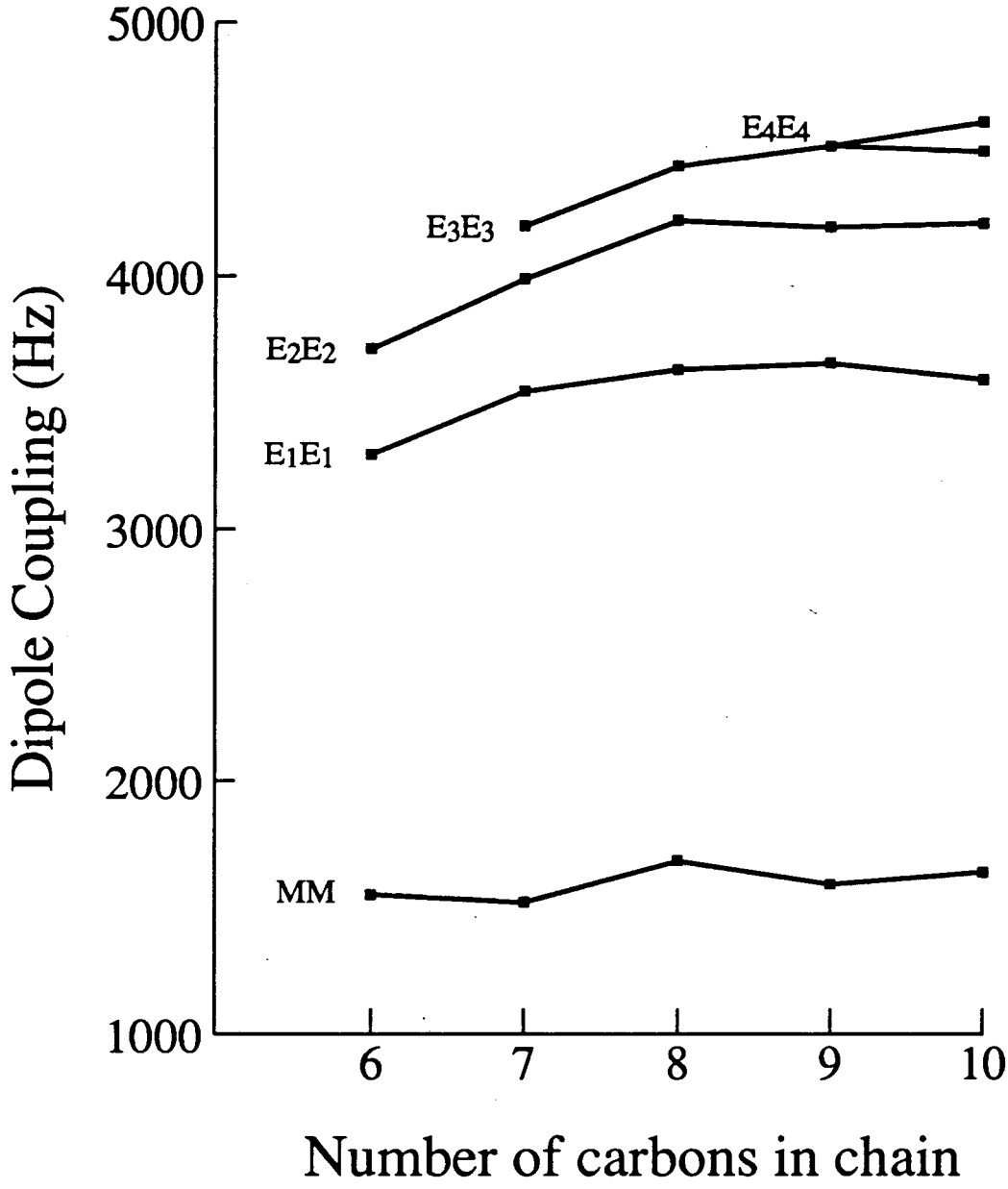

Figure 2.25: Comparison of the geminal (E_nE_n) dipole couplings for the series of alkanes. The coupling strength, in Hertz, is plotted as a function of chain length. Note the even-odd oscillation for the MM couplings.

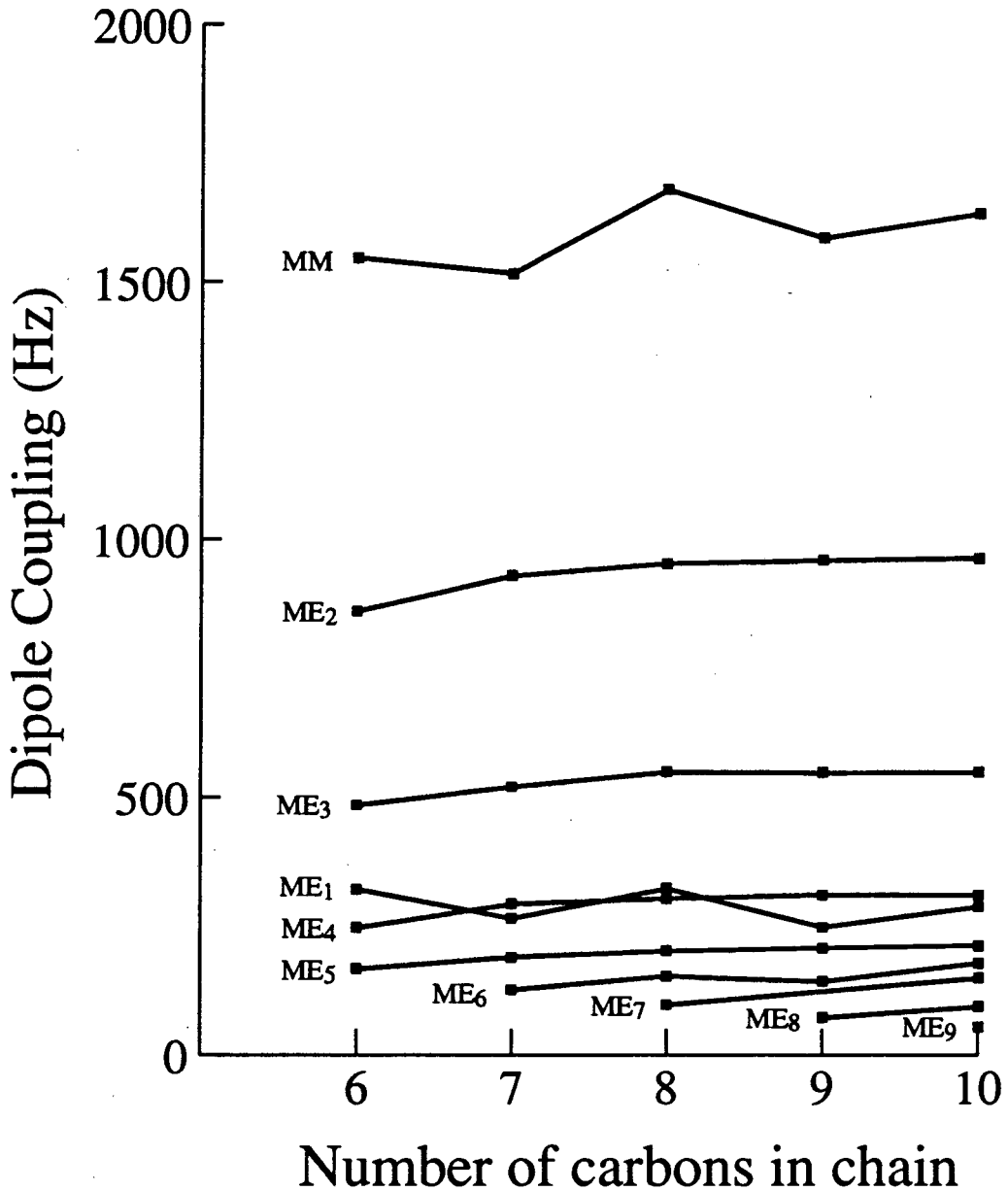

Figure 2.26: Comparison of the methyl-ethyl and methyl-methyl dipole couplings for the alkane series. These coupling give information about distance along the chain axis. Note the even-odd effect for the MM and ME_1 couplings.

ethyl couplings for the chains scale similarly, suggesting a comparable ordering environment for the chains.

2.4 Model Calculations

Given the experimental average dipole couplings, $\langle D_{ij} \rangle$, models are used in which these couplings serve as constraints for the determination of the model parameters. The models treat the liquid crystalline solvent as a uniform medium that interacts with the alkane solute through a mean-field potential. These calculations yield order parameters and conformational distributions for the solute molecules.

As a simplifying step, we assume a fixed number of discrete conformational states for the alkane as prescribed by the rotational isomeric state (RIS) approximation, [65]. This restricts rotation about each carbon-carbon bond to three minima: trans (the lowest energy conformation), gauche$^+$ and gauche$^-$ (slightly higher energy), giving 3^{n-3} possible conformations for the entire chain. Thus the dipole couplings can be calculated from a finite sum over conformers [66],

$$\langle D_{ij} \rangle = \frac{2}{3} \sum_n \sum_{\alpha,\beta} P^n S^n_{\alpha\beta} D^n_{ij,\alpha\beta}. \tag{2.9}$$

P^n is the probability of conformer n and $S^n_{\alpha\beta}$ its order tensor in a molecule-fixed coordinate frame. The order tensor is defined as

$$S^n_{\alpha\beta} = \frac{1}{2} \langle 3 \cos\theta_\alpha \cos\theta_\beta - \delta_{\alpha\beta} \rangle, \tag{2.10}$$

where θ_χ ($\chi = x, y, z$) is the angle between the director and the molecular χ axis.

The dipole coupling tensor components of conformer n for spin pair $i - j$ in the molecular frame are

$$D^n_{ij,\alpha\beta} = -\frac{\gamma^2 h}{4\pi^2} \frac{1}{r^3_{ij}} (3 \cos\theta^{ij}_\alpha \cos\theta^{ij}_\beta - \delta_{\alpha\beta}), \tag{2.11}$$

with θ_{χ}^{ij} the angle between the internuclear vector $\mathbf{r}_{ij}$ and the molecular χ axis.

In general, the product $P^n S_{\alpha\beta}^n$ is inseparable because of the complex conformational and reorientational averaging. Therefore, determining the structure of a flexible molecule requires the development of a parametrized model to describe the orientations and energies of the various conformers, and optimization of the parameters by least-squares minimization with respect to the experimental data. While to date only deuterium quadrupole couplings have been available for any sizeable alkane chain, the dipole couplings from this work presents a much richer set of constraints. In the following we will use two models [43, 44] to analyze our experimental data.

2.4.1 Parametrization of the Models

Following the treatment by Emsley and Luckhurst [67], the total energy of a solute conformer n in the liquid crystal is separated into an isotropic part describing the internal energy of the conformer and an orientation-dependent part describing the solute–solvent interaction:

$$U_{tot}^n = U_{int}^n + U_{ext}^n(\theta, \phi). \tag{2.12}$$

The internal energy is calculated using the RIS approximation:

$$U_{int}^n = n_g E_{tg} + n_{g^+g^-} E_{g^+g^-}, \tag{2.13}$$

where n_g is the number of gauche bonds in the given conformer, E_{tg} is the difference in energy between a trans and a gauche bond, and the second term accounts for the pentane effect [65] by penalizing adjacent g^+g^- bonds. The gauche energy, E_{tg}, is used as an adjustable parameter, while the g^+g^- energy, $E_{g^+g^-}$, whose variation

has only a minor effect on the results is taken as a constant of 12.55 kJ/mole [65] in our calculations. An alternative for the second term of Equation 2.13 is to use a Lennard-Jones interaction between pairs of united atoms (treating the methyl and methylene groups as single atoms) which are three or more bonds apart. This form of U^n_{int} was used, for example, by Samulski and coworkers [43].

For the external part of the energy, U^n_{ext}, several models have been described in the literature (*e.g.* [43, 44, 68, 69, 70, 61, 62]). In some models each solute conformer is treated as an entity whose interaction with the liquid crystal mean field is based primarily on its size and shape. In other models, the interaction is assumed to be the sum of contributions from the various segments of the conformer. In the following, two realizations of the former approach are described.

Samulski and coworkers [43] used a model (referred to hereafter as model A) in which each conformer is approximated by a rectangular parallelepiped with length L, breadth B, and width W. They used this model to simulate quadrupole couplings of several n-alkanes ranging in size from pentane up to hexadecane [43]. The values of L, B, and W are chosen equal to twice the semiaxes of the inertia ellipsoid [68] of the conformer, where the semiaxes A_α are aligned along the principal moments of inertia:

$$A_\alpha = \sqrt{\frac{5}{2m}(-I_{\alpha\alpha} + I_{\beta\beta} + I_{\gamma\gamma})}, \tag{2.14}$$

with $A_z \parallel L \geq A_y \parallel B \geq A_x \parallel W$, and m equal to the mass of the ellipsoid. The solute–liquid crystal interaction is described by the excluded volume interaction of the parallelepipeds [71]. This interaction is parametrized as

$$U_{ext}(\theta, \phi) = \varepsilon[u_{20}d^2_{00}(\theta) + 2u_{22}d^2_{02}(\theta)\cos(2\phi)], \tag{2.15}$$

with the coefficients u_{2n} quantifying the excluded volume:

$$u_{20} = \frac{1}{3}\left[6LBW + L(W^2 + B^2) - 2W(L^2 + B^2) - 2B(W^2 + L^2)\right], \tag{2.16}$$

$$u_{22} = \frac{1}{\sqrt{6}}\left(L^2 - BW\right)\left(B - W\right), \tag{2.17}$$

the reduced Wigner matrix elements describing the orientation dependence:

$$d^2_{00}(\beta) = \frac{1}{2}[3\cos^2(\beta) - 1], \tag{2.18}$$

$$d^2_{02}(\beta) = \frac{\sqrt{6}}{4}[\sin^2(\beta)], \tag{2.19}$$

and the adjustable interaction energy parameter ε [43] which is varied along with the trans-gauche energy difference, E_{tg}, to fit the experimental data.

Burnell and coworkers [44, 45, 72, 73, 74] modelled the liquid crystalline matrix as an elastic continuum which exerts an orienting force on the solute. This harmonic potential (referred to hereafter as model B) was originally used to simulate dipole and quadrupole couplings for small solutes [44, 72, 73, 74]. More recently, it was used to model deuterium quadrupole couplings for flexible alkyl groups on the liquid crystal 4-n-pentyl-4′-cyanobiphenyl [45]. Here, the interaction energy assumes the form:

$$U_{ext}(\theta, \phi) = \frac{k}{2}c^2(\theta, \phi), \tag{2.20}$$

where c is the circumference of the projection of the molecular shape, approximated by a group of van der Waals spheres, onto a plane perpendicular to the director of the liquid crystal. The "minimum circumference" shown in Figure 2.27, gives slightly better results than the "maximum circumference" [44], which follows the perimeter of the projection faithfully. The force constant, k, and the trans-gauge energy differential, E_{tg} are adjusted to fit the data.

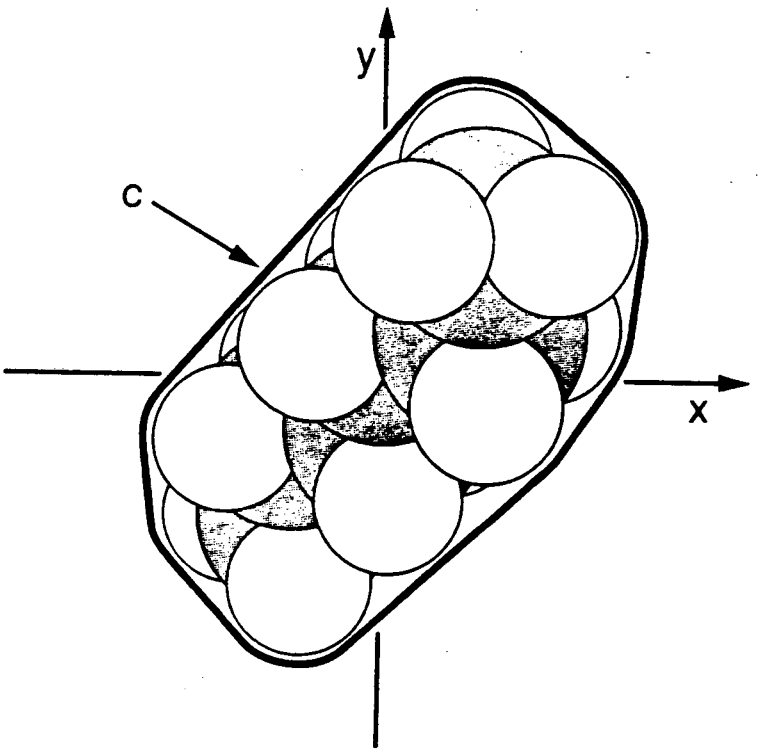

Figure 2.27: Minimum circumference projection of an alkane, used to parametrize the elastic tube model. The "footprint" of the alkane in the plane perpendicular to the director is traced out with the minimum path length.

Table 2.9: Alkane structural parameters used in the mean field model calculations.

length of C–H bond	1.09 Å
length of C–C bond	1.53 Å
bond angle HCH of methylene group	109.0°
bond angle HCH of methyl group	109.47°
bond angle CCC	112.0°
dihedral angles for gauche conformations	±112.5°
van der Waals radius of H	1.2 Å
van der Waals radius of C	1.7 Å

With these two parametrizations for the energy, we can calculate the conformer probabilities, P^n, and order matrices, $\mathbf{S}^n$, by standard statistical mechanical methods. The conformer probability is given by

$$P^n = \exp(-\frac{U^n_{int}}{\mathrm{k}T})\ \frac{Z^n_{ext}}{Z_{tot}}, \tag{2.21}$$

with the total partition function

$$Z_{tot} = \sum_n \exp(-\frac{U^n_{int}}{\mathrm{k}T}) Z^n_{ext} \tag{2.22}$$

and the orientational partition function

$$Z^n_{ext} = \int_0^{2\pi} \int_0^{\pi} \exp(-\frac{U^n_{ext}(\theta,\phi)}{\mathrm{k}T}) \sin\theta\, \mathrm{d}\theta\, \mathrm{d}\phi. \tag{2.23}$$

The order matrix is obtained according to Equation 2.10 by

$$S^n_{\alpha\beta} = \frac{1}{2Z^n_{ext}} \int_0^{2\pi} \int_0^{\pi} (3\cos\theta_\alpha \cos\theta_\beta - \delta_{\alpha\beta}) \exp(-\frac{U^n_{ext}(\theta,\phi)}{\mathrm{k}T}) \sin\theta\, \mathrm{d}\theta\, \mathrm{d}\phi. \tag{2.24}$$

With the geometric parameters of the hexane molecule given in Table 2.9, the average dipolar couplings can be calculated from Equations 2.9, 2.11, 2.21 and 2.22.

2.4.2 Results and Discussion of the Model Calculations

Both models, each with only two adjustable parameters (E_{tg} and ε for model A and E_{tg} and k for model B), were fitted to the experimental couplings from the COSY experiment by minimizing the root-mean-square deviation of the simulated couplings from the experimental

$$R = \sqrt{\frac{1}{n}\sum_{i,j}(\langle D_{ij}\rangle^{exp} - \langle D_{ij}\rangle^{calc})^2}. \tag{2.25}$$

where the sum is performed over the n chosen dipole couplings. The least-squares fit was performed for both the temperature-corrected and uncorrected data, with the results shown in Tables 2.4, 2.5, 2.6, 2.7, and 2.8. In Table 2.10, we summarize the values of the adjustable parameters E_{tg}, ε, k, and the deviation R.

The probabilities of the different conformers obtained for the best fits shown in Tables 2.11 and 2.12 are similar for both models. The probabilities of conformers with the same number of gauche bonds are fairly insensitive to the position along the chain at which those gauche bonds occur. Therefore, we can simplify the summary of the results by grouping all the conformers with a given number of gauche bonds. Conformers with adjacent g^+ and g^- bonds have negligibly low ($\leq$ 0.0002) probabilities and are grouped in one category for each alkane. Our values of E_{tg} (3.13 – 4.46 kJ mol^{-1} for model A and 3.24 – 4.45 kJ mol^{-1} for model B) are at the upper end of the widely varying range of E_{tg} values previously measured for liquid alkanes (between ca. 2.0 and 3.8 kJ mol^{-1}, see for example [75, 76, 77, 78, 79, 80, 81, 82, 83, 84]). (Recently, Photinos *et al.* [61, 62, 85] have given a parametrization of U_{ext} with which good fits of experimental couplings can be obtained for the nominal E_{tg} value of 2.09 kJ mol^{-1}.)

Table 2.13 lists the average order matrices $\langle$S$\rangle$ in the principal axis systems of

Table 2.10: Results of the least-squares fits for the temperature-corrected dipole couplings.

Model	E_g (kJ mol^{-1})	ε (10^7 J m^{-3})	k (10^{-3} N m^{-1})	R (Hz)
n-hexane				
A	3.13	12.77		37.9
B	3.24		3.71	82.1
n-heptane				
A	3.38	9.67		52.1
B	3.37		3.14	93.8
n-octane				
A	3.74	7.48		84.7
B	3.77		2.68	94.9
n-nonane				
A	4.03	5.68		110.7
B	4.03		2.25	133.3
n-decane				
A	4.46	4.36		110.4
B	4.45		1.90	125.19

Table 2.11: Distribution of conformers for *n*-hexane and *n*-heptane and *n*-octane. The conformers are grouped by the number of gauche bonds, regardless of their position along the chain. Chains with adjacent gauche$^+$/gauche$^-$ bonds are listed in a separate category. For each model, both the aggregate probability for a given number of gauche bonds, and an average probability for a specific conformer, are listed. Conformers with probabilities lower than .01 are listed as such.

		Model A		Model B	
Gauche Bonds	# of Conformers	Prob.	Average	Prob.	Average
n-hexane					
0	1	.29	.29	.27	.27
1	6	.50	.08	.50	.08
2	8	.20	.02	.21	.03
3	2	.01	.01	.02	.01
g^+g^-	10	<.01	<.01	<.01	<.01
n-heptane					
0	1	.22	.22	.15	.15
1	8	.46	.06	.47	.06
2	18	.27	.02	.31	.02
3	12	.05	<.01	.06	.01
4	2	<.01	<.01	<.01	<.01
g^+g^-	40	<.01	<.01	<.01	<.01
n-octane					
0	1	.19	.19	.15	.15
1	10	.42	.04	.41	.04
2	32	.30	.01	.33	.01
3	38	.08	<.01	.10	<.01
4	16	.01	<.01	.01	<.01
5	2	<.01	<.01	<.01	<.01
g^+g^-	144	<.01	<.01	<.01	<.01

Table 2.12: Distribution of conformers for *n*-nonane and *n*-decane. The conformers are grouped by the number of gauche bonds, regardless of their position along the chain. Chains with adjacent gauche$^+$/gauche$^-$ bonds are listed in a separate category.

		Model A		Model B	
Gauche Bonds	# of Conformers	Prob.	Average	Prob.	Average
n-nonane					
0	1	.16	.16	.13	.13
1	12	.39	.03	.37	.03
2	50	.32	.01	.34	.01
3	88	.11	<.01	.13	<.01
4	66	.02	<.01	.02	<.01
5	20	<.01	<.01	<.01	<.01
6	2	<.01	<.01	<.01	<.01
g^+g^-	490	<.01	<.01	<.01	<.01
n-decane					
0	1	.15	.15	.13	.13
1	14	.37	.03	.34	.02
2	72	.32	<.01	.35	<.01
3	170	.13	<.01	.15	<.01
4	192	.02	<.01	.03	<.01
5	102	<.01	<.01	<.01	<.01
6	24	<.01	<.01	<.01	<.01
7	2	<.01	<.01	<.01	<.01
g^+g^-	1610	<.01	<.01	<.01	<.01

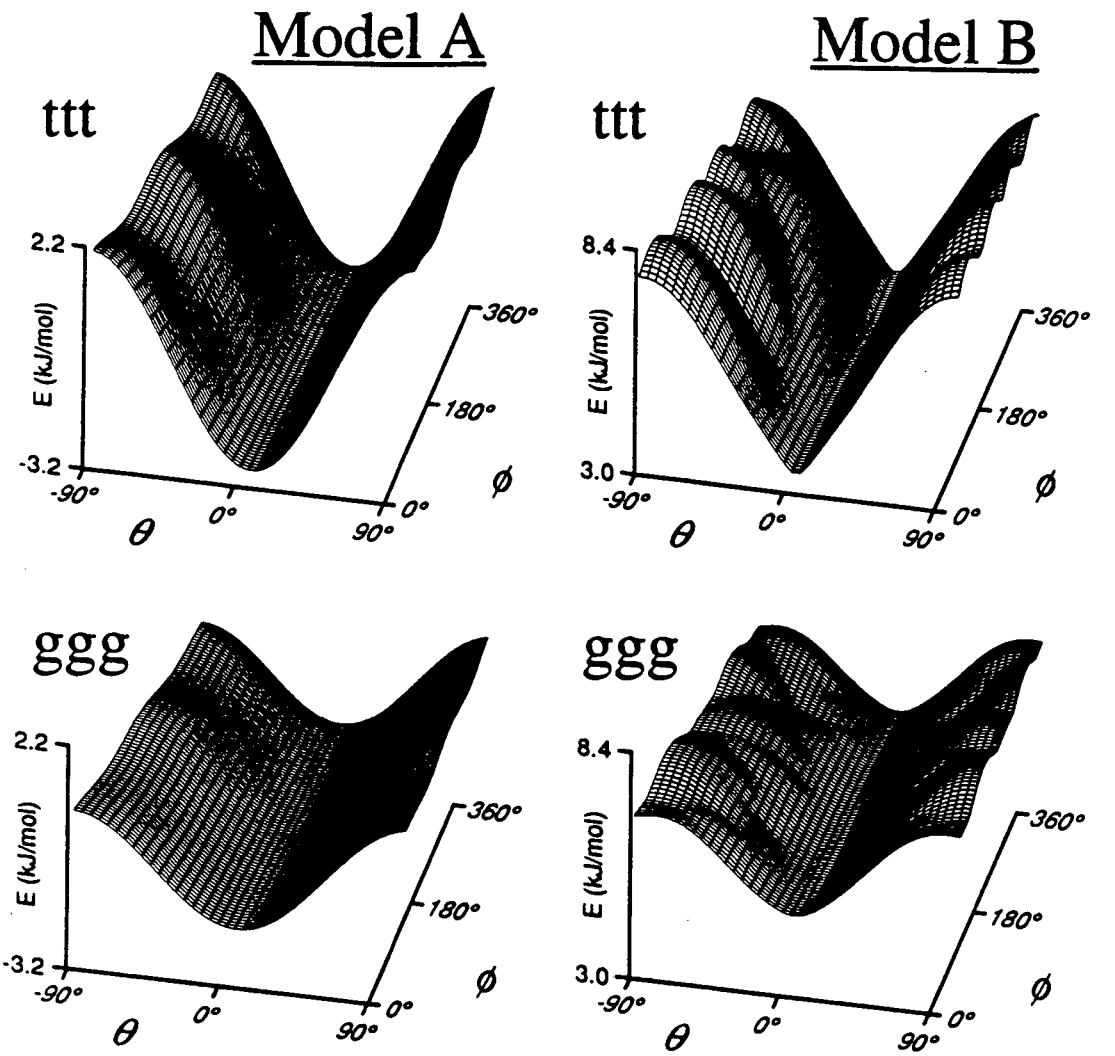

Figure 2.28: Orientational potential energy surfaces predicted by the two models for two disparate *n*-hexane conformers, *ttt* and *ggg*. The all-trans molecule, with its larger aspect ratio, has a steeper orientational potential than the all-gauche conformer. For longer chains, this difference between the two surfaces becomes even greater. There is a dc offset in the energy surface for Model B, to account for the non-zero circumference for all conformers.

Table 2.13: Primary components of the order parameters for the average conformation of each alkane (given in the principal axis system of the inertia tensor, the z axis corresponding to the long axis of the molecule).

Alkane	Model A		Model B	
	S_{zz}	$S_{xx} - S_{yy}$	S_{zz}	$S_{xx} - S_{yy}$
n-hexane	0.1693	−0.05633	0.1939	−0.01823
n-heptane	0.1944	−0.06089	0.2158	−0.02831
n-octane	0.2141	−0.06713	0.2317	−0.03329
n-nonane	0.2202	−0.07170	0.2376	−0.03251
n-decane	0.2242	−0.07624	0.2417	−0.03533

the inertia tensors of each molecule. While the matrices $\langle \mathbf{S} \rangle$ are diagonal in those frames for model A, they have non-vanishing but small components S_{xy}, S_{xz} and S_{yz} for model B, reflecting the different symmetries of the potentials. The order parameters of models A and B differ slightly, but both follow the same trends for the alkanes. As expected, the order parameter scales with chain length.

2.5 Conclusions

The model calculations demonstrate that both model A and model B together with the NMR data describe the main features of the orientation of a flexible molecule in a nematic liquid crystal and give reasonable estimates of the probabilities of the different conformers. There is some question, though, about the accuracy of the calculated E_{tg} values. Raman and infrared studies of gas-phase and liquid-phase alkanes derive E_{tg} values of ~3.8 kJ/mole for the gas, and ~2.3 kJ/mole in liquids [86]. Reduction of the trans-gauche conversion energy in liquids seems reasonable, since we would expect the compressive forces of the liquid to stabilize

the higher energy gauche conformations. Our model calculations indicate that the anisotropic averaging in the liquid crystal leaves the alkane preferentially aligned (in an elongated conformation) along the director axis. Thus we expect the trans-gauche energy differential to be higher than for isotropic liquids (*cf.* Table 2.10). On the other hand, the E_{tg}'s predicted by the models climb above the gas-phase value. This implies that the liquid crystalline environment is extremely ordered, and restrictive to solute reorientation. It is more probable that the E_{tg} values should climb above the liquid values, but not as dramatically as they do. Part of this problem may be attributable to the nature of the excluded volume model, which treats the solute-solvent interaction as occurring between the overall shape of the alkane and the mean field. A more promising model, developed recently [61, 62, 85], treats the interaction energy as piecewise-additive local interactions between subunits of the alkane and the mean field. This model calculates the potential by summing the interaction of the mean field with the chord connecting the midpoints of two carbon-carbon bonds. The model considers primarily those chords connecting bonds separated by zero or one intermediate carbon atoms, but can be extended to include bonds further separated along the chain.

An interesting question is whether the method for determining dipole couplings which has been presented here can be applied to larger molecules. With increasing size of the solute molecule, two problems arise: more lines appear in the spectrum, and the intensities of the individual lines decrease. The first problem is illustrated in Table 2.14. As the length of the alkane chain increases from six to twenty carbon atoms, the number of square patterns in the COSY spectrum increases rapidly; hence spectra will be more crowded and more difficult to interpret. The

Table 2.14: Number of unique 2-proton isomers (number of unique dipole couplings), $Z(2)$, as a function of chain length for n-alkanes. This gives a measure of the complexity of the spectra as chain length increases.

Number of carbon atoms	6	8	10	12	14	16	18	20
$Z(2)$	16	29	46	67	92	121	154	191

second problem is illustrated in Figure 2.29 showing the probability of two-proton isomers as a function of deuteration for various n-alkanes. The maxima in the curves decrease rapidly as the length of the alkane chain increases. The maxima are a measure of the relative intensities of the peaks in the spectrum for different chain lengths. For example, for n-decane one expects about three times as many lines as for n-hexane, each line at about one third the intensity, and for n-octadecane one expects a tenfold increase in complexity and a tenfold reduction in signal intensity. We expect that it is feasible with this method to analyze spectra for alkanes with up to twelve carbon atoms.

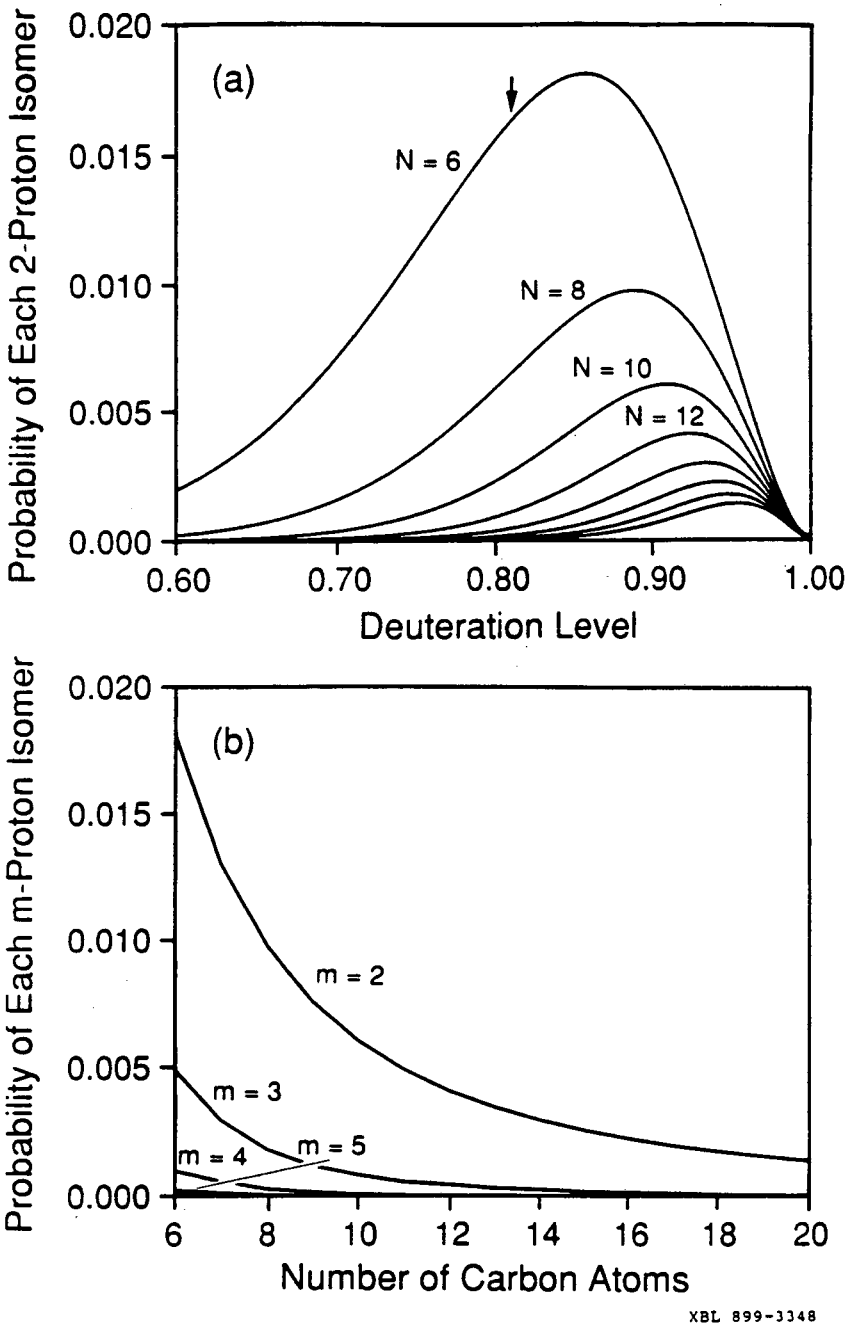

Figure 2.29: Isomer statistics for higher n-alkanes (N = number of carbon atoms). (a) Probability of each 2-proton isomer, *i.e.* probability of 2-proton molecules divided by the number of different 2-proton isomers, as a function of deuteration level. The arrow indicates the level of deuteration of the sample used for our experiments. (b) Probability of each m-proton isomer evaluated at the maxima of the curves in (a) as a function of the number of carbon atoms.

Chapter 3

Homonuclear Cross-Polarization

3.1 Introduction

Structural elucidation is usually a precondition to determining or predicting the reactive behavior of large biomolecules. Traditionally, though, chemists have relied on x-ray diffraction of single crystals to provide this information. Two-dimensional nuclear magnetic resonance [87, 49] provides a powerful technique for determining the structures of large molecules in their native solution state, without the need for single crystals. Correlation spectroscopy in liquids [4, 88] capitalizes on the J-couplings between spins to create coherences which can be used to elucidate the spin coupling network in the molecule. This information provides a set of experimental constraints for determining the primary structure of the molecule.

A variety of techniques for performing such correlation experiments has been demonstrated in the last decade. To catalog them here would be a prohibitively lengthy enterprise, and the reader is referred to several modern treatises on the subject [87, 49, 89, 90, 91]. We are concerned here with presenting a class of

experiments, known variously as rotating frame cross-polarization, homonuclear Hartmann-Hahn (HOHAHA), or total correlation spectroscopy (TOCSY), experiments [92, 93, 94, 95, 96, 97, 98, 99, 100, 101], and specifically, the application of a new broadband decoupling sequence, DIPSI-2, to effect this cross-polarization. Unlike the COSY-type experiments, where coupled spins evolve under a weak coupling Hamiltonian, in the Hartmann-Hahn experiments cancellation of the chemical shift terms in the spin evolution Hamiltonian allows the spin system to evolve under a pure scalar coupling, and facilitates efficient magnetization exchange between coupled spins.

3.2 The TOCSY Experiment

3.2.1 The Isotropic Mixing Hamiltonian

Homonuclear cross-polarization differs from previously described coherence transfer experiments, such as COSY (*cf.* Section 1.2.1), in that it allows net magnetization transfer, rather than differential transfer. The COSY experiment generates a spectrum of zero integrated intensity, because of its antiphase (up/down) cross-peak patterns and 90° phase shift between the cross peaks and the diagonal. The drawback of such an experiment manifests itself with closely-spaced resonances, or inhomogeneous B_0 fields, where the anti-phase lines will interfere destructively, reducing the signal-to-noise. The TOCSY, or TOtal Correlation SpectroscopY, experiment generates a two-dimensional spectrum with both the cross peaks and diagonal peaks in-phase.

In the weak coupling regime (J-coupled spins evolving freely in a static field),

the evolution Hamiltonian can be written as a sum of the Zeeman interaction and a spin-spin coupling term

$$\mathcal{H}_{\text{total}} = \mathcal{H}_Z + \mathcal{H}_J = \sum_i -\omega_i I_{iz} + 2\pi \sum_{i \neq j} J_{ij} I_{iz} I_{jz} \tag{3.1}$$

where the first term includes the single-spin chemical shift information, and the second term defines the J-coupling between the spins. To optimize the exchange of polarization, we seek to eliminate the chemical shift terms (linear spin operators) of the spin network, and allow it to evolve under a pure scalar coupling Hamiltonian (bilinear operators)

$$\mathcal{H}_Z \rightarrow 0 \qquad \mathcal{H}_{\text{total}} \rightarrow 2\pi \sum_{i \neq j} J_{ij} \mathbf{I}_i \cdot \mathbf{I}_j \tag{3.2}$$

For the case of two spins, we can write the basis set as sum and difference terms for the linear and bilinear spin operators, following the derivation of Braunschweiler and Ernst [92]. For the three Cartesian coordinates, $\alpha, \beta = x, y, z$ we have

$$\begin{aligned}
\Sigma_\alpha &= \tfrac{1}{2}(I_{1\alpha} + I_{2\alpha}) \\
\Delta_\alpha &= \tfrac{1}{2}(I_{1\alpha} - I_{2\alpha}) \\
\Sigma_{\alpha\beta} &= \tfrac{1}{2}(I_{1\alpha} I_{2\beta} + I_{1\beta} I_{2\alpha}) \\
\Delta_{\alpha\beta} &= \tfrac{1}{2}(I_{1\alpha} I_{2\beta} - I_{1\beta} I_{2\alpha})
\end{aligned} \tag{3.3}$$

If we can create a purely scalar Hamiltonian, $\mathcal{H}_J$, during the mixing period, we need only consider the following commutation relations for the evolution of the system

$$\begin{aligned}
[\mathcal{H}_J, \Sigma_\alpha] &= 0 \\
[\mathcal{H}_J, \Delta_\alpha] &= i\Delta_{\beta\gamma}
\end{aligned}$$

$$\begin{aligned}\left[\mathcal{H}_J, \Sigma_{\alpha\beta}\right] &= 0 \\ \left[\mathcal{H}_J, \Delta_{\beta\gamma}\right] &= -i\Delta_\alpha,\end{aligned} \tag{3.4}$$

where (α, β, γ) is the cyclic permutation of the Cartesian indices (x, y, z). This implies that the sum of the linear and bilinear terms are preserved independently, while the mixing Hamiltonian exchanges single-spin difference terms with two-spin difference terms. The consequent equations of motion during our radiofrequency pulse sequence are

$$\begin{aligned}\Delta_\alpha &\xrightarrow{\mathcal{H}_J\tau_m} \Delta_\alpha \cos(2\pi J\tau_m) + \Delta_{\beta\gamma} \sin(2\pi J\tau_m) \\ \Delta_{\beta\gamma} &\xrightarrow{\mathcal{H}_J\tau_m} \Delta_{\beta\gamma} \cos(2\pi J\tau_m) - \Delta_\alpha \sin(2\pi J\tau_m)\end{aligned} \tag{3.5}$$

A difference in polarization between the two spins, (for example $I_{1z} - I_{2z}$) will allow magnetization to be transferred from spin 1 to spin 2. Expressing the magnetization vector I_{1z} as a sum of $\sum_\alpha$ and Δ_α terms clarifies this:

$$I_{1z} = \tfrac{1}{2}(I_{1z} + I_{2z}) + \tfrac{1}{2}(I_{1z} - I_{2z}) = \sum_z + \Delta_z \tag{3.6}$$

During a mixing period of length, $\tau_m = 1/2J$, the inital magnetization component, I_{1z}, evolves under the purely scalar Hamiltonian, $\mathcal{H}_J$, to yield

$$\sum_z + \Delta_z \xrightarrow{\mathcal{H}_J\tau_m} \sum_z - \Delta_z \tag{3.7}$$

or, more simply

$$I_{1z} \xrightarrow{\mathcal{H}_J\tau_m} I_{2z} \tag{3.8}$$

where we've used the J-coupling to transfer magnetization from one spin to its coupling partner. During the mixing period, the initial difference magnetization, $(I_{1z} - I_{2z})$, oscillates through a zero-quantum coherence, $(I_{1x}I_{2y} - I_{1y}I_{2x})$ to a state

of $(I_{2z} - I_{1z})$. For transverse initial states (I_{1x} or I_{1y}), the intermediate state is an antiphase coherence of the form $(I_{1\alpha}I_{2z} - I_{1z}I_{2\alpha})$, where $\alpha = x, y$. It is important to note that the total polarization $(I_{2z} + I_{1z})$ is conserved by the mixing process, and exchange occurs only for difference states.

3.3 Generating a Pure Scalar Evolution Operator

An effective cross-polarization sequence seeks to eliminate the linear spin operators (chemical shift), while leaving the bilinear operators (J-coupling) unperturbed. Several pulse sequences have been suggested to effect this condition. The earliest, the Hartmann-Hahn match [102], involves continuous irradiation of the coupled spins. Braunschweiler and Ernst, in introducing the TOCSY experiment, suggested windowed trains of 180° and 90° pulses to improve the performance [92]. Newer sequences, developed for use in broadband spin decoupling [103, 104, 105, 106, 107, 108, 109, 110, 111], improve upon this performance. Recent efforts in the decoupling of scalar-coupled protons from a heteronucleus have resulted in a new class of sequences, known as the DIPSI sequences, which optimize not only the removal of the chemical shift, but attempt to generate as pure a scalar coupling between protons as possible.

The mixing sequences needed to effect magnetization transfer are applied with relatively weak RF fields (a few kilohertz) for periods of several tens of milliseconds. In this limit, the mixing sequence does not behave as a concatenation of ideal δ-pulses, but rather manifests imperfections such as offset effects, RF inhomogeneity, and tip angle misset. Coherent averaging theory [112, 113, 114] allows us to analyze the behavior of the sequence with respect to a variety of imperfections.

Consider the Hamiltonian for two coupled spins with different chemical shift offsets during RF irradiation:

$$\mathcal{H} = \underbrace{-\gamma B_1 I_{1x} - \gamma B_1 I_{2x}}_{\mathcal{H}_{RF}} \underbrace{-\Delta\omega_1 I_{1z} - \Delta\omega_2 I_{2z} + 2\pi J \mathbf{I}_1 \cdot \mathbf{I}_2}_{\mathcal{H}_{int}}. \tag{3.9}$$

Assuming irradiation resonant with spin 1, we can decompose the Hamiltonian into an internal part,

$$\mathcal{H}_{int} = -\Delta\omega_2 I_{2z} + 2\pi J \mathbf{I}_1 \cdot \mathbf{I}_2 \tag{3.10}$$

and an external part, corresponding to the RF irradiation,

$$\mathcal{H}_{RF} = -\gamma B_1 I_{1x} - \gamma B_1 I_{2x}. \tag{3.11}$$

If there exists an operator, $U(t)$ that satisfies the Schrödinger equation,

$$\dot{U}(t) = -i\mathcal{H}(t)U(t) \tag{3.12}$$

then that operator is of the form

$$U(t) = \mathbf{T}\exp\left(-i\int_0^t \mathcal{H}(\tau)d\tau\right) \tag{3.13}$$

where $\mathbf{T}$ is the Dyson time-ordering operator. To ease numerical calculations, we would like a solution to the differential equation that does not involve the time-ordering operator. Namely, we would like like to convert to a form

$$U(\tau) = \exp(-i\overline{\mathcal{H}}\tau), \tag{3.14}$$

where $\overline{\mathcal{H}}$ is an *average* Hamiltonian. The Magnus expansion allows us to expand this as a sum of operators

$$\overline{\mathcal{H}} = \overline{\mathcal{H}}^{(0)} + \overline{\mathcal{H}}^{(1)} + \overline{\mathcal{H}}^{(2)} + \ldots \tag{3.15}$$

where

$$\begin{aligned}
\overline{\mathcal{H}}^{(0)} &= \frac{1}{\tau}\int_0^{\tau}\mathcal{H}(\tau)dt_1 \\
\overline{\mathcal{H}}^{(1)} &= \frac{-i}{2\tau}\int_0^{\tau}dt_1\int_0^{t_1}dt_2[\mathcal{H}(t_2),\mathcal{H}(t_1)] \\
\overline{\mathcal{H}}^{(2)} &= \frac{-1}{6\tau}\int_0^{\tau}dt_1\int_0^{t_1}dt_2\int_0^{t_2}dt_3[\mathcal{H}(t_1),[\mathcal{H}(t_2),\mathcal{H}(t_3)] \\
&\qquad +[\mathcal{H}(t_3),[\mathcal{H}(t_2),\mathcal{H}(t_1)]]
\end{aligned} \tag{3.16}$$

For short times, τ, we often need consider only the zeroth order average Hamiltonian. Longer evolution times, or cases where Hamiltonians of different time slices do not commute, necessitate inclusion of higher order terms in the expansion.

Transforming the Hamiltonian of Equation 3.9 into a reference frame defined by $\mathcal{H}_{RF}$, allows decomposition of the propagator, U, into a product of two operators, U_{RF} and U_{int}, with the chemical shift offset and J-couplings as error terms on the ideal transformation U_{RF}. Writing the Hamiltonian as

$$\mathcal{H} = \mathcal{H}_{RF} + V \tag{3.17}$$

with

$$V = -\Delta\omega_2 I_{2z} + 2\pi J\mathbf{I}_1\cdot\mathbf{I}_2. \tag{3.18}$$

The propagator for the error term, $U_v(\tau)$, becomes

$$U_v(\tau) = \mathbf{T}\exp\left(-i\int\tilde{V}(t)dt\right) \tag{3.19}$$

where

$$\tilde{V}(t) = U_{RF}^{-1}(t)VU_{RF}(t), \tag{3.20}$$

or

$$\tilde{V}(t) = U_{RF}^{-1}(t)(-\Delta\omega_2 I_{2z} + 2\pi J\mathbf{I}_1\cdot\mathbf{I}_2)U_{RF}(t). \tag{3.21}$$

For the general case, we would like to choose U_{RF} to eliminate the chemical shift contribution, and leave an effective average Hamiltonian of

$$U_v(\tau) = \exp(-2\pi\tau J \mathbf{I}_1 \cdot \mathbf{I}_2). \tag{3.22}$$

Several schemes for generating such Hamiltonians are discussed in Section 3.5.

3.4 Cross-Polarization Schemes

3.4.1 One-Dimensional Experiment

As discussed in Section 3.2.1, in order to effect magnetization transfer between two coupled spins, a difference between I_{1z} and I_{2z} must first exist. A selective 180° pulse applied to one of the spins will create a difference state, $I_{1z} - I_{2z}$. Application of the mixing sequence will cause oscillatory transfer of magnetization between the two spins, as described earlier. After a period $1/2J$, the sign of the difference state will have reversed, leaving $I_{2z} - I_{1z}$. Figures 3.1 and 3.2 show experimental interferograms for such an experiment for the two-spin system of 2,3-dibromothiophene. This AX spin system has a chemical shift difference, $\Delta\omega$, of 224 Hz (.56 ppm), and a J-coupling of 5.9 Hz. Selective inversion of the downfield doublet generates the longitudinal magnetization difference state. Subsequent irradiation with the mixing sequence will invert the sign of this difference, representing polarization transfer to the coupling partner.

The performance of the mixing sequence can be tracked by interferometrically monitoring the intensity of the upfield doublet while incrementing the number of cycles of the cross-polarzation sequence applied. Figure 3.1 compares the performance of DIPSI-2 and WALTZ-16, each applied with an RF field strength of 4.0 kHz. Such

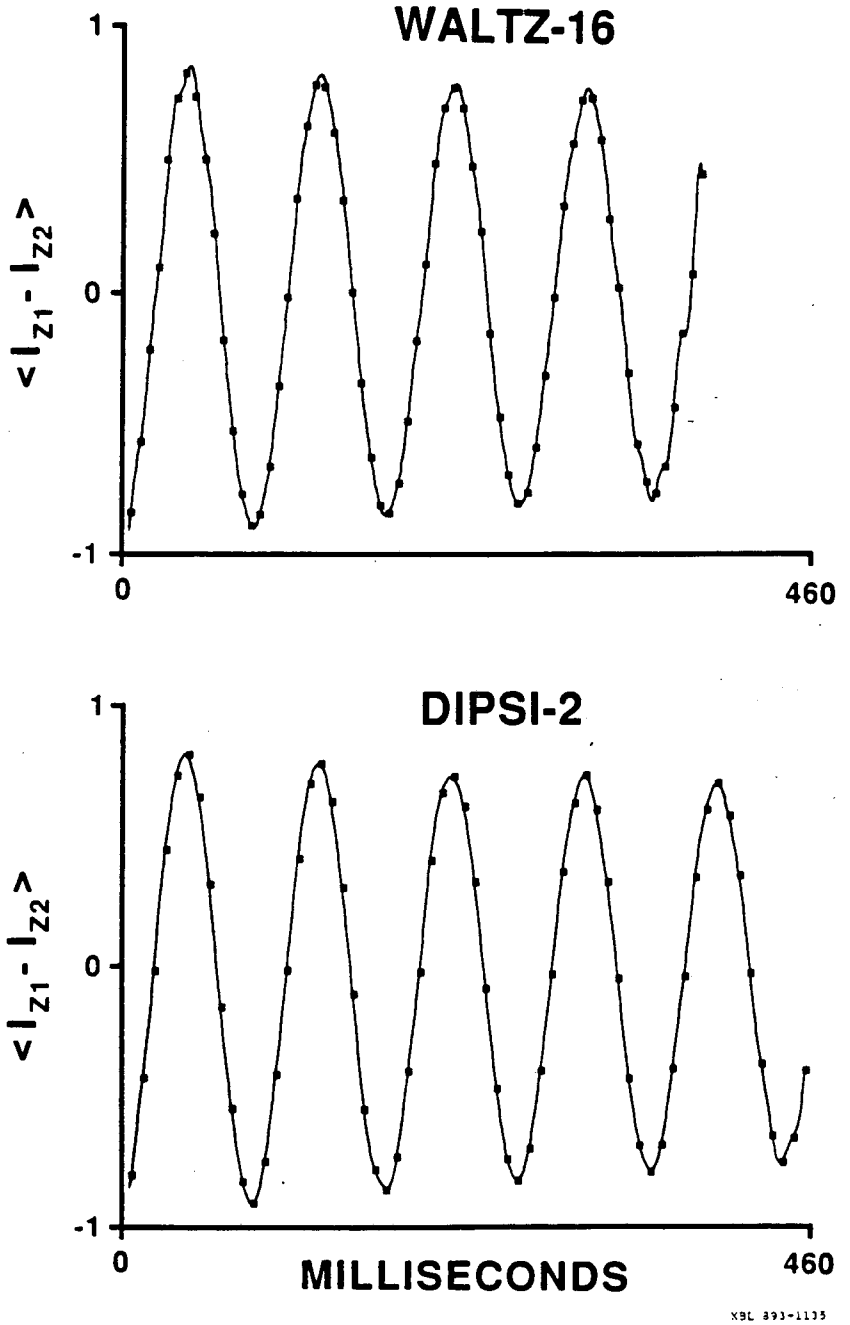

Figure 3.1: Experimental interferogram showing the progress of magnetization transfer between the two protons on 2,3-dibromothiophene. The chemical shift offset is 224 Hz, and the RF field strength is 4000 Hz.

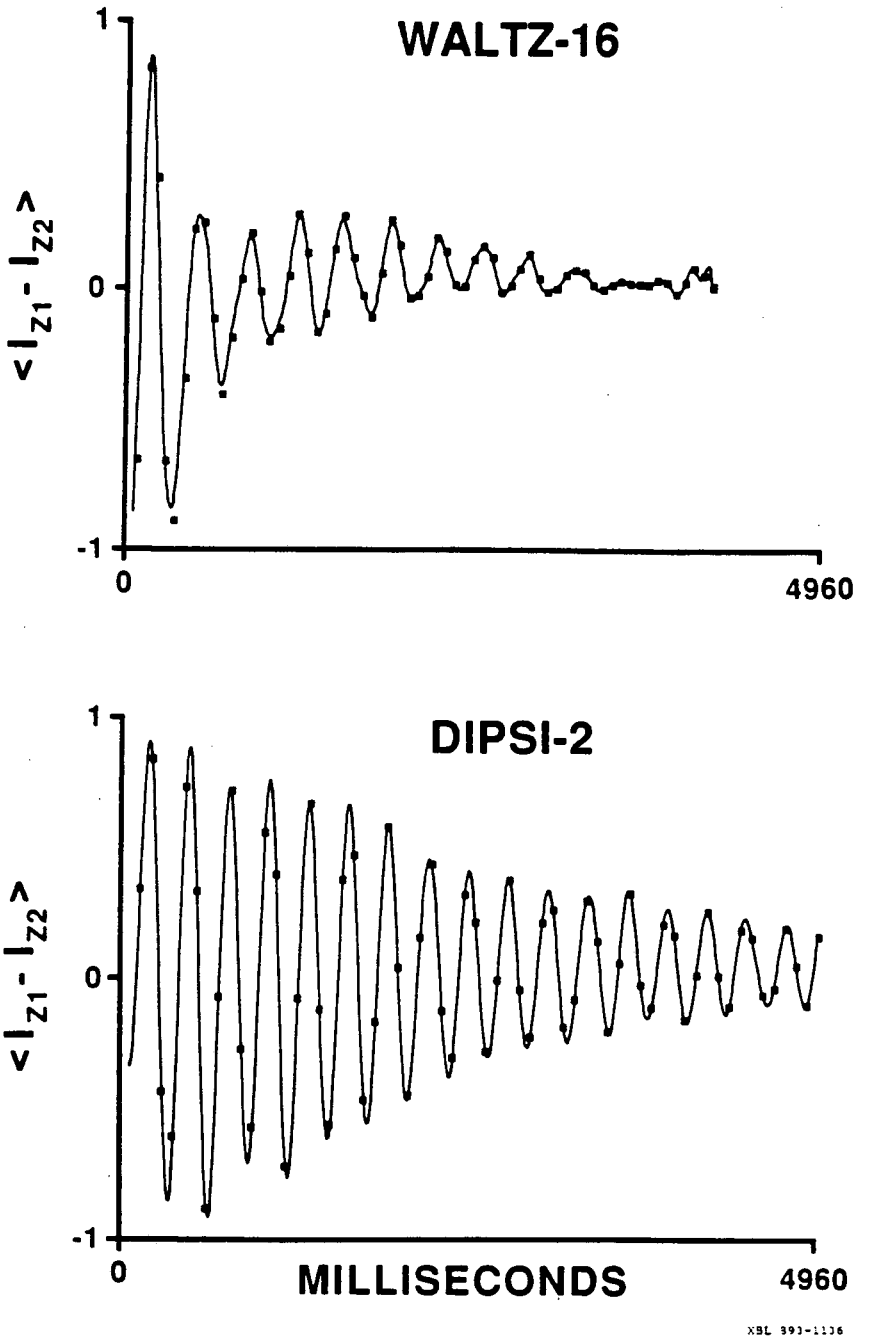

Figure 3.2: Experimental interferogram showing the progress of magnetization transfer between the two protons on 2,3-dibromothiophene. The chemical shift offset is 224 Hz, and the RF field strength is 400 Hz.

Table 3.1: Effective polarization transfer rates (in Hz) for WALTZ-16 and DIPSI-2 decay with a diminution of the B_1 field strength. The cycle time listed (in msec) is that required to complete one $R\overline{RR}R$ cycle.

	WALTZ – 16		DIPSI – 2	
RF field strength	Cycle time	Transfer rate	Cycle time	Transfer rate
4000 Hz	6.00	5.76	7.19	5.79
2688 Hz	8.93	5.71	10.71	5.79
2032 Hz	11.81	5.65	14.16	5.72
1445 Hz	16.61	5.50	19.92	5.65
1000 Hz	24.00	5.21	28.78	5.41
526 Hz	45.00	4.22	54.70	4.70
371 Hz	64.61	3.08	77.47	3.63

a field strength (nearly 20 times the chemical shift difference of 224 Hz) masks imperfections in the mixing sequence. DIPSI-2 more closely approximates the natural J-coupling, as is evidenced by the oscillation frequencies for the transfer (DIPSI-2: 5.79 Hz, and WALTZ-16: 5.76 Hz).

At weaker field strengths, such as the interferograms of Figure 3.2 (with B_1 = 371 Hz), imperfections in the mixing sequence degrade both the extent of magnetization transfer, and the rate at which it occurs (DIPSI-2: 3.62 Hz, WALTZ-16: 3.08 Hz). Such low field strengths provide a sensitive and necessary test of the sequences, since application of the HOHAHA experiment to biological samples requires cross-polarization over large bandwidths, with a minimimum of RF power deposited in the sample (to avoid excessive heating). Table 3.1 compares the effective polarization transfer rates of WALTZ-16 and DIPSI-2 for a series of RF field strengths.

In order to resolve coupling partners in a complicated spectrum, the sequence

can be modified as a difference experiment. Subtracting an experiment of the form [95]:

$$90^\circ - \text{MIX} - \text{detect} \tag{3.23}$$

from:

$$180^\circ_{\text{selective}} - 90^\circ - \text{MIX} - \text{detect} \tag{3.24}$$

will yield subspectra of the selectively irradiated spin and all its coupling partners.

3.4.2 Two-Dimensional Experiment

Elucidation of a complicated spectrum through selective irradiation of each resonance, as described in the previous section, is not generally feasible. In order to render such problems more tractable, we turn to two-dimensional version of the cross-polarization experiment. The J-coupling, by its scalar nature, can exchange a magnetization difference along any axis. Braunschweiler and Ernst [92] originally proposed the exchange of transverse magnetization, with an effective spin lock applied along the $\hat{x}$-axis. Figure 3.3a shows the form of this experiment. An initial 90° pulse tips the spins into the transverse plane, where they evolve for a time, t_1. The magnetization difference along $\hat{x}$ generated during t_1 is then mixed by application of the cross-polarization sequence, and an FID collected during the period t_2. Interferometric incrementation of t_1 and double Fourier transformation yield a correlation map, with the one-dimensional spectrum along the diagonal, and off-diagonal cross-peaks for coupled spins only.

The scheme presented in Figure 3.3b presents a similar approach. During the t_1 evolution period, spins will precess different amounts, depending on their chemical shift offset. Applying a second flip-back 90° pulse will flip the magnetization

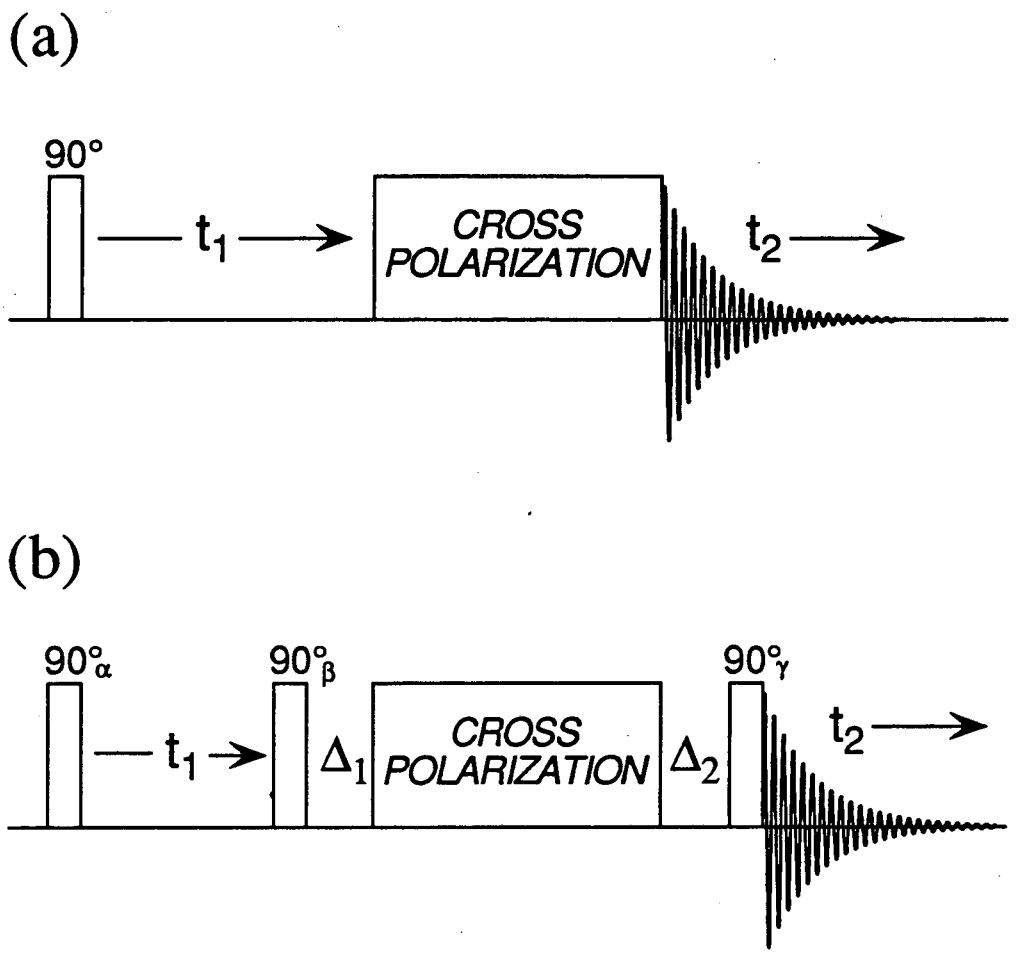

Figure 3.3: Magnetization transfer can be effected either in the transverse plane (a), or along the z-axis (b).

isochromats back along the $\hat{z}$-axis. The phase angle accrued during precession will then manifest itself as a difference in $\hat{z}$ magnetization. This conversion of a chemical shift offset into a magnetization difference, Δ_z, frequency labels the spins. The mixing sequence can then transfer longitudinal polarization between coupled spins. A subsequent 90° pulse flips the magnetization back into the transverse plane for detection. Section 3.5 discusses the merits of these schemes more thoroughly.

3.5 Comparison of Experimental Results

The design criteria for mixing sequences closely parallel those for heteronuclear decoupling sequences. In both cases, we seek to flip a group of spins in synchrony, regardless of their resonance offset. Many such sequences have been employed, and we will deal here with several of the more common. Continuous wave irradiation provides the simplest means to effect the rotation, although Fourier theory dictates a narrow excitation bandwidth. For a long low-amplitude pulse, the Fourier transform (frequency spectrum) will yield a sinc function, the primary lobe of which will narrow as $1/T$. Several heteronuclear decoupling sequences have been designed by iterating windowless sandwiches of phase-shifted RF pulses. Two of the more popular such sequences, the MLEV [106] and WALTZ [109] families, demonstrate substantially better resistance to pulse imperfections and demonstrate a wider bandwidth.

The DIPSI sequences were developed to decouple J-coupled protons from carbon nuclei. Their strength as cross-polarization sequences, *vis a vis* the older sequences, derives from the fact that the DIPSI sequences were designed not only to remove the chemical shift linear spin operators, but also to maximize the effective bilinear

scalar coupling between the protons, and preserve all three Cartesian components of the coupling.

3.5.1 CW Mixing

In their study of cross-polarization in solids, Hartmann and Hahn first proposed their famous condition for efficient spin energy exchange [102]

$$\gamma_I B_{1I} = \gamma_S B_{1S} \tag{3.25}$$

where B_1 is the applied RF field for the **I** or **S** nucleus, and γ its gyromagnetic ratio. This matches the precession frequencies of the nuclei in their respective rotating frames, to yield the precession condition:

$$\omega_I = \omega_S, \tag{3.26}$$

facilitating polarization transfer. Building upon this matching condition, the cross-polarization mediated by dipole-coupled spins in the solid state is described most easily by spin-thermodynamical arguments [49]. The Hartmann-Hahn matching condition can be relaxed [115] to:

$$|\omega_I - \omega_S| < \nu_{IS} \tag{3.27}$$

where ν_{IS} is the coupling strength for the two nuclei. In solid-state NMR, the spin-spin interaction is mediated by a dipole coupling (usually of several kilohertz), resulting in very fast polarization transfer. Transfer of polarization in liquids is more difficult to achieve, since the J-coupling is only of the order of 140 Hz for ^{1}H-^{13}C couplings, and a few hertz for ^{1}H-^{1}H couplings.

Figures 3.4, 3.5, and 3.6 show two-dimensional cross-polarization experiments performed with monochromatic irradiation on a sample of sparteine (Dodecahydro-7,14-methano-2H,6H-dipyrido[1,2-a;1′,2′-e][1,5]diazocine) with RF field strengths of 4 kHz, 1.7 kHz, and 1.2 kHz respectively. The extent of magnetization transfer increases with the strength of the applied RF field (all spectra were acquired with a mixing period of 28.0 msec), but even with a 4 kHz B_1 field strength, the cross peak intensity is sub-optimal, and cross peaks in the upfield region exhibit substantial lineshape distortion.

Unfortunately, the CW spin lock rapidly dephases magnetization components not aligned along the applied field axis. Also, the effective transfer rate achieved by the sequence falls far short of the J-coupling between the coupled spins. Thus, during the necessarily long irradiation period, significant $T_{1\rho}$ relaxation can occur, especially for large biomolecules with long correlation times. A phase-alternating spin-lock, suggested by Davis and Bax [94] can overcome the bandwidth limitation to some extent.

3.5.2 MLEV Mixing

Development of cross-polarization and heteronuclear decoupling sequences share the goal of creating an offset-independent 2π rotation for all the proton spins. Therefore, it seems reasonable that pulse sequences developed for broadband decoupling would be good candidates for homonuclear cross-polarization. To this end, Bax and Davis modified the MLEV-16 pulse sequence (*cf.* Table 4.2) by the concatenation of an additional 180° to generate the MLEV-17 mixing sequence shown in Figure 3.7. The rationale behind the additional 180° pulse is that pulse imperfections in the

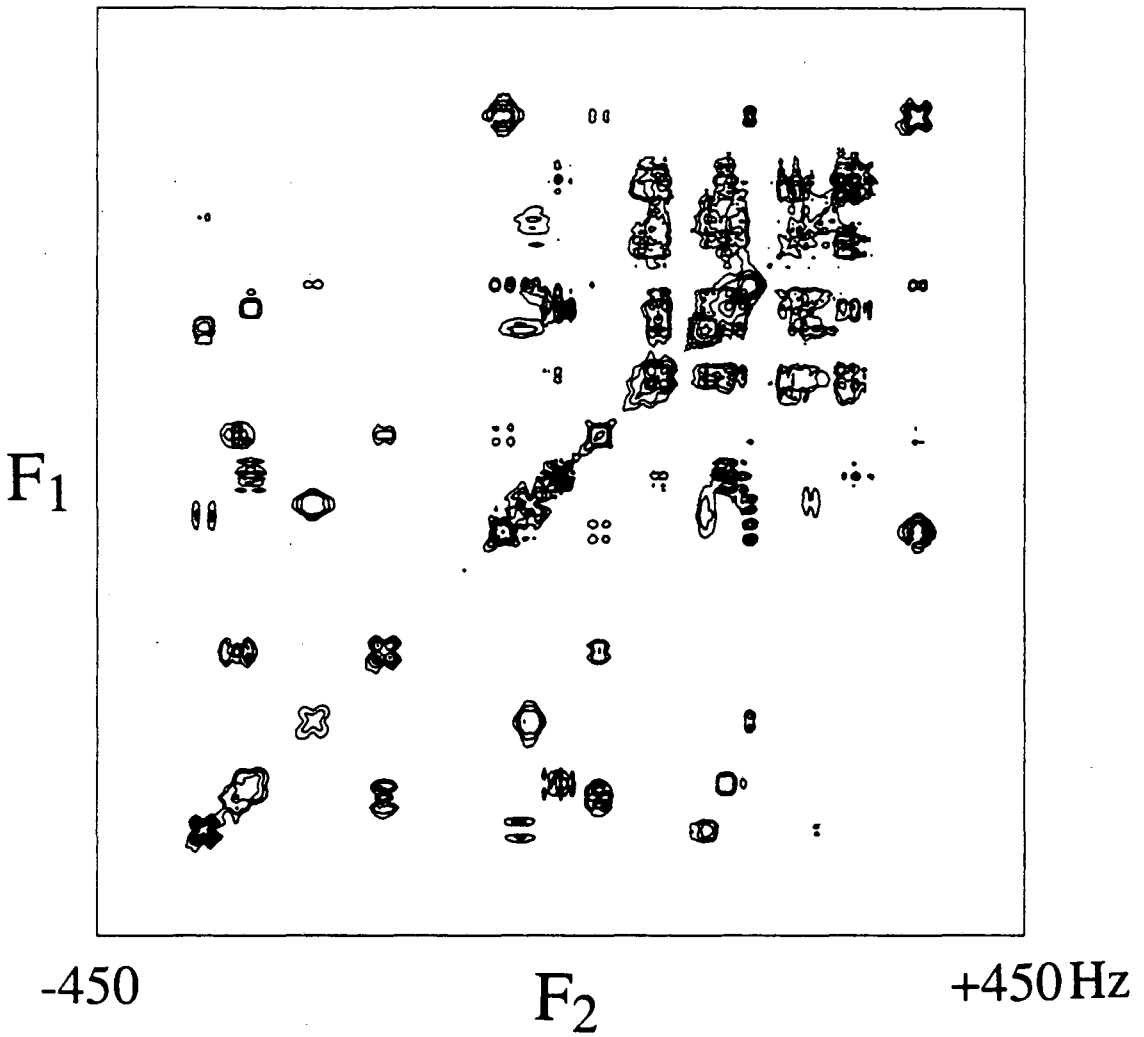

Figure 3.4: Cross-polarization with a monochromatic 4 kHz RF field, and a mixing period of 28.0 msec. Data sets of 1024 × 1024 data points were collected in the time domain, and double Fourier-transformed with a hypercomplex Fourier transform (to yield phase sensitive spectra). The sweep width was 1200 Hz, although only a 900 Hz band is shown here and in the following spectra.

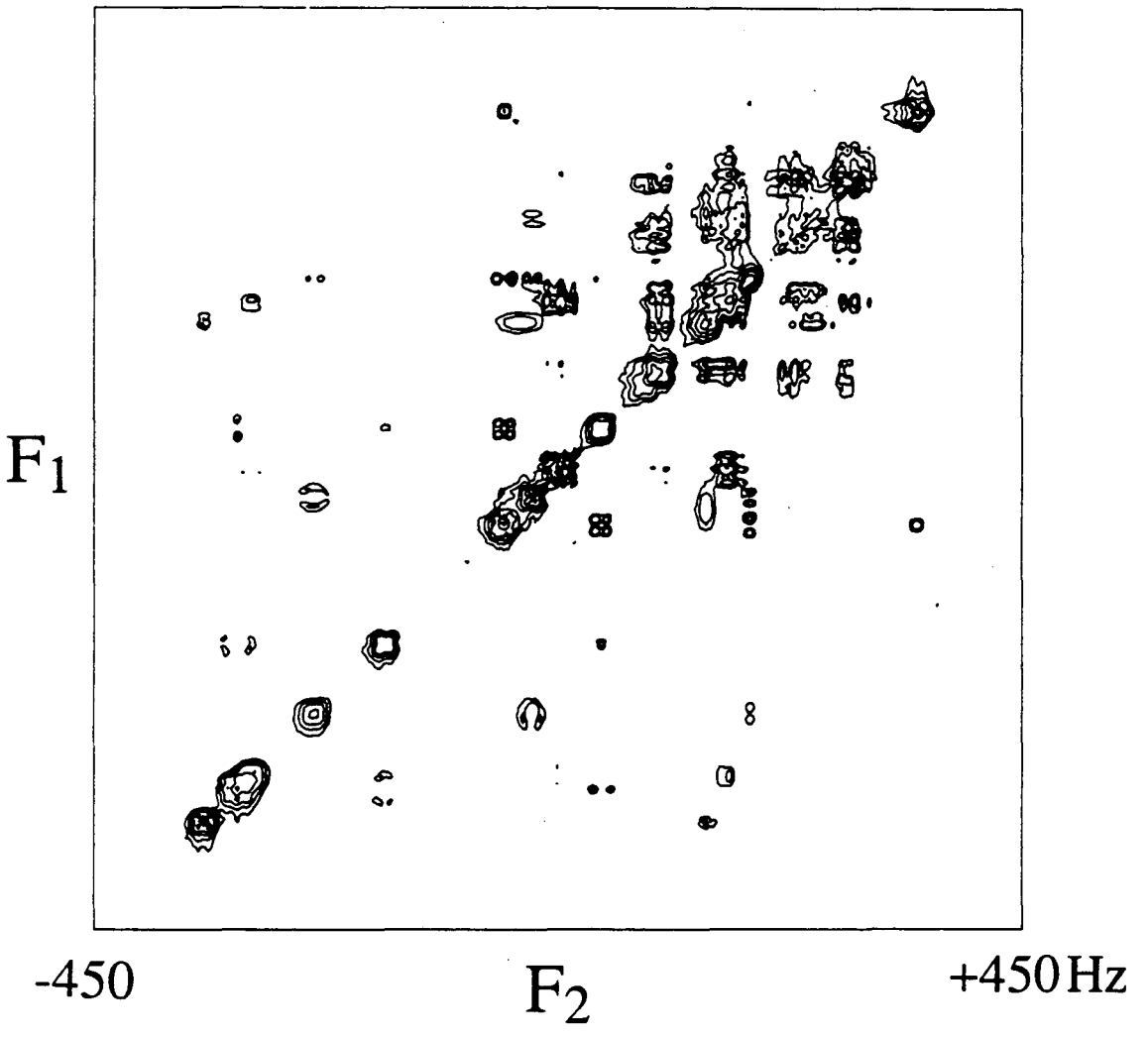

Figure 3.5: Cross-polarization with a cw 1.7 kHz RF field, and a mixing period of 28.0 msec.

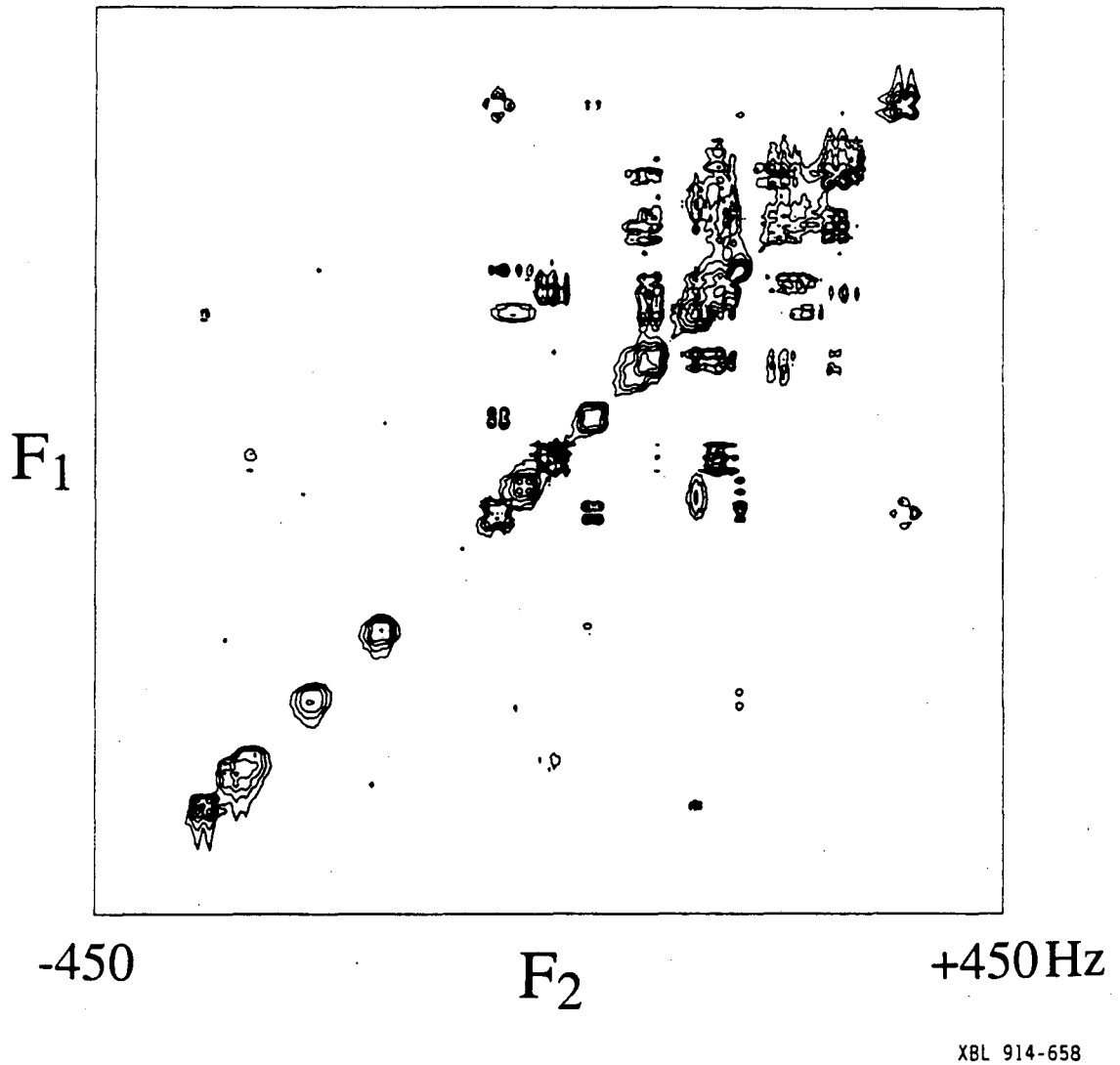

Figure 3.6: Cross-polarization with a cw 1.2 kHz RF field for 28.0 msec. Cross-polarization here is very inefficient, with very low cross-peak intensity.

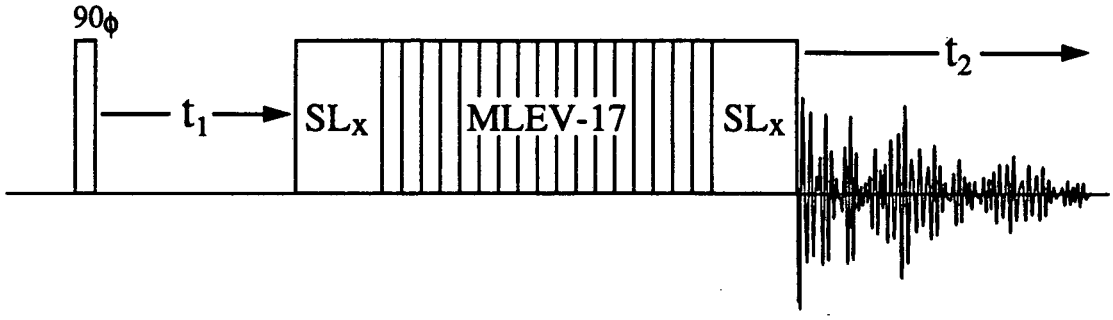

Figure 3.7: The MLEV-17 cross-polarization sequence comprises an MLEV-16 pulse train followed by an additional 180° pulse. The resulting sequence is sandwiched between two spin-locking "trim pulses" which select for magnetization along a specified axis, thereby allowing phase-sensitive representation of the data.

MLEV-16 sequence will leave some component of the magnetization away from the applied field axis. The 180° pulse will invert the phase of this error term after each application, cancelling the error after an even number of MLEV-17 cycles. This amounts to an interleaved Carr-Purcell train within the MLEV-16 mixing sequence. The MLEV-17 sequence possesses an effective bandwidth of $\pm 0.3\nu_{RF}$, where ν_{RF} is the applied RF field strength.

The spin-lock trim pulses preceding and following the MLEV-17 mixing sequence are designed to select transverse magnetization along one axis (*e.g.* $I_{1x} - I_{2x}$) by dephasing all other coherences through RF inhomogeneity. This is to allow presentation of the spectrum in pure absorption-mode [116, 117]. The spin-lock does not select transverse magnetization with 100% efficiency, and antiphase terms such as $I_{1y}I_{2z} - I_{1z}I_{2y}$ remain. These residual coherences manifest themselves as phase distortions of the multiplet structures of the two-dimensional spectrum.

Sørensen *et al.* [118] proposed an alternative method to select a magnetization component. This method, referred to as a z filter, stores the magnetization along the $\hat{z}$ axis for a period τ_z in the following fashion. A 90° pulse following the mixing sequence (applied along an axis perpendicular to the virtual spin-lock axis) will convert $I_{1\alpha} - I_{2\alpha}$ $(\alpha = x, y)$ to $\hat{z}$ magnetization $I_{1z} - I_{2z}$. More importantly, it will convert all antiphase terms $I_{1\alpha}I_{2z} - I_{1z}I_{2\alpha}$ $(\alpha = x, y)$ into zero-quantum coherences (ZQC). The zero-quantum coherences will oscillate at a frequency $(\omega_1 - \omega_2)$ during τ_z, while longitudinal terms of the form $I_{1z} - I_{2z}$ will decay monotonically with a time constant, T_1. A 90° pulse after τ_z will convert both the longitudinal and zero-quantum terms into observable magnetization. Coaddition of a series of FIDs with varied zero-quantum evolution periods will modulate the contributions from the ZQCs (averaging them to zero) while leaving the longitudinal terms unaffected, except for T_1 relaxation. This facilitates collection of a pure absorption-mode spectrum.

Ideally, one would like to co-add two FIDs (with the ZQCs 180° out of phase) for each coupled pair of spins in the sample. In a sample with n different couplings, this would require acquisitions with 2^n different τ_z values, so that the zero-quantum coherence generated by each proton pair could be coadded with 0° and 180° accumulated phase. Clearly, this criterion for selecting τ_z values necessitates extremely lengthy averaging for a molecule of relevant complexity, yet in practice it is found that acquisition of a handful of FIDs with randomly set delays is adequate.

Recently, another method was proposed to remove the effect of zero-quantum coherence generated during the mixing period [119]. Rather than applying a single 90° pulse to flip magnetization up along the $\hat{z}$-axis for the z filter, the magneti-

zation along the preferred transverse axis is spin-locked with a strong RF field. This field is then adiabatically frequency-swept until the magnetization lies aligned with the $\hat{z}$-axis. RF inhomogeneity in the coil will dephase all those components not initially aligned along the preferred axis. Antiphase terms $I_{1\alpha}I_{2z} - I_{1z}I_{2\alpha}$ are dephased, rather than being converted to zero-quantum coherence. With the adiabatic frequency sweep, the averaging involved in z filtration can be replaced by a single experiment.

Figure 3.8 shows a two-dimensional cross-polarization spectrum acquired with MLEV-17 mixing. The element R was generated with the composite 180° rotation: $90^\circ_{-y}180^\circ_{x}90^\circ_{-y}$. The mixing period comprised 5 cycles of the MLEV-17 mixing sequence (20.63 msec) and two trim pulses (8.0 msec). CYCLOPS phase cycling [120] is applied to the MLEV train and the phase of the initial 90° pulse is cycled to allow for phase-sensitive acquisition of the spectrum. A sweep width of 1200 Hz was chosen, with 1024 points collected in each time dimension.

The MLEV sequences were devised originally to decouple single spins from carbon nuclei, without regard for the proton-proton scalar coupling. Numerical calculations [97] show that effective Hamiltonian during the mixing period assumes the form:

$$\mathcal{H}_{eff} = \sum_{\alpha=x,y,z} c_\alpha \cdot \mathbf{I}_1 + \sum_{\alpha=x,y,z} c_\alpha \cdot \mathbf{I}_2 + \sum_{\alpha,\beta=x,y,z} c_{\alpha\beta} I_{1\alpha} I_{2\beta}. \tag{3.28}$$

For the case of perfect performance of the sequence, $c_\alpha = 0$, and $c_{xx} = c_{yy} = c_{zz}$. This represents a pure scalar isotropic mixing Hamiltonian. Similar results have been described as a "three-spin effect" in heteronuclear decoupling [121]. In addition to generation of substantial contribution from terms of the form $I_{1x}I_{2y} - I_{1y}I_{2x}$ there is considerable deviation from perfect scalarity of the J coupling, as the terms c_{xx},

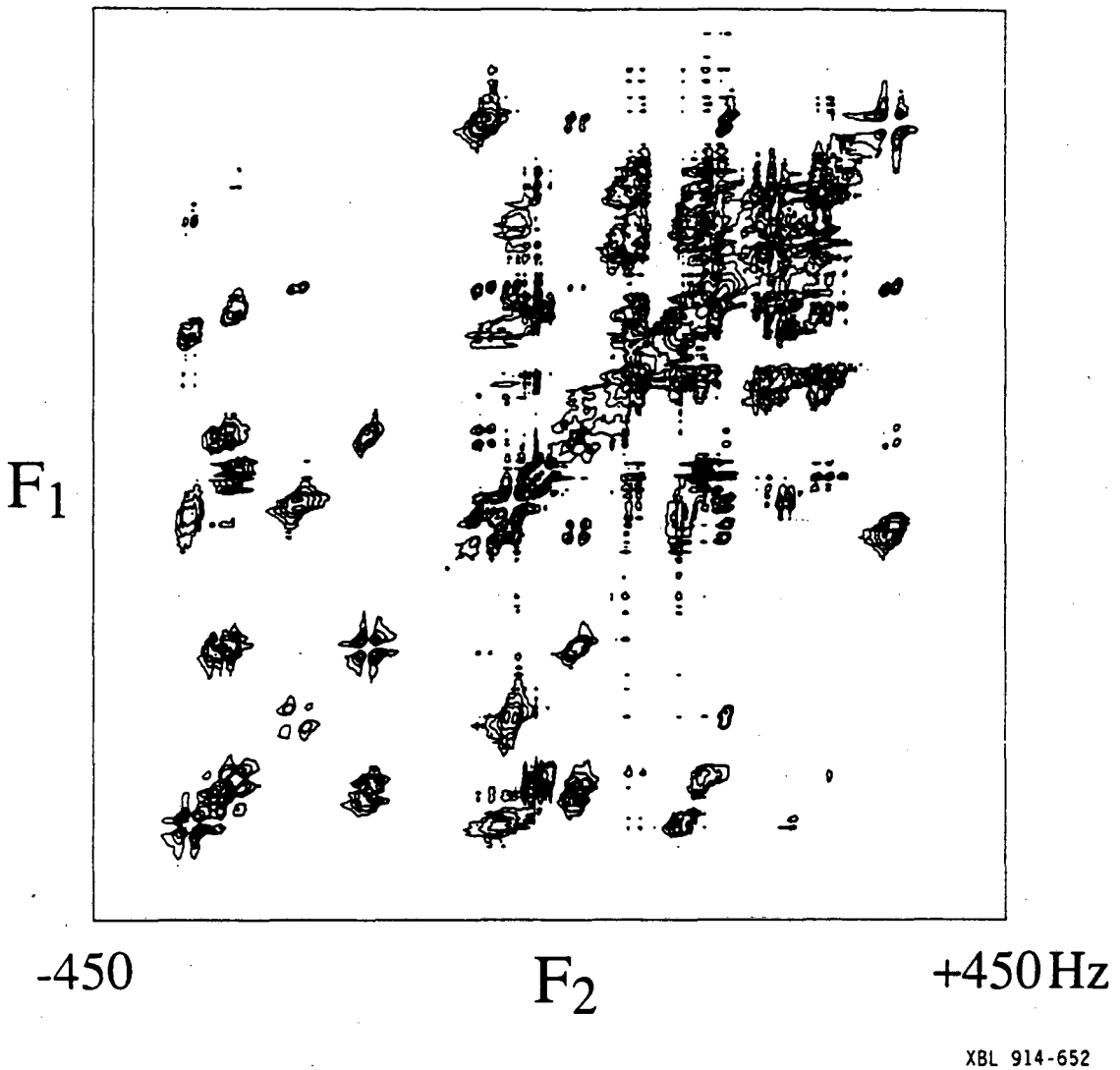

Figure 3.8: Cross-polarization performed with the MLEV-17 sequence, without trim pulses.

Table 3.2: Alternating-phase composite pulses for the rotation element R in the DIPSI sequences.

Sequence	Flip angles	Bandwidth	Length
DIPSI-1	$365\ \overline{295}\ 65\ \overline{305}\ 350$	± 0.4	1380
DIPSI-2	$320\ \overline{410}\ 290\ \overline{285}\ 30\ \overline{245}\ 375\ \overline{265}\ 370$	± 0.6	2590
DIPSI-3	$\overline{245}\ 395\ \overline{250}\ 275\ \overline{30}\ 230\ \overline{360}\ 245\ \overline{370}\ 340\ \overline{350}$		
	$260\ \overline{270}\ 30\ \overline{225}\ 365\ \overline{255}\ 395$	± 0.8	4890

c_{yy}, and c_{zz} become unequal. The DIPSI family of sequences [122] were developed with the goal of maintaining equality in the amplitudes of each bilinear term, $I_{\alpha\alpha}$.

3.5.3 DIPSI Mixing

The DIPSI sequences, like the earlier WALTZ sequences [109] assume the form $R\overline{R}\overline{R}R$, where R denotes a composite pulse of either 0° phase (R), or 180° phase ($\overline{R}$). The constituent pulses elements for the R operators are listed in Table 3.2. These sequences arose from a study of decoupling in three-spin systems, where scalar-coupled protons are coupled to a carbon nucleus of interest. This improves upon the earlier MLEV and WALTZ sequence in two aspects.

First, DIPSI minimizes non-scalar behavior. As discussed above, while the earlier sequences cancel linear spin operators across a wide bandwidth, during the mixing cycle, they also generate bilinear zero-, single-, and double quantum operators, leading to a decay in the amplitude of polarization transfer, as exhibited in Figures 3.1, and 3.2. Second, DIPSI generates a larger effective J-coupling over a wider bandwidth than the earlier sequences. A plot of J_{eff}

$$J_{\text{eff}} = \frac{\langle J \rangle}{J} = \frac{(J_{xx} + J_{yy} + J_{zz})}{3J} \tag{3.29}$$

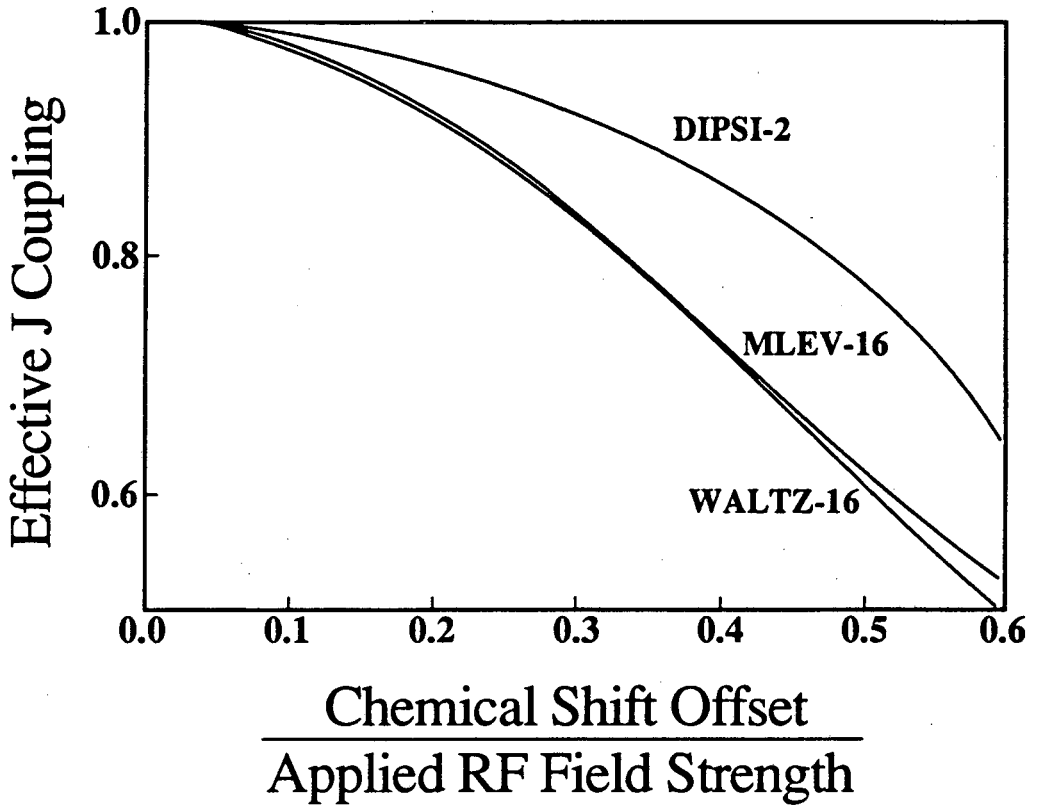

Figure 3.9: Comparison of the magnetization transfer for the three sequences, DIPSI-2, WALTZ-16, and MLEV-16. The extent to which the sequences approximate the ideal J-coupling is plotted against the ratio of chemical shift offset to RF field strength. The common operating area for most experiments would be on the right-hand side of the plot, where a broad chemical shift range is to be cancelled by a weak field.

in Figure 3.9 shows a calculation for the effective coupling as a function of offset. Since J_{eff} averages the bilinear terms $J_{\alpha\alpha}$, it masks performance decay caused by deviations from scalarity, and thus casts MLEV and WALTZ in a more favorable light. The effective bandwidth increases as the DIPSI composite pulse grows in length. In practice, though, the mixing sequence is applied with a minimum of power (to avoid sample heating). The reduction in B_1 field strength necessitates a concomitant lengthening of the mixing period; hence a shorter intrinsic sequence (DIPSI-2 *vs.* DIPSI-3) is preferable.

Figures 3.11 and 3.12 show the results of two cross-polarization spectra acquired with DIPSI-2 mixing, using the pulse sequence of Figure 3.3b and an RF field strength of 4 kHz. In Figure 3.11, six DIPSI-2 cycles were used (for a mixing time of 43.16 msec), while 10 cycles were used in Figure 3.12 (for a 71.93 msec mixing time). In both cases, the zero-quantum removal delay periods, Δ_1 and Δ_2, were varied randomly over a period of 10 to 30 msec. The initial 90° pulse phase, α, was cycled by 90° to allow for phase-sensitive acquisition. β was cycled to remove axial peaks caused by relaxation during t_1, and γ was cycled to select for longitudinal magnetization.

Longer mixing periods elucidate weak couplings, and can also be used to detect indirectly coupled spins through relayed magnetization transfer, in analogy with the RELAY experiment [123, 124]. With these longer mixing periods, the complicated spectra do not exhibit the same oscillatory nature of magnetization transfer demonstrated by the 2,3-dibromothiophene sample. Complicated spin networks can be treated in analogy with classical systems of many coupled oscillators, where the energy of one mode is quickly distributed to all the coupling partners. To pre-

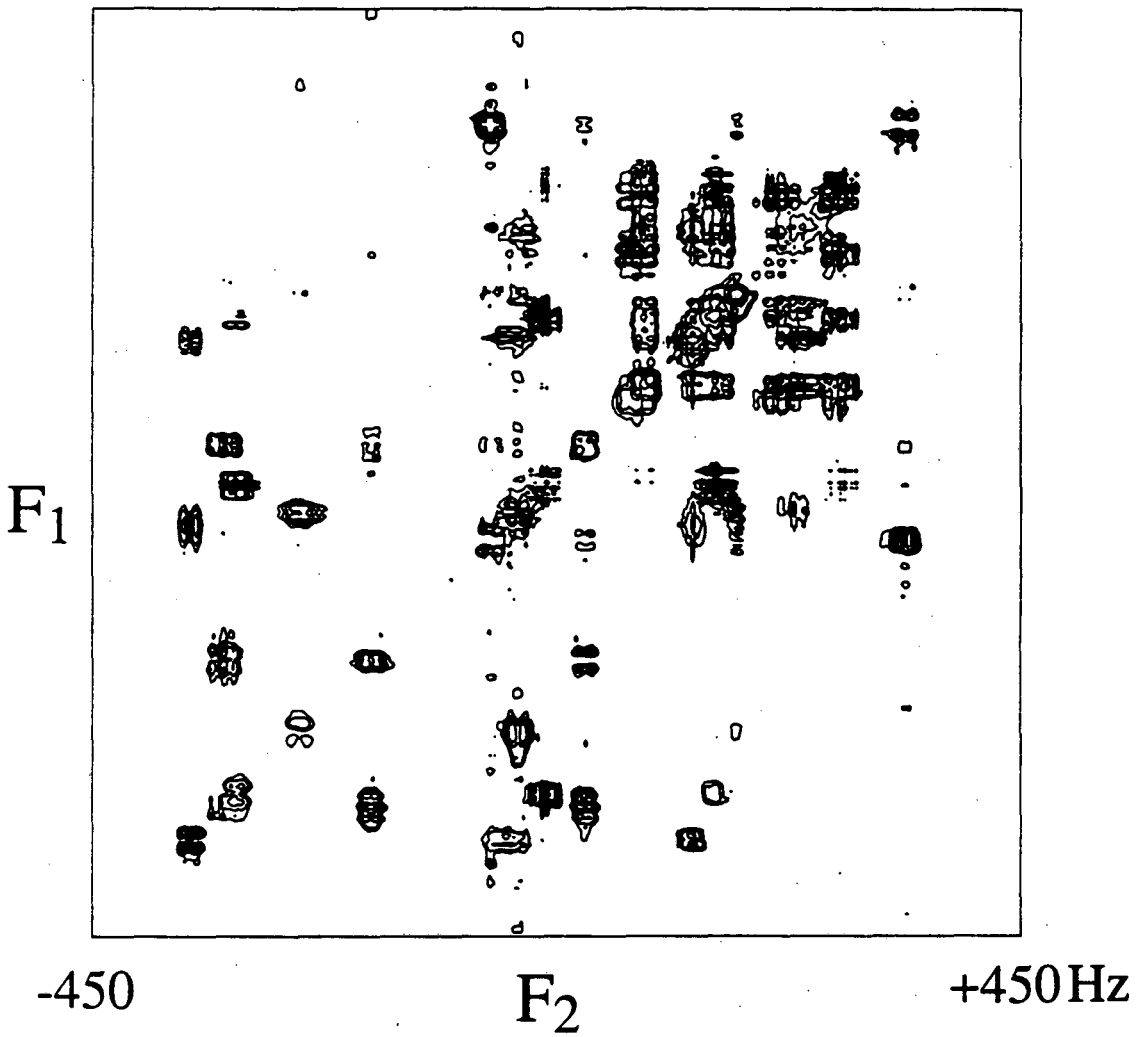

Figure 3.10: Cross-polarization with 4 cycles of the DIPSI-2 mixing sequence. Two values for the random delays, Δ_1 and Δ_2 were chosen.

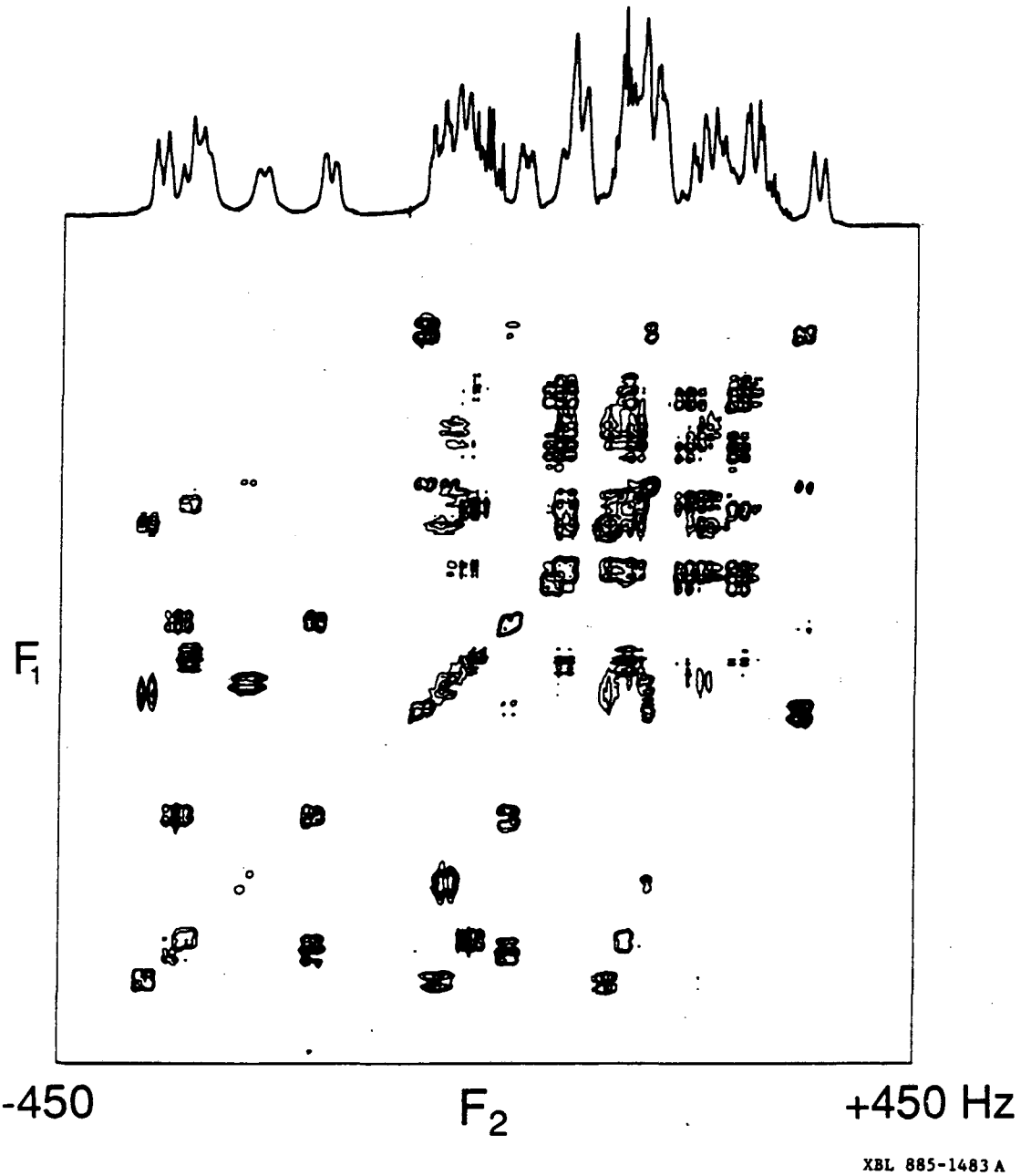

Figure 3.11: Cross-polarization with 6 cycles of the DIPSI-2 mixing sequence. Across the top of the two-dimensional spectrum is a one-dimensional projection of the sparteine spectrum.

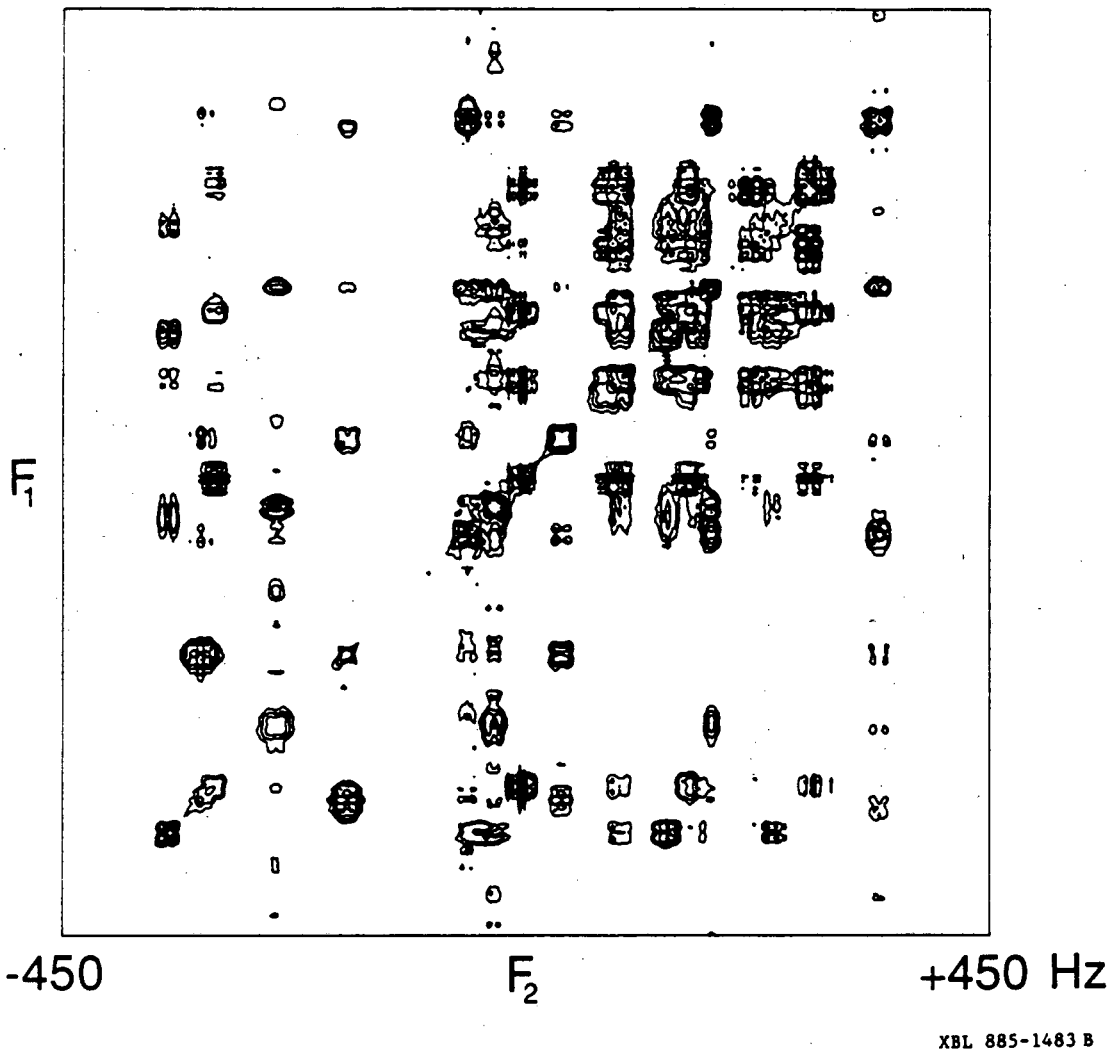

Figure 3.12: Cross-polarization with 10 cycles of DIPSI-2. Two random delays averaged away zero-quantum coherences.

dict rates of polarization transfer in such systems, one usually resorts to numerical solutions [125, 126, 127].

3.6 ROESY Interference

Spin-spin relaxation during the mixing sequence can cause cross-peaks to lose intensity, or even appear with a 180° phase shift relative to the diagonal peaks and Hartmann-Hahn cross-peaks. Such cross-relaxation is the basis for Rotating frame Overhauser Enhancement SpectroscopY (ROESY) [128, 129], known also as CAMELSPIN (Cross-relaxation Appropriate for Mini-molecules Emulated by Locked SPINs) [130]. The ROESY experiment is performed with a sequence analogous to that of Figure 3.3a, except that the cross-polarization sequence is replaced by an "inferior" spin-lock.

After the initial 90° pulse, the spins are frequency labeled by evolution for a period t_1. At this point, a spin-lock is applied along an axis perpendicular to the phase of the initial pulse. The spins are locked along this field, with the effective field experienced by a spin:

$$|\mathbf{B}_{\text{eff}}| = \sqrt{\frac{4\pi^2(\omega - \omega_a)^2}{\gamma^2} + |\mathbf{B}_1|^2}, \tag{3.30}$$

where $(\omega - \omega_a)$ is the resonance offset between the carrier and spin. If we define θ as the angle between this effective field and the spin-lock axis, then

$$\tan\theta = \frac{2\pi(\omega - \omega_a)}{(\gamma|\mathbf{B}_1|)}. \tag{3.31}$$

Magnetization perpendicular to the spin-lock axis will dephase quickly due to RF inhomogeneity. Protons that are spatially close on the molecule can then undergo

dipole-dipole cross-relaxation, with a cross-peak intensity in the spectrum proportional to $\cos^2(\theta_a)\cos^2(\theta_b)$, with θ_a and θ_b the effective angles of the RF field for each spin. A typical experiment would involve a 2 kHz RF field to irradiate a proton spectral width of 3 kHz, with a spin-lock period of 200 msec.

In a ROESY experiment, Hartmann-Hahn magnetization transfer creates spurious peaks, since the cross-polarization peaks point up, and the cross-relaxation peaks point down. Oscillatory magnetization transfer occurs simultaneously during such experiments, with a transfer rate:

$$R = \frac{J^2[1+\cos(\theta_a-\theta_b)]^2}{4(\omega_a-\omega_b)^2 + J^2[1+\cos(\theta_a-\theta_b)]^2}. \tag{3.32}$$

In the ROESY experiment, these spurious peaks can be minimized by applying a weak field, so that the effective fields will have different values of θ, and setting the carrier frequency such that the Hartmann-Hahn condition is not inadvertently satisfied for any pair of spins (this latter condition being rather tedious to achieve in a complicated spectrum).

The converse to spurious TOCSY peaks in the ROESY spectrum, of course, is caused by transverse NOEs during the isotropic mixing sequence. If poor cancellation of linear spin operators or a weak J_{eff} characterize the mixing sequence, then a longer mixing period will be required to effect the magnetization transfer. During the longer sequence, there will necessarily be a greater opportunity for cross-relaxation between neighboring spins. A more insidious artifact, known as a combined TOCSY-ROESY cross-peak [131, 132, 133], can be pictured by considering a three-spin system AMX, where $J_{AM} \neq 0$. Initial HOHAHA transfer from A to M can cross-relax further to spin X, ultimately giving the appearance that spins A and X are J-coupled. The DIPSI sequences, by creating the best approximation

to the intrinsic J-coupling, will result in the fastest magnetization transfer, thereby allowing virtually no ROESY interference.

3.7 Conclusions

Homonuclear Hartmann-Hahn spectroscopy yields the well-resolved spectra necessary to elucidate the J-coupling networks of large molecules. The application of DIPSI-2 as a cross-polarization sequence creates a polarization transfer rate that very closely resembles the natural J-coupling between the spins, because the DIPSI sequence not only removes the linear spin operators of the weak-coupling Hamiltonian, but also seeks to preserve the three components of the scalar coupling.

Shaka *et al.* have recently proposed a newer family of sequences, FLOPSY-8 and FLOPSY-16 [134, 135], developed by analyzing the evolution of $I_{1z} - I_{2z}$ in a reference frame defined by the axes $I_{1z} - I_{2z}$, $I_{1x}I_{2x} + I_{1y}I_{2y}$, and $I_{1y}I_{2x} - I_{1x}I_{2y}$. By constructing an effective Hamiltonian composed of both zero-quantum and J-coupling terms, broadband zero-quantum 180° pulses can be generated to transfer polarization between coupled spins. The bandwidth of this sequence exceeds that of DIPSI-2, and DIPSI-3, rendering it useful for cross-polarization between ^{13}C nuclei.

Chapter 4

Iterative Carr-Purcell Trains

4.1 Introduction

Many applications of NMR rely on multiple pulse experiments. These range from solid state experiments, where multiple pulse sequences are employed to truncate line-broadening interactions, such as dipole-dipole couplings, to liquid-state structural studies and imaging experiments. Applications in imaging often require the collection of multiple echoes from refocusing magnetization in order to measure physical transport of the spins, to select volume elements, or to enhance the signal-to-noise in an experiment. Ideally, a pulse sequence would allow the acquisition of an arbitrary number of echoes. Unfortunately, the number of spin echoes attainable is limited by the natural dephasing time for the spins (T_2) and imperfections in the pulses used to refocus the magnetization.

This chapter describes a new multiple pulse echo sequence [136] developed by applying the iterative scheme of the MLEV decoupling sequences to the experiment of Carr and Purcell [137]. By modulating the phase of the radio frequency pulses

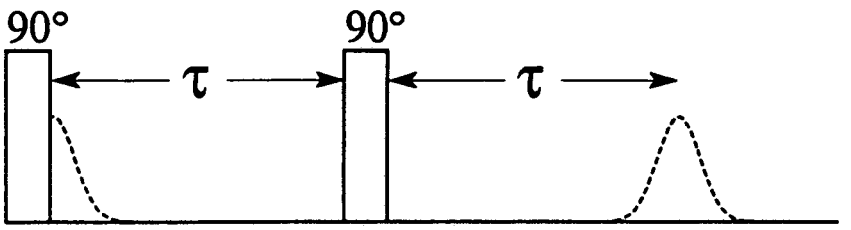

Figure 4.1: Schematic diagram for the Hahn echo experiment. The second 90° pulse will recover the seemingly lost magnetization signal.

in the echo train, the performance of the Carr-Purcell experiment can be improved substantially. We will consider briefly the original Carr-Purcell experiment, and the modifications of Meiboom and Gill [138], before discussing their weaknesses, and how the new series of pulse sequences can overcome them.

4.2 Background

The original multiple echo experiment of Carr and Purcell was based on the discovery of the spin echo by Hahn [139]. The coherent oscillation of nominally identical spins precessing in a magnetic field will dephase in the presence of inhomogeneities in the field. When the spins have dephased, no signal is detected in the receiver coil.

Hahn found that the decaying oscillations induced by a 90° pulse could be recovered if an additional 90° pulse was applied after a time, τ. An echo formed at a time τ later. This is shown graphically in Figure 4.1. The intensity of the echo varied inversely with the interpulse time delay. By performing the experiment for a series of τ values, the natural decay envelope of the line can be measured

interferometrically.

Carr and Purcell expanded upon this line of reasoning [137] and developed the following extension. Rather than performing the experiment repetitively, with different values of τ, they replaced the second 90° pulse with a train of 180° pulses. The 180° pulses refocused the spread in evolution of the isochromats caused by magnetic field inhomogeneities, and allowed the natural linewidth to be determined by measuring the decay of the echo amplitudes. Their modification is shown schematically in Figure 4.2. The determination of the natural T_2 was extremely sensitive to amplitude errors in the 180° pulses, resulting in reproducibility problems.

Four years later, Meiboom and Gill [138] improved the performance of the Carr-Purcell sequence immensely with two modifications. First, the successive pulses were coherent, unlike the Carr-Purcell experiment. Second, the phase of the echo train was shifted by 90 degrees relative to the initiating pulse.

Consider the case of the echo train having the same phase as the 90° pulse. As the spins dephase in the xy plane, the applied 180° pulse should flip the fanned-out isochromats about the applied field axis. If there is an amplitude error in the applied pulse (corresponding to a 175° flip angle, rather than 180° , for example), then the cluster of isochromats will be driven further and further out of the xy plane, because of the cumulative errors. The echo signal will alternate between positive and negative amplitude, and will decay quickly. If, on the other hand, the echo train is phase-shifted by 90 degrees relative to the initial 90° pulse, then the errors induced by one 180° pulse will be cancelled by the following pulse.

The Meiboom-Gill modification preserves the magnitude of the magnetization component parallel to the applied RF field during the echo train, but it does not pre-

serve the quadrature component. Maudsley [140] has argued that in many Fourier imaging experiments [141, 142], where magnetic field gradients spatially encode the phase of the magnetization vector, the phase of any voxel is not known *a priori*. Therefore, it would be desirable (necessary) to preserve the full magnetization vector, and not merely its projection along x or y. To this end, Maudsley proposed employing the pulse sequence:

$$90_y - [180_x \cdot 180_y \cdot 180_x \cdot 180_y]^n. \tag{4.1}$$

Through proper phase cycling of the receiver, a series of echoes of the same phase can be coadded to enhance the signal-to-noise of the experiment. Reference [140] presents simulations demonstrating the performance of this sequence in refocussing both the "in-phase" and "out-of-phase" magnetization components. This can be tested by comparing 90° prepulses with x and y phases in separate experiments.

4.3 Iterative Schemes

In our experiments, we have employed an iterative scheme for generating the sequence of refocussing pulses. An iterative scheme defines a procedure for generating a radio-frequency pulse by concatenating phase-shifted pulse elements. This bears analogy to the creation of fractal-dimensional objects, where some arbitrary initial shape is modified repetitively by a function known as the generator [143]. The application of iterative schemes to NMR has provided a wealth of new pulse sequences [144, 145]. These have found use in broadband decoupling [103, 146], broadband, narrowband, and passband inversion [6, 147, 148, 149], or excitation [150, 151], and compensation for instrumental imperfections [110, 111].

In our experiments, we have capitalized on the wide bandwidth of a family of such sequences, known as the MLEV sequences, by interleaving the constituent pulses with data acquisition, thereby creating an exceptionally well-compensated echo train.

4.3.1 The MLEV Sequences

These are based on the MLEV sequences developed by Levitt *et al.* [105, 106] to extend the bandwidth of spin-flip pulse sequences used in heteronuclear decoupling [152].

For analysis, the rotation operator for an RF pulse decomposes into the product of an ideal component, U_{RF}, and an error term, U_v:

$$U = U_{RF} U_v \tag{4.2}$$

The four successive pulses of the MLEV-4 sequence yield the following decomposition into ideal and error terms:

$$U \cdot U \cdot \overline{U} \cdot \overline{U} = U_{RF} U_v \cdot U_{RF} U_v \cdot \overline{U}_{RF} \overline{U}_v \cdot \overline{U}_{RF} \overline{U}_v, \tag{4.3}$$

where the terms can be relabeled for easier analysis:

$$U U \overline{U} \overline{U} \rightarrow U_4 U_{v4} U_3 U_{v3} U_2 U_{v2} U_1 U_{v1} \tag{4.4}$$

The treatment of errors in RF pulse sequences benefits from the grouping of all the ideal pulse elements and error elements into separate clusters. As a first step towards this goal, we can insert identity operators, represented by the underbraced elements, into the sequence.

$$= U_4 \underbrace{U_3 U_2 U_1 U_1^{-1} U_2^{-1} U_3^{-1}} U_{v4} U_3 \underbrace{U_2 U_1 U_1^{-1} U_2^{-1}} U_{v3} U_2 \underbrace{U_1 U_1^{-1}} U_{v2} U_1 U_{v1} \tag{4.5}$$

Merely by shifting the braces, we can visualize the pulse train as a sequence of four ideal pulses, U_4 through U_1, followed by a series of unitarily transformed error terms:

$$= U_4U_3U_2U_1\,\overbrace{U_1^{-1}U_2^{-1}U_3^{-1}}\overbrace{U_{v4}U_3U_2U_1}\,\underbrace{U_1^{-1}U_2^{-1}U_{v3}U_2U_1}\,\overbrace{U_1^{-1}}\overbrace{U_{v2}U_1}\,U_{v1} \qquad (4.6)$$

Replacing each so transformed error term U_v, by a term $\tilde{U}_v$, gives the following expression for the pulse sequence.

$$= U_4U_3U_2U_1\tilde{U}_{v4}\tilde{U}_{v3}\tilde{U}_{v2}\tilde{U}_{v1} \qquad (4.7)$$

In effect, we have now rearranged the MLEV-4 sequence into a series of ideal pulses followed by a series of error pulse elements. The error terms expand to:

$$\begin{aligned}
\tilde{U}_{v4} &= U_1^{-1}U_2^{-1}U_3^{-1}U_{v4}U_3U_2U_1 \\
\tilde{U}_{v3} &= U_1^{-1}U_2^{-1}U_{v3}U_2U_1 \\
\tilde{U}_{v2} &= U_1^{-1}U_{v2}U_1 \\
\tilde{U}_{v1} &= U_{v1} \qquad (4.8)
\end{aligned}$$

Table 4.1 lists the rotation operator for each of the error pulses assuming an initial error of $\epsilon \cdot \mathbf{I}$. The complete MLEV pulse train sums all these errors, to cancel all errors of first order in ϵ. Such errors comprise, for example, flip angle missets, chemical shift frequency offsets, and frequency offsets due to static field gradients.

If we consider an element, R, of the echo train as consisting of a π pulse sandwiched between two delay times, τ, then the propagator can be expressed as:

$$\exp(-i\phi I_z)R\exp(i\phi I_z) = R_0\exp(-i\phi I_z)R_\epsilon\exp(i\phi I_z) \sim U_{RF}U_v \qquad (4.9)$$

where $\phi = \Delta\omega\tau$, the phase evolution due to resonance offset. If we express the rotation operator R_ϵ as a power series in ϵ, then in the limit of ideal behavior for

Table 4.1: Compensation of pulse errors for MLEV-4 sequence.

Element	I_x	I_y	I_z
$\tilde{U}_{v4}$	ϵ_x	$-\epsilon_y$	$-\epsilon_z$
$\tilde{U}_{v3}$	ϵ_x	ϵ_y	ϵ_z
$\tilde{U}_{v2}$	$-\epsilon_x$	ϵ_y	$-\epsilon_z$
$\tilde{U}_{v1}$	$-\epsilon_x$	$-\epsilon_y$	ϵ_z

Table 4.2: Cycles for the MLEV family of pulse trains.

Sequence	Pulse Phases							
MLEV-4	$RR\overline{R}\overline{R}$							
MLEV-8	$RR\overline{R}\overline{R}$	$\overline{R}RR\overline{R}$						
MLEV-16	$RR\overline{R}\overline{R}$	$\overline{R}RR\overline{R}$	$\overline{R}\overline{R}RR$	$R\overline{R}\overline{R}R$				
MLEV-32	$RR\overline{R}\overline{R}$	$\overline{R}RR\overline{R}$	$\overline{R}\overline{R}RR$	$R\overline{R}\overline{R}R$	$RRR\overline{R}$	$\overline{R}\overline{R}RR$	$\overline{R}\overline{R}\overline{R}R$	$RR\overline{R}\overline{R}$
MLEV-64	$RR\overline{R}\overline{R}$	$\overline{R}RR\overline{R}$	$\overline{R}\overline{R}RR$	$R\overline{R}\overline{R}R$	$RRR\overline{R}$	$\overline{R}\overline{R}RR$	$\overline{R}\overline{R}\overline{R}R$	$RR\overline{R}\overline{R}$
	$\overline{R}\overline{R}RR$	$R\overline{R}\overline{R}R$	$RR\overline{R}\overline{R}$	$\overline{R}RR\overline{R}$	$\overline{R}\overline{R}\overline{R}R$	$RR\overline{R}\overline{R}$	$RRR\overline{R}$	$\overline{R}\overline{R}RR$

the sequence, R_ϵ reduces to the identity operator. The MLEV-4 pulse sequence will cancel error terms to first order in ϵ. The error compensation of the MLEV sequence can be extended to higher orders through successive cyclic permutations and phase inversions of the base sequence [103].

By cyclically permuting one pulse in MLEV-4, another compensated cycle, $\overline{R}RR\overline{R}$ is generated, which when concatenated with $RR\overline{R}\overline{R}$ yields MLEV-8. The eight-pulse sequence cancels errors to second order in ϵ. The next iteration in the MLEV family is generated by concatenating a phase-inverted copy of MLEV-8, generating MLEV-16. In this fashion, higher order error terms in the expansion can be canceled. The cost of better cancellation is an increase in the cycle time required for the sequence. Table 4.2 lists the phases for sequences through MLEV-64.

4.4 Simulations and Experimental Results

The MLEV compensation schemes were tested on a sample of dilute H_2O in D_2O. The experiments were performed on a Bruker AM-400 spectrometer. The probe coil was detuned to yield a radio-frequency field strength of 10 kHz at full power. A weak RF field provides a sensitive test of the performance of our echo pulse sequences, and allowed us to better compare the iterative sequences with the standard Carr-Purcell, and Carr-Purcell-Meiboom-Gill sequences.

The experiment is performed as follows. A 90° pulse aligns the magnetization vector along either the x or y axis. A train of 180° pulses follows, with the phase of each pulse either fixed (in the case of Carr-Purcell and Carr-Purcell-Meiboom-Gill) or varied according to the phase cycle determined by the MLEV supercycle. Figure 4.2 shows a schematic for the experiment. The magnetization is sampled during a 1 microsecond window between every other pair of 180° pulses. In this fashion, 64 samples are collected from a set of 128 echoes. The receiver phase is set carefully, to assure that the signal falls entirely into one of the quadrature channels. The entire experiment is performed both on resonance, and at a resonance offset of 2 kHz. In the off-resonance case, the initial 90° pulse does not align the magnetization perfectly along the y axis, causing a detectable, yet inconsequential, phase shift in the signal.

Figure 4.3 shows a simulation of the magnetization signal for the case of a single spin with on-resonance irradiation. The simulation assumes a nominal RF field strength of 10 kHz (corresponding to a 50 μsec 180° pulse), and a 20 msec interpulse delay (τ=10 msec). Figure 4.4 shows the simulation for the same conditions except that here the transmitter has a resonance offset of 2 kHz. Neglecting relaxation due

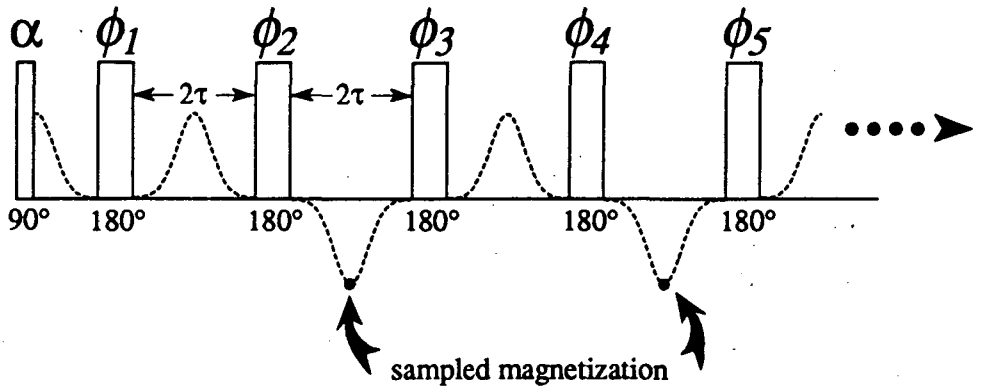

Figure 4.2: Schematic diagram for the Carr-Purcell experiments. The phase (α) of the initial 90° pulse is cycled in tandem with the receiver to select only magnetization originating from the first pulse. The phases, ϕ_i, for the 180° pulses are either fixed, in the case of the Carr-Purcell and Meiboom-Gill experiments, or are alternated according to the MLEV-2^n iteration schemes.

to magnetic field inhomogeneity, a single resonance offset is assumed for all of the spins in the sample (Δ=0). Due to the finite geometry of the sample and the probe coil, there is a measurable RF inhomogeneity over the sample volume. We have integrated over a distribution of RF field strengths that was modelled by the sum of a Lorentzian and Lorentzian-squared field strength profile, with the distribution represented by 191 discrete bins.

The simulations assume that the echo pulse train is applied with a relative RF phase of y. The simulations shown in Figures 4.3 and 4.4 correspond to a 90° pulse that aligns the magnetization along the y axis initially (the left-hand series of decays), and along the x axis (right-hand series). The standard Meiboom-Gill sequence (applied with phase y), preserves the intensity of the y-component of the magnetization, but works very poorly for the x component. An RF pulse train applied with the same phase as the magnetization component to be preserved, *i.e.*

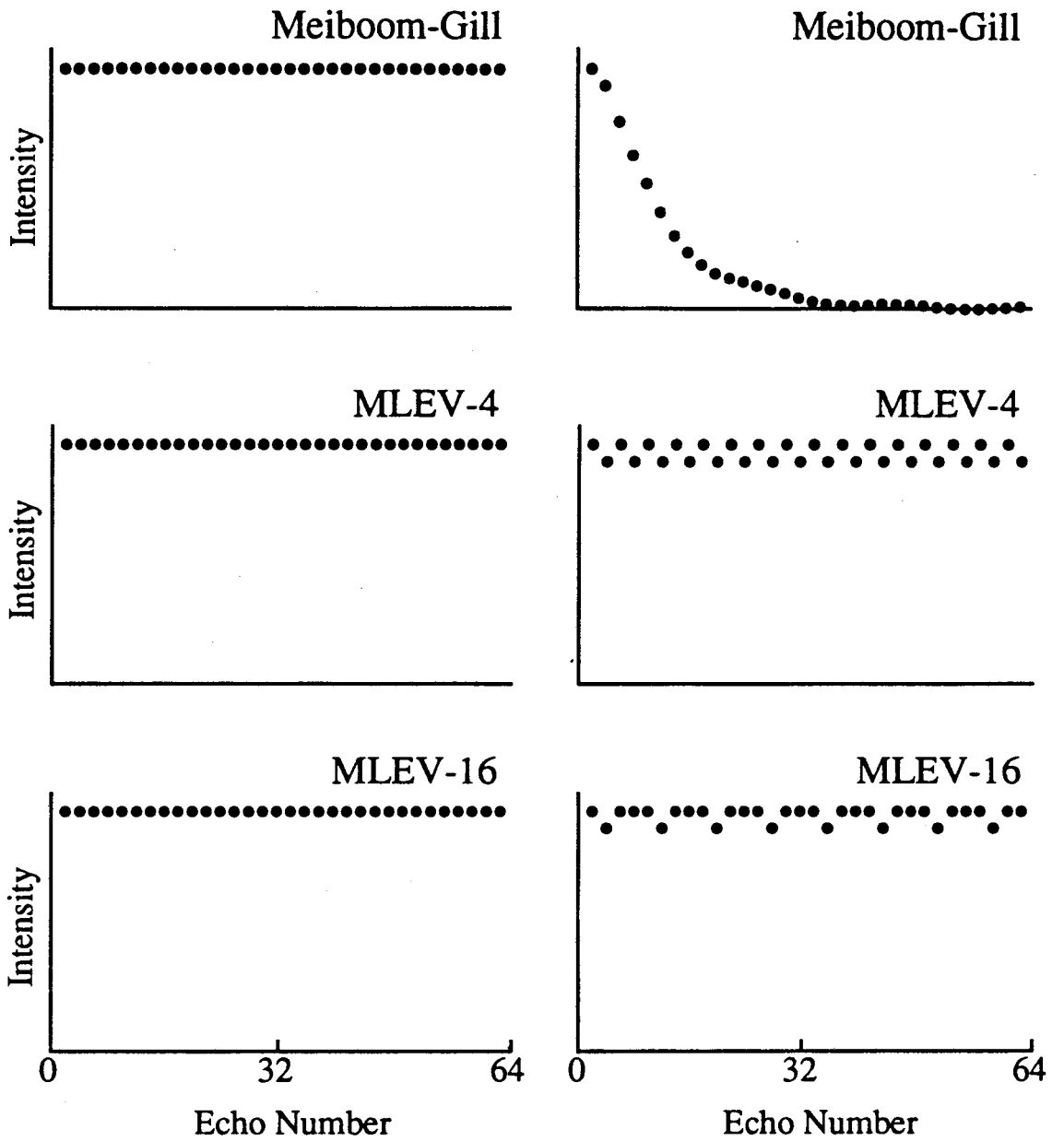

Figure 4.3: Simulated time-domain signal for echo trains applied on resonance. In each case, the initial magnetization (after the 90° pulse) lies along the y axis in the rotating frame. For the left-hand column of decays, the 180° pulses were applied with a relative phase along y; for the right-hand column, they were applied along x.

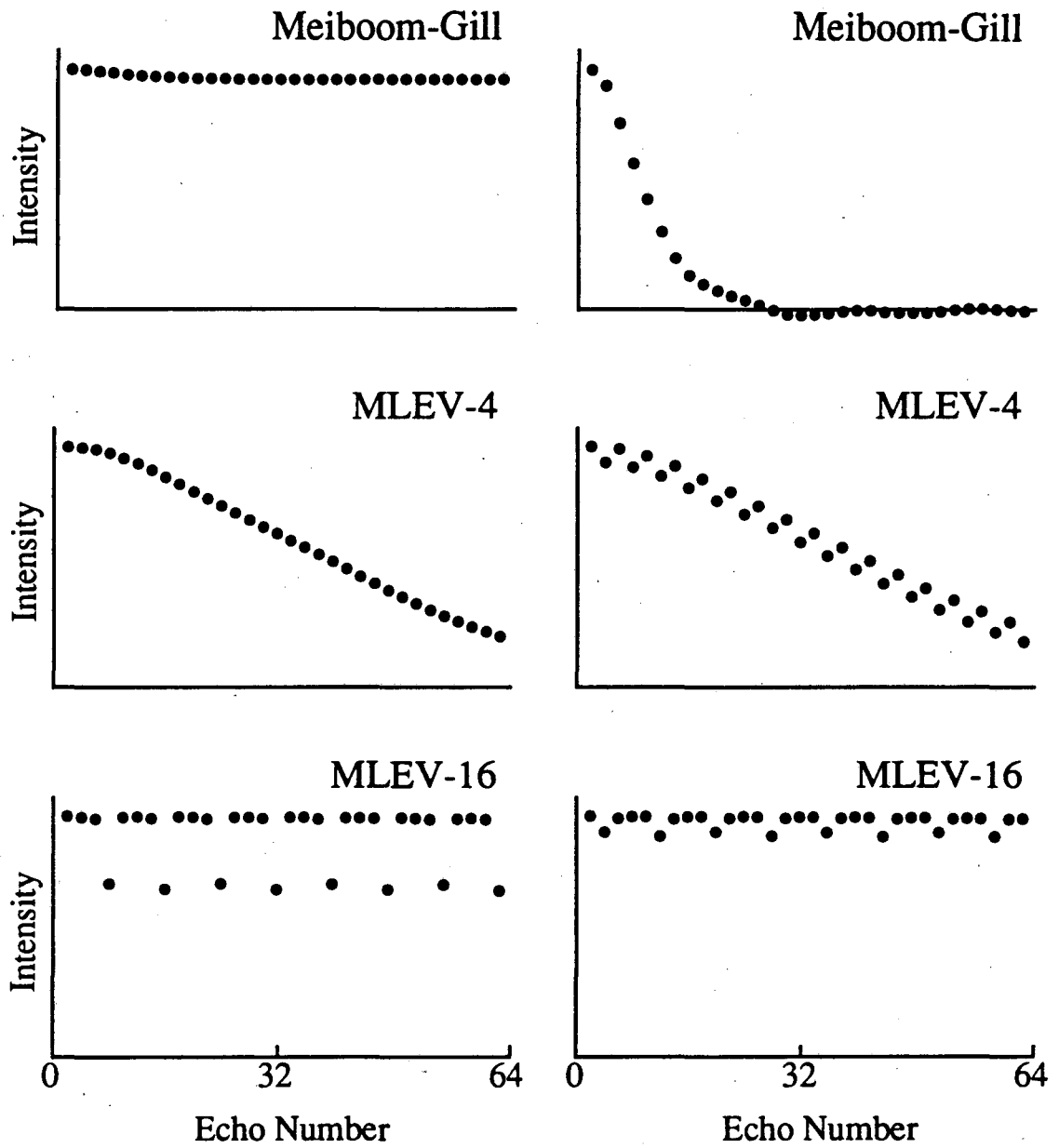

Figure 4.4: Simulated time-domain signal for echo trains applied 2 kHz off resonance. Otherwise, the conditions are identical as Figure 4.3.

a pulsed spin lock, is remarkably robust with respect to resonance offset and flip angle misset. Its performance in preserving the quadrature component is poor under all conditions.

The higher order MLEV sequences are composed of 4-pulse subsections with differing performance levels. That is, any four pulse section of a longer train may not perform as well as MLEV-4. Therefore, during the longer cycles necessary for MLEV-16 and higher, there are periods when the magnetization will deviate quite substantially from perfect refocussing. In heteronuclear decoupling, this manifests itself as cycling sidebands (when the heteronuclear magnetization must be sampled at a rate faster than the cycle time for the sequence) [111]. Here it manifests itself as a periodic dip in the echo envelope.

The experimental results agree very closely with the simulations. Figures 4.5 and 4.6 show the results for echo decays collected with the transmitter on resonance, and 2 kHz off resonance, respectively. The refocusing pulses were applied with a flip angle of 180° . On resonance, the spin-locked echo train refocuses very well, while the quadrature component dephases quickly due to RF inhomogeneity. In the case of off-resonance excitation, its performance is similarly disappointing. The MLEV-4 echo train preserves both components of the magnetization equally, but still decays relatively quickly. The MLEV-16 train, on the other hand, demonstrates substantial improvements in the length of the recorded echo train. As discussed above, the modulation of the MLEV-16 echo train is deeper than that for MLEV-4, since the propagator for the echo train deviates further from identity during the cycle.

The robustness of the MLEV-based sequences relative to the Meiboom-Gill mod-

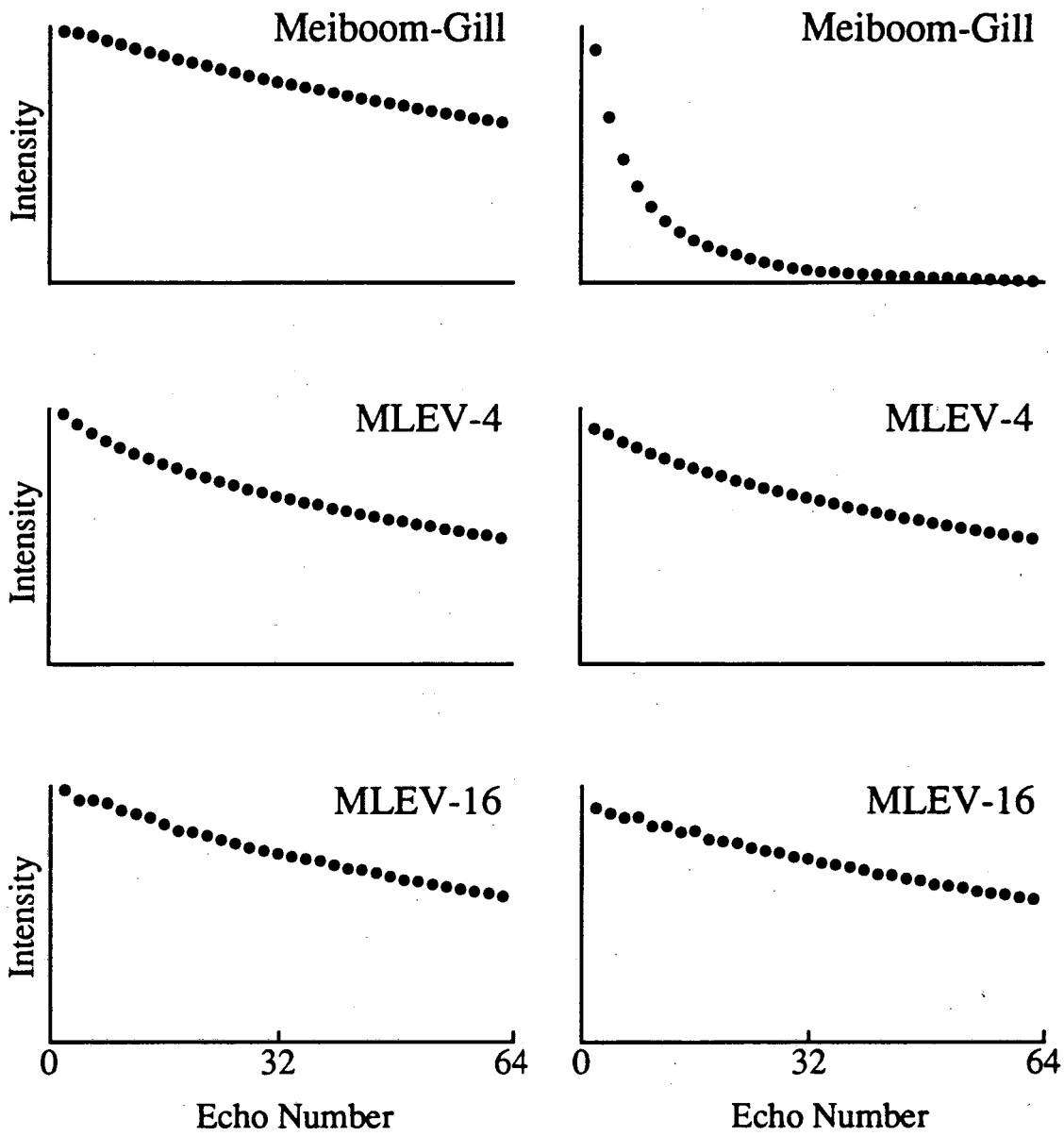

Figure 4.5: Experimental time-domain signal for echo trains applied on resonance. An initial pulse aligning the magnetization along the y axis is followed by an echo train of phase y (in the left column), or phase x (in the right column).

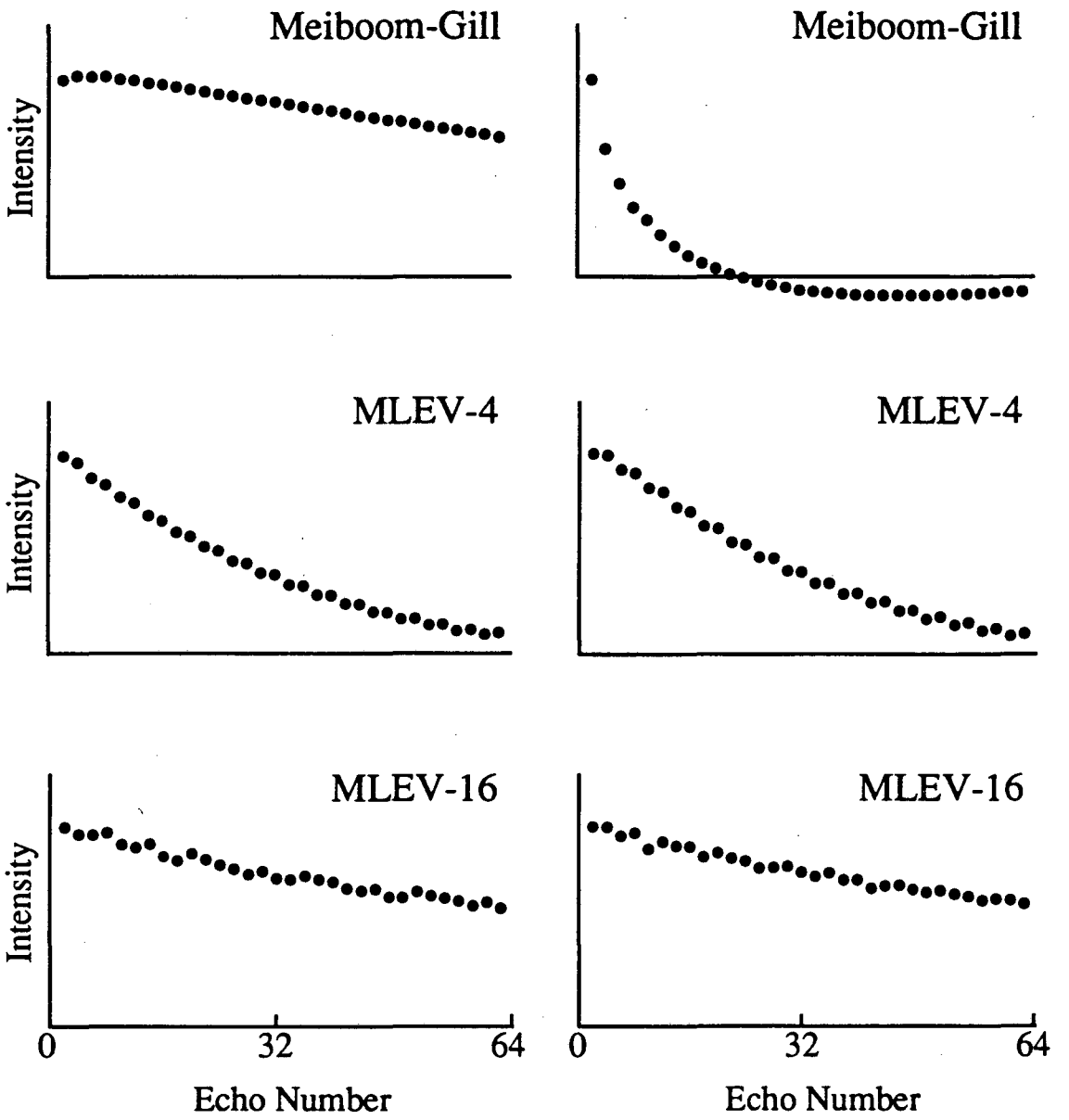

Figure 4.6: Experimental time-domain signal for echo trains applied 2 kHz off-resonance. Otherwise conditions are identical to those in Figure 4.5.

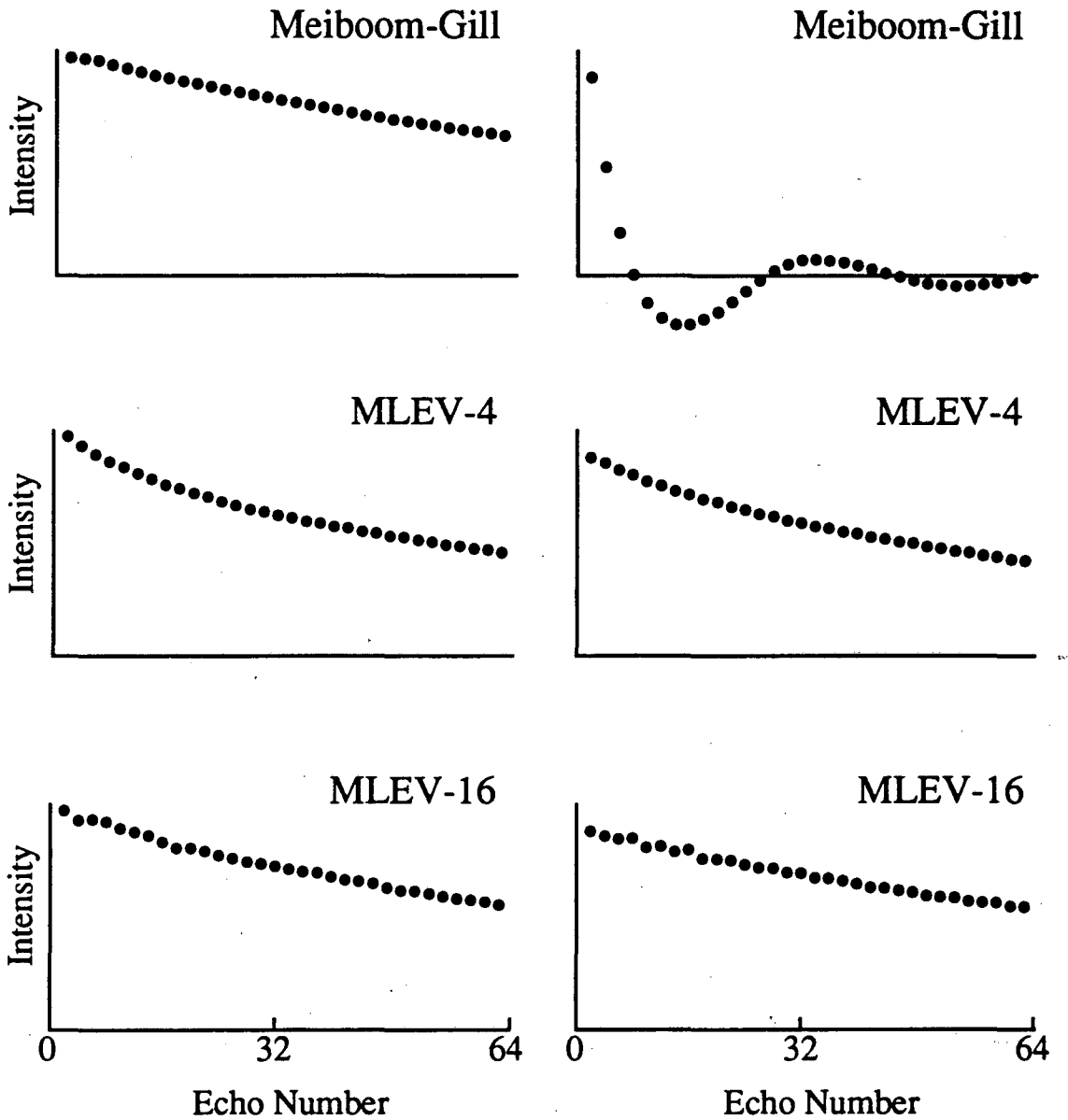

Figure 4.7: Experimental time-domain signal for echo trains applied on resonance. The flip angle for the refocussing pulse has been set to 175° .

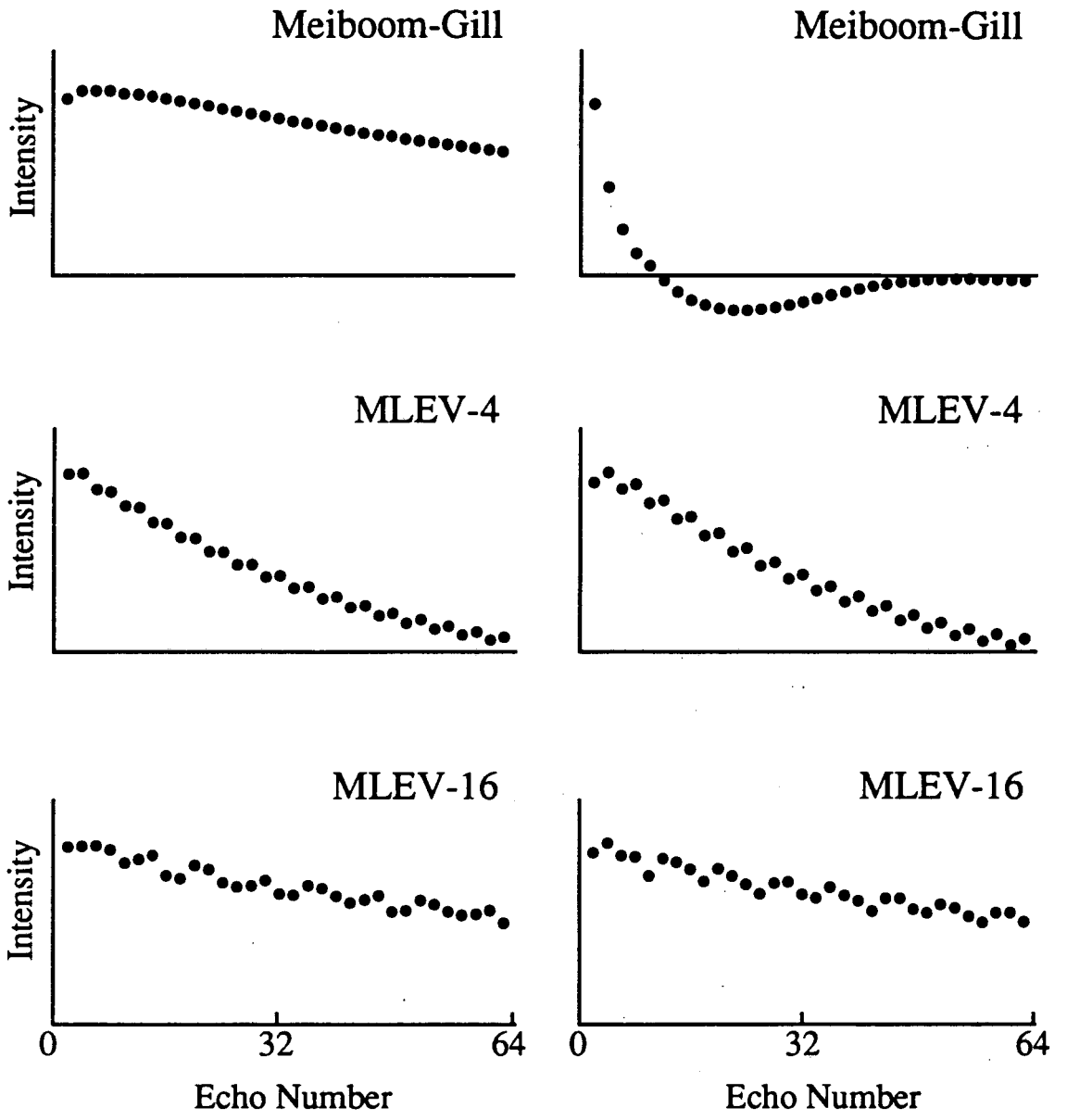

Figure 4.8: Experimental time-domain signal for echo trains with misset refocussing pulses applied 2 kHz off-resonance. Otherwise conditions are identical to those in Figure 4.7.

ification can be tested further by missetting the flip angle of the 180° pulses. Figures 4.7 and 4.8 show the experimental decays measured with a 175° flip angle, rather than the nominal 180°. For the Meiboom-Gill echo train, the spin-locked component of the magnetization still refocuses well, both on resonance, and off. The quadrature component, however, decays extremely quickly, and the refocussing of the magnetization is modulated by the error in pulse length. On-resonance, both MLEV-4 and MLEV-16 compensate both magnetization components well. Off-resonance, MLEV-16 maintains both components of the magnetization much better than MLEV-4. Both on-resonance and off, the MLEV trains do not display the modulation evident in the constant-phase echo train.

4.5 Conclusions

Applying error-compensated multiple-pulse schemes to the Carr-Purcell echo sequence imbues the sequence with a tolerance for pulse errors, and a wide effective bandwidth. By phase-shifting successive pulses in the echo train according to the phases prescribed by the MLEV family of decoupling sequences, much longer echo trains can be acquired than was previously possible. This results from the ability of the MLEV sequences to preserve both the in-phase and out-of-phase components of the magnetization. This proves critical in imaging experiments, where phase-encoding gradients may generate an initial magnetization vector of unknown phase.

Chapter 5

The Geometric Amplitude

5.1 Introduction

Adiabatic rapid passage [1] has found many applications in NMR, including cross-polarization [153, 154, 155, 115, 119] and selective excitation [156, 157, 158]. Laboratory-frame and rotating-frame adiabatic rapid passage have found use in tests of spin thermodynamics [159, 160, 161]. This chapter describes the contribution of the geometry of an evolution Hamiltonian to the inversion behavior of a spin-$\frac{1}{2}$, during a frequency-swept adiabatic pulse.

Recent work has shown that, even in few-level quantum mechanical systems, analysis by separation into subsystems typically involves effective interactions between the subsystems that are naturally described in terms of gauge fields [11, 26] (*cf.* Section 1.3.1). Such fields arise for subsystems consisting of dynamical variables (as in the Born-Oppenheimer approximation) and when one of the subsystems consists of external parameters. Examples giving rise to abelian and nonabelian gauge fields have been treated theoretically and experimentally [11, 26]. Abelian gauge

fields have been shown to alter the phases of the wavefunctions they act on; in the adiabatic limit the phases are shifted by Berry phases [10](*cf.* Section 1.3.2). Nonabelian fields alter both phases and populations. In a significant recent development, Berry has shown how a *Berry phase* in a driven two-level system fundamentally changes the *transition probability* in that system [162]. This chapter presents the experimental confirmation of this prediction [163].

We have considered the case of a two-level system (spin-$\frac{1}{2}$) unitarily evolving under a radio-frequency field sweep applied in the near-adiabatic limit. Effective abelian and nonabelian gauge potentials applicable to nonadiabatic behavior have been discussed from several points of view, both for unitary [164, 165, 166, 167, 168] and non-unitary [169, 170, 171, 172] evolution; while the nonabelian theories permit both phase and population changes, these treatments of abelian fields describe population changes geometrically only in the case of non-unitary evolution. Several authors have also considered geometric effects on the phase of the transition *amplitude* in a unitarily evolving two-level system [173, 174, 175]. The recent work of Berry derives a wholly new result: it predicts a geometric component of the transition *probability* in a unitarily evolving two-level system. This geometric component depends only on the curve followed by the Hamiltonian in its space of parameters, and not on how fast the curve is followed. The transition probability is the product of the geometric factor (Γ_g) which depends only on the *shape* of the magnetization trajectory, and a dynamical factor (Γ_d), which is exponentially small in the rate of change of the parameters:

$$P = \exp(+\Gamma_g)\exp(-\Gamma_d) \tag{5.1}$$

thus although the geometric factor is nonzero even in the adiabatic limit, the com-

plete transition probability still goes to zero as the rate of change goes to zero.

Section 5.2 briefly outlines the theory of Berry, showing its roots in the Landau-Zener and Dykhne formulas for the transition probability in two-level systems in order to fix notation and make our presentation more self-contained. We then discuss how the measurement is carried out, and the experimental significance of the parameters in the theory. Sections 5.4 and 5.5 present results of these experiments and indicate possible future directions and applications for this work.

5.2 Theory

Landau-Zener theory (*cf.* Section 1.3.3) provides an exact expression for the nonadiabatic transition probability in a two-level system described by the following Hamiltonian:

$$\mathcal{H} = \begin{bmatrix} E_0 + \alpha t & E_{12} \\ E_{12} & E_0 - \alpha t \end{bmatrix}, \tag{5.2}$$

where E_0, E_{12} and α are real, constant parameters, and t is the time [27, 28]. This Hamiltonian provides a simple model for a wide variety of phenomena, such as rapid passage experiments in NMR and nonadiabatic processes in atomic and molecular scattering. The instantaneous (adiabatic) eigenvalues of this system are

$$E_{1,2} = E_0 \pm \sqrt{\alpha^2 t^2 + E_{12}^2}\,, \tag{5.3}$$

and thus represent an avoided crossing as t varies from $-\infty$ to ∞. The complete time-dependent wavefunction for this two-level system can be expressed in terms of the adiabatic eigenvalues and wavefunctions as follows (in units where $\hbar = 1$):

$$\psi(t) = c_1(t) \exp\left[-i \int_{-\infty}^{t} dt' E_1(t')\right] \phi_1(t) + c_2(t) \exp\left[-i \int_{-\infty}^{t} dt' E_2(t')\right] \phi_2(t). \tag{5.4}$$

Here $\{\phi_1(t), \phi_2(t)\}$ are the instantaneous eigenfunctions of the Hamiltonian of Equation 5.2, and $c_1(t)$ and $c_2(t)$ are complex expansion coefficients. Landau-Zener theory provides an exact expression for the nonadiabatic transition probability P, where

$$P = |\langle\phi_2(+\infty)|\psi(+\infty)\rangle|^2, \tag{5.5}$$

assuming the initial condition $c_1(-\infty) = 1, c_2(-\infty) = 0$. Physically, P is the probability of finding the system in state 2, given that it began in state 1 and was transported at a constant rate through the avoided crossing. This is shown in Figure 5.1.

In terms of the matrix elements of the Hamiltonian of Equation 5.2, $P = \exp(-\pi E_{12}^2/\alpha)$. Note that P is exponentially small in α; as the rate of change of the Hamiltonian goes to zero, P goes to zero, in accordance with the adiabatic theorem. Section 5.3.1 treats the application to inversion of a spin-$\frac{1}{2}$ more thoroughly.

For a two-state Hamiltonian with more complicated time-dependence, Landau-Zener theory does not apply. Dykhne showed, however, that in the case of a real two-state Hamiltonian with an avoided crossing, a Landau-Zener-like expression for P is valid asymptotically, as the adiabatic limit is approached [176, 177, 178]. In Dykhne's solution, time is analytically continued into the complex plane, and although the energy levels of the system do not cross for any real value of time, there can be some complex value of time, which we denote t_c, where they do cross (*cf.* Figure 5.2). At this value of time, the energies are complex as well. Near t_c, barring accidental cancellations of the individual matrix elements of the Hamiltonian, the analytic structure of the energy level splitting is determined by $(t - t_c)^{1/2}$ [179]. The double-valued nature of the complex square root gives rise to the transitions in

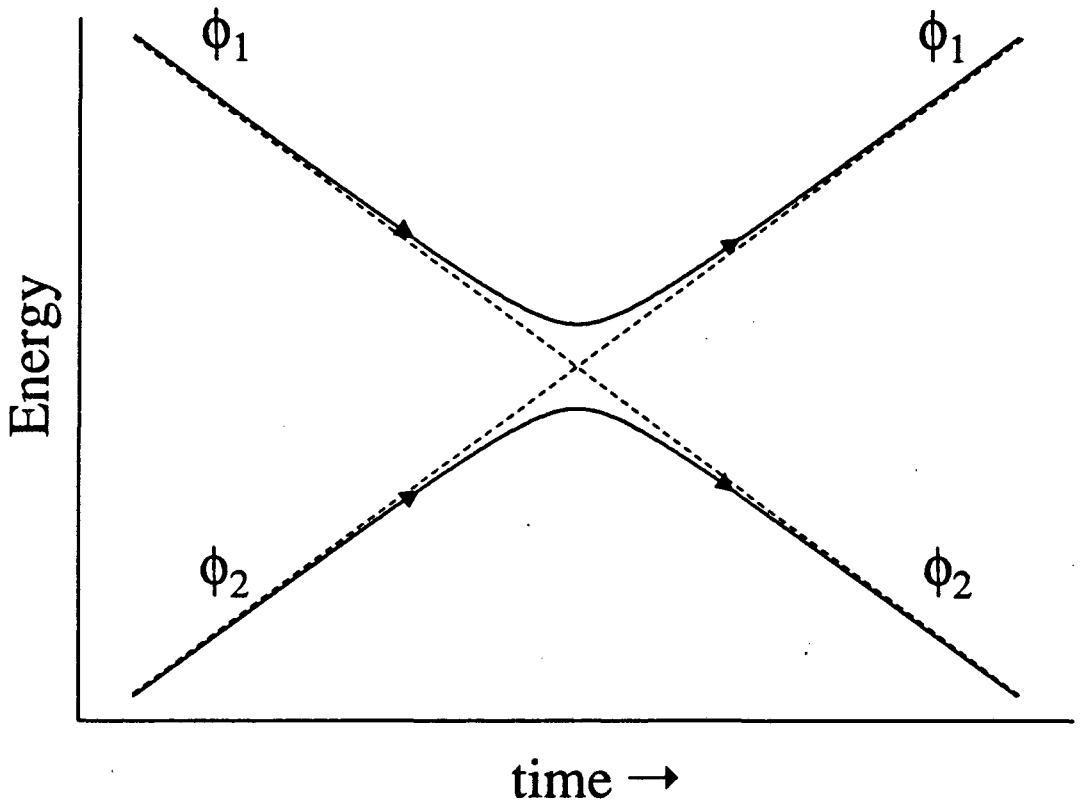

Figure 5.1: For adiabatic passage in time, a system initially in state ϕ_1 will have zero probability of transition to state ϕ_2 as t traverses $(-\infty, +\infty)$.

this picture—the eigenvectors are associated with the Riemann sheets of the square root, and can therefore interchange labels as they pass by the crossing point. The complex crossing point nearest the real axis dominates the transition probability as the adiabatic limit is approached; Dykhne shows that P is given asymptotically by

$$P = \exp\left[-\frac{4}{\delta}\,\mathrm{Im}\int_0^{\tau_c} E_2(\tau) - E_1(\tau)d\tau\right]. \tag{5.6}$$

In this formula, scaled time, defined by $\tau = \delta t$, is used, where δ measures the adiabaticity, or slowness, of passage. τ_c is the crossing point nearest the real time axis, and E_1 and E_2 are the (complex) instantaneous energies. This expression

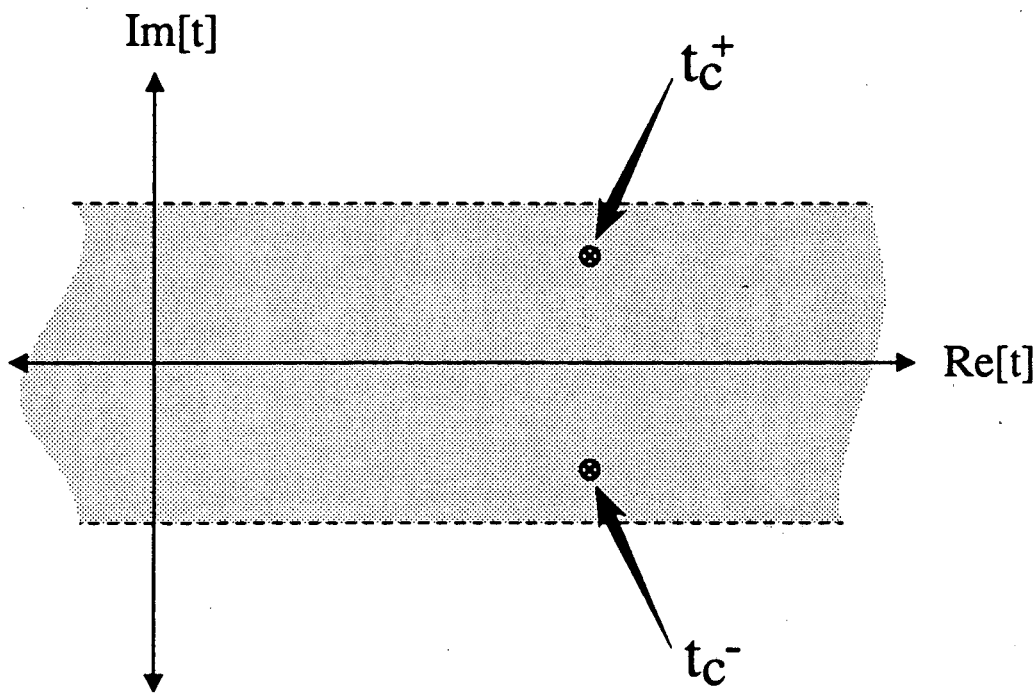

Figure 5.2: Crossing points $t_c(\pm)$ in the complex time plane. The closer the crossings lie to the real time axis, the slower the traverse needs to be performed to maintain adiabaticity.

for P requires that the matrix elements of the Hamiltonian be analytic in a strip that includes both the real time axis and τ_c, so that the phase integral may be analytically continued off the real time axis to the crossing point. Like the Landau-Zener expression, Dykhne's formula for P is exponentially small in the rate of change of $\mathcal{H}$.

Berry's contribution removes the restriction to real Hamiltonians [162]. He

considers the general Hermitian two-state Hamiltonian

$$\mathcal{H}(\tau) = \begin{bmatrix} Z(\tau) & X(\tau) - iY(\tau) \\ X(\tau) + iY(\tau) & -Z(\tau) \end{bmatrix}, \tag{5.7}$$

or, in spherical polar coordinates (H, θ, φ),

$$\mathcal{H}(\tau) = H(\tau) \begin{bmatrix} \cos\theta(\tau) & \sin\theta(\tau)\exp[-i\varphi(\tau)] \\ \sin\theta(\tau)\exp[i\varphi(\tau)] & -\cos\theta(\tau) \end{bmatrix}. \tag{5.8}$$

The expression for the full wavefunction, Equation 5.4, must be modified in this case by the geometric phase (Berry's phase), since here, unlike in the real case, it is not necessarily possible to globally choose the phase of the basis wavefunctions to be real [10](*cf.* 1.3.2). The appropriate wavefunction is then

$$\begin{aligned} \psi(t) &= c_1(t)\exp\left[-i\int_{-\infty}^{t} dt' E_1(t')\right]\exp(i\gamma_1)\phi_1(t) \\ &\quad + c_2(t)\exp\left[-i\int_{-\infty}^{t} dt' E_2(t')\right]\exp(i\gamma_2)\phi_2(t). \end{aligned} \tag{5.9}$$

Here γ_i is the geometric phase of state i, and can be expressed in terms of a line integral over the path C followed by the parameters X, Y, Z, as $\gamma_i = \int_C \mathbf{A}\cdot d\mathbf{R}$, with $\mathbf{A} = \langle\phi_i|\nabla_{\mathbf{R}}\phi_i\rangle$ and $\mathbf{R}$ the vector of parameters [10]. $\mathbf{A}$ is a vector potential (gauge potential), and in the two-state problem under consideration here it is abelian: it takes the form of a magnetic monopole vector potential located at the origin of parameter space [10].

As in the case considered by Dykhne, if the matrix elements of the Hamiltonian of Equation 5.7 are sufficiently analytic, an asymptotic expression for P can be developed, now by analytic continuation of both the energy difference and the geometric phase difference. We quote the result from Berry, in spherical coordinates [162]:

$$P = \exp\left[-\frac{4}{\delta}\,\mathrm{Im}\int_0^{\tau_c} d\tau H(\tau)\right]\exp\left[-2\,\mathrm{Im}\int_0^{\tau_c} d\tau \frac{d\varphi(\tau)}{d\tau}\cos\theta(\tau)\right] \tag{5.10}$$

$$= \exp(-\Gamma_d)\exp(+\Gamma_g). \tag{5.11}$$

The first factor, $\exp(-\Gamma_d)$, due to continuation of the energy difference, is the same as Dykhne's formula, and is exponentially small in the adiabaticity parameter. This factor is thus dynamical. The second factor, $\exp(+\Gamma_g)$, is due to continuation of the geometric phase, that is, to the abelian gauge potential $\mathbf{A}$ defined above, and is independent of the adiabaticity parameter. Γ_g is geometric in that it depends on the shape of the path followed by the Hamiltonian, but is independent of how fast the path is traversed. The geometric term is therefore constant, even under adiabatic evolution; it is multiplied, however, by a term which goes to zero in this limit so the adiabatic theorem is satisfied [9]. Note that the derivation of Γ_g makes no reference to closed paths in parameter space, a feature of earlier work on geometric phases that was important for the unambiguous definition of phase shifts [11, 10].

Berry discusses several conditions on $\mathcal{H}$ that must be satisfied to yield a non-zero Γ_g [162]:

1. $\mathcal{H}$ must be complex Hermitian, rather than real symmetric.

2. The Hamiltonian curve, $\mathcal{H}(\tau)$ must not lie in a plane through the origin, nor on a path that can be transformed to its time-reversed path through rigid rotation about an axis passing through the origin.

We will examine these more closely in the discussion of the measurement of the geometric component.

5.3 Experimental Implementation

5.3.1 Generating the Hamiltonian

In order to measure the geometric transition probability, $\exp(+\Gamma_g)$, we use a variant of a standard technique in NMR, adiabatic rapid passage (ARP) [1, 159]. The basic ARP experiment works by sweeping a radio-frequency field slowly through a Zeeman resonance. To describe the process thermodynamically, the inversion must proceed more slowly than the dephasing time, T_2, *(adiabatic)* to prevent the creation of coherences, yet faster than the longitudinal relaxation time, T_1, *(rapid)* to prevent coupling to the lattice [161, 160].

The adiabatic inversion can be visualized as a spin-locking radio-frequency field that smoothly transports magnetization aligned along the $+\hat{z}$ axis to an alignment along the $-\hat{z}$ axis. A condition for adiabaticity [1]

$$\frac{d\vec{\Omega}}{dt} \ll \omega_1^2 \tag{5.12}$$

requires that the rate of change of the direction of the applied RF field be smaller than the square of the field strength.Violation of this condition will cause magnetization to precess through large angles about the applied field axis, resulting in incomplete inversion. This is known as the strong condition for adiabatic transport. In practice, it is found that substantially faster passage through resonance still allows adiabatic inversion.

This process is described by the Hamiltonian (expressed in frequency units)

$$\mathcal{H}(t) = -\gamma \mathbf{I} \cdot (\mathbf{B}_0 + \mathbf{B}_{\mathrm{RF}}) = -\omega_0 I_z - 2\omega_1 I_x \cos\varphi(t), \tag{5.13}$$

where γ is the magnetogyric ratio of the nucleus; $\mathbf{B}_0$ is the static magnetic field,

taken along z, which determines the Larmor frequency $\omega_0 = \gamma|\mathbf{B}_0|$; $\mathbf{B}_{\mathrm{RF}}$ is the radio-frequency (RF) magnetic field, taken in the x direction, with amplitude $2\omega_1/\gamma$ and phase $\varphi(t)$; and I_z and I_x are components of the nuclear spin $\mathbf{I}$. In a frame of reference rotating about z in phase with the applied RF field, the Hamiltonian becomes

$$\mathcal{H}(t) = \Delta\omega(t)I_z - \omega_1 I_x = \omega_{\mathrm{eff}} \cdot \mathbf{I}. \tag{5.14}$$

Here the resonance offset $\Delta\omega(t) = \dot{\varphi}(t) - \omega_0$ and the RF amplitude ω_1 define the components of an effective magnetic field ω_{eff}, that has magnitude $|\omega_{\mathrm{eff}}(t)| = [\Delta\omega^2(t) + \omega_1^2]^{1/2}$ and makes an angle with the z axis of $\theta(t) = \arctan[-\omega_1/\Delta\omega(t)]$ [1, 159].

For a large, initially positive resonance offset, ω_{eff} begins along the $+z$ axis, decreases in length as it sweeps down to exact resonance along the $+x$ axis (reaching its minimum length ω_1), and then lengthens again to finish along the $-z$ axis. For a sufficiently slow sweep, the magnetization will follow this field and also end up aligned along the $-z$ axis. Faster sweeps leave progressively more magnetization behind, causing incomplete population transfer and residual coherence. For linear sweeps ($\dot{\varphi} \propto t$) such as is shown in Figure 5.3, the actual population transfer is described exactly by the Landau-Zener formula, because the Hamiltonian shown in Equation 5.14 has precisely the form of the Hamiltonian of Equation 5.2 in this case.

It turns out that Γ_g is zero for the standard Landau-Zener case. Consideration of the formula for Γ_g shows that it is zero for a Hamiltonian curve that can be rigidly rotated into itself about an axis passing through zero [162], where by Hamiltonian curve we mean a curve in the space of parameters X, Y, Z (I_x, I_y, I_z in the spin

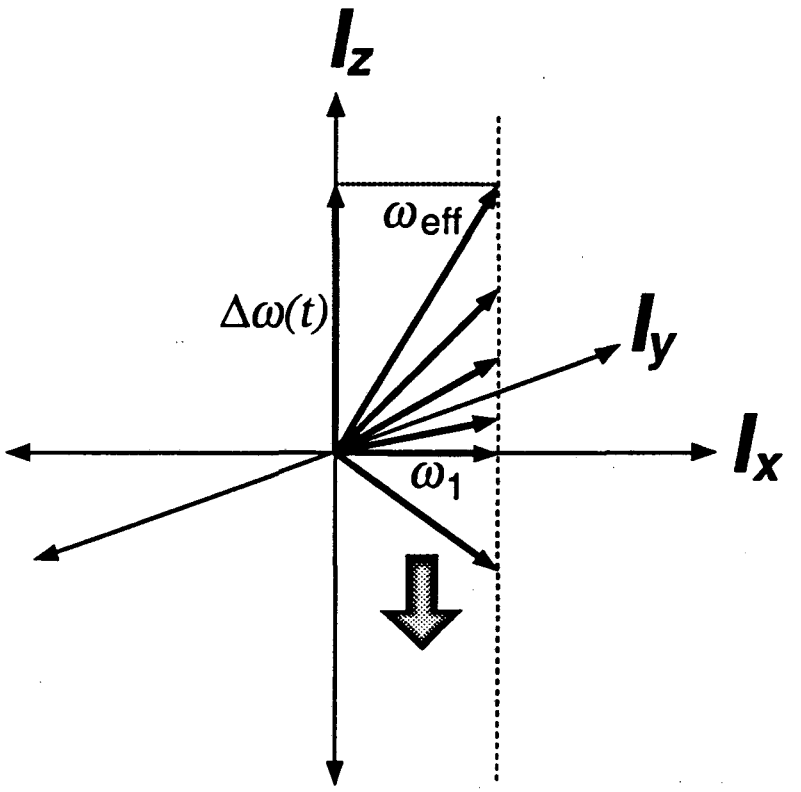

Figure 5.3: A straight line represents the simple Landau-Zener scenario of Equation 5.2; the transition probability for this curve has zero geometric component.

case) and parameterized by τ. A Hamiltonian curve that cannot be so rotated is shown in Figure 5.4 (and reference [162]); this is the curve used in our experiment, and represents the Hamiltonian

$$\mathcal{H}(\tau) = A\tau I_z - \omega_1 I_x \cos B\tau^2 - \omega_1 I_y \sin B\tau^2. \tag{5.15}$$

This Hamiltonian is generated experimentally by independently varying the the excitation and detection frequencies. Implicit in the discussion of the simple linear sweep was the idea that the signal would be detected in the instantaneous rotating frame defined by the RF. In fact, the resonance offset term, $\Delta\omega$ or $A\tau$, is defined by the difference between the Larmor frequency ω_0 and the detector frequency ω_{det}; trajectories of ω_{eff} in the xy plane of the rotating frame are generated by a transmitter-detector frequency offset. To generate the Hamiltonian shown in Equation 5.15, then, it is necessary to sweep both the detector and the RF frequencies linearly through resonance, while offsetting them in a way that the offset decreases linearly to zero as both pass through the Larmor frequency, and then increases linearly again.

A final complication lies in the time parameterization. Rather than choosing the time interval $(-\infty, \infty)$, we use the closed interval $t \in [0, T]$, since our experiments have a definite beginning and end. Then it is natural to use $\delta = 1/T$ as the scale of adiabaticity, and take scaled time in the interval $\tau \in [0, 1]$. Finally, we symmetrize the Hamiltonian about the origin of parameter space (so that the center of the chirp pulse occurs at time $\tau = 1/2$), giving the final form

$$\mathcal{H} = 2A(\tau - 1/2)I_z - \omega_1 I_x \cos B(\tau - 1/2)^2 - \omega_1 I_y \sin B(\tau - 1/2)^2. \tag{5.16}$$

The procedure used to generate this Hamiltonian is illustrated in Figure 5.5.

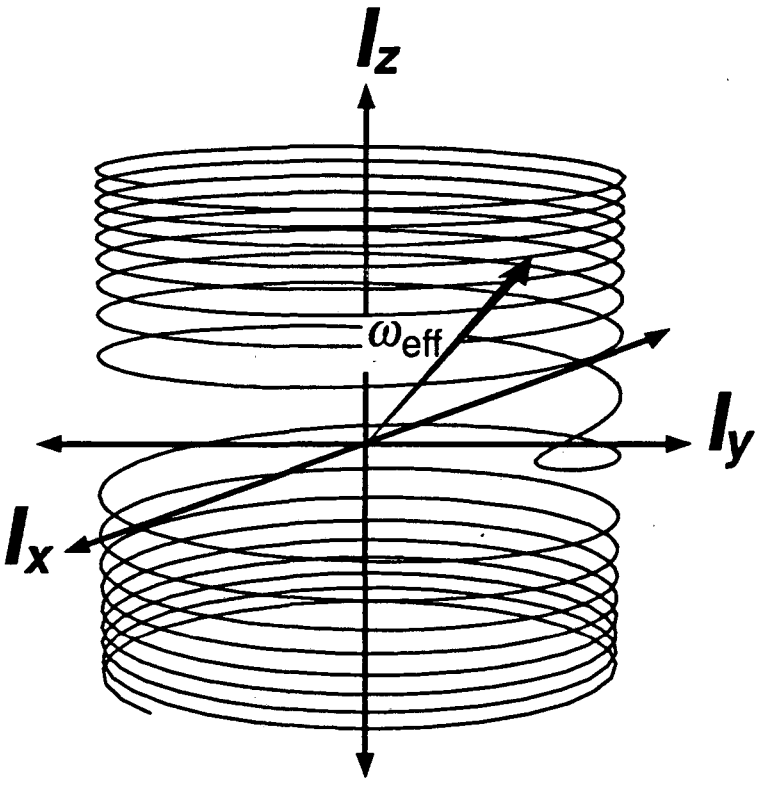

Figure 5.4: The non-uniform helix of Equation 5.15, is used in our experiments. The effective field, ω_{eff} traces out a spiral that displays a non-zero geometric component in the transition probability.

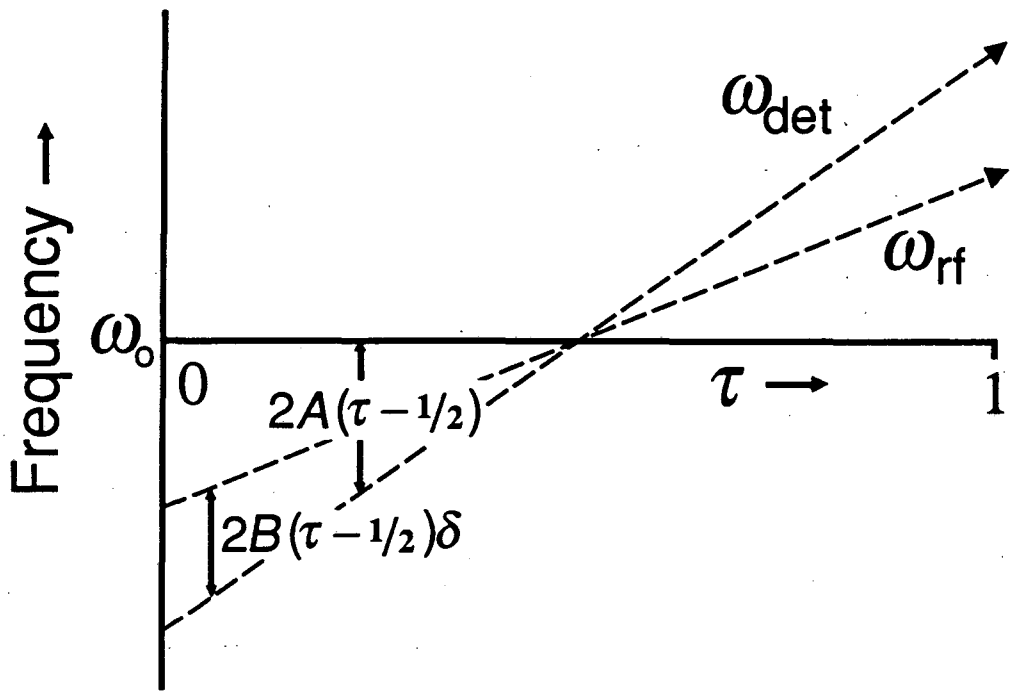

Figure 5.5: The transmitter and detector frequencies necessary to generate the Hamiltonian shown in Equation 5.16 (Figure 5.4). The detector frequency is swept linearly through resonance, to give the proper offset behavior ($\omega_0 - \omega_{\text{det}} = 2A(\tau - 1/2)$); also, the RF and detector frequencies are offset by $2B(\tau - 1/2)\delta$, so that the phase of ω_{eff} in the xy plane is $B(\tau - 1/2)^2$.

The complex crossing point is found to be

$$\tau_c = \frac{1}{2} \pm \frac{\omega_1}{2A} i. \tag{5.17}$$

The plot of the complex time plane (Figure 5.2) showing the crossing points, $\tau_c(\pm)$ reveals two experimental constraints. First, in order to avoid edge effects due to starting and ending the experiment at finite times it is necessary to choose $\omega_1 \ll A$, so the time integrals can be extended to $\pm\infty$. Second, in order to guarantee adiabatic passage, we must approach the crossing points slowly (along the real time axis) relative to the size of $\omega_1/2A$. Then the dynamic and geometric contributions to the transition probability are evaluated as

$$\Gamma_d = \frac{\pi\omega_1^2}{4\delta|A|}, \tag{5.18}$$

$$\Gamma_g = -\frac{\pi\omega_1^2 B}{4|A|\,A}. \tag{5.19}$$

It will be argued that moving the detector frequency can have no physical effect in an NMR experiment, a point which is certainly true. The detector frequency serves only to define a convenient reference frame. In the present case, by choosing a different detector frame, we can even make our complex Hamiltonian look real. Does this remove the geometric component from the transition probability? Not at all. By synchronizing the detector with the RF, rather than using the frame described above, the Hamiltonian of Equation 5.16 is transformed into

$$\mathcal{H} = 2(A - B\delta)(\tau - 1/2)I_z - \omega_1 I_x; \tag{5.20}$$

note the appearance of δ in the resonance offset term. In this frame, $\Gamma_g = 0$ by symmetry. When Landau-Zener theory is applied to this transformed Hamiltonian (now a valid procedure because it has the form of the Hamiltonian of Equation 5.2),

the transition probability for all values of δ is obtained:

$$P = \exp\left(-\frac{\pi\omega_1^2}{4\delta|A(1-B\delta/A)|}\right). \tag{5.21}$$

Expansion around $\delta = 0$, the adiabatic limit, yields

$$P = \prod_{n=-1}^{\infty} \exp\left[-\frac{\pi\omega_1^2}{4|A|}\left(\frac{B}{A}\right)^{n+1}\delta^n\right], \tag{5.22}$$

which shows that, even though $\Gamma_g = 0$ in this frame, the geometric component of P, $\exp[-\pi\omega_1^2 B/(4A|A|)]$, does not vanish. This expansion also gives a useful bound on where the asymptotic theory of Berry should be valid, namely, $A/(B\delta) \gg 1$.

The above analysis demonstrates that Γ_g and Γ_d are gauge-dependent quantities, that is, that their values depend on the basis (reference frame) in use. The original reference frame of Equation 5.16 is conceptually convenient, because in it, the geometric and dynamic transition probabilities separate cleanly into Γ_g and Γ_d. The current reference frame, Equation 5.20, lacks this clean separation, but is experimentally convenient. The practical signature of the lack of a clean separation in a given frame is the appearance of δ in the Hamiltonian expressed in that frame. If δ appears explicitly, then in that frame the geometry of the curve and its time parameterization are entangled, and one cannot draw conclusions about the appearance of a geometric transition probability from the shape of such a curve alone.

The existence of a real form of the Hamiltonian (Equation 5.20) is not due to any special features of the complex curve (Equation 5.16). Any complex Hamiltonian curve can be locally transformed to a real version, to which Dykhne's theory can be applied. The resulting transition probability will be qualitatively different, however, from the usual Dykhne and Landau-Zener results, if the Hamiltonian curve in a δ-independent frame is both complex and sufficiently asymmetric. The new feature

in P is, of course, the δ-independent component ($\exp \Gamma_g$ in a δ-independent basis). The fact that Γ_g vanishes in some frames but P retains its δ-independent factor is the analog of the removability of Berry's phase, that is, the fact that Berry's phase can always be locally transformed away but nevertheless observables still show the underlying geometry of the system [180]. This freedom of choice of basis is a manifestation of the gauge-invariance of P. We take advantage of this freedom by measuring P in the frame of Equation 5.20, and analyzing the data in the frame of Equation 5.16, for easier comparison with Berry's results.

5.3.2 Measurement of P

The Zeeman resonance in ^{13}C-enriched carbon disulfide provided the two-level system for our experiments. We used an 11.7 Tesla magnet, corresponding to a ^{13}C resonance frequency of 125.6 MHz; the static magnetic field was shimmed to give a line of full width at half maximum of 15 Hz. This linewidth is due almost entirely to inhomogeneity in the static magnetic field. The NMR spectrum of this sample consists of a single line, since most (99%) of the spin-1/2 ^{13}C is bonded to spin-0 sulfur. The longitudinal relaxation time (T_1) for our sample was 22 seconds, determined with an inversion-recovery experiment, which defines the time scale for rapid passage experiments: they must be short compared to T_1. All results presented below were acquired with sweep times ≤ 0.6 seconds. The data were collected on a Chemagnetics CMX-500 NMR spectrometer, using a Sciteq direct digital synthesizer for control of the detector and RF frequencies. The frequency chirp is represented by a windowless sequence of 1792 pulses, each with the frequency incremented by an amount dictated by the sweep profile.

Measuring P amounts to measuring the diagonal elements of the density matrix. The initial density matrix in our experiment is essentially I_z [1, 159]; after subjecting this to an RF sweep with an RF field strength of approximately 400 Hz, the component remaining along the z axis is proportional to $2P - 1$. A 90° pulse, with a field strength of 20 kHz, following the sweep brings this component to the xy plane in the rotating frame, where it can be detected in the time domain. The 90° "interrogation" pulse is applied on-resonance. The pulse sequence is shown schematically in Figure 5.6. A standard CYCLOPS (quadrature) phase cycle is applied to the 90° pulse and detector, to remove residual coherences and hardware imperfections [120]. The experiment is repeated for a variety of sweep times, ranging from 5 to 600 msec. For each iteration, the ^{13}C resonance is integrated to improve signal-to-noise, and provide immunity against lineshape distortions. The (signed) area of the peak in the frequency domain, S, is proportional to $2P - 1$, and is normalized to the signal from a very slow (adiabatic) sweep, S_{max}, for which $P = 0$. Thus P is extracted from the measured peak areas as $P = \frac{1}{2}(1 - S/S_{\mathrm{max}})$.

5.4 Results

We demonstrate generation of Hamiltonian 5.16 by showing, in Figure 5.7, the response of the sample magnetization to it, for $\delta = 1.66$ sec^{-1} ($A/(B\delta) = 18.9$), that is, nearly adiabatic evolution. For such a case, the magnetization vector tracks the direction of the Hamiltonian vector shown in Figure 5.4, and gives a direct picture of the geometry of the Hamiltonian curve.

The experimental trajectory of Figure 5.7a was measured in a "two-dimensional" interferometric experiment, where the pulse sequence of Figure 5.6 was applied with

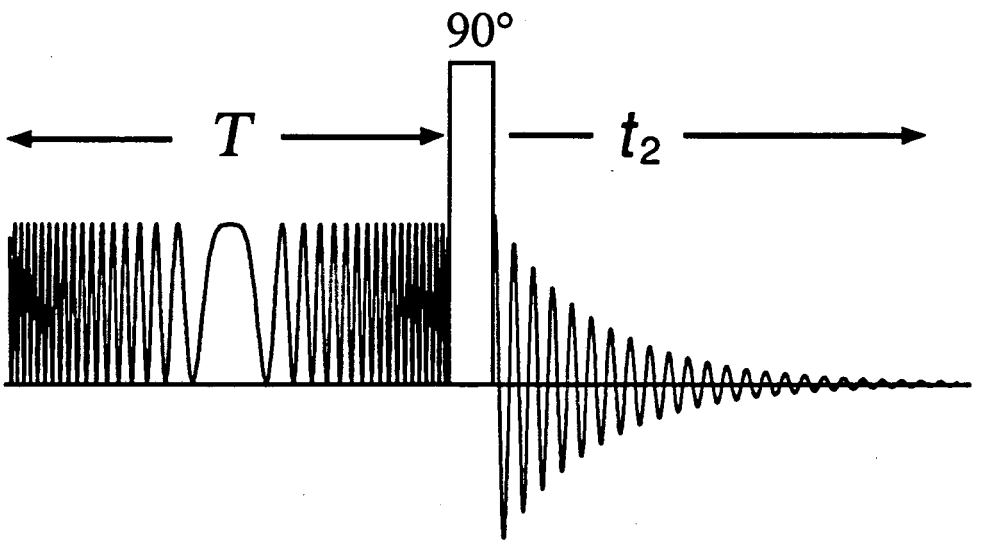

Figure 5.6: The experimental sequence used to measure P, the nonadiabatic transition probability. First, the RF frequency sweep is applied over the time interval $[0, T]$. P is related to the resulting component of magnetization along z; this is probed with the 90° pulse, which tips it into the xy plane in the rotating frame, where it is detected in the time domain during the interval t_2. Fourier transformation to the frequency domain yields a peak whose intensity is proportional to $2P - 1$. Four such experiments, with phase shifted probe pulses and detector frames (to cancel residual coherences and artifacts in the electronics), are co-added and integrated to yield a single data point.

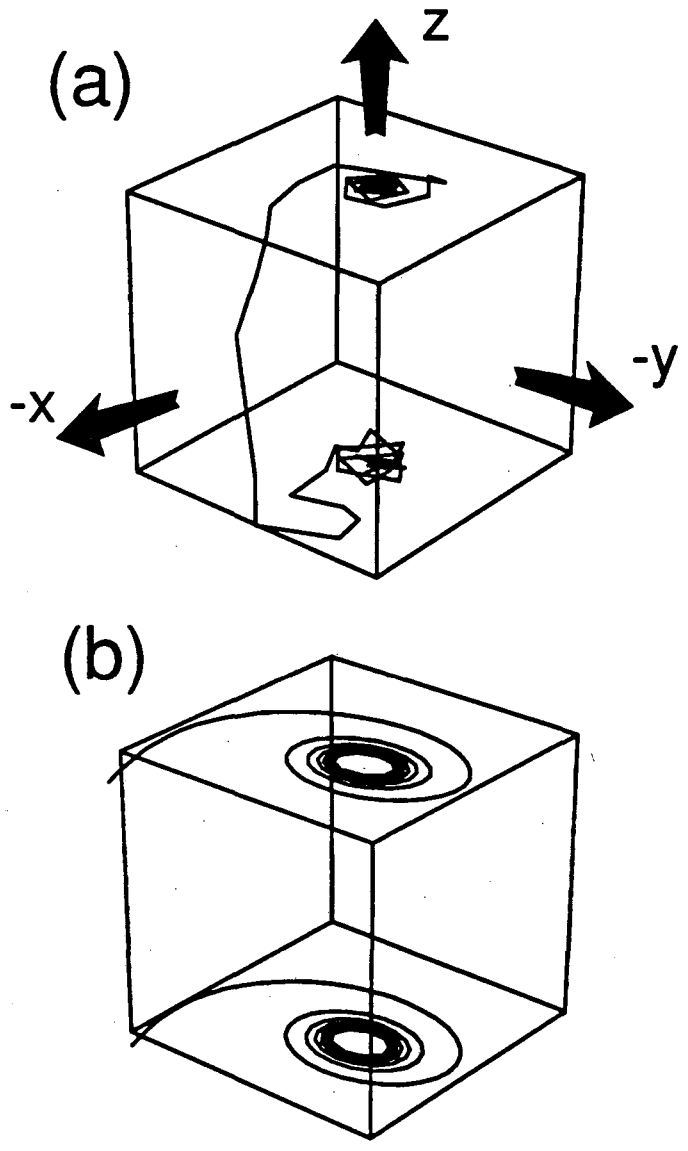

Figure 5.7: (a) Response of the sample magnetization to the Hamiltonian of Equation 5.16 (Figure 5.4), in the adiabatic regime. (b) For clarity, an expanded (and truncated) theoretical curve of the magnetization is shown.

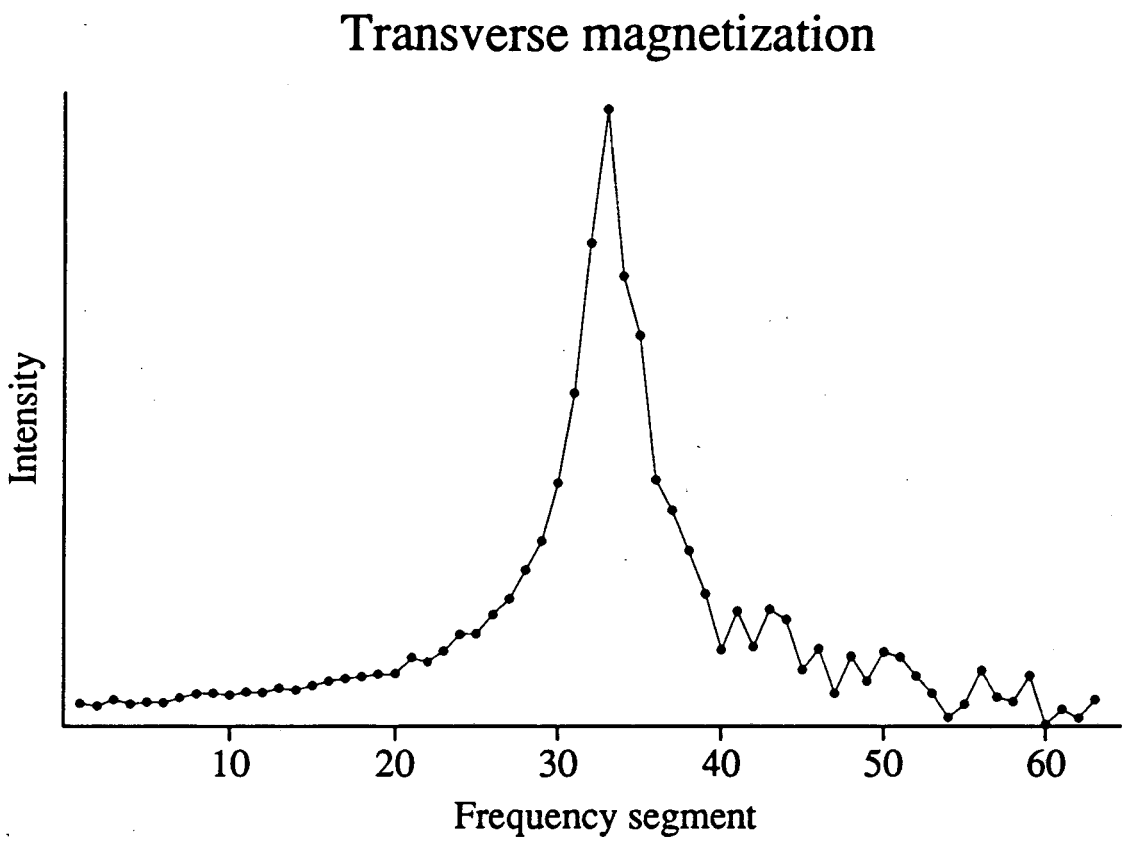

Figure 5.8: Plot of the transverse excursion of the magnetization vector during the RF field sweep.

successively longer fragments of a complete frequency chirp. It is interesting to note, that during the chirp pulse (composed of 1792 different frequency elements), most of the excursion of the magnetization vector occurs in the middle 16 frequency increments. The interrupted detection scheme employed to measure the trajectory depicted in Figure 5.7 used the 90° read pulse to resolve the position of the magnetization vector at the end of each frequency segment. By integrating each spectrum so obtained, we are able to track the magetization as it passes through the transverse plane. Figure 5.8 shows such a plot.

Figure 5.7 shows the same data, except there, a reverse phase correction has

been applied to each data point, to correct for the fact that the transmitter and receiver were locked with zero phase offset for each point in the acquisition. In effect, this allows us to map the data of Figure 5.8 back onto the sphere, to obtain the laboratory frame trajectory.

Since the dynamical term overwhelms the geometric contribution to the transition probability in the adiabatic regime, measurement of Γ_g requires nonadiabatic traversal of the Hamiltonian curve, for which the magnetization no longer keeps up with the Hamiltonian. We take advantage of the fact that we have an expression for P valid for all δ, by fitting the theory to our measurements of P over a range of sweep times. The results are shown in Figure 5.9. The experimental parameters are $A = 50$ kHz, $B = \pm 5,000$ rad, and $\omega_1 = 393$ Hz. Determination of these parameters is discussed below. Changing the sign of B is equivalent to the transformation $H(\tau) \rightarrow H(-\tau)$, that is, time-reversal [162]. Close agreement between the exact theory, Equation 5.21, and experiment is obtained over the full range of δ. We have performed the same experiment with different values of $|B|$ and ω_1, and the graphs of P (not shown) scale according to Equation 5.21.

5.5 Discussion

5.5.1 Determination of Γ_g

Using the data shown in Figure 5.9 we can extract the geometric contribution to P in two ways [162]. In the adiabatic limit, we can consider only the first two terms in the product expansion of equation 5.22:

$$P = \prod_{n=-1}^{\infty} \exp\left[-\frac{\pi\omega_1^2}{4|A|}\left(\frac{B}{A}\right)^{n+1}\delta^n\right] \tag{5.23}$$

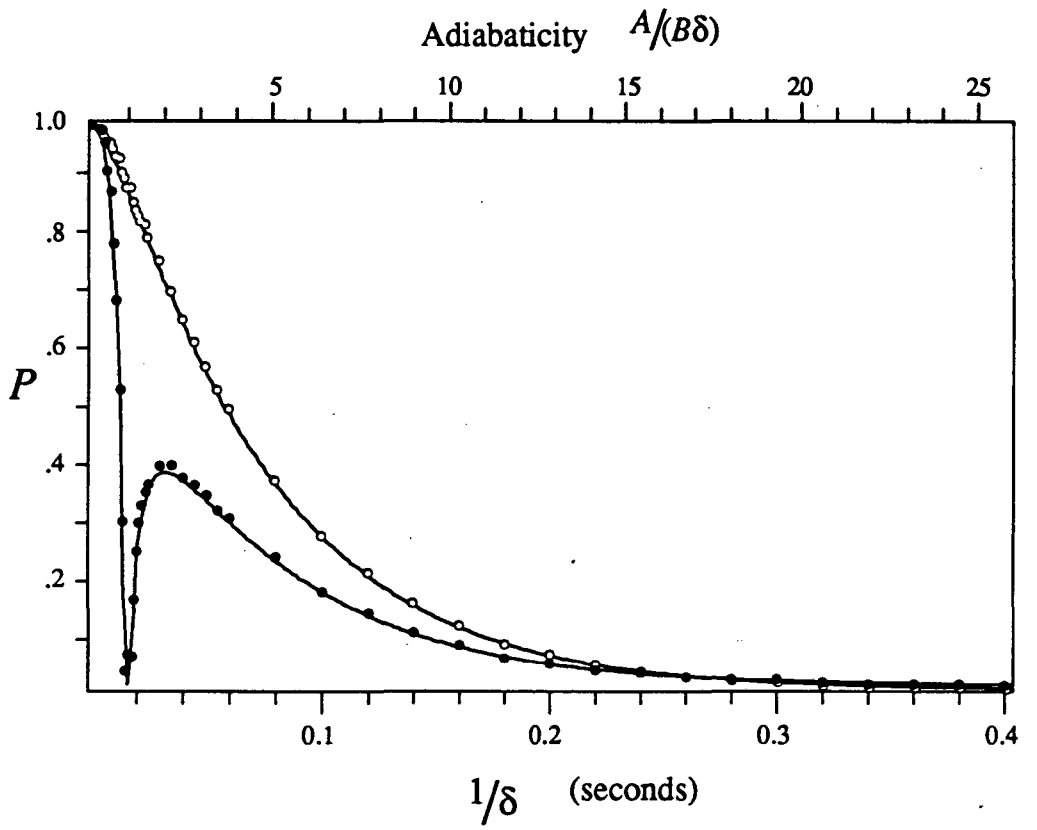

Figure 5.9: The nonadiabatic transition probability, measured as a function of adiabaticity parameter for the Hamiltonian of Equation 5.16. Parameters are $A = 50$ kHz, $B = \pm 5,000$ rad, and $\omega_1 = 393$ Hz. Changing the sign of B amounts to traversing the curve in time-reversed fashion. The filled circles are for $B = +5,000$ rad, and the open circles for $B = -5,000$ rad. The solid curves show the theory for this case, Equation 5.21, which is exact, describing both the adiabatic and nonadiabatic limits. $A/(B\delta)$, shown on the top axis, is a dimensionless adiabaticity parameter (see text), which scales out the specific values of the constants used in the experiment.

$$\approx \exp\left(-\frac{\pi\omega_1^2}{4|A|}\frac{1}{\delta}\right)\exp\left(-\frac{\pi\omega_1^2}{4|A|}\frac{B}{A}\right). \tag{5.24}$$

Taking the logarithm of each side yields

$$\log\left(\frac{1}{P}\right) = \left(\frac{\pi\omega_1^2}{4|A|}\frac{1}{\delta}\right) + \left(-\frac{\pi\omega_1^2 B}{4|A|A}\right) \tag{5.25}$$

$$= \Gamma_d - \Gamma_g = \delta(\Gamma_d)\frac{1}{\delta} - \Gamma_g \tag{5.26}$$

First we plot $\log(1/P)$ versus $1/\delta$, (*i.e.* versus sweep time). In the nearly adiabatic regime, such a plot should be linear, with slope $\delta\Gamma_d$ and intercept $-\Gamma_g$. The non-zero intercept reflects the fact that the geometric component persists into the adiabatic limit, although $P \rightarrow 0$ in this limit so it cannot be measured there. The data are plotted this way in Figure 5.10, and three regimes can be identified. At short sweep times the data are non-linear, as expected; the asymptotic theory should not apply here. Also, at the shortest times, $P \rightarrow 1$, and $\log(1/P) \rightarrow 0$ as shown in Figure 5.11. At very long times, $P \approx 0$, and we cannot measure it accurately due to our signal-to-noise constraints. The intermediate regime, however, shows the expected linear behavior, with offset. Equation 5.22 shows that Berry's theory should hold, for the present Hamiltonian, when $A/(B\delta) \gg 1$. The data show linearity for $A/(B\delta) \gtrsim 4$. As mentioned in Section 5.3.1, theoretical requirements for adiabatic evolution are frequently harsher than those encountered experimentally. Finally, note that the intercepts in Figure 5.9 are positive and negative, as B is changed in sign; this is due to the fact that Γ_g changes sign under time-reversal, but Γ_d does not [162].

Berry's theory predicts, for the values of A, B, and ω_1 listed above, that $|\Gamma_g| = 0.243$ and $\delta\Gamma_d = 15.3\ \text{sec}^{-1}$. These lines are plotted in Figures 5.10 and 5.11. Least-squares fits to our data give $\Gamma_g = 0.26$ and $\delta\Gamma_d = 16\ \text{sec}^{-1}$, for $B = -5,000$ rad, and $\Gamma_g = -0.23$, $\delta\Gamma_d = 15\ \text{sec}^{-1}$, for $B = +5,000$ rad. Quantitative agreement, while

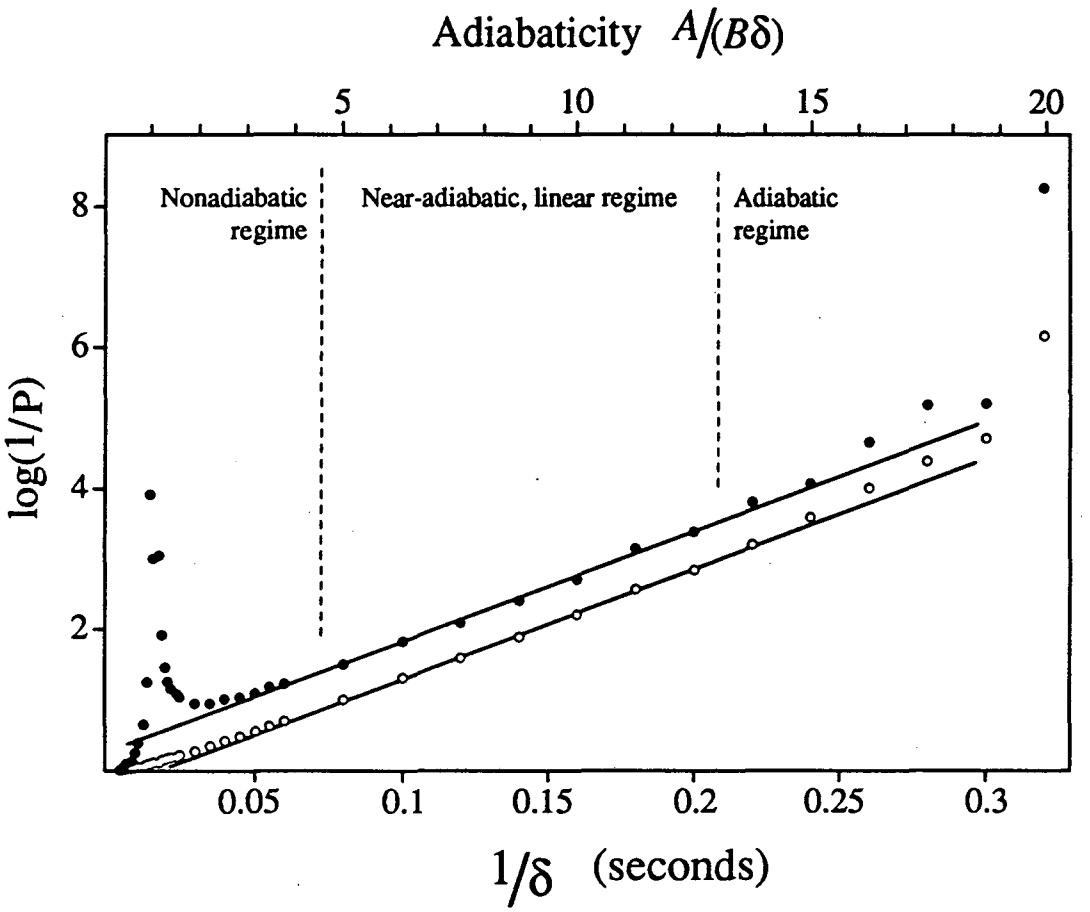

Figure 5.10: The same data as shown in Figure 5.9, now plotted as $\log(1/P)$ versus $1/\delta$ in order to extract the geometric transition probability. At small values of $1/\delta$ the dynamics are strongly nonadiabatic, and the asymptotic theory of Berry is not valid here. For large $1/\delta$, the adiabatic limit, P is too small to measure accurately in our experiment, as is evidenced by the increased scatter in the data at long sweep times. The intermediate regime, however, is accessible to experiment and is described by Berry's theory. The figure also shows the theory of Berry, which appears as straight lines of slope $\delta\Gamma_d = 15.3$ sec^{-1} and intercept $\Gamma_g = \pm 0.243$. The sign-change in Γ_g is due to its behavior under time-reversal.

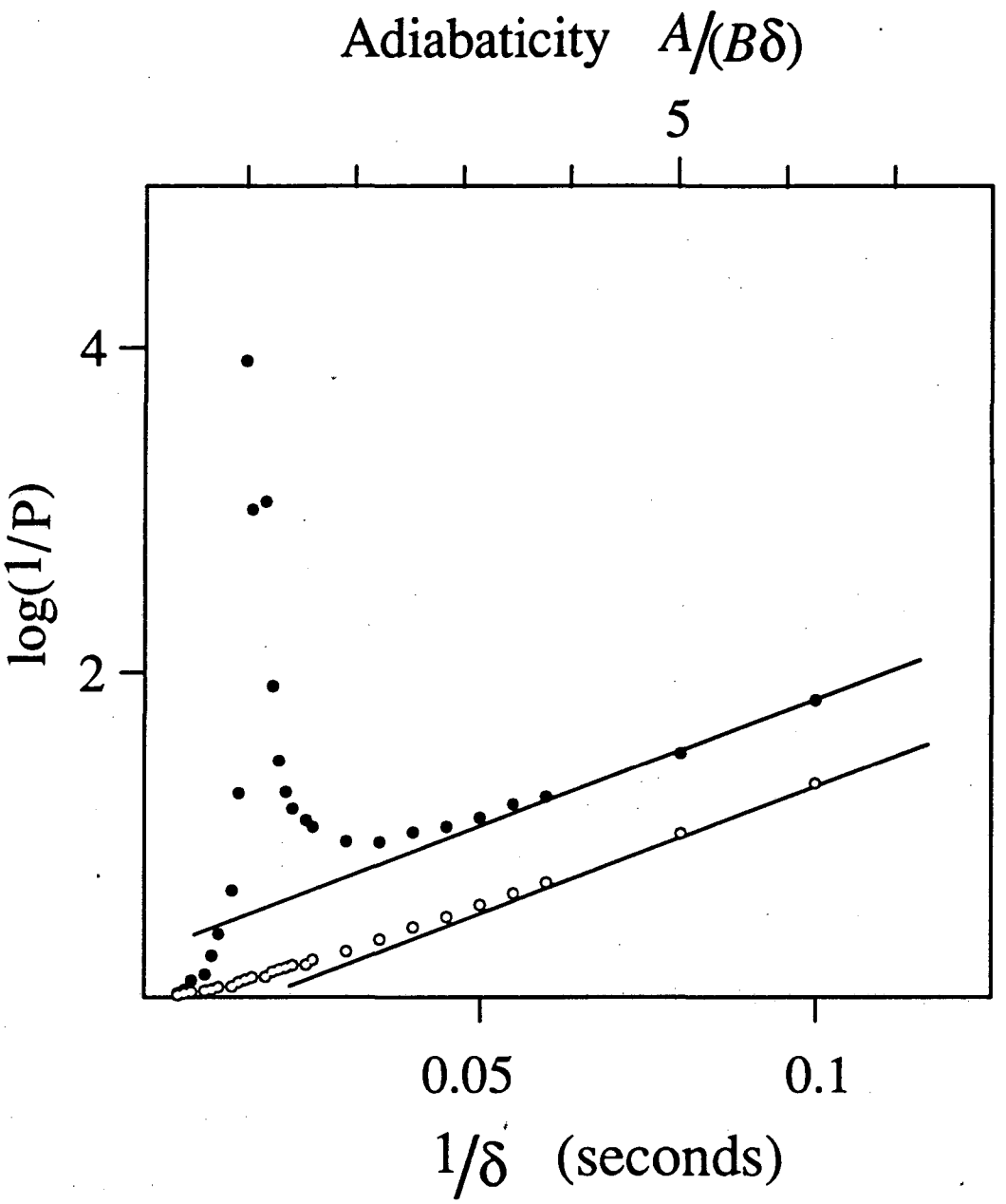

Figure 5.11: The intercepts from Figure 5.10 are shown more clearly in this figure, which also shows the behavior for small $1/\delta$; both experimental curves go to zero here, since $P \rightarrow 1$ in this limit.

not perfect, is reasonable, given the amplification of errors at small P introduced by the logarithmic plot and the difficulty of precisely measuring ω_1, the amplitude of the RF field, in our apparatus. Section 5.5.3 discusses this difficulty.

The above-stated time-reversal behavior affords a second way to extract Γ_g. Plotting $\frac{1}{2}\log(P_{B>0}/P_{B<0})$ versus sweep time should give a line of zero slope with intercept Γ_g; the data plotted this way are shown in Figure 5.12. This determination yields $\Gamma_g = -0.26 \pm 0.01$, to be compared with the theoretical value of $\Gamma_g = -0.243$. The same three regimes observed in Figure 5.10 can be identified, as $1/\delta$ changes from small to large values.

5.5.2 Behavior with Respect to Time-Reversal

In the previous section we used the behavior of P under time-reversal to extract Γ_g. Near the adiabatic limit, where the asymptotic theory is valid, this behavior is expressed simply by the sign change in Γ_g. Figure 5.9 shows that, farther from this limit, the behavior of P for $B > 0$ differs qualitatively from that for $B < 0$: for $B > 0$ an inversion notch is observed, where $P \rightarrow 0$, even though $B\delta/A$ is not small, while no such notch is observed for $B < 0$. Though this feature occurs outside the regime of validity of Berry's asymptotic theory, its sensitivity to time-reversal and the fact that no such behavior occurs in the conventional Landau-Zener Hamiltonian (Equation 5.2) merit attention.

We first consider how the RF frequency depends on the sweep time $1/\delta$. As discussed above, the shape of the Hamiltonian curve of Figure 5.4 will be independent of sweep rate for fixed parameters A and B. However, the situation is quite different in the frame defined by the RF (Equation 5.20): Figure 5.5 indicates that

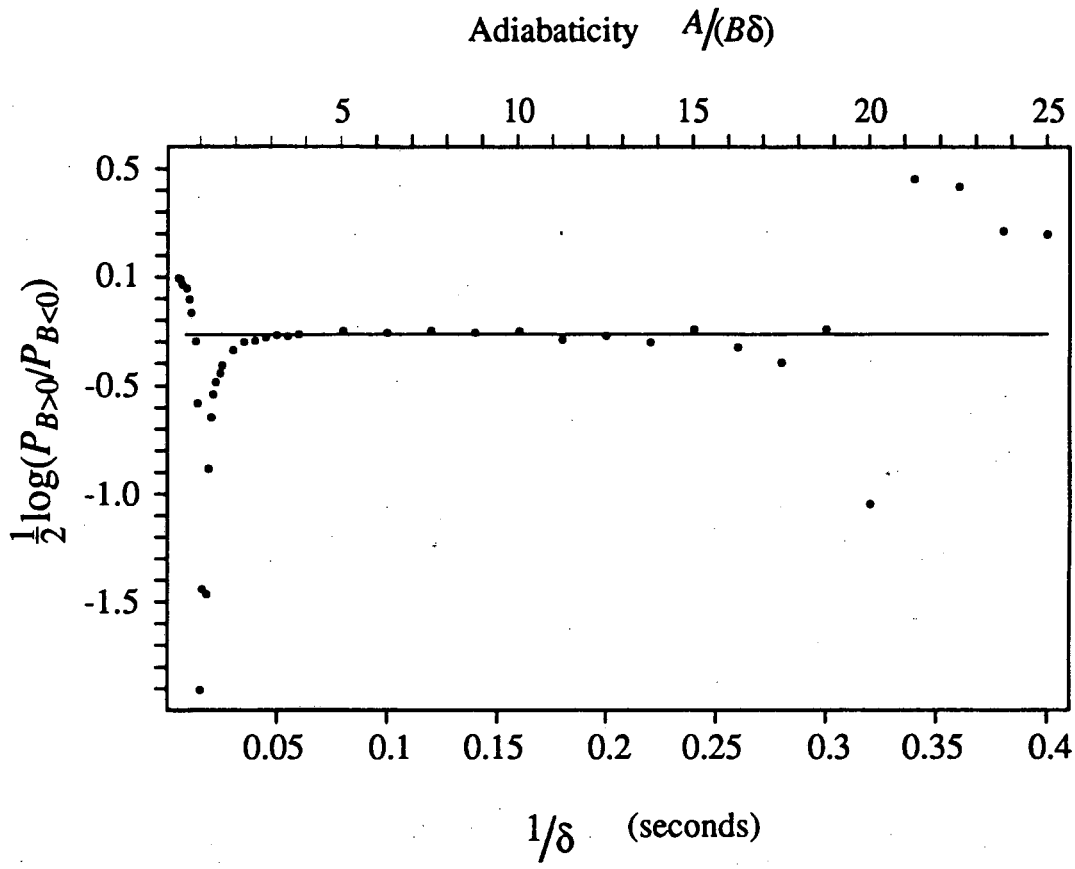

Figure 5.12: The data of Figure 5.9, plotted as $\frac{1}{2}\log(P_{B>0}/P_{B<0})$ versus $1/\delta$. Due to the behavior under time-reversal, Γ_g adds, while Γ_d cancels; the asymptotic theory thus predicts a line of slope zero and intercept Γ_g for this plot. The theory is confirmed, and the same three regions of Figure 5.10 can be identified.

the RF field sweeps through a total range of $2(A - B\delta)$ as it crosses the Larmor frequency. For $B > 0$, the range is swept from negative to positive offsets for small δ, and positive to negative for large δ; when $\delta = A/B$, the range is not swept at all. For $B < 0$, all sweeps are negative to positive. Physically, $\delta = A/B$ "sweeps" correspond to continuous resonant irradiation. This condition represents a pathological solution to the Landau-Zener problem, in that P becomes an oscillatory function of time at this point. Experimentally, this pathology is easy to avoid, because it is very narrow: the transition occurs while the resonance offset is in a range around zero of order ω_1. Thus the data of Figure 5.9 near the notch satisfy the condition that the initial and final resonance offsets are large on the scale of the transition itself, so for these points one may still think in terms of an inversion of the magnetization. The reason that the inversion becomes nearly perfect here, even though $A/(B\delta) \approx 1$, is that the rate of change of the sweeping field, compared to the effective field strength, is very small. Thus while ω_{eff} is in the transition region it changes slowly, and adiabatic behavior is observed.

It is also instructive to consider the origin of the notch in the frame of Equation 5.16, that is, the frame of Figure 5.4. In this frame, the curves corresponding to the two signs of B can be derived from each other by inversion through the origin, the main effect of which is to reverse their helicities. Thus for $B > 0$, the helicity is decreasingly positive as the crossing is approached, and increasingly negative afterwards, while the opposite holds for $B < 0$. As is well-known from conventional NMR theory, only one sense of circularly polarized irradiation can effect a transtion, that sense being defined relative to the sign of the applied static field [1, 159]. Therefore, we expect transitions when the sense and rate of helicity are

properly correlated with swept resonance offsets as defined by the detector frame. This immediately explains why the notch appears only for $B > 0$. Furthermore, the spin inversion to which the notch corresponds appears here as a rather intricate spin trajectory, quite unlike the smooth adiabatic inversion of the conventional Landau-Zener picture (Equation 5.20).

In the context of the helical Hamiltonian, the crossing point when $A/(B\delta) \approx 1$ is decidedly nonadiabatic. This is acceptable: the description of a transition as adiabatic is frame-dependent. We see that by viewing the Hamiltonian of Equation 5.16 as a simple Landau-Zener problem, by using the frame of Equation 5.20, we arrive at a simple picture of the inversion process, for which, however, the geometrical component of the transition probability comes out only after a complete analysis. In the original frame, the geometry is evident, but description of the transition itself becomes more difficult. Each frame has advantages, and of course the same result is obtained for P in either case.

5.5.3 Determination of ω_1

The results shown above provide a simple determination of the geometric component of the transition probability. We encountered one difficulty in making the measurements, which we now discuss in some detail. The various expressions for P, whether exact or asymptotic, are quite sensitive to ω_1, the RF field amplitude, as they depend exponentially on ω_1^2. The other parameters in these expressions, A and B, are offsets that are programmed into the digital synthesizer and hence are known. ω_1 must be measured independently, however. Such a measurement is typically accomplished by determining the length of time needed for a 360° pulse

on resonance, t_{360}, because $\omega_1 t_{360} = 2\pi$. Measuring the null generated by a 180° pulse would proivide an alternative method, but the 180° pulse is extremely sensitive to resonance offset. Since we needed to measure a relatively weak RF field ($\sim$ 400 Hz) relative to a broad line ($\sim$ 15 Hz FWHM), the inherent ability of the 360° pulse to compensate for offset effects favored this method for measuring the null. Furthermore, in the presence of radiation damping, the 180° "inversion" (unlike a 360° pulse) will yield an abnormally low value for the field strength. We found that our data could be fit precisely by the theory only when the value of ω_1 used in the formulas for P was adjusted to a lower value from the value given by $2\pi/t_{360}$, typically about 10% lower. This discrepancy does not seriously undermine our confidence in our test of the theory, however, primarily because of Figure 5.9. In this figure P is plotted for a wide range of δ, and should be fit by Equation 5.21. By using a non-linear least-squares fitting procedure with this formula, and ω_1 as the only adjustable parameter, very good agreement with the data is obtained. The goodness of fit suggests that ω_1 as obtained from t_{360} is slightly high, but that other features of the experiment work as expected, because the functional form for P agrees closely with the theory. We describe below several possible mechanisms that might account for this discrepancy in the value of ω_1.

One likely source of error is inhomogeneity in the magnetic fields. There are two possibilities: inhomogeneity in the static field and in the RF field. We rule out the former as a source of error, because experiments carried out with a range of shim settings, corresponding to resonance linewidths ranging from 2 Hz to 30 Hz, gave no change in the discrepancy in ω_1 values. This is not surprising, since in our experiments the initial and final resonance offsets (which are $\sim$ 50 kHz) are much

greater than this small spread in ω_0. Thus all spins in the system will be affected equally by the sweep, though possibly at slightly different times during the sweep.

We now turn to RF inhomogeneity. Our experiments were performed with a Chemagnetics broadband ^{1}H-,X-nucleus magic angle spinning (MAS) probe. Several features of this setup conspired to yield a rather nonuniform RF field profile. The size of the coil ($\sim$ 8 mm diameter, $\sim$ 2 cm length) was comparable to the size of the sample. Furthermore, the CS_2 did not fill the sample holder completely. Since the coil and sample vessel are inclined at an angle of 54.7°, we expect the non-uniform distribution of the CS_2 to exacerbate the effects of the inhomogeneity inherent in the coil design. The observable consequence of RF inhomogeneity is to give a distribution of ω_1 field strengths over the sample volume, rather than a single value. We were able to measure this distribution approximately, and average the theory with respect to it; this procedure does not significantly change the functional form predicted for P, and could account for 10–30% of the discrepancy in ω_1 values.

The RF homogeneity can be measured by applying a train of 90° pulses with windowed acquisitions during which the position of the magnetization is determined (*cf.* Figure 5.13). The short interpulse delay (.001 sec) prevents significant spin-spin relaxation. For a train of 256 pulses, the sole cause of signal decay is dephasing caused by the distribution of ω_1 field strengths, and a Fourier transform of the resultant echo train yields the profile of this distribution. Figure 5.14 shows the spread for our experimental setup, determined with sequence 5.13. By symmetrizing about the distribution peak, and fitting each so-generated data set with the sum of a Lorentzian and a Lorentzian-squared profile, a functional form for the field distribution can be generated. Then for each appearance of ω_1 in the transition

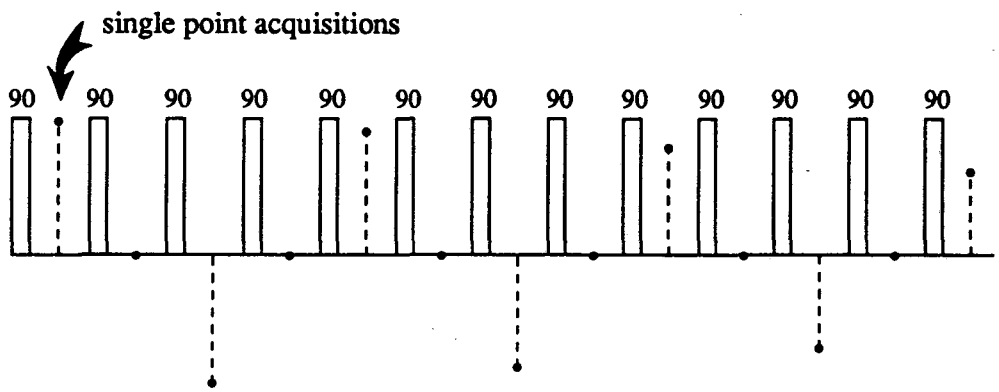

Figure 5.13: A train of 90° pulses can be interleaved with acquisitions of single data points. A Fourier transform of the resultant data set yields a distribution of ω_1 field strengths over the sample volume as a function of tip angle.

probability expression, an integation over the weighting function is performed. As mentioned earlier, this procedure reduces the ω_1 discrepancy by approximately 10-30%.

Radiation damping, that is, secondary effects due to the re-radiation of the RF field generated in the coil by the relaxing magnetization [1], is another possible source of error. This mechanism has already been considered in the context of ARP experiments [181, 182]. Numerical integration of the Bloch equations in the presence of a small (3 Hz) amount of radiation damping shows that the form of the graph of P is essentially unchanged, but is shifted to an effective value of ω_1 about 3% smaller than the nominal value. Thus the correction is in the same direction

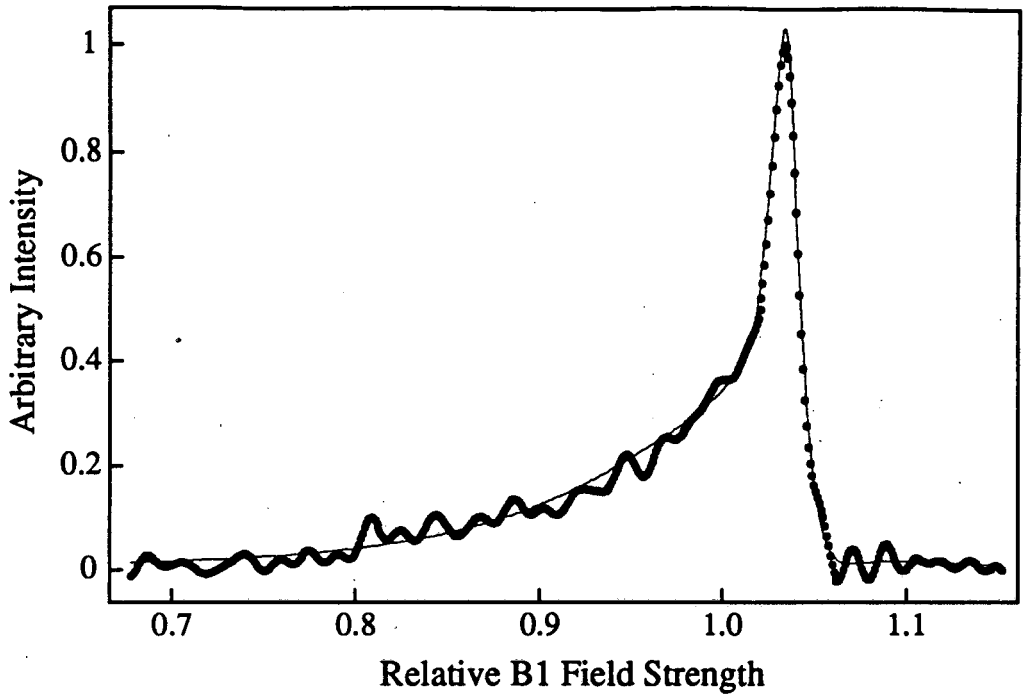

Figure 5.14: The experimental distribution of ω_1 field strengths over the sample volume.

as our observed discrepancy, but it is likely that the amount of radiation damping present in our system is substantially less than 3 Hz.

Other possible sources of error are the digital generation of the frequency sweeps, and changing probe response as a function of resonance offset. We were able to show experimentally and by simulation that the number of digitization steps we used (1792) was sufficiently large to leave the results unaffected, and that the relatively low probe Q of 230 yielded flat response within 2% over the frequency range used.

While we could not quantitatively account for the entire difference between the independent measurement of ω_1 and the fit to measured values of P, RF inhomogeneity seems the most likely mechanism to cause the observed discrepancy. This conjecture could be checked by performing a more quantitative independent measurement of the coil characteristics than we were able to, or possibly by using a very

small, symmetrically constructed sample container. As an aside, the sensitivity of this experiment to the value of ω_1 might provide a very precise way to calibrate small RF field strengths in other NMR measurements.

5.6 Conclusions

These studies provide the first experimental verification of the geometric transition probability recently described by Berry [162]. Various features of the theory were tested, including the independence of the geometric factor to the rate of change of the Hamiltonian; the theory is confirmed in all respects.

We anticipate that the geometric transition probability will prove to be an important consideration in a wide variety of experiments. Observing the probability is quite straight-forward—no complicated intereference experiments are necessary, nor are closed loops in parameter space needed, as they are in the case of Berry's phase, for unambiguous determination. In chemical physics, Landau-Zener treatments are frequently used in the study of scattering and dissociation processes; when fields or other mechanisms which break time-reversal symmetry are present, we expect that the geometric term will play a role.

A simple extension of this work is a modification of the experiment used to generate the data shown in Figure 5.7, to measure the population change as a function of τ *during* the sweep—a simple formula for this is derived in another recent paper by Berry [183].

At this point an important theoretical problem is to extend the treatment of Berry to the case of multiple avoided crossings. This has been considered for real Hamiltonians by Pechukas and co-workers [177, 178], and the difficulties increase

much faster than the number of avoided crossings (degeneracies in the complex time plane). The effect of multiple degeneracies is not simply additive. Such problems will also apply to the geometric case, but must be addressed in order to apply the theory to many realistic molecular systems. A general geometric framework for Γ_g, analogous to the type developed by Simon for Berry's phase [184], could be helpful here, but it is not clear to us how to develop one for open paths parameterized by complex time.

Chapter 6

Two-Channel Spectrometer

6.1 Introduction

This chapter describes the revision of a two-channel spectrometer, designated the Delta, whose original construction was described in the thesis of Drobny [185]. It is a proton/heteronucleus system based on a narrowbore (52mm) 360 MHz magnet, and was used for the liquid crystal experiments described in this thesis. Irradiation and detection are performed with a superheterodyne architecture, employing a 30 MHz intermediate frequency. A 392.12 MHz local oscillator for protons, and an 85.588 MHz LO for deuterons, mixed with the IF yield the radio frequencies of 362.12 MHz and 55.588 MHz for proton and deuterium irradiation, respectively. All phase shifting is performed at 30 MHz. The primary modification of the spectrometer comprises the implementation of a new pulse programmer (designed by Tecmag, Inc. [186]) based on a Digital Equipment Corporation *VAXStation II* minicomputer.

Section 6.2 presents the geometry and field specifications for the magnet. Figure 6.1 provides a schematic overview of the spectrometer electronics. The first three

sections of the chapter introduce the intermediate and radio frequency generation hardware, and the local oscillator generation. Section 6.6 gives a brief introduction to the sample probe used in the experiments, and Section 6.8 describes the receiver.

6.2 Superconducting Magnet

The superconducting magnet solenoid (Bruker SN BZH-01840070 [187]), originally housed in an Oxford Instruments dewar [188], has been redewared by Nalorac Cryogenics Corporation [189]. The new ultra-low loss dewar (Type: ULL/2.0V, SN V-117) has a helium hold time of 100 days, and a nitrogen hold time of 16 days. An American Magnetics, Inc. [190] platinum resistor level sensor coupled to a Model 110A level meter measures the helium level in the dewar.

The field center lies 59.4 cm below the top flange of the new dewar. Figure 6.2 shows a profile of the magnetic field along the $\hat{z}$ axis obtained by measuring the ^{1}H resonance frequency for a 25 μL sphere of water at various positions along the field axis. With only the superconducting shims, the field is homogeneous to within 7 parts per million over a 2 cm section at the field center.

6.3 Intermediate Frequency

The 30 MHz intermediate frequency (IF) is generated (in the frequency tripler chassis) by tripling the 10 MHz reference signal generated by the PTS 160 [191]. This scheme does not differ from that described in Figure 53 of Drobny's thesis [185]. Proton channel quadrature phase generation differs substantially from the earlier design. Two-dimensional NMR experiments, as well as most multiple-pulse solid

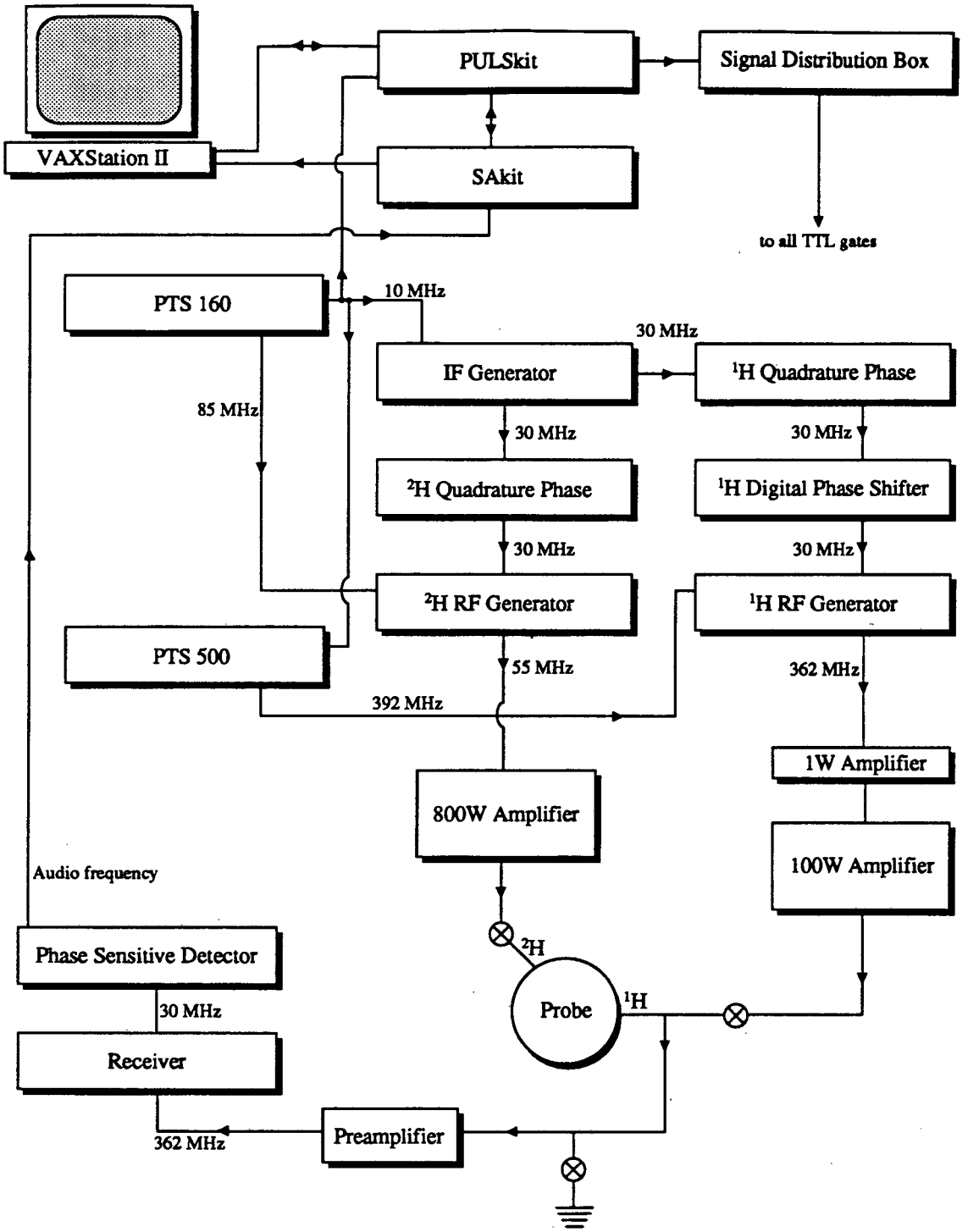

Figure 6.1: Schematic diagram of the Delta spectrometer.

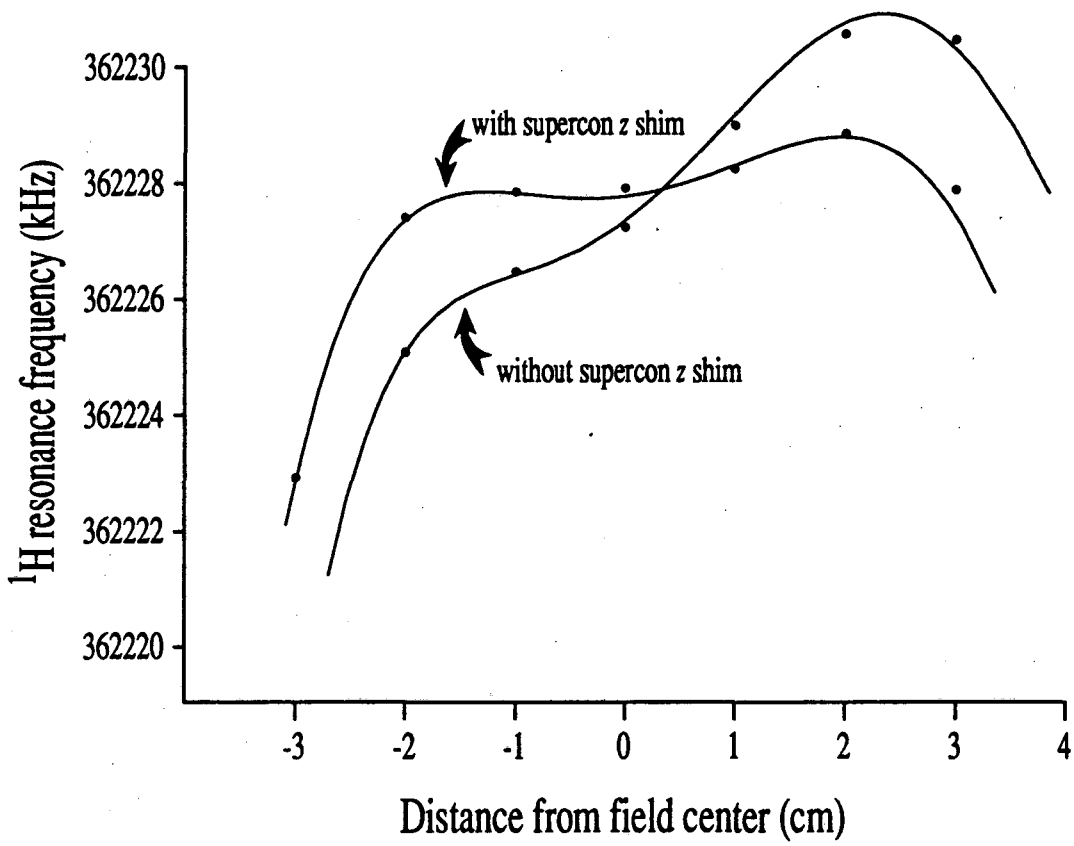

Figure 6.2: Plot of the magnetic field strength as a function of distance from the field center along the $\hat{z}$ axis.

state NMR experiments, rely on extremely stable RF electronics [192, 193, 87, 49]. A new quadrature phase generator, described earlier [194, 195], was added to provide accurate and stable quadrature phases for the proton channel. The deuterium decoupling necessary for the liquid crystal experiments does not depend on the RF phase, and therefore, no effort was undertaken to improve upon earlier designs. For phase-coherent double resonance experiments, this would certainly be a consideration.

Briefly, the proton quadrature phase generator employs extremely stable dc voltage references to bias the IF port of a double balanced mixer (DBM). This design, depicted schematically in Figure 6.3 allows accurate setting of phase and amplitude, and also provides for independent adjustment of the phase and amplitude. The 30 MHz input to the quad box is split into in-phase and quadrature components. These are then recombined in the output mixer, with coefficients determined by the reference voltages biasing the switching mixers. Phase incrementation in steps as small as 1.4° is performed with a digital phase shifter (built around a Daico phase shifter Model 100D0898) described previously [185].

6.4 Local Oscillator

The PTS 160 generates the local oscillator (LO) for the X channel (with an LO range of .1 - 160 MHz), with a deuterium LO of 85.59 MHz. For the proton channel, the PTS 500 provides a range of 1-500 MHz, with an LO of 392.1 MHz. For better stability, the proton LO is no longer generated by tripling a 130 MHz signal, as in the prior design [185]. The synthesizer outputs (approximately 1.2 V_{pp}) are routed to the RF generators, where they are mixed with the phase-shifted IF, in order to

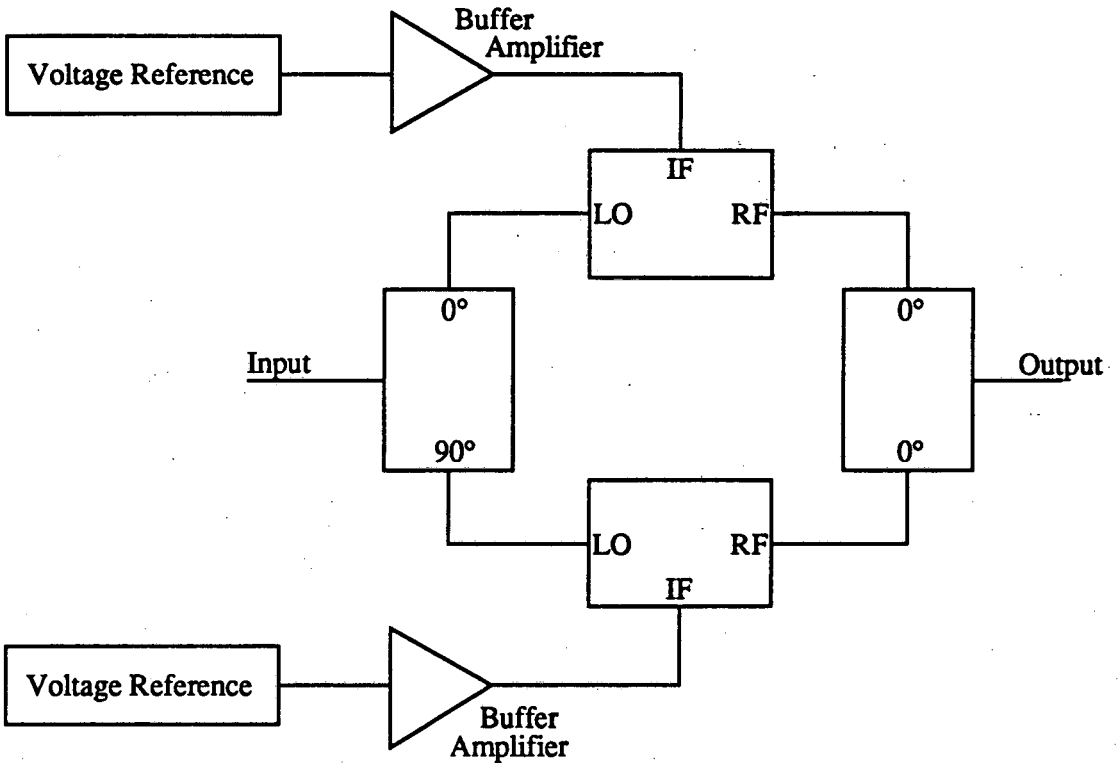

Figure 6.3: Schematic diagram of the quadrature phase generation box. For the x and $\overline{x}$ phases, the upper arm forms the in-phase component, and the lower arm provides the trim. For the y and $\overline{y}$ phases, the roles are reversed. There are a total of eight voltage references: four for the phases, and four for the amplitudes.

generate the RF Larmor frequency.

The PTS 500 can be frequency-switched to perform selective irradiation experiments, or difference spectroscopy. The digital interface encodes the frequency in a relatively inefficient binary coded decimal (BCD) representation. The PULSkit does not have a sufficiently wide microcontrol word to allow for arbitrary frequency encoding, but a hop between two frequencies, requiring only one bit, was facilitated by a digital board designed to connect to the rear of the PTS 500 via a 50-pin ribbon cable. Figure 6.4 provides the mask for the printed circuit board. Settings on eight-element DIP switches determine the synthesizer's alternate frequency.

6.5 Radiofrequency Generation

The phase-shifted 30 MHz intermediate frequency signal is filtered and mixed with the 392 MHz local oscillator in the rado frequency generator box. Figure 6.5 shows a block diagram schematic for the RF generator stage. The resultant sidebands at 362 and 422 MHz are filtered and amplified to yield the 362 MHz proton signal. A single pole two-throw gallium arsenide switch (Anzac SW-231) can switch the output through either a 64 dB attenuator, or through two serially connected Watkins-Johnson S11 RF switches. The attenuator output level can be adjusted (with a switching time of 6 milliseconds) either by front panel switches, or with TTL signal lines from the signal distribution box (*cf.* Figure 6.12) buffered by a pair of 74LS06 open-collector hex inverter buffer drivers

For optimum performance, the transmitter should have a very high on/off ratio (of at least 60 dB), to prevent amplifier leakage into the receiver during the acquisition period. The higher power RF channel has at least two RF switches in line

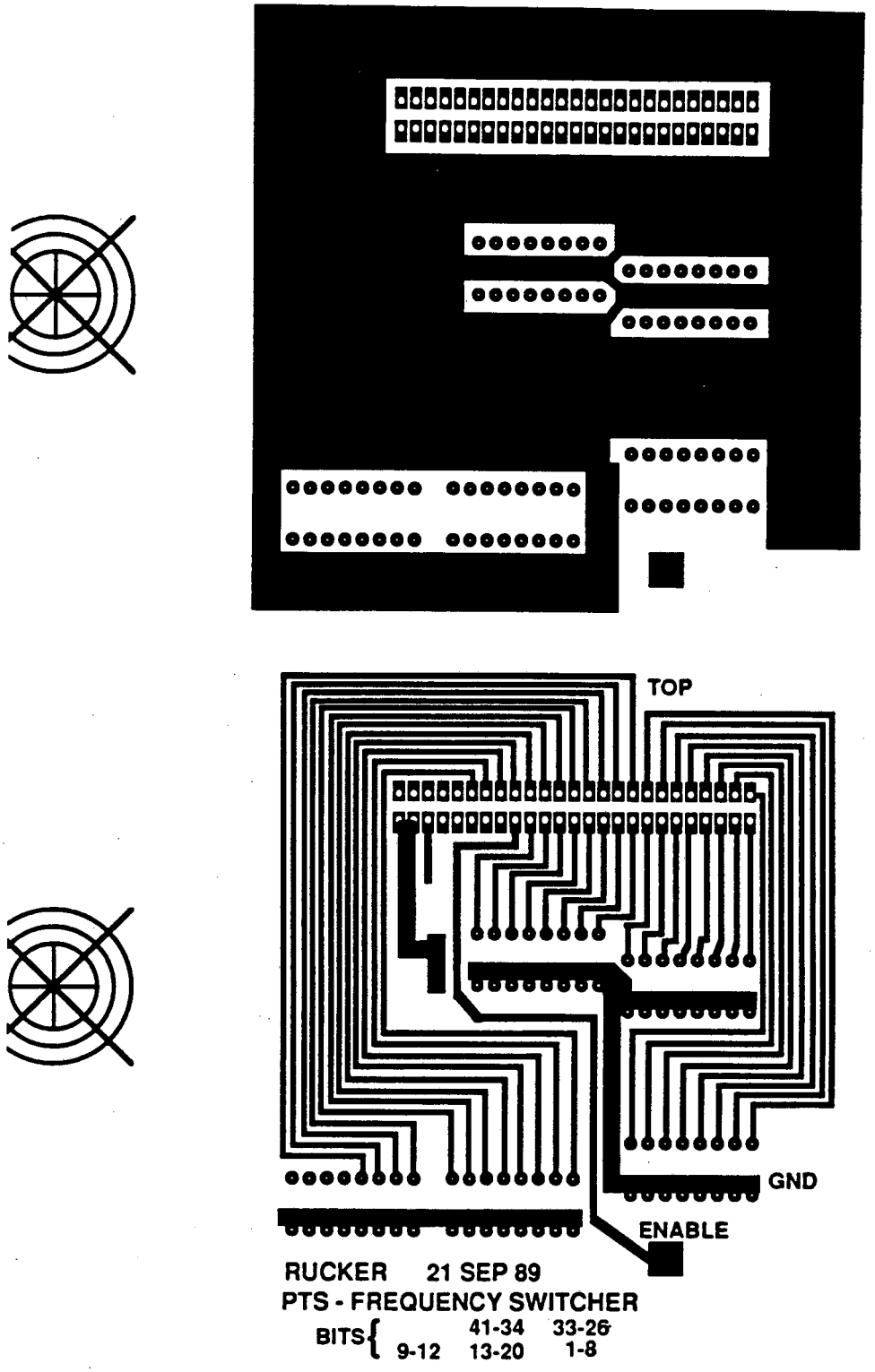

Figure 6.4: Printed circuit board mask (at 100%) for the PTS 500 frequency switching card.

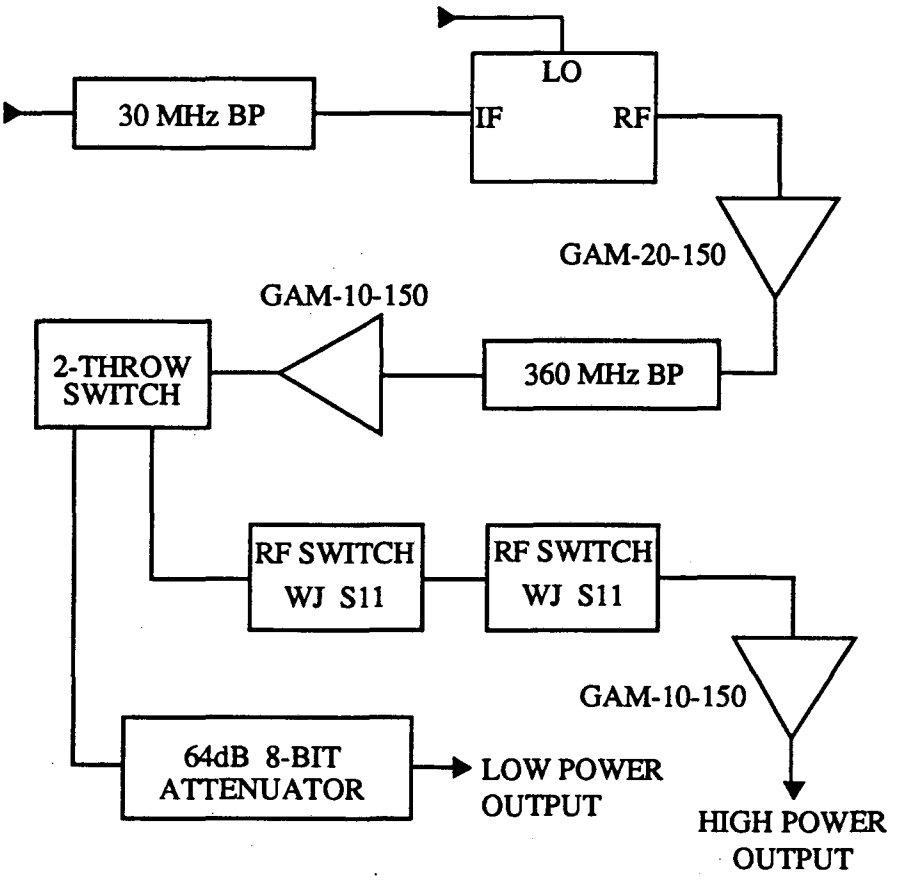

Figure 6.5: Schematic diagram for the radio frequency generator chassis.

to provide the necessary isolation. Furthermore, crossed microwave diodes lie in the signal path between the ENI 5100L-NMR high power amplifier and the probe, to block noise injection. Unfortunately, the junction capacitance of the diodes precludes absolute attenuation of the noise, and several sets of diodes are traditionally required, attenuating the high power pulse amplitudes. By tuning the junction capacitance with a small parallel inductance (three to four .3-inch turns of 18 gauge copper wire), the parasitic capacitance can be lowered sufficiently to necessitate only three sets of crossed diodes.

A critical feature in S/N improvement is the ability to blank the output of the ENI amplifier. A TTL gating pulse from AUX gate B2 (bit 7 of the microcontrol word) enables the dc supply voltage for the power amplifier modules within the ENI, and remains active during pulsing. Since the transition time for blanking requires 10 microseconds, it is switched during the receiver dead time, so that the output is blanked only during acquisition.

6.6 Sample Probe

The alkane/liquid crystal experiments suffer from a low concentration of protons. Therefore, the geometry of the RF probe must optimize detection of the available signal. To this end, a probe (designed by Cryomagnet Systems [196]) featuring an inverse detection scheme was used. The inverse probe has a proton detection coil coaxial with, and inside of, a broadband decoupling coil, in contrast to most broadband heteronuclear probes. The circuit diagram for the probe is shown in Figure 6.6.

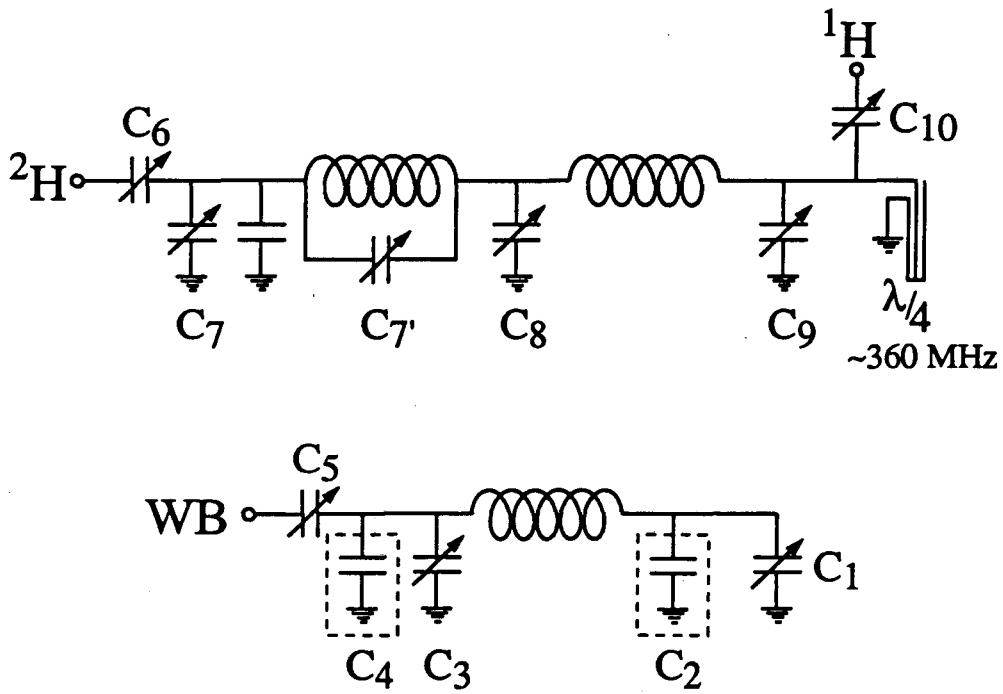

Figure 6.6: Circuit diagram for the inverse detection probe. Schematic (a) shows the proton and deuterium lock channels. C_6 through C_{10} are trimmable capacitors with a range of 0.4-6pF. C_6 and C_7 have a tuning range of 1-30pF. C_8 and C_9, the tuning capacitors for the proton channel should be adjusted in tandem. For the wideband decoupler channel, the tuning can be adjusted with C_1 and C_3, and two removable capacitors, C_2 and C_4 (51pF). With the capacitors in place the range is 54-64 MHz, and with them removed, the range covers 84-220 MHz.

6.7 Temperature Controller

In thermotropic liquid crystals, the phase behavior of the molecule is determined by temperature [57]. Often, the range over which a molecule or molecular mixture displays mesophasic behavior is extremely narrow. In studies of flexible alkanes in liquid crystalline solutions, an accurate measurement of the temperature is necessary to determine the conversion energy between different conformers. Therefore, stable and precise temperature control of the sample is critical to the reproducibility of nmr measurements in these solutions [197].

Stabilizing the sample temperature is hindered by fluctuations in room temperature, and by periodic deposition of radiofrequency power into the sample. Deuterium decoupling in our experiments irradiates the sample with 85 millisecond pulses of 50 watts of rf power. This section discusses the construction of a temperature controller designed to stabilize the sample temperature by directing compressed air (heated with a resistive coil) in a tube coaxial with the sample.

Figure 6.7 shows a schematic diagram for the controller. An Omega [198] CN9000 microprocessor-based temperature controller allows the user to set time constants for derivative and integral control of the set point temperature. This allows the IRF631 n-channel enhancement mode MOSFET to adjust the heater current with minimum response time and minimum overshoot. The supply current for the probe heater coil is provided from an external power supply capable of supplying at least 2 Amperes into a 3.5Ω load. The heater coil requires a maximum of approximately 12.5 Watts to heat the sample to 60°C with a compressed air pressure of 8 lbs.

A Copper-Constantan thermocouple located 1 cm below the probe measures

the temperature of the sample. The controller box is designed to accept input from either Copper-Constantan or Chromel-Alumel thermocouples. The CN9000 compares the measured temperature to the setpoint, and adjusts its output (the gate voltage for the IRF631) accordingly. A Newport digital panel voltmeter [199] measures the heater current (across a 1Ω sensing resistor, and displays the value on the front panel. This controller setup stabilizes the temperature to within a range of ±0.1°C, for the duration of the experiment (usually as long as two days), despite fluctuations in room temperature as large as ±7°C.

6.8 Receiver

To optimize the signal-to-noise, the receiver preamps reside in an aluminum chassis at the base of the magnet, minimizing the path length for the unamplified signal. Furthermore, noise immunity is improved by routing all analog signals through Belden 9310 coaxial cable (which has an aluminum foil-clad dielectric with 100% coverage). For the Delta, three BNC-selectable preamps, covered in Table 6.1, currently cover the spectrometer's bandwidth. In the receiver chassis, a Motorola MHW590-based cable television amplifier further boosts the signal before its down-conversion to the IF. Beyond this point, the analog signal processing remains that described in Sections 4.4 and 4.5 of Drobny's thesis.

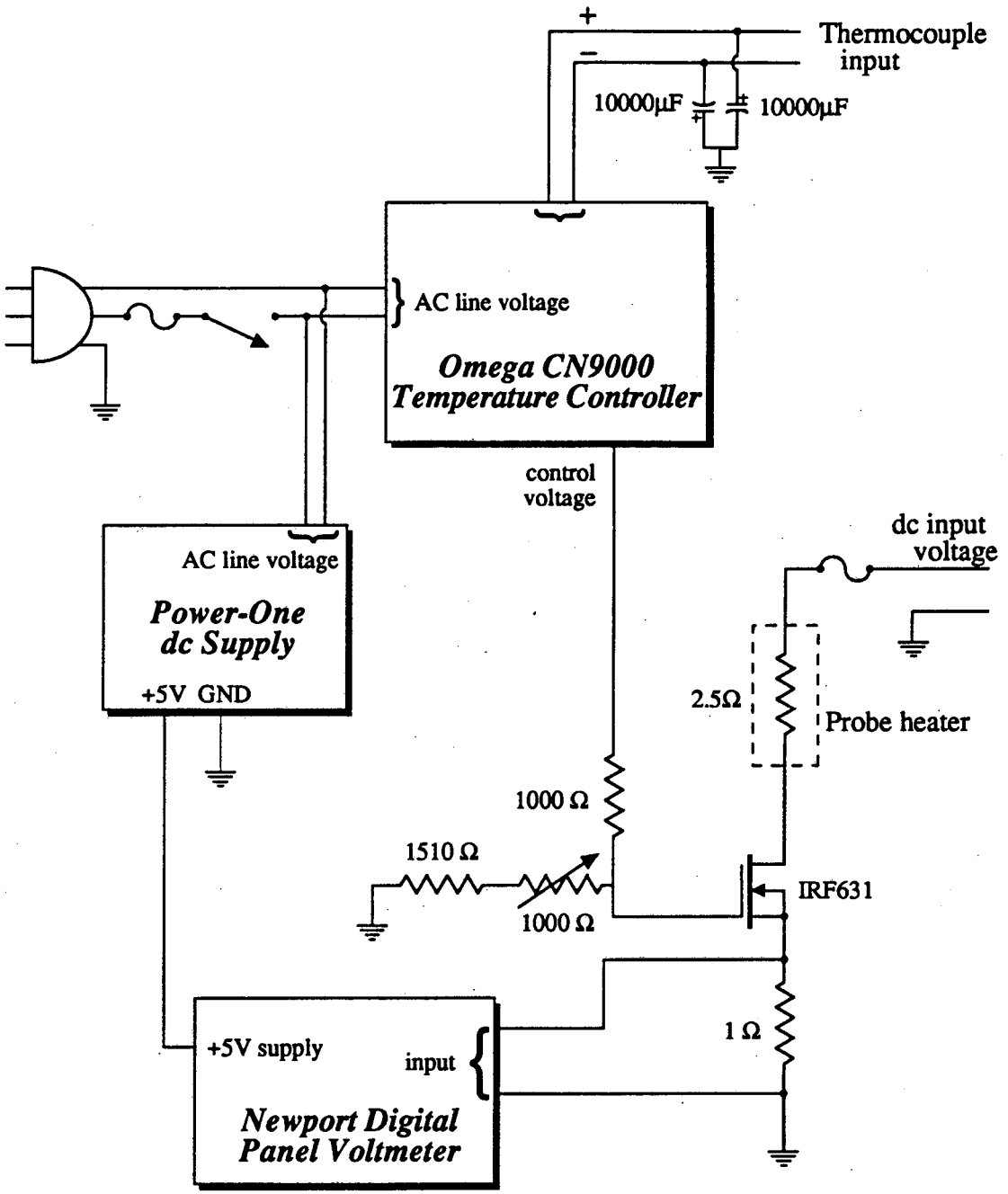

Figure 6.7: Schematic diagram of the Delta's temperature controller.

Table 6.1: Preamp specifications for the Delta spectrometer.

Model number	Bandwidth (MHz)	Gain (dB)	Noise figure (dB)
AMC-147	5–500	17	1.8(55), 2.4(362)
PB-CM	51–60	19.25	1.95
PK	344–380	17.35	1.13

6.9 Digital Section

6.9.1 Computer

A *VAXStation II* minicomputer controls the operation of the spectrometer. The system is configured with 16MB of RAM and 410MB of hard disk storage. A 95MB cartridge tape drive provides backup capability, and the system is linked by Ethernet (operating with the DECNET protocol) to several other computers in the laboratory.

Two MDB Systems [200] DR-11W parallel interface cards link the *VAXStation* to the pulse programmer and the signal averager. These cards provide a 16-bit parallel bus for loading microcode into the pulse programmer and uploading data from the signal averager. The data transfer rate for the cards is 100 kB/second.

6.9.2 Pulse Programmer

The pulse programmer, also known as the PULSkit (designed by Tecmag), is a 128-bit word generator based on an AMD 2910 instruction sequencer. Of these 128 lines, 76 are user-definable, with the remainder used for internal control functions. The pulse programmer operates with a clock speed of 10 MHz provided as an external reference by the PTS 160 synthesizer.

The memory provided in the PULSkit allows pulse programs up to 2048 lines long. With the PULSkit in LOAD mode, the pulse programs are downloaded in 8 16-bit sections, until each 128-bit word is complete. During execution, the microsequencer clocks out the 128 bits in parallel.

Figure 6.8 shows the assignments for the 128 bits in the microcontrol word. The time length for each event, in 100 nsec increments, is encoded in 2's complement notation, and requires bits 48-79 in the microcontrol word. Five loop counters, controlled by an AMD 9513 are available, with the loop counter selection defined by bits 112-116, and the loop branch address defined by bits 96-106. Bit 117 allows the pulse programmer execution to be triggered by an external TTL pulse. In this fashion, the PULSkit can be employed to generate an asynchronous decoupling sequence under the control of a master pulse programmer. The sequencer instruction (E - continue, 3 - conditional jump, 2 - unconditional jump) occupies bits 108-111.

The PULSkit controls the signal averager (SAkit) timing and coaddition through bits 80-95 of the microcontrol word. Bit 87, set true during the initial delay of each pulse sequence, resets the signal averager address to the first word in memory. In order to perform phase cycling, it is necessary to be able to swap buffers (bit 90), and change the sign of addition for each buffer (bits 91 and 92 for boards 1 and 2, respectively). Bit 93 triggers the ADC.

6.9.3 Software

The software operating environment comprises three separate programs, TECMAG.EXE located in the directory DUB0:[TECMAG], which controls real-time acquisition functions, and NMR1D.EXE and NMR2D.EXE in the subdirectory

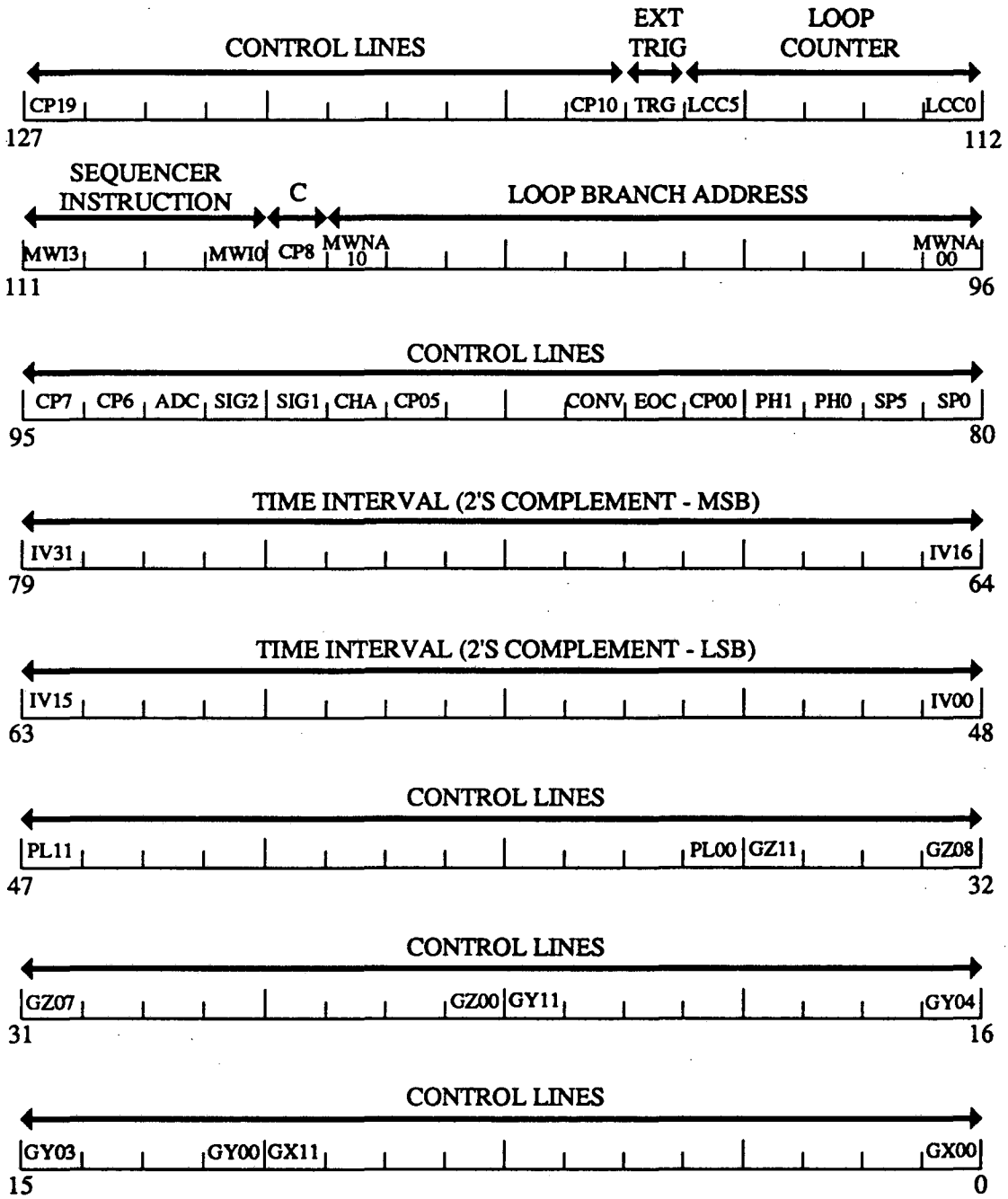

Figure 6.8: The microcontrol word bit assignments.

[TECMAG.DATA], which provide data processing and visualization facilities in separate windows on the display. For faster computation, the data can be transmitted by ethernet to a Stellar GS-1000 graphics workstation. On the *VAXStation*, two-dimensional Fourier transformation and processing are performed by the program 2DFT.EXE.

TECMAG, to be described in greater detail elsewhere [201], allows the user to load pulse program microcode into the pulse programmer (PULSkit), and dynamically change event times and acquisition parameters. The files of microcode follow the naming convention *.MIC, and reside in the subdirectory [TECMAG.MIC]. Appendix A lists several of the most common pulse programs used to perform the liquid crystal experiments. Each line in the program represents a timing event (such as an RF pulse, an evolution delay, or an acquisition dwell time) in the pulse sequence. The output states of the pulse programmer gates are defined by a 128-bit microcontrol word, with the bit assignments listed in Figure 6.8. For convenience, a hexadecimal digit represents each four-bit nibble in the microcontrol word.

The TECMAG program allows delay and pulse widths to be changed after the microcode is loaded into the PULSkit. To effect this, each timing event is given a two-digit alphanumeric mnemonic, listed to the right of the four-digit hexadecimal line number. P0..P9,PA..PZ denote rf pulses, and D0..D9,DA..DZ denote evolution delay periods. The mnemonics A and AL are codes used for the data acquisition lines, to be discussed later.

The mnemonics are followed by three columns of numbers defining RF phase tables for the proton and heteronucleus channels and for the receiver, respectively. These tables reside in the [TECMAG.PHASE] directory in files 1.PHASE,

2.PHASE, *etc.* Each table appears as a column of numbers 0,1,2,3 repersenting the four quadrature phases 0°, 90°, 180°, 270°. A fourth column can contain an optional character, I to increment the digital phase shifter, or R to reset it. A comment field begins ten spaces to the right of the phase shifter control digit.

Execution of a pulse program writes four files to the [TECMAG.DATA] directory: *.DATA containing data, *.ACQ and *END.ACQ storing a copy of the microcode and a list of the acquisition parameters, and *.PAR containing processing parameters for NMR1D and NMR2D. The data is written as a concatenation of the real data and the imaginary, each as four-byte integers. A sample *.ACQ file is shown here, with the acquisition parameters listed below the microcode, and four lines of loop counter information. Figure 6.9 explains the acquisition parameters, and lists some additional commands for loading and executing pulse programs.

```
0000 E000 0080 FC20 2DC0 0000 0000 0080      0000 D0
0000 E000 0000 FFFF FFD2 0001 0110 0091      0001 P1 1
0000 E000 0000 FFFF FE5F 0000 0000 0091      0002 D1
0000 E000 0000 FFFF FFA5 0001 0110 0091      0003 P2 1
0000 E000 0000 FFFF FE5F 0000 0000 0091      0004 D1
0000 E000 0000 FFFF FFD2 0001 0110 0091      0005 P1 1
0000 E000 0000 FFFF FFEC 0000 0000 0091      0006 D4
0000 E000 0000 FFFF FFA5 0001 0110 0091      0007 P2 2
0000 E000 0000 FFFF FFEC 0000 0000 0091      0008 D4
0000 E000 0000 FFFF FFD2 0001 0110 0091      0009 P1 2
0000 E000 0000 FFFF B9B0 0000 0000 0091      000A D6
0000 E000 0000 FFFF FFA5 0001 0110 0091      000B P2 2
0000 E000 0000 FFFF B9B0 0000 0400 0091      000C D6
0000 E000 2C00 FFFF FFFA 0000 0000 0031      000D A    3
0000 E000 0C00 FFFF FCC5 0000 0000 0031      000E AL   3
0000 E000 2C40 FFFF FFFE 0000 0000 0031      000F A    3
0000 E000 0C00 FFFF FFFE 0000 0000 0031      0010 A    3
0000 E000 0C20 FFFF FFFE 0000 0000 0031      0011 A    3
0002 300F 0C00 FFFF FCC5 0000 0000 0031      0012 AL   3
0000 E800 0000 FFFF FF9C 0000 0000 0000      0013 D3
0000 2000 0000 FFFF D8F0 0000 0200 0000      0014 D5
87E8 8301 8221 82A1 8309 823C 8200 8302
8221 82A2 830A 8200 8204 8303 8221 82A3
830B 82A0 8201 8304 8221 82A4 830C 8201
8200 8305 8221 82A5 830D 8201 8200 835F
NF =        416          SW =    12000.0
NA =         60          DW =       83.3
NB =       1024          AT =    85333.3
P1 =        4.6     P1 INC. =        0.0     PI1NA =    0     PI1NF =    0
```

```
P2 =        9.1     P2 INC. =       0.0     PI2NA =    0     PI2NF =    0
D0 =  6500000.0     D0 INC. =       0.0     DI0NA =    0     DI0NF =    0
D1 =       41.7     D1 INC. =      41.7     DI1NA =    0     DI1NF =    1
D3 =       10.0     D3 INC. =       0.0     DI3NA =    0     DI3NF =    0
D4 =        2.0     D4 INC. =     600.0     DI4NA =    4     DI4NF =    0
D5 =     1000.0     D5 INC. =       0.0     DI5NA =    0     DI5NF =    0
D6 =     1800.0     D6 INC. =       0.0     DI6NA =    0     DI6NF =    0
FSNA = 0    FSNF = 0    PSRNA = 0    PSRNF = 0    PSINA = 0    PSINF =    0
PH1 :  0  1  2  3
PH2 :  0
PH3 :  0  2
```

6.9.4 Signal Distribution Box

The output lines of the PULSkit are latched with 74LS244 high impedance line drivers. In order to interface these latches with the TTL gates throughout the spectrometer, and to provide noise immunity for the gating pulses, it is advantageous to buffer them with 50Ω line drivers, and distribute them through coaxial cable. To this end, a signal distribution box was constructed, which accepts 40-pin ribbon cable inputs from the PULSkit, buffers the signals with 74LS128 50Ω line drivers, and outputs them through a series of BNC connectors.

Each printed circuit board in the signal distribution box conditions 4 separate signal lines. Figure 6.10 shows the schematic for this circuit, and Figure 6.11 provides the mask (at 100%) for creating the printed circuit board.

An incoming pulse from the PULSkit is buffered and inverted twice. A solderable jumper selects either positive- (tap the second output) or negative-true (tap the first output) logic for the output pulse (which is routed to a BNC bulkhead connector at the rear of the chassis). A copy of the positive-true pulse triggers a dual retriggerable monostable (74LS123) with a 10 msec time constant. Its output, Q, and a copy of the original pulse are NOR'd to light a front panel LED for either the duration of the pulse, or 10 msec, whichever is longer. In this fashion, the progress of a pulse

AT	set acquisition time
D0..D9,DA..DZ	set delay time (microseconds)
DIx	set delay time increment
DW	set dwell time
FS	set when frequency shift bit (A7) is on
GO	start pulse program without zeroing SAkit memory
LC4,LC5	set loop counter
NA	set number of averages per t_1 experiment
NB	number of complex points to acquire
NF	number of t_1 experiments
PG	read in pulse program
P0..P9,PA..PZ	set RF pulse width (microseconds)
PI0..PI9,PIA..PIZ	set RF pulse width increment
PSI	set when digital phase shifter is to be incremented
PSR	set when digital phase shifter is to be reset
QU	quit TECMAG program
RP	read parameter file of an earlier experiment
ST	stop pulse program execution immediately
SW	set sweep width (in Hz)
UL	upload data from SAkit (during acquisition)
WL	type words to be loaded into loop counters
WM	type currently loaded pulse program
WPA	type currently loaded acquisition parameters
WPH	type currently loaded phase table
ZE	zero SAkit memory
ZG	zero SAkit memory and start pulse program

Figure 6.9: Commands for pulse program loading/execution for the PULSkit, and data acquisition with the SAkit.

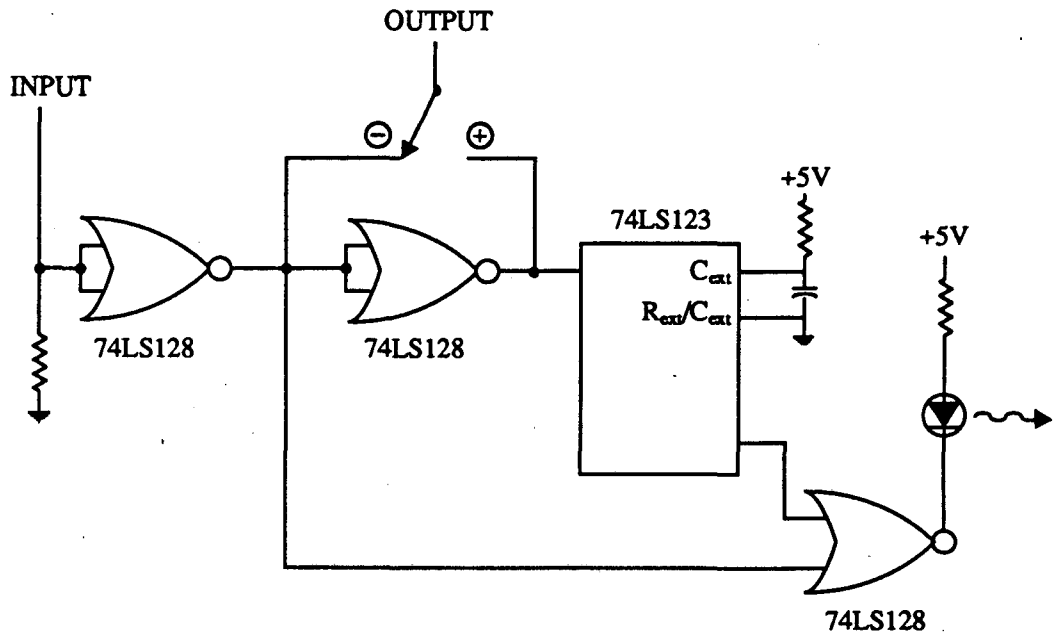

Figure 6.10: Functional schematic diagram for the signal distribution box buffer/LED circuit.

sequence can be tracked visually.

6.9.5 Signal Averager

The signal averager (SAkit), based on a pair of Analog Devices HAS-1201 analog-to-digital converters, simultaneously samples two channels with up to a 1 MHz sampling rate, and digitizes the signal with 12 bits of dynamic range. The PULSkit resides in the same chassis as the SAkit, and generates all the data acquisition pulses and triggers.

The PULSkit generates the "start conversion" (CONV) and "end conversion" (EOC) pulses which control sampling by the HAS-1201's. A 32-bit multiplexer, controlled by bit 90 of the microcontrol word, performs buffer swapping, and routes

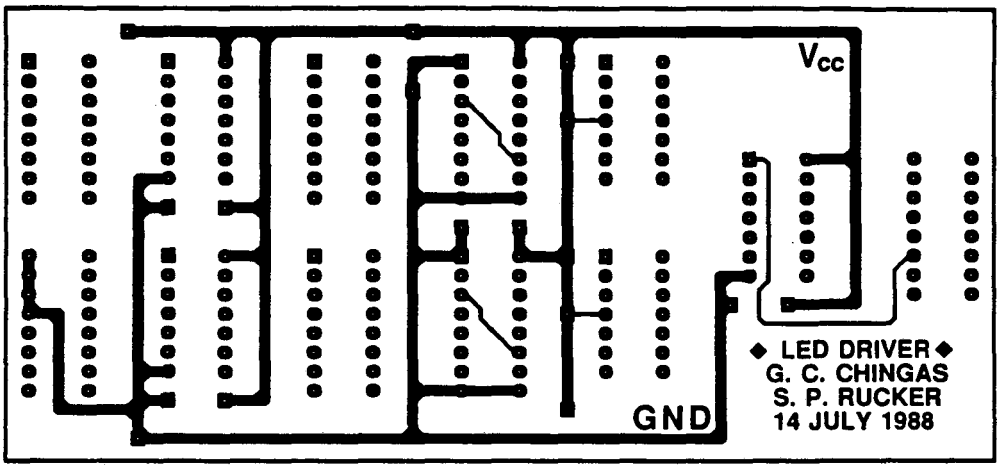

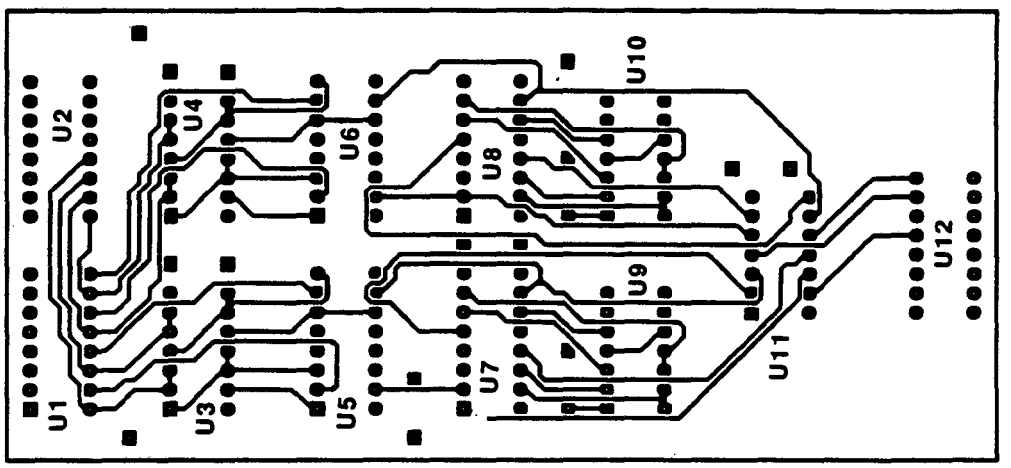

Figure 6.11: Printed circuit board mask (at 100% scale) for the signal distribution box buffer/LED circuit. U1 is the input/ouput connector for the TTL signals, and U12 connects to the front panel LEDs. U2 is a parallel resistor pack that ties each input to ground with a 330Ω resistor. U3, U4, and U11 are the 74LS128 inverting NOR chips, and U7 and U8 the 74LS123 monostables. U9 and U10 hold header packs containing the timing elements for the monostables. Solderable jumpers on headers in sockets in U5 and U6 allow selection of positive- or negative-true logic for the board output.

	Bit Number	Code	Function	
CONNECTOR J11	GZ10	A10		
	GZ09	A9		
	GZ08	A8	RF switch #2	
	GZ07	A7	PTS-500 local/remote frequency toggle	
	GZ06	A6	Toggle	digital phase shifter
	GZ05	A5	Reset	
	GZ04	A4	Increment	
	GZ03	A3	Aux gate A3	
	GZ02	A2	Aux gate A2	
	GZ01	A1	Aux gate A1	
	GZ00	ARF	RF switch #1	
	GY11	AY	$\overline{Y}$	A-channel quad gates
	GY10	AX	$\overline{X}$	
	GY09	AY	Y	
	GY08	AX	X	
CONNECTOR J10	GY07			
	GY06			
	GY05			
	GY04			
	GY03			
	GY02	B9	64 dB	A-channel attenuator
	GY01	B8	32 dB	
	GY00	B7	16 dB	
	GX11	B6	8 dB	
	GX10	B5	4 dB	
	GX09	B4	2 dB	
	GX08	B3	1 dB	
	GX07	B2	Aux gate B2 - ENI deblanking	
	GX06	B1	Aux gate B1	
	GX05	BRB	Receiver deblanking	
	GX04	BRF	RF switch	
	GX03	BY	$\overline{Y}$	B-channel quad gates
	GX02	BX	$\overline{X}$	
	GX01	BY	Y	
	GX00	BX	X	

Figure 6.12: Assignment of bits in the microcontrol word to distribution box gates.

the signal to two 32-bit adder/subtracters (controlled by bits 91 and 92) which determine the sign for coaddition of the scan with data already resident in memory. The digital boards in the SAkit allow collection of up to 128K words of 32-bit data for the real and imaginary buffers. Under computer control, the data is uploaded in 16-bit increments after the completion of each t_1 experiment.

Appendix A

Pulse Programs

The pulse programmer (PULSkit) outputs a 128-bit microcontrol word of which 76 bits are user-definable, with the bit assignments listed in Figures 6.8 and 6.12. It is convenient to represent the microcode with each four-bit nibble represented by a hexadecimal digit. This appendix lists the microcode in this fashion for several of the most common sequences used to acquire the data presented in Chapter 2, and also to tune up the spectrometer.

A.1 Pulse-acquire

The simplest experiment, pulse-acquire, is performed with the following sequence (H_ACQ_D.MIC):

```
0000 E000 0080 FFFF FFFB 0000 0200 0080      0000 D1                PPG3
0000 E000 0000 FFFF FFFB 0001 0310 0091      0001 P1 1
0000 E000 0000 FFFF FFFB 0000 0200 0011      0002 D2
0000 E000 2C00 FFFF FFFA 0000 0400 0031      0003 A    3
0000 E000 0C00 FFFF FFFC 0000 0000 0031      0004 AL   3
0000 E000 2C40 FFFF FFFE 0000 0000 0031      0005 A    3
0000 E000 0C00 FFFF FFFE 0000 0000 0031      0006 A    3
0000 E000 0C20 FFFF FFFE 0000 0000 0031      0007 A    3
0002 3005 0C00 FFFF FFFC 0000 0000 0031      0008 AL   3
0000 E800 0000 FFFF FFFB 0000 0000 0031      0009 D3             Rep Delay
0000 2000 0000 FFFF FFFB 0000 0200 0000      000A D5             Idle
```

As with all the pulse programs executed with the PULSkit, the first line in the pulse program must have a duration of at least 0.01 seconds to avoid a fatal controller error.

The ENI 5100L-NMR power amplifier has a TTL-gated deblanking option, whereby the dc voltage to the amplifier modules can be switched off. The transition time for this deblanking is 10 microseconds – too long to shut off the amplifier between pulses, but short enough to permit amplifier blanking during the detection period. In this fashion, we can reduce noise injection into the receiver. Bit 7 of the microcontrol word enables the ENI output (positive-true logic)and is switched off during the dead time, D2. Bits 0 and 4 are active during pulsing and acquisition in order to decouple deuterium.

Lines 0003-0004 provide the timing for the data acquistion. Figure A.1 shows the sequences for these pulses. The ADC command in line 0003 digitizes the first point, and line 0004 defines the dwell time delay. Line 0005 digitizes the second point, while adding the prior point with the first datum in memory. After a 200 nsec settling period, that sum is written back to memory by line 0007. Line 0008 provides the remainder of the dwell period, and loops back to line 0005 for the remainder of the acquisition.

To measure the ninety degree pulse width for a given field strength, the pulse-acquire sequence can be run as a two-dimensional experiment. In the acquisition parameter list, DI1 can be set to increment by a fixed amount after each t_1 experiment.

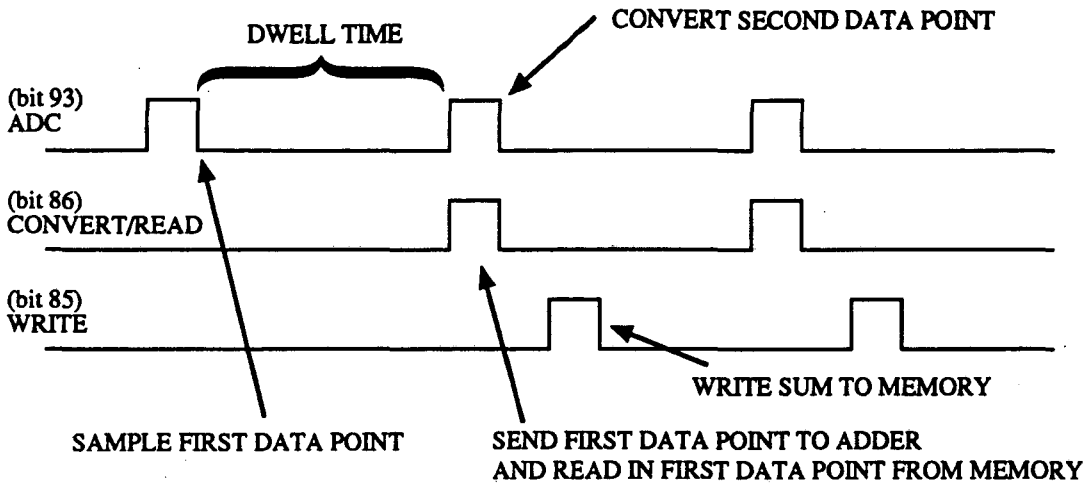

Figure A.1: Timing diagram for data acquisition with the SAkit. All pulses are generated by the PULSkit.

A.2 Hahn Echo

The Hahn echo pulse sequence (HAHNECHO_D.MIC):

```
0000 E000 0080 FFFF FFFB 0000 0000 0080      0000 D1                PPG3
0000 E000 0000 FFFF FFFB 0001 0110 0091      0001 P1 1
0000 E000 0000 FFFF FFFB 0000 0000 0091      0002 D2
0000 E000 0000 FFFF FFFB 0001 0110 0091      0003 P2 2
0000 E000 0000 FFFF FFFB 0000 0400 0011      0004 D4
0000 E000 2000 FFFF FFFA 0000 0000 0031      0005 A    3
0000 E000 0000 FFFF FFFC 0000 0000 0031      0006 AL   3
0000 E000 2040 FFFF FFFE 0000 0000 0031      0007 A    3
0000 E000 0000 FFFF FFFE 0000 0000 0031      0008 A    3
0000 E000 0020 FFFF FFFE 0000 0000 0031      0009 A    3
0002 3007 0000 FFFF FFFC 0000 0000 0031      000A AL   3
0000 E800 0000 FFFF FFFB 0000 0000 0000      000B D3                Rep Delay
0000 2000 0000 FFFF FFFB 0000 0200 0000      000C D5                Idle
```

bears an obvious similarity to the simpler pulse-acquire sequence. The delay periods, D2 and D4 are independently settable to allow for acquisition for the entire echo. Independent phase tables, declared after the event mnemonic, govern each pulse, to allow for either a 90_x - 180_x or 90_x - 90_y echo. Note that the ENI amplifier remains enabled through the 90 - τ - 90 period, while decoupling is active during the entire pulsing and acquisition period. This sequence can be modified

to yield a two-dimensional sequence for inversion-recovery or saturation-recovery experiments by setting the DI2 parameter in TECMAG.EXE to increment D2 after each t_1 experiment.

A.3 2-Quantum Filter

The two-quantum filter described in Figure 2.7 is effected with the following microcode (2QT_D.MIC):

```
0000 E000 0080 FFFF FFFB 0000 0000 0080      0000 D0                PPG3
0000 E000 0000 FFFF FFFB 0001 0110 0091      0001 P1 1
0000 E000 0000 FFFF FFFB 0000 0000 0091      0002 D1
0000 E000 0000 FFFF FFFB 0001 0110 0091      0003 P2 1
0000 E000 0000 FFFF FFFB 0000 0000 0091      0004 D1
0000 E000 0000 FFFF FFFB 0001 0110 0091      0005 P1 1
0000 E000 0000 FFFF FFFB 0000 0000 0091      0006 D4
0000 E000 0000 FFFF FFFB 0001 0110 0091      0007 P2 2
0000 E000 0000 FFFF FFFB 0000 0000 0091      0008 D4
0000 E000 0000 FFFF FFFB 0001 0110 0091      0009 P1 2
0000 E000 0000 FFFF FFFB 0000 0000 0091      000A D6
0000 E000 0000 FFFF FFFB 0001 0110 0091      000B P2 2
0000 E000 0000 FFFF FFFB 0000 0400 0091      000C D6
0000 E000 2000 FFFF FFFA 0000 0000 0031      000D A    3
0000 E000 0000 FFFF FFFC 0000 0000 0031      000E AL   3
0000 E000 2040 FFFF FFFE 0000 0000 0031      000F A    3
0000 E000 0000 FFFF FFFE 0000 0000 0031      0010 A    3
0000 E000 0020 FFFF FFFE 0000 0000 0031      0011 A    3
0002 300F 0000 FFFF FFFC 0000 0000 0031      0012 AL   3
0000 E800 0000 FFFF FFFB 0000 0000 0000      0013 D3                Rep Delay
0000 2000 0000 FFFF FFFB 0000 0200 0000      0014 D5                Idle
```

The initial $\frac{\pi}{2} - \pi - \frac{\pi}{2}$ and second $\pi - \frac{\pi}{2} - \pi$ sections have the independently settable phases needed to generate the two-quantum filter. The ENI remains enabled during pulsing, and decoupling occurs for all times exclusive of the reccycle delay, D3 + D0.

A.4 Multiple-Quantum NMR

The multiple-quantum excitation sequence, MQT_D.MIC:

```
0000 E000 0000 FFFF FFFB 0000 0000 0000      0000 DA    I          PPG3
0000 E000 0080 FFFF FFFB 0000 2000 0080      0001 D0    R          PPG3
0000 E000 0000 FFFF FFFB 0001 0110 0091      0002 P1 1             90
0000 E000 0000 FFFF FFFB 0000 0000 0091      0003 D4
0000 E000 0000 FFFF FFFB 0001 0110 0091      0004 P2 1             180
0000 E000 0000 FFFF FFFB 0000 0000 0091      0005 D4
0000 E000 0000 FFFF FFFB 0001 0110 0091      0006 P1 1             90
0000 E000 0000 FFFF FFFB 0000 4000 0091      0007 D1
0000 E000 0000 FFFF FFFB 0001 0110 0091      0008 P2 2             180
0000 E000 0000 FFFF FFFB 0000 0000 0091      0009 D1
0000 E000 0000 FFFF FFFB 0001 0110 0091      000A P1 1             90
0000 E000 0000 FFFF FFFB 0000 0000 0091      000B D6
0000 E000 0000 FFFF FFFB 0001 0110 0091      000C P2 1             180
0000 E000 0000 FFFF FFFB 0000 4400 0011      000D D6
0000 E000 2000 FFFF FFFA 0000 0000 0031      000E A     3          Point 1
0000 E000 0000 FFFF FFFC 0000 0000 0031      000F AL    3
0000 E000 2040 FFFF FFFE 0000 0000 0031      0010 A     3          Points 2..N
0000 E000 0000 FFFF FFFE 0000 0000 0031      0011 A     3
0000 E000 0020 FFFF FFFE 0000 0000 0031      0012 A     3
0002 300F 0000 FFFF FFFC 0000 0000 0031      0013 AL    3
0000 E800 0000 FFFF FFFB 0000 0000 0000      0014 D3               Rep Delay
0000 2015 0000 FFFF FFFB 0000 0200 0000      0015 D5               Idle
```

differs from the two-quantum sequence in that the phase shifts of the constituent pulses are no longer necessarily quadrature multiples. The phases for the first three pulses of the sequence shown in Figure 2.8 are incremented in steps of ϕ by the digital phase shifter. The toggle bit (30) allows the second $\pi - \frac{\pi}{2} - \pi$ sequence to be applied with the unincremented quadrature phase.

After each t_1 experiment (for time-proportional phase incrementation [50]) the phase shifter can be controlled during the delay, DA. Incrementation is controlled by the PSINA and PSINF parameters. Also, the phase shifter can be reset to its starting phase (bit 29 high during the delay, D0) as dictated by PSRNA and PSRNF. The I and R mnemonics tag their respective lines of code to alert the TECMAG program to set those optional bits true when the increment or reset counter condition is satisfied.

A.5 Quadrature Phase Test

The quadrature phases can be adjusted for amplitude and phase with the QBOX-TEST.MIC sequence:

```
0000 E000 0080 FFFF FF9C 0000 0800 0080 0     0000 D1
0000 E000 0000 FFFF FF9C 0000 0000 0000 0     0001 P5
0000 E000 0000 FFFF FF9C 0001 0510 0091 0     0002 P1
0000 E000 0000 FFFF FF38 0000 0000 0000 0     0003 P5
0000 E000 0000 FFFF FF9C 0001 0120 0092 0     0004 P2
0000 E000 0000 FFFF FF38 0000 0000 0000 0     0005 P5
0000 E000 0000 FFFF FF9C 0001 0140 0094 0     0006 P3
0000 E000 0000 FFFF FF38 0000 0000 0000 0     0007 P5
0000 E000 0000 FFFF FF9C 0001 0180 0098 0     0008 P4
0000 E800 0000 FFFF FF9C 0000 0000 0000 0     0009 P4
0000 2000 0000 FFF0 BDC0 0000 0000 0000 0     000A D5
```

Customarily, the sequence is run with different pulse lengths (1 – 4 msec) for each RF pulse, so that the output levels and switching times can be monitored easily on an oscilloscope. For longer times (on the order of seconds or minutes), the quadrature phase and amplitude can be adjusted with a vector voltmeter.

Bibliography

[1] A. Abragam, *Principles of Nuclear Magnetism* (Oxford University Press, Oxford, 1962).

[2] M. Gochin. *Two-Dimensional NMR of Liquids and Oriented Molecules.* PhD thesis, University of California, Berkeley, 1987.

[3] A. Carrington and A. D. McLachlan, *Introduction to Magnetic Resonance* (Harper & Row, New York, 1967).

[4] W. P. Aue, E. Bartholdi, and R. R. Ernst, *J. Chem. Phys.* **64**, 2229–2246 (1976).

[5] O. W. Sørensen, G. W. Eich, M. H. Levitt, G. Bodenhausen, and R. R. Ernst, *Prog. NMR Spectrosc.* **16**, 163–192 (1983).

[6] A. J. Shaka and R. Freeman, *J. Magn. Reson.* **59**, 169 (1984).

[7] U. Piatini, O. W. Sørensen, and R. R. Ernst, *J. Am. Chem. Soc.* **104**, 6800 (1982).

[8] K. Moriyasu, *An Elementary Primer on Gauge Theory* (World Scientific, Singapore, 1983).

[9] A. Messiah, *Quantum Mechanics* (Wiley, New York, 1958).

[10] M. V. Berry, *Proc. R. Soc. London A* **392**, 45–57 (1984).

[11] A. Shapere and F. Wilczek, *Geometric Phases in Physics* (World Scientific, Singapore, 1989).

[12] M. V. Berry, *Physics Today* **43**, 34–40 (1990).

[13] M. V. Berry, *Scientific American* pages 46–52 (1988).

[14] A. Tomita and R. Chiao, *Phys. Rev. Lett.* **57**, 937–940 (1986).

[15] M. V. Berry, *Nature* **326**, 277–278 (1987).

[16] D. Suter, G. C. Chingas, R. A. Harris, and A. Pines, *Mol. Phys.* **61**, 1327–1340 (1987).

[17] D. Suter, K. T. Mueller, and A. Pines, *Phys. Rev. Lett.* **60**, 1218–1220 (1988).

[18] R. Tycko, *Phys. Rev. Lett.* **58**, 2281–2284 (1987).

[19] A. Zee, *Phys. Rev. A* **38**, 1–6 (1988).

[20] C. A. Mead, *Phys. Rev. Lett.* **59**, 161–164 (1987).

[21] B. Zygelman, *Phys. Lett. A* **125**, 476–481 (1987).

[22] G. Delacrétaz, E. R. Grant, R. L. Whetten, L. Wöste, and J. W. Zwanziger, *Phys. Rev. Lett.* **56**, 2598–2601 (1986).

[23] J. H. Hannay, *J. Phys. A* **18**, 221–230 (1985).

[24] M. V. Berry, *J. Phys. A* **18**, 15–27 (1985).

[25] A. Shapere and F. Wilczek, *J. Fluid Mech.* **198**, 557–585 (1989).

[26] J. W. Zwanziger, M. Koenig, and A. Pines, *Ann. Rev. Phys. Chem.* **41**, 601 (1990).

[27] N. Rosen and C. Zener, *Phys. Rev.* **40**, 502 (1932).

[28] C. Zener, *Proc. R. Soc. London* **137**, 696 (1932).

[29] A. Saupe and G. Englert, *Phys. Rev. Lett.* **11**, 462 (1963).

[30] P. Diehl and C. L. Ketrapal, *NMR - Basic Principles and Progress* **1**, 1 (1969).

[31] J. W. Emsley and J. C. Lindon, *NMR Spectroscopy using Liquid Crystal Solvents* (Pergamon Press, Oxford, 1975).

[32] C. L. Ketrapal and A. C. Kunwar, *Adv. in Liquid Cryst.* **6**, 173 (1983).

[33] ed. J. W. Emsley, *Nuclear Magnetic Resonance of Liquid Crystals* (Reidel Publishing Company, Dordrecht, 1985).

[34] P. Diehl and J. Jokisaari, in *NMR in Stereochemical Analysis*, volume 6 (VCH Publisher, Inc., New York, 1986). Y. Takeuchi and A. P. Marchand, eds.

[35] C. L. Ketrapal, B. S. Kumar, and S. Raghothama, in *Nuclear Magnetic Resonance*, volume 17 (The Royal Society of Chemistry, London, 1988).

[36] A. Khan, in *Nuclear Magnetic Resonance*, volume 18 (The Royal Society of Chemistry, London, 1989).

[37] R. C. Hewitt, S. Meiboom, and L. C. Snyder, *J. Chem. Phys.* **58**, 5089 (1973).

[38] Z. Luz and S. Meiboom, *J. Chem. Phys.* **59**, 1077 (1973).

[39] S. Meiboom, R. C. Hewitt, and Z. Luz, *J. Chem. Phys.* **66**, 4041 (1977).

[40] M. Gochin, K. V. Schenker, H. Zimmermann, and A. Pines, *J. Am. Chem. Soc.* **108**, 6813 (1986).

[41] M. Gochin, D. Hugi-Cleary, H. Zimmermann, and A. Pines, *Mol. Phys.* **60**, 205 (1987).

[42] M. Gochin, H. Zimmermann, and A. Pines, *Chem. Phys. Lett.* **137**, 51 (1987).

[43] B. Janik, E. T. Samulski, and H. Toriumi, *J. Phys. Chem.* **91**, 1842 (1987).

[44] A. J. van der Est, M. Y. Kok, and E. E. Burnell, *Mol. Phys.* **60**, 397 (1987).

[45] G. L. Hoatson, A. L. Bailey, A. J. van der Est, G. S. Bates, and E. E. Burnell, *Liquid Cryst.* **3**, 683 (1988).

[46] K. Balasubramanian, *Theoret. Chim. Acta, (Berlin)* **51**, 37 (1979).

[47] K. Balasubramanian, *J. Chem. Phys.* **73**, 3321 (1980).

[48] O. W. Sørensen, M. H. Levitt, and R. R. Ernst, *J. Magn. Reson.* **55**, 104 (1983).

[49] R. Ernst, G. Bodenhausen, and A. Wokaun, *Principles of Magnetic Resonance in One and Two Dimensions* (Oxford University Press, Oxford, 1990).

[50] D. P. Weitekamp, *Adv. Mag. Reson.* **11**, 111 (1983).

[51] G. Drobny, D. P. Weitekamp, and A. Pines, *Chem. Phys.* **108**, 179 (1986).

[52] E. Diez, J. Santoro, and A. L. Esteban, *J. Magn. Reson.* **46**, 440 (1982).

[53] A. Pines, S. Vega, and M. Mehring, *Phys. Rev. B* **18**, 112 (1978).

[54] G. Drobny, A. Pines, S. Sinton, D. P. Weitekamp, and D. E. Wemmer, *Faraday Division of the Chemical Society Symposium* **13**, 49 (1979).

[55] G. Bodenhausen, R. L. Vold, and R. R. Vold, *J. Magn. Reson.* **37**, 93 (1980).

[56] M. Gochin, A. Pines, M. E. Rosen, S. P. Rucker, and C. Schmidt, *Mol. Phys.* **69**, 671–695 (1990).

[57] P. G. de Gennes, *The Physics of Liquid Crystals* (Clarendon Press, Oxford, 1974).

[58] W. Maier and A. Saupe, *Z. Naturf.* **A13**, 564 (1958).

[59] W. Maier and A. Saupe, *Z. Naturf.* **A14**, 882 (1959).

[60] W. Maier and A. Saupe, *Z. Naturf.* **A15**, 287 (1960).

[61] D. J. Photinos, E. T. Samulski, and H. Toriumi, *J. Phys. Chem.* **94**, 4688 (1990).

[62] D. J. Photinos, E. T. Samulski, and H. Toriumi, *J. Phys. Chem.* **94**, 4694 (1990).

[63] S. Marčelja, *J. Chem. Phys.* **60**, 3599–3604 (1974).

[64] W. H. de Jeu, J. van der Veen, and W. J. A. Goossens, *Solid State Commun.* **12**, 405 (1973).

[65] P.J. Flory, *Statistical Mechanics of Chain Molecules* (Wiley, New York, 1969).

[66] J. W. Emsley, G. R. Luckhurst, and C. P. Stockley, *Proc. R. Soc. London A* **381**, 117 (1982).

[67] J. W. Emsley and G. R. Luckhurst, *Mol. Phys.* **41**, 19 (1980).

[68] E. T. Samulski and R. Y. Dong, *J. Chem. Phys.* **77**, 5090 (1982).

[69] J. W. Emsley, N. J. Heaton, G. R. Luckhurst, and G. N. Shilstone, *Mol. Phys.* **64**, 377 (1988).

[70] E. J. Delikatny and E. E. Burnell, *Mol. Phys.* **67**, 775 (1989).

[71] J. P. Straley, *Phys. Rev. A* **10**, 1881 (1974).

[72] A. Weaver, A. J. van der Est, J. C. T. Rendall, G. L. Hoatson, G. S. Bates, and E. E. Burnell, *Liquid Cryst.* **2**, 633 (1987).

[73] M. Y. Kok, A. J. van der Est, and E. E. Burnell, *Liquid Cryst.* **3**, 485 (1988).

[74] E. E. Burnell, A. J. van der Est, G. N. Patey, C. A. de Lange, and J. G. Snijders, *Liquid Cryst.* **9**, 4 (1987).

[75] S. Mizushima and H. Okazaki, *J. Am. Chem. Soc.* **71**, 3411 (1949).

[76] N. Sheppard and G. J. Szasz, *J. Chem. Phys.* **17**, 86 (1949).

[77] A. Abe, R. J. Jernigan, and P. J. Flory, *J. Am. Chem. Soc.* **88**, 631 (1966).

[78] J. Devaure and J. Lascombe, *Nouv. J. Chim.* **3**, 2013 (1979).

[79] L. Colombo and G. Zerbi, *J. Chem. Phys.* **73**, 2013 (1980).

[80] S. Kint, J. R. Schere, and R. S. Snyder, *J. Chem. Phys.* **73**, 2599 (1980).

[81] L. Rosenthal, J. F. Rabolt, and J. Hummel, *J. Chem. Phys.* **76**, 817 (1982).

[82] P. T. Wong, H. H. Mantsch, and R. G. Snyder, *J. Chem. Phys.* **79**, 2369 (1983).

[83] I. Kanesaka, R. G. Snyder, and H. L. Strauss, *J. Chem. Phys.* **84**, 395 (1986).

[84] F. M. Menger and L. L. D'Angelo, *J. Am. Chem. Soc.* **110**, 8241 (1988).

[85] D. J. Photinos, B. J. Poliks, E. T. Samulski, A. F. Terzis, and H. Toriumi, *Mol. Phys.* **72**, 333–344 (1991).

[86] K. B. Wiberg and M. Murcko, *J. Am. Chem. Soc.* **110**, 8029–8038 (1988).

[87] A. Bax, *Two-Dimensional Nuclear Magnetic Resonance in Liquids* (Delft University Press, Dordrecht, 1982).

[88] J. Jeener, in *Amperè International Summer School* (Basko Polje, Yugoslavia, 1971).

[89] G. Wider, S. Macura, A. Kumar, R. R. Ernst, and K. Wüthrich, *J. Magn. Reson.* **56**, 207–234 (1984).

[90] D. L. Turner, *Prog. NMR Spectrosc.* **17**, 281–358 (1985).

[91] A. Bax and L. Lerner, *Science* **232**, 960–967 (1986).

[92] L. Braunschweiler and R. R. Ernst, *J. Magn. Reson.* **53**, 521–528 (1983).

[93] S. P. Rucker and A. J. Shaka, *Mol. Phys.* **68**, 509–517 (1989).

[94] D. G. Davis and A. Bax, *J. Am. Chem. Soc.* **107**, 2820–2821 (1985).

[95] D. G. Davis and A. Bax, *J. Am. Chem. Soc.* **107**, 7197 (1985).

[96] A. Bax and D. G. Davis, *J. Magn. Reson.* **65**, 355–360 (1985).

[97] J. S. Waugh, *J. Magn. Reson.* **68**, 189 (1986).

[98] S. Subramanian and A. Bax, *J. Magn. Reson.* **71**, 325–330 (1987).

[99] M. Rance, *J. Magn. Reson.* **74**, 557 (1987).

[100] R. Bazzo and J. Boyd, *J. Magn. Reson.* **75**, 452–466 (1987).

[101] R. Bazzo and I. D. Campbell, *J. Magn. Reson.* **76**, 358 (1988).

[102] S. R. Hartmann and E. L. Hahn, *Phys. Rev.* **128**, 2042 (1962).

[103] M. H. Levitt, R. Freeman, and T. Frenkiel. *Advances in Magnetic Resonance*, volume 11, pages 47–110. Academic Press, New York, 1983. J. S. Waugh, ed.

[104] J. S. Waugh, *J. Magn. Reson.* **50**, 30 (1982).

[105] M. H. Levitt and R. Freeman, *J. Magn. Reson.* **43**, 502–507 (1981).

[106] M. H. Levitt, R. Freeman, and T. Frenkiel, *J. Magn. Reson.* **47**, 328–330 (1982).

[107] M. H. Levitt, R. Freeman, and T. Frenkiel, *J. Magn. Reson.* **50**, 157 (1982).

[108] A. J. Shaka, T. Frenkiel, and R. Freeman, *J. Magn. Reson.* **52**, 159 (1983).

[109] A. J. Shaka, J. H. Keeler, T. Frenkiel, and R. Freeman, *J. Magn. Reson.* **52**, 335 (1983).

[110] A. J. Shaka, J. H. Keeler, and R. Freeman, *J. Magn. Reson.* **53**, 313 (1983).

[111] A. J. Shaka and J. H. Keeler, *Prog. NMR Spectrosc.* **19**, 47 (1987).

[112] U. Haeberlen and J. S. Waugh, *Phys. Rev.* **175**, 453 (1968).

[113] W. Magnus, *Commun. Pure Appl. Math.* **7**, 649 (1954).

[114] P. Pechukas and J. C. Light, *J. Chem. Phys.* **44**, 3897 (1966).

[115] G. C. Chingas, A. N. Garroway, R. D. Bertrand, and W. B. Moniz, *J. Chem. Phys.* **74**, 127 (1981).

[116] D. J. States, R. A. Haberkorn, and D. J. Ruben, *J. Magn. Reson.* **48**, 286 (1982).

[117] D. Marion and K. Wüthrich, *Biochem. and Biophys. Res. Commun.* **113**, 967–974 (1983).

[118] O. W. Sørensen, M. Rance, and R. R. Ernst, *J. Magn. Reson.* **56**, 527–534 (1984).

[119] J. .J. Titman, A. L. Davis, E. D. Laue, and J. Keeler, *J. Magn. Reson.* **89**, 176–183 (1990).

[120] D. I. Hoult and R. E. Richards, *Proc. R. Soc. London A* **344**, 311 (1975).

[121] A. J. Shaka, P. B. Barker, and R. Freeman, *J. Magn. Reson.* **71**, 520–531 (1987).

[122] A. J. Shaka, C. J. Lee, and A. Pines, *J. Magn. Reson.* **77**, 274–293 (1988).

[123] G. W. Eich, G. Bodenhausen, and R. R. Ernst, *J. Am. Chem. Soc.* **104**, 3731 (1982).

[124] P. H. Bolton and G. Bodenhausen, *Chem. Phys. Lett.* **89**, 139 (1982).

[125] J. Cavanagh, W. J. Chazin, and M. Rance, *J. Magn. Reson.* **87**, 110–131 (1990).

[126] S. J. Glaser and G. P. Drobny, *Adv. Mag. Reson.* **14**, 35–58 (1990).

[127] M. L. Remerowski, S. J. Glaser, and G. P. Drobny, *Mol. Phys.* **68**, 1191–1218 (1989).

[128] A. Bax and D. G. Davis, *J. Magn. Reson.* **63**, 207–213 (1985).

[129] J. Jeener, B. H. Meier, P. Bachmann, and R. R. Ernst, *J. Chem. Phys.* **71**, 4546–4553 (1979).

[130] A. A. Bothner-By, R. L. Stephens, J. Lee, C. D. Warren, and R. W. Jeanloz, *J. Am. Chem. Soc.* **106**, 811–813 (1984).

[131] K. Elbayed and D. Canet, *Mol. Phys.* **71**, 979–993 (1990).

[132] R. Bazzo, C. J. Edge, M. R. Wormald, T. W. Rademacher, and R. A. Dwek, *Chem. Phys. Lett.* **174**, 313–319 (1990).

[133] D. Neuhaus and M. P. Williamson, *The Nuclear Overhauser Effect in Structural and Conformational Analysis* (VCH Publishers, New York, 1989).

[134] M. Kadkhodaie, O. Rivas, M. Tan, A. Mohebbi, and A. J. Shaka, *J. Magn. Reson.* **91**, 437–443 (1991).

[135] A. Mohebbi and A. J. Shaka, *Chem. Phys. Lett.* **178**, 374–378 (1991).

[136] A. J. Shaka, S. P. Rucker, and A. Pines, *J. Magn. Reson.* **77**, 606–611 (1988).

[137] H. Y. Carr and E. M. Purcell, *Phys. Rev.* **94**, 630 (1954).

[138] S. Meiboom and D. Gill, *Rev. Sci. Instrum.* **29**, 688 (1958).

[139] E. Hahn, *Phys. Rev.* **80**, 580 (1950).

[140] A. A. Maudsley, *J. Magn. Reson.* **69**, 488–491 (1986).

[141] A. Kumar, D. Welti, and R. R. Ernst, *J. Magn. Reson.* **18**, 69 (1975).

[142] W. A. Edelstein, J. M. S. Hutchison, G. Johnson, and T. Redpath, *Phys. Med. Biol.* **25**, 751 (1980).

[143] B. Mandelbrot, *The Fractal Geometry of Nature* (W. H. Freeman, New York, 1977).

[144] R. Tycko. *Broadband Excitation in Nuclear Magnetic Resonance.* PhD thesis, University of California, Berkeley, 1984.

[145] H. M. Cho. *Theory and Applications of Maps on SO(3) in Nuclear Magnetic Resonance.* PhD thesis, University of California, Berkeley, 1987.

[146] J. S. Waugh, *J. Magn. Reson.* **49**, 517 (1982).

[147] M. H. Levitt and R. R. Ernst, *J. Magn. Reson.* **55**, 247 (1983).

[148] R. Tycko and A. Pines, *Chem. Phys. Lett.* **111**, 462 (1984).

[149] R. Tycko, A. Pines, and J. Guckenheimer, *J. Chem. Phys.* **83**, 2775 (1985).

[150] H. Cho, J. Baum, and A. Pines, *J. Chem. Phys.* **86**, 3089 (1987).

[151] A. J. Shaka, C. Bauer, and R. Freeman, *J. Magn. Reson.* **60**, 479 (1984).

[152] R. Freeman, S. P. Kempsell, and M. H. Levitt, *J. Magn. Reson.* **35**, 447–450 (1979).

[153] A. G. Anderson and S. R. Hartmann, *Phys. Rev.* **128**, 2023 (1962).

[154] M. Goldman, *Spin Temperature and NMR in Solids* (Oxford University Press, London, 1970).

[155] R. D. Bertrand, W. B. Moniz, A. N. Garroway, and G. C. Chingas, *J. Am. Chem. Soc.* **100**, 5227 (1978).

[156] J. Baum, R. Tycko, and A. Pines, *Phys. Rev.* **32**, 3435 (1985).

[157] M. S. Silver, R. I. Joseph, and D. I. Hoult, *J. Magn. Reson.* **59**, 347 (1984).

[158] C. J. Hardy, W. A. Edelstein, and D. Vatis, *J. Magn. Reson.* **66**, 470 (1986).

[159] C. P. Slichter, *Principles of Magnetic Resonance*, 3rd edition (Springer Verlag, New York, 1989).

[160] A. Abragam and W. G. Proctor, *Phys. Rev.* **109**, 1441–1458 (1958).

[161] A. G. Redfield, *Science* **164**, 1015–1023 (1969).

[162] M. V. Berry, *Proc. R. Soc. London A* **430**, 405–411 (1990).

[163] J. W. Zwanziger, S. P. Rucker, and G. C. Chingas, *Phys. Rev. A* **43**, 3232–3240 (1991).

[164] M. V. Berry, *Proc. R. Soc. London A* **414**, 31–46 (1987).

[165] Y. Aharanov and J. Anandan, *Phys. Rev. Lett.* **58**, 1593 (1987).

[166] J. Anandan, *Phys. Lett. A* **133**, 171 (1988).

[167] N. Datta, G. Ghosh, and M. H. Engineer, *Phys. Rev. A* **40**, 526 (1989).

[168] B. Zygelman, *Phys. Rev. Lett.* **64**, 256 (1990).

[169] J. Samuel and R. Bhandari, *Phys. Rev. Lett.* **60**, 2339 (1988).

[170] J. C. Garrison and E. M. Wright, *Phys. Lett. A* **128**, 177 (1988).

[171] S.-I. Chu, Z.-C. Wu, and E. Layton, *Chem. Phys, Lett.* **157**, 151 (1989).

[172] J. Anandan and A. Pines, *Phys. Lett. A* **141**, 335 (1989).

[173] P. V. Coveney, D. S. F. Crothers, and J. H. Macek, *J. Phys. B* **21**, L165 (1988).

[174] E. A.Solov'ev, *Topological Phases in Quantum Theory* (World Scientific, Singapore, 1989). B. Markovski and S. I. Vinitsky, eds.

[175] J. Moody, A. Shapere, and F. Wilczek, *Geometric Phases in Physics* (World Scientific, Singapore, 1989). A. Shapere and F. Wilczek, eds.

[176] A. M. Dykhne, *Sov. Phys. JETP* **14**, 941 (1962).

[177] J. P. Davis and P. Pechukas, *J. Chem. Phys.* **64**, 3129 (1976).

[178] J.-T. Hwang and P. Pechukas, *J. Chem. Phys.* **67**, 4640 (1977).

[179] P. Pechukas, T. F. George, K. Morokuma, F. J. McLafferty, and J. R. Laing, *J. Chem. Phys.* **64**, 1099 (1976).

[180] G. Giavarini, E. Gozzi, D. Rohrlich, and W. D. Thacker, *J. Phys. A* **22**, 3513 (1989).

[181] M. Odehnal and V. Petricek, *Phys. Lett. A* **41**, 359 (1972).

[182] W. S. Warren, S. L. Hammes, and J. L. Bates, *J. Chem. Phys.* **91**, 5895 (1989).

[183] M. V. Berry, *Proc. R. Soc. London A* **429**, 61 (1990).

[184] B. Simon, *Phys. Rev. Lett.* **51**, 2167 (1983).

[185] G. P. Drobny. *NMR Studies of Liquid Crystals and Molecules Dissolved in Liquid Crystal Solvents.* PhD thesis, University of California, Berkeley, 1982.

[186] Tecmag Inc., 6006 Bellaire Blvd., Houston, TX 77081.

[187] Bruker Instruments Inc., Manning Park, Billerica, MA 01821.

[188] Oxford Instruments, North America, 3A Alfred Circle, Bedford, MA 01730.

[189] Nalorac Cryogenics Corp., 837 Arnold Dr. Suite 600, Martinez, CA 94553.

[190] American Magnetics Inc., P.O. Box 2509, Oak Ridge, TN 37831-2509.

[191] Programmed Test Sources Inc., 9 Beaver Brook Rd., Littleton, MA 01460.

[192] A. J. Shaka, D. N. Shykind, G. C. Chingas, and A. Pines, *J. Magn. Reson.* **80**, 96 (1988).

[193] U. Haubenreisser and B. Schnabel, *J. Magn. Reson.* **35**, 175 (1979).

[194] D. N. Shykind, G. C. Chingas, A. Pines, and A. J. Shaka, *Rev. Sci. Instrum.* **61**, 1474–1479 (1990).

[195] D. N. Shykind. *Phase Shifting and Imaging in Solid State NMR.* PhD thesis, University of California, Berkeley, 1989.

[196] Cryomagnet Systems Inc., 4101 Cashard Ave. #103, Indianapolis, IN 46203.

[197] R. L. Vold and R. R. Vold, *J. Magn. Reson.* **55**, 78–87 (1983).

[198] Omega Engineering Inc., One Omega Dr. Box 4047, Stamford, CT 06907-0047.

[199] Newport Electronics Inc., 2229 S. Yale St., Santa Ana, CA 92704-4426.

[200] MDB Systems Inc., 1995 N. Batavia St., Orange, CA 92613-5508.

[201] M. E. Rosen. PhD thesis, University of California, Berkeley, to be submitted.

LAWRENCE BERKELEY LABORATORY
UNIVERSITY OF CALIFORNIA
INFORMATION RESOURCES DEPARTMENT
BERKELEY, CALIFORNIA 94720